12-1-2012

Ore and Gangue Mineral Paragenesis of the Cortez Hills Carlin-Type Gold Deposit, Nevada: Evidence for Coincident High-Grade Gold Deposition and Collapse Brecciation

Lindsey R. Clark
University of Nevada, Las Vegas, clarkl6@unlv.nevada.edu

ORE AND GANGUE MINERAL PARAGENESIS OF THE CORTEZ HILLS CARLIN-TYPE GOLD DEPOSIT, NEVADA: EVIDENCE FOR COINCIDENT HIGH-GRADE GOLD DEPOSITION AND COLLAPSE BRECCIATION

by

Lindsey R. Clark

Bachelor of Science in Geoscience
University of Nevada, Las Vegas
2009

A thesis submitted in partial fulfillment
of the requirements for the

Master of Science in Geoscience

Department of Geoscience
College of Sciences
The Graduate College

University of Nevada, Las Vegas
December 2012

THE GRADUATE COLLEGE

We recommend the thesis prepared under our supervision by

Lindsey Clark

entitled

Ore and Gangue Mineral Paragenesis of the Cortez Hills Carlin-Type Gold Deposit, Nevada: Evidence for Coincident High-Grade Gold Deposition and Collapse Brecciation

be accepted in partial fulfillment of the requirements for the degree of

Master of Science in Geoscience
Department of Geoscience

Jean S. Cline, Ph.D., Committee Co-Chair

Adam C. Simon, Ph.D., Committee Co-Chair

John L. Muntean, Ph.D., Committee Member

Barbara Luke, Ph.D., Graduate College Representative

Tom Piechota, Ph.D., Interim Vice President for Research &
Dean of the Graduate College

December 2012

ABSTRACT

Ore and Gangue Mineral Paragenesis of the Cortez Hills Carlin-Type Gold Deposit, Nevada: Evidence for Coincident High-Grade Gold Deposition and Collapse Brecciation

by

Lindsey R. Clark

Dr. Jean S. Cline, Examination Committee Co-chair
Professor
University of Nevada, Las Vegas

Dr. Adam C. Simon, Examination Committee Co-chair
Associate Professor
University of Michigan

The Cortez Hills Carlin-type gold deposit (CTGD), located on the Battle Mountain-Eureka trend of Northern NV, is hosted in a conical shaped polylithic breccia whose central axis strikes parallel to the imbricate Voodoo fault system. Gold grades at the center of the Cortez Hills Breccia Zone (CHBZ) are locally in excess of an ounce per ton. Gold mineralization within the refractory ore at Cortez Hills shares many characteristics with other well studied CTGDs. However, new observations during this study have recognized 1) fragmented realgar that are rimmed by gold-bearing iron-sulfide minerals in four samples, 2) a Hg- and Tl-rich late-ore stage characterized by rare minerals, and 3) textural relationships show that ore-stage mineralizing fluids enhanced porosity through decarbonatization, resulting in contemporaneous brecciation and Au mineralization.

The primary objectives of this thesis project were to produce a paragenesis and characterize mineralization at the Cortez Hills deposit with an emphasis on the CHBZ in order to test the hypothesis that the CHBZ contains typical Carlin-type mineralization and

alteration. The data collected indicate that the CHBZ refractory ore exhibits the following paragenetic relationships. 1) Diagenetic pyrite was deposited in passive margin carbonate sediments. 2) A pre-ore suite of minerals apparently associated with low-grade contact metamorphism includes sphalerite, chalcopyrite, and tremolite. 3) Ore stage alteration minerals include illite, ore-stage jasperoid, and Au- and trace element-rich iron sulfides. 4) Hg- and Tl-rich minerals including aktashite ($Cu_6Hg_3As_4S_{12}$) and christite ($TlHgAsS_3$) precipitated during a late-ore stage directly following the precipitation of Au-bearing iron sulfides. 5) Late- to post-ore stage minerals include realgar and calcite that are associated with cooling and collapse of the hydrothermal system.

As a secondary goal, data were collected to test the hypothesis that Carlin-type mineralization occurred contemporaneously with brecciation throughout the CHBZ; understanding this relationship is necessary to understand how the CHBZ formed. Transects through host rocks that transition from negligible to high Au concentrations show a succession from primarily recrystallized calcite into rocks that contain Au-bearing iron sulfides, illite, fine grained calcite, and insoluble residual material precipitated in dissolution seams. As Au concentrations continue to increase within the ore body, host rocks that contain dissolution seams transition into heavily brecciated rocks with strongly mineralized clasts and a lightly mineralized matrix. Late-ore stage realgar precipitated in open space throughout the breccia, which is evident because it commonly conforms to euhedral crystal faces and cements zones of intense fracturing and areas of high porosity. This study concludes that the dissolution seams reveal Carlin ore fluid pathways through the carbonate host rocks, and extensive fluid-rock interaction along these seams ultimately resulted in brecciation.

Late-ore-stage realgar precipitation in open space throughout the breccia signifies that brecciation terminated with cessation of the ore fluid incursion throughout the majority of the CHBZ. However, an area within the CHBZ contains fragmented realgar clasts with Au-bearing iron-sulfide rims, indicating localized mineralization both post- and pre-brecciation. The consistent association between fragmentation and mineralization of realgar clasts indicates that the same process that fragmented the realgar also allowed the ore fluid to be reintroduced to previously mineralized rocks. Reactivation along a fault may have fragmented the realgar and reduced pressure sufficiently to allow the Au-bearing fluid to encounter an area that was previously cooler and collapsing, thus mineralizing the same area twice.

ACKNOWLEDGEMENTS

First and foremost, I would like to thank Dr. Jean Cline and Dr. Adam Simon, my committee co-chairs, for always making themselves available to answer questions, discuss my ideas, advise me, and provide direction in every aspect. Thank you to Dr. John Muntean for being an actively involved third committee member and providing significant insight into my research and to Dr. Barbara Luke, the graduate college representative.

I am also grateful to Barrick Gold Corporation for funding this project, and specifically the Cortez Hills GeoServices group. Special thanks to Page Anderson for all of the time dedicated to assisting me in so many aspects of this project, including sample collection, compiling background information, and suggestions on the presentation of data. Thank you to Roger Bond for handling the financial logistics, allowing Page Anderson to dedicate so much of her time, and for making this project possible. Also, thank you to Tom Whittle, Kerry Hart, and Roger Bond for originally getting this project started.

I would also like to acknowledge the Society of Economic Geologists (SEG), Northern California Geological Society, UNLV Graduate and Professional Student Association (GPSA), and the UNLV Geosciences Department for the fellowships, grants, and scholarships that I was awarded throughout my graduate studies.

Additionally, special thanks to everyone who helped me collect data and the hours of discussion that came along with it, including Alan Koenig at the USGS Denver LA-ICP-MS lab, Christopher Adcock and Minghua Ren at the UNLV EMiL lab, and Oliver Tschauner and John Howard at the UNLV XRD lab.

TABLE OF CONTENTS

LIST OF TABLES

LIST OF FIGURES

CHAPTER 1

INTRODUCTION

The Cortez Hills ore deposit, discovered in 2002, is located on the Battle Mountain-Eureka trend in Nevada, U.S.A., amidst multiple world-class Carlin-type gold deposits (CTGD) (Fig. 1). Nevada is the type locality for CTGDs, which constitute the second largest concentration of Au in the world, with more than 76 million ounces of Au produced from the Carlin trend alone by the end of 2010 (Nevada Bureau of Mines and Geology, 2010). The CTGDs in Nevada were estimated to have contained more than 200 million ounces of gold before mining began (Cline et al., 2005; Sillitoe, 2008). The Cortez property has proven and probable reserves of 14.5 million ounces of Au; it is one of the world's largest and lowest cost gold mines (Barrick, 2011).

Many CTGDs have been studied in great detail because of their large Au endowments. Published studies (Cline, 2001; Cline et al., 2005) suggest that CTGDs resulted from channelized flow of auriferous-hydrothermal fluids along preexisting fault conduits. As ore fluids traveled up the conduits, low-permeability siliceous and intrusive rocks generally acted as seals while underlying porous and permeable carbonate rocks reacted extensively with the ore fluid. The deposits are replacement ore bodies that formed as the ore fluid decarbonatized the silty carbonate host rocks and simultaneously deposited gold by fluid-rock reactions and host rock sulfidation. CTGD ore characteristically contains Au that is present in solid solution or as submicron sized particles in trace metal-rich pyrite or marcasite (Palenik et al., 2004; Reich et al., 2005; Cline et al., 2005), resulting in Au that is invisible to the unaided eye and conventional optical microscopes. Additionally, the ore deposition processes typically result in very

subtle alteration patterns, which make some mineralized zones difficult to identify (Cline et al., 2005).

The extensive decarbonatization associated with the formation of most CTGDs causes an increase in porosity and permeability that can result in host rock brecciation due to volume loss and gravitational collapse, exemplified in deposits such as the Meikle breccia (Evans, 2000; Emsbo et al., 2003). The Cortez Hills breccia zone (CHBZ) is a discordant, upward-flaring conical breccia pipe that spans 2,500 vertical feet; however, Barrick Gold Corp. exploration geologists at the Cortez Mine interpret many features of the CHBZ as being characteristic of a hydrothermal breccia rather than a collapse breccia (Jackson et al., 2010). Characteristics that support this interpretation include angular clasts in a fine-grained clastic infill, interpreted upward movement of individual clasts, and the absence of bell shaped breccia geometries (Jackson et al., 2010). The Cortez Hills deposit is unique because of the strong correlation of anomalously high gold (up to 30.5 oz/t) with an unusual polylithic breccia zone.

Previous studies (e.g., Groff et al., 1997; Cline and Hofstra, 2000; Cline, 2001: Almeida et al., 2010) of CTGDs provided a paragenetic sequence (Fig. 2), which constrains temporal relationships among pre-ore, syn-ore, and late-ore-stage mineralization. Ore fluids precipitated spatially associated alteration minerals that commonly include quartz, kaolinite and illite, though these minerals are not always present and are not necessarily well zoned around Au. As individual ore systems collapsed and cooled during influx of meteoric waters, a suite of late-ore minerals precipitated that includes orpiment, realgar, stibnite, and calcite (Fig. 2) (Cline, 2001).

The main objectives of this thesis project were to deduce a paragenesis and characterize mineralization at the Cortez Hills deposit with an emphasis on the CHBZ in order to test the hypothesis that the CHBZ contains typical Carlin-type mineralization and alteration. Research focused on a detailed macro- and micro-scopic characterization of the ore, which allowed constraint of paragenetic relationships among pre-ore, syn-ore, and late-ore-stage mineralization and provided insight into how the chemistry of the ore fluid may have changed through time within the CHBZ.

A second objective of this thesis research was to test the hypothesis that Carlin-type mineralization and brecciation occurred contemporaneously throughout the CHBZ, which is critical to developing a formation model for the Cortez Hills deposit. This was accomplished by investigating the temporal relationships between mineralization and brecciation through examination of crosscutting relationships among ore-stage minerals, breccia clasts and matrix. Additionally, transects within sulfide-bearing rocks that transition from high-grade mineralization to low-grade mineralization over short distances (e.g., two to sixteen feet) were collected. Such transects are valuable because they minimize variations in primary lithology so that changes in mineralogy and texture can be related to the mineralization processes.

CHAPTER 2

BACKGROUND

Carlin-type Gold Deposit Genetic Models and Geologic History

Carlin-type gold deposits across northern Nevada share similar mineralization and alteration characteristics; however, there is not a widely accepted genetic model that explains all observations and, notably, the source of gold. Multiple geological models have been proposed to explain the formation of CTGDs: 1) deeply sourced magmatic ore fluid was generated during the Eocene as the Farallon plate was decoupled from western North America, allowing an influx of mantle-derived mafic magmas, causing partial melting and exsolution of mantle-derived volatiles (Cline et al., 2005; Muntean et al., 2011); 2) a metamorphic model that invokes devolatilization of sedimentary rocks during prograde metamorphism (Hofstra and Cline, 2000) and the ascent of metamorphic fluids during significant Eocene Basin and Range extension (Seedorff, 1991); 3) an epizonal intrusion model that states that CTGDs are related to relatively shallow magma intrusions of intermediate to silicic compositions (Sillitoe and Bonham, 1990; Johnston and Ressel, 2004), which implies a genetic relationship to porphyry-style mineralization; and 4) a meteoric model that invokes convection of meteoric fluids to depths >10 km, where gold was leached from Neoproterozoic rocks (Ilchik and Barton, 1997).

Although there is no consensus on any one of the aforementioned genetic models, it is generally accepted that all CTGDs in Nevada formed at similar geologic conditions as a result of the same geologic processes. The western margin of the North American continent is interpreted to represent a passive margin from approximately Late Precambrian to the Late Devonian (Poole et al., 1992). Prior to the development of the

passive margin, rifting occurred in North America. The main stage of rifting is believed to have started around 600 Ma (Saleeby et al., 1987; Poole et al., 1992). Rifting resulted in the formation of deep, basement penetrating crustal scale faults that are hypothesized to have become fluid conduits for Eocene Carlin-type mineralization, providing an explanation for the locations of CTGDs along linear trends (Tosdal et al., 2000; Crafford and Grauch, 2002; Cline et al., 2005). During sedimentation along the passive margin, a eugeoclinal sequence developed that was comprised of deep water sedimentary rocks to the west, including siliceous chert, shale, quartzite, and mafic volcanic rocks that are interbedded with calcareous units. To the east, more shallow-water sedimentary rocks, including continental shelf carbonate rocks, dolomite, and minor shale and siltstone were deposited (Stewart, 1980).

Passive margin sedimentary rocks were deformed by a series of regional compression events that began during the Late Devonian and Early Mississippian, beginning with the Antler orogeny (385-345 Ma) (Roberts, 1958). Less reactive eugeoclinal siliciclastic sedimentary rocks were thrust eastward over reactive shelf-slope miogeoclinal carbonate rocks, forming the Roberts Mountain Thrust (RMT). Compression continued along the western margin of North America, with subduction of the Farallon plate beneath the North American plate beginning in the late Triassic (~210 Ma) (Dickinson, 2004). The Farallon plate is thought to have coupled to the bottom of the North American plate during shallow subduction beginning around 65 Ma (Humphreys, 1995).

A transition from contractional deformation to extension began during the mid-Eocene (45 Ma) as a result of the Farallon plate decoupling from the North American

plate. This slab rollback allowed hot asthenospheric mantle to impinge on the base of a hydrated North American plate, producing high K calc-alkaline magmatism that swept through Nevada from north to south (Armstrong and Ward, 1991; Seedorff, 1991; Henry and Boden, 1998; Ressel and Henry, 2006). Geochronological studies suggest that CTGDs formed between 36 to 42 Ma, which overlaps in time with the calc-alkaline volcanism (Ressell and Henry, 2006; Muntean et al., 2011).

Eocene extension reactivated compressional structures facilitating ore fluid flow. Ore fluids ascended and decarbonatized lower plate carbonate rocks below the less permeable and siliciclastic upper plate rocks of the RMT. Ore-stage fluid inclusions have been used to reconstruct the depths of gold mineralization to within a few kilometers of the paleosurface (Cline et al., 2005). The fluid inclusion data indicate that the CTGD ore fluids were moderate temperature (~180°-240°C), low salinity (~2-3 wt% NaCl equiv), CO_2 bearing (<4 mol%), and CH_4 poor (<0.4 mol %), with sufficient H_2S (10^{-1}-10^{-2} m) to transport Au (Cline and Hofstra, 2000). Fluid-rock reaction caused carbonate dissolution and replacement by quartz simultaneously with gold deposition as ore fluids sulfidized host rock Fe.

At approximately 17 Ma, Basin and Range style extension commenced in Nevada, which resulted in steeply-dipping, deep-rooted, widely-spaced normal faults and tilted fault blocks that are separated by alluvium (Stewart, 1980). Local zones of major extension are characterized by closely spaced normal faults (Colgan et al., 2011). For most CTGDs, the tilted fault blocks aided in exposing the lower plate of the RMT by tilting many mineralized regions closer to the surface, although this is not documented at Cortez Hills.

Cortez Hills Breccia Zone

Local Stratigraphy

The CHBZ mineralization is hosted in the lower plate passive margin Silurian to Devonian slope, basin, and platform carbonate rocks of the RMT, which includes the Silurian Roberts Mountains (Srm) Formation, the Devonian Wenban (Dw) Formation, and the lowermost portion of the Upper Devonian Horse Canyon (Dhc) formation (Jackson et al., 2010) (Fig. 3). Cortez Hills Lower Zone (CHLZ) mineralization is hosted in the Ordovician Hansen Creek and Silurian Roberts Mountains formations. The Devonian Wenban and Upper Devonian Horse Canyon formations are stratigraphically correlative to the Devonian Popovich and Devonian Rodeo Creek formations of the northern Carlin trend (Jackson et al., 2010). The Cortez Hills host rock stratigraphy is down dropped adjacent to the Mill Canyon stock by the Cortez Fault (Figs. 4-5). Eocene quartz porphyry dikes (Epd) typically crosscut the Paleozoic formations (Figs. 4-5).

The Roberts Mountains Formation is approximately 350 meters thick (L.P. Anderson, Barrick Cortez GeoServices, pers. comm., 2012) in regions that are not heavily faulted and is primarily composed of black thinly laminated silty slope-to-basin limestone that contains sparse interbedded turbidites (Harry Cook, Barrick Internal Report, 2008; Jackson et al., 2010). The Roberts Mountains Formation commonly contains black phosphate nodules in specific members and can be altered to calc-silicate marble owing to contact metamorphism (Jackson et al., 2010) (Fig. 5). A one to three meter thick fossil hash debris flow located in the upper surface of the Roberts Mountains Formation represents the stratigraphic boundary between the Robert Mountains

Formation and the overlying Devonian Wenban Formation (Harry Cook, Barrick Internal Report, 2008; Jackson et al., 2010).

The Wenban Formation is approximately 850 m thick (L.P. Anderson, Barrick Cortez GeoServices, pers. comm., 2012) and is primarily composed of a thin-bedded to thin-laminated dark grey to black micrite and silty micrite that contains black phosphate nodules and diagenetic pyrite within some laminae of the basal unit (Jackson et al., 2010). Soft sediment deformation is common in the basal unit. Going up-section, the Wenban Formation becomes extensively bioturbated and there is an increase in brachiopod fragments (Harry Cook, Barrick Internal Report, 2008; Jackson et al., 2010). Additionally, the formation becomes more thinly-bedded with an increase in carbonate and silt grains (L.P. Anderson, Barrick Cortez GeoServices, pers. comm., 2012). Below the uppermost Wenban Formation, soft sediment slumps are dominant; the uppermost 90 meters are relatively heterogeneous and include lime mudstones, turbidites, and debris flows (Harry Cook, Barrick Internal Report, 2008; Jackson et al., 2010). Within the Cortez Hills window, the Wenban and Roberts Mountains formations are thickened by thrust faults and associated compressive folding (Jackson et al., 2010). The Wenban Formation formed along the platform margin or higher on the slope than the Roberts Mountains Formation, and contains more bioclastic and carbonate material and significantly less clastic material than the Roberts Mountains Formation.

The Horse Canyon formation as exposed at Cortez Hills is composed of interbedded calcareous siltstone and chert-rich members. The formation is highly deformed possibly owing to its locality at the base of the RMT; however, the RMT is not visible in the locality of the deposit. The formation is hypothesized to have an erosional

contact with the Wenban Formation, evident by Wenban clasts incorporated within the base of the Horse Canyon Formation (Jackson et al., 2010). Field relationships exposed in the Cortez Hills open pit indicate that much of the deformation in the Horse Canyon may be due to local brecciation rather than a regional compressional event (L.P. Anderson, Barrick Cortez GeoServices, pers. comm., 2012).

The Jurassic Mill Canyon stock is a quartz monzonite and diorite that is enriched in hornblende and biotite and located approximately 0.5 kilometers northeast of the deposit (Figs. 4-5) (Jackson et al., 2010). The stock is in contact with Paleozoic rocks and it has been proposed by Venendaal (2007) that the thermal aureole of the stock metamorphosed the units in the vicinity of the CHBZ, forming marble and calc-silicate minerals. However, Gilluly and Masursky (1965) mapped the stock and report a narrow metamorphic aureole. Alternatively to Venendall (2007), other researchers (Henry and Muntean, 2012) interpret a 104 Ma quartz monzonite intrusive with a wide metamorphic aureole to be responsible for contact metamorphism of Cortez Hills. This intrusive was discovered in a drill hole approximately 4km west of Cortez Hills and does not outcrop (Henry and Muntean, 2012).

Eocene quartz porphyry dikes and sills are abundant within the area of CHBZ and 13 sanidine analyses yielded an average $^{40}Ar/^{39}Ar$ date of 35.69 Ma (±0.06) (Colgan et al., 2011). A second study also concludes an average $^{40}Ar/^{39}Ar$ date of 35.29 Ma (±0.08), yielded from five samples (Artz, 2004). The dikes and sills are rhyolitic in composition and commonly have quartz, sanidine, and biotite phenocrysts (Jackson et al., 2010). Some dikes and sills are extensively altered to clay minerals and contain pyrite.

Throughout CHBZ, most dikes crosscut the mineralization; however, in some areas, realgar, pyrite, and low Au concentrations occur within the dikes.

Structure

Owing to compression that commenced in Nevada in the Late Devonian, the Cortez district contains abundant low-angle faults, duplex folds, and imbricate fault zones that are commonly parallel with bedding (Jackson et al., 2010). The Roberts Mountains Formation experienced extensive deformation due to thin beds that allow the bedding planes to slip, whereas the Wenban Formation responded to strain differently, resulting in ramping, faulting, and decoupling within its lower members (Jackson et al., 2010). The fold architecture of the Roberts Mountains and Wenban formations is cut by the Pondorosa Fault Zone, a very low angle thrust zone that breaks and duplicates the Wenban and Roberts Mountains formations. This fault zone has been described as a feeder zone to the base of CHBZ and a control on mineralization in the CHLZ (Fig. 5) (Jackson et al., 2010). Mineralization is present within this zone, but not associated with the main breccia body, as brecciation is relatively absent within the CHLZ.

The CHBZ contains both low- and high- angle structures with apparent reverse, normal, and right-lateral displacement (L.P. Anderson, Barrick Cortez GeoServices, pers. comm., 2012). The Voodoo Fault, which has been measured in drill core as striking approximately 325° and dipping 34°SW cuts through the center of the CHBZ (Fig. 5). There is no significant displacement of the CHBZ by the Voodoo fault, and mineralization occurs in the hanging and foot walls. The F Canyon Fault cuts across the western contact of the CHBZ (Fig. 5), and no significant brecciation is associated with the fault. This fault strikes 334° and dips 70°SW. The Pizarro Fault (Fig. 5) was a

conduit for a large Eocene dike swarm that strikes 200° and dips 66°NW. All three of these faults flatten as they merge into the Ponderosa Fault Zone (Fig. 5).

Breccia Body

The characteristics of the CHBZ were described by Jackson et al. (2010) and are briefly summarized here. The CHBZ has a conical geometry and a generally concentric internal organization that consists of a polylithic breccia at the center and a monolithic crackle breccia that displays limited dilation along the margin (Fig. 6). The polylithic breccia has been interpreted to contain evidence of upward transport; petrographic studies on the polylithic breccia report distinctive Wenban subunits that contain laminated bedding, authigenic pyrite, and high carbon content located 50 m above their stratigraphic level within the breccia, consistent with upward movement (Jackson et al., 2010). The locations of these clasts were not documented in Jackson et al. (2010) and were not observed in the current study. Other observations interpreted to be consistent with a polylithic breccia include the occurrence of bleached clasts adjacent to less altered clasts (Fig. 7a). The central polylithic breccia grades outwards into a monolithic breccia that contains rotated clasts, and then grades further outwards into a monolithic crackle breccia. The concentration of Au varies throughout the CHBZ, but generally the highest grades correlate closely with the central breccia zone and the lowest grades occur in the outer crackle breccia (Fig. 8).

Clastic and chemical infill have been documented and described in hand sample by Jackson et al. (2010). The clastic infill ranges in grain size from coarse sand to silt, interpreted to be a result of mechanical milling or extensive dissolution (Fig. 7b) (Jackson et al., 2010). Primarily altered and unaltered limestone clasts comprise the clastic infill.

This material usually does not react with dilute hydrochloric acid, which suggests decarbonatization (Jackson et al., 2010). Chemical infill is dominated by calcite and realgar; the infill completely fills former voids and forms the matrix of some breccia samples (Fig. 7c), or is less abundant in other samples (Fig. 7a). Realgar in some samples is located within clasts of the breccia and truncated at the clast margins (Fig. 7a). Jackson et al. (2010) did not observe silica or pyrite within the breccia infill.

The breccia clast size encountered in drill core ranges from clay-size particles to 20-meter blocks of limestone (Jackson et al., 2010). The finest-grained breccia is immediately adjacent to the largest clasts, which the authors interpreted as a result of fluidization around large clasts and pressure shadows that developed as the block moved downward. The authors interpret upward and downward moving clasts within the breccia. Jackson et al. (2010) reported that the clasts are angular to subangular with a complete absence of extremely rounded clasts. However, multiple samples collected for this study did contain subrounded clasts (Fig. 7d).

The sequence of events postulated by Jackson et al. (2010) to have formed the CHBZ is summarized in Figure 9. The authors concluded that the brecciation was associated with Carlin-type hydrothermal fluids and mechanically energetic fluids, suggesting an energy release within a Carlin-type hydrothermal system. They concluded that the characteristics of the CHBZ are not consistent with the collapse-breccia model of Jebrak (1997), but instead are more analogous to a volcanic-hydrothermal diatreme-style breccia (Sillitoe, 1985) that resulted from thermo-hydraulic energy release (Kurszlaukis and Lorenz, 2006, personal communication *in* Jackson et al., 2010). The authors do not state the detailed mechanisms that form brecciation, but hypothesize that proximity to the

paleosurface, high water temperatures, and the opportunity to overpressure the fluid by tectonic processes, may have resulted in the fluid becoming overpressured within the system via thermohydraulic forces. These combined factors may result in explosive brecciation without direct magmatic or phreatomagmatic input into the system (Jackson et al., 2010)

Oxidation

The majority of the rocks in the CHBZ are oxidized, containing no sulfide minerals. Jackson et al. (2010) have observed the iron-oxide minerals hematite, goethite, jarosite, and other unidentified oxide and arsenate minerals. The cause of oxidation has not been constrained; however, the observation that the entire matrix and all of the clasts in some rocks are oxidized is interpreted to indicate that oxidation post-dates brecciation (Jackson et al., 2010). Jackson et al. (2010) noted that oxidation contacts are very sharp and abrupt against sulfide-bearing rocks and liesegang banding is common. The authors concluded that the oxidizing fluid reacted with pyrite to produce acid, which resulted in significant volume loss, which is evident where oxidation has crosscut calcite-infilled breccia, removed calcite, and decreased clast sizes.

Geochemical Patterns

All of the geochemistry and interpretation in this section is summarized from Venendaal (2007). The author conducted an investigation of the geochemical zoning within the Cortez Hills deposit prior to the discovery of CHLZ. Carbonate staining on individual samples was done in order to map the distribution of Ca, Sr, Mg, and Mn along a cross section to identify possible zoning of carbonate mineralogy. The study located zones of calcite and determined that iron-bearing carbonate minerals are spatially

associated with mineralized rocks on the hand sample scale. Venendaal (2007) did not observe large-scale carbonate zoning at Cortez Hills and concluded that carbonate zoning possibly existed at an earlier time, but later oxidation altered an early record of dolomitization and subsequent decarbonatization.

Geochemical analysis by using the ALS CEMEX ME-MS41 package with aqua regia digestion allowed Venendaal (2007) to conclude that there are five different overlapping geochemical populations within Cortez Hills: lithologically controlled, tungsten-related, base metal, Carlin-type, and supergene oxidation. The rocks along the contact between the Roberts Mountains Formation and Wenban Formation are enriched in Mo, Ni, Fe, P, U, and V, interpreted by Venendaal (2007) as a typical lithological controlled suite of enriched elements in black shale rocks. The suite of elements W, Bi, Cu, Mo, Sn, and Te are typical of tungsten skarn deposits (Venendaal, 2007; Newberry, 1982). This tungsten suite of elements is enriched along the deep portions of the Voodoo Fault, referred to as High Grade Fault in Venendaal (2007), which was interpreted to indicate that the fault was in place when the Mesozoic intrusions that may be responsible for the skarn were emplaced. The base metal suite of elements shows a weak spatial correlation and includes Ag, Bi, Cu, Fe, Pb, and Zn, which are typical elements of intrusion-related polymetallic mineralization (Venendaal, 2007; Seedorff et al., 2005). The author concludes that these elements also correlate with the Voodoo fault.

Venendaal (2007) reported that for the Carlin suite, Tl and Hg correlate best with Au, followed by As, Sb, and Ag. The author concluded that the suite observed at Cortez Hills is similar to Carlin-type systems discussed in Cline et al. (2005). This element suite is enriched along the Voodoo fault and there are also elevated concentrations along the

Roberts Mountains Formation-Wenban Formation contact. Venendall (2007) reports that oxidation currently reaches at least 2000 feet below the surface in the area of the Voodoo Fault and that the oxidizing fluid followed the same pathways as earlier tungsten, base metal, and Carlin mineralizing fluids. The author concludes that the primary elements that display mobilization by the oxidizing fluid are Fe, Mn, Zn, U, and V.

CHAPTER 3

METHODS

Sample Collection

For this study, three hundred and seventy samples were collected from thirteen drill holes through the CHBZ (Fig. 10; Appendix C) and forty samples from three drill holes through the CHLZ. Samples were collected from drill holes that are within 200 feet of a selected northeast oriented long section through the breccia zone (along A-A' from Fig. 4). The coordinates for the section are 40.167468663N, 116.611112789W and 40.169401386N, 116.608316283W. The section was selected because it crosscuts the Voodoo fault and runs parallel with the long axis of the breccia zone. Core photos and Au assays were examined from each drill hole that intersects the section in order to identify transects through sulfide-bearing rocks that transition from high-grade mineralization to low- or undetectable Au-grade (0.0001 oz/t Au detection limit) over as short of a distance as possible. Such transects minimize variations in primary lithology, and changes in mineralogy and texture can be more confidently related to the mineralization processes. Sulfide-bearing rocks were studied because they preserve the original depositional location of Au within CTGDs. Alternatively, in oxidized rock, Au may have been remobilized. Within the CHBZ, ideal transects for sampling proved to be rare because of pervasive oxidation and abrupt changes in Au concentration at lithologic contacts.

Optical Petrography

Transmitted and reflected light microscopy were the primary tools used to determine the paragenetic sequence within the CHBZ. A total of 102 polished thin

sections were cut from core samples within the CHBZ and 18 from CHLZ (Appendix C). All thin sections were stabilized with blue epoxy. Thin sections were cut from rocks that represent transects through sulfide-bearing ore, from high-grade sulfide-bearing rocks, high-grade oxidized rocks, and samples that contain multiple mineral phases and cross-cutting relationships between minerals.

Electron Probe Microanalysis

A JEOL-8900 Electron Probe Microanalyzer (EPMA) at University of Nevada Las Vegas (UNLV) Electron Microanalysis and Imaging Laboratory (EMiL) was used to quantify the major, minor and trace element chemistry of texturally and spatially diverse pyrite grains as well as to identify unknown sulfide minerals. Probe conditions for analysis are provided in Table 2. The suite of elements quantified in the pyrites and their standard conditions are provided in Table 3. Two analyses were performed iteratively for each 1 to 2 micrometer point, one for the major elements and one for trace elements, so that the beam current can be modified to optimize for the full range of elements of interest. See Muntean et al. (2011) for all EPMA method techniques and standards. All samples selected for EPMA were carbon coated.

X-Ray Diffraction

Fine-grained clays were difficult to identify by using transmitted light microscopy owing to the close proximity of opaque sulfides and the blue epoxy. After extensive thin section petrography, X-ray diffraction (XRD) was used to identify the clays present in twelve rocks with varying mineral assemblages and Au concentrations. Additionally, XRD was used in an attempt to distinguish between sulfide minerals with similar chemical compositions, which were first determined by using EPMA. Rock samples

were broken up with an iron mortar and pestle and then ground into a fine powder by using a shatter box for two to five seconds. Samples were analyzed by using a PANalytical X'PERT Pro X-ray Diffraction Spectrometer housed in the UNLV XRD/XRF laboratory; XRD settings are reported in Table 4. The raw XRD patterns were interpreted by using X'Pert Highscore Plus and Match!2 software packages.

Scanning Electron Microscopy

A JEOL-5600 Scanning Electron Microscope (SEM) was used to provide semi-quantitative chemical compositions that aided in the identification of clay and carbonaceous materials. Thin sections with carbonaceous material were analyzed without carbon coating while all other thin sections used in the SEM were carbon coated. High resolution microscopy was conducted by using the SEM to observe and document clay and Au-bearing iron-sulfide textural and spatial relationships.

Cathodoluminescence

An Oxford/Gatan Mini-CL Cathodoluminescence Detector mounted inside the electron microprobe column located at UNLV EMIL laboratory and a K.E. Developments panchromatic Centaurus CL detector mounted on a JEOL 5800LV scanning electron microscope at the United States Geological Survey (USGS), Denver, CO, were used in an attempt to observe varying luminescence of quartz and calcite generations in four thin sections. No variation in luminescence, or luminescence itself, in calcite and/or quartz crystals was observed by using either CL detector.

Laser Ablation Inductively-Coupled Plasma Mass Spectrometry

Trace element relative counts and concentrations were determined by using laser ablation inductively-coupled plasma mass spectrometry (LA-ICP-MS) at the USGS

Denver laboratory. A Photon Machines Analyte G2 LA system (193 nm, 4 ns Excimer laser) was coupled to a PerkinElmer DRC-e Inductively Coupled Plasma Mass Spectrometer. Typical operating conditions for these analyses are listed in Table 5. Thin section mineralogy was first characterized by using optical petrography and trace element concentrations were pre-determined by using EPMA as described above.

Pyrite grains were analyzed by performing 5 micrometer spot analyses and line scans. Spot concentrations and detection limit calculations were conducted by using the protocol of Longerich et al. (1996), and ^{57}Fe was used as the internal standard. Spot data were collected to measure elements that were below EPMA method detection limit (MDL). Line scans were used to observe relative changes in trace-element concentrations along a single line that traversed from breccia matrix to clasts and/or from pyrite rims to pyrite cores. Methods for mapping pyrites are similar to those reported in Koenig et al. (2009). The reference material (MASS-1) was analyzed 5-10 times at the beginning of the analytical session and reanalyzed throughout the session to correct the mass spectra for drift that can occur during the analytical session. The transient signals were screened visually for heterogeneities such as micro-inclusions and/or zoning.

CHAPTER 4

PRE-ORE STAGE

The pre-ore-stage is defined as the period of time prior to the Carlin ore-fluid being introduced to the system. Pre-ore-stage minerals encompass the primary constituents of the host rocks, which includes calcite, carbonaceous material, and detrital quartz. Additionally, there are other pre-ore-stage minerals, such as sulfide minerals, hydrothermal quartz, and tremolite that are not typically associated with the deposition of limestone. These other minerals most commonly occur in limestone that is primarily composed of recrystallized calcite and low to undetectable Au concentration, located along the periphery of the CHBZ ore zones; however, they may also occur in strongly Au mineralized samples.

Limestone Minerals

The data described in this section were collected by using optical petrography on samples located on the periphery of the deposit that do not contain detectable Au. Samples collected from the Devonian Wenban and Silurian Roberts Mountains formations are primarily composed of calcite, silt sized quartz, and carbonaceous material (Fig. 11), although variation between the formations does exist. The calcite within the Devonian Wenban Formation is usually recrystallized as fine to medium subhedral calcite crystals (Fig. 11B), and is more coarse and homogenous than the mottled, or fine-grained and dirty, calcite within the Silurian Roberts Mountains Formation (Fig. 11D). There is more dark opaque carbonaceous material within the Silurian Roberts Mountains Formation than the Devonian Wenban Formation (Fig. 11B, D-E). The formations also differ in silt content, with the Silurian Roberts Mountains Formation containing

significantly more and coarser detrital quartz, whereas it is difficult to detect detrital quartz within the Devonian Wenban Formation (Fig. 11E). The larger component of detrital quartz and carbonaceous material within the Silurian Roberts Mountains Formation results in clearly visible laminae that vary in silt and carbon content (Fig. 11D).

Pyrite Classification

Three types of pre-ore-stage pyrites were observed and classified according to their petrographic characteristics, chemistry, and associated minerals (Table 6): pre-ore pyrite 1 (PO1), pre-ore pyrite 2 (PO2), and pre-ore pyrite 3 (PO3). PO1 (Fig. 12A-B) is coarse anhedral pyrite that is primarily visually differentiated from PO2 and PO3 by its irregularly textured interior. The PO1 pyrites are the prevalent pyrite type in rocks that do not contain Au, and are commonly elongated along bedding laminae of the host rocks within the CHBZ and CHLZ. The PO1 pyrites are less commonly observed with Au-bearing iron-sulfide rims in rocks with high Au concentrations. The PO2 pyrite grains (Fig. 12C) are subhedral to euhedral with bright white reflectivity, and are differentiated from other pyrites by their resemblance to cubic, stoichiometric pyrite. The PO3 pyrites are distinguished petrographically from PO1 and PO2 pyrites by the presence of abundant pore spaces, which are commonly elongated and parallel to each other (Fig. 12D). The PO3 pyrite grains are spatially associated with chalcopyrite (Fig. 12E-F), sphalerite, tremolite, and quartz. Some PO3 pyrites have Au-bearing iron-sulfide rims of less than 1 micron.

The element chemistry of PO1 and PO2 pyrites is plotted in Figure 13. EPMA data were not collected for PO3 pyrites because they were not identified at the time of

analysis. All EPMA data points plotted in Figure 13 are located within PO1 pyrites that are greater than 5 micrometers from Au-bearing iron-sulfide rims in order to avoid analytical overlap and are located within the most visually distinctive crystals of each pyrite type. The plots reveal significant variation within the majority of the elements plotted for each pyrite type; however, Pb and Co are consistently elevated in both PO1 and PO2 pyrites. Nickel is consistently elevated in PO1 pyrites and As is consistently elevated within PO2 pyrites.

Figure 14 better displays elemental patterns for each pyrite type. The EPMA trace element chemistry from PO1 (n = 21) and PO2 (n = 14) pyrite points that are greater than 5 micrometers from Au-bearing iron-sulfide rims are plotted (Fig. 14). The bar and whisker diagrams show the median value as the center vertical line, the length of the bar displays the range that 50% of the values plot, and the horizontal lines indicate the minimum (left) and maximum (right) values for each element. The elements that are elevated in PO1 pyrites are Ni, Co, Pb, and Ag. The concentrations of As, Sb, and Sn are usually elevated within PO2 pyrites.

Other Minerals

In addition to the three pyrite types described above, pre-ore-stage minerals includes chalcopyrite, sphalerite, pyrrhotite, tremolite, and quartz. These minerals are commonly spatially associated with PO3 pyrites as well as each other. The minerals discussed in this section were observed along and within the planes of laminae as well as crosscutting laminae. PO3 pyrites are commonly within close proximity of chalcopyrite; the two minerals have complex boundaries and resemble puzzle pieces (Fig. 12E) or have a wispy texture (Fig. 12F) between the two minerals. PO3 pyrite has fuzzy edges along

its crystal boundary and is the mineral displaying the wispy texture. Chalcopyrite conforms to euhedral calcite rhombohedrons and the original fine grained mottled calcite that comprises the majority of the rock (Fig. 15A), and is observed adjacent or surrounding millerite (NiS) in two samples. Figure 15B shows chalcopyrite inclusions within sphalerite, known as chalcopyrite disease, which is interpreted to be a result of the replacement of sphalerite by chalcopyrite (Barton and Bethke, 1987). The PO3 pyrite and chalcopyrite conform to euhedral tremolite (Fig. 15C) and PO3 pyrite replaced tremolite (Fig. 15D-E). Figure 15F displays unaltered radiating tremolite surrounded by recrystallized calcite. Pyrrhotite, which has been documented at the Getchell CTGD as a skarn and intrusion-related mineral (Groff et al., 1997), is present within the CHBZ rimmed by pre-ore pyrite (Fig. 16A). PO3 pyrites are also found in contact with quartz, commonly displaying a banded zebra-like pattern or texture between quartz and PO3 (Fig. 16B) and occasionally PO3 pyrite is observed conforming to euhedral quartz crystals (Fig. 16C).

CHAPTER 5

ORE-STAGE

Ore-stage mineralogy and alteration include three types of Au-bearing iron-sulfide minerals, illite, and jasperoid, all of which commonly occur together. The iron-sulfide minerals are not referred to as pyrite or marcasite because they are not coarse enough to reveal strong birefringence. This section describes the mineralogy and chemistry associated with ore-stage iron-sulfide minerals. Spatial relationships of ore-stage minerals with porosity and breccia textures are described. Additionally, sample transects from unmineralized to Au-bearing rocks are described in terms of mineralogy, rock type, pore space, and texture.

Ore-stage Iron-sulfide Minerals

Three distinct iron-sulfide minerals containing Au and trace elements that correlate with Au (As, Tl, Hg, Cu) have been characterized throughout the CHBZ (Table 7). The three iron-sulfide minerals were first differentiated petrographically by their physical properties and crystal morphologies. The most prevalent Au-bearing iron sulfide is OP1, which is widely distributed throughout the CHBZ (Fig. 17; Appendix D). The other two iron sulfide types are not as common throughout CHBZ (Fig. 17; Appendix D). The chemistry of OP2 and OP3 were characterized by using EPMA; however, unlike OP1, data from OP2 and OP3 were not collected from multiple samples.

The OP1 is a low relief anhedral iron sulfide that has a Mohs hardness of approximately 3, determined by the similar hardness of OP1 and adjacent realgar by a nail (hardness = 5.5) scratch test. OP1 is easily recognized because of lower relief and reflectivity compared to the pyrite cores they surround (Fig. 18A). The EPMA data

collected from OP1s generally indicate As >> (Tl+Hg+Cu) > (Au±Bi±Sb) > Ag and Au has a negative to no correlation with Pb (Figs. 18C-D, 19C-D; Table. 7). Associated ore-stage elements increase in concentration from the pyrite core into the OP1 rim (Fig. 18C-D, 19C-D). The LA-ICP-MS raw intensity data (Fig. 19B) and EPMA data (Fig. 19D) indicate that the largest OP1s observed, which reach 50 micrometers, do not have chemically zoned rims. The concentration of Au appears to be lower in the rim directly adjacent to the pyrite cores in the LA-ICP-MS map (Fig. 19B). This is likely due to signal mixing as a 5 micron analysis will analyze both core and rim along the contact. Microprobe data verify that where Au is elevated, Tl, Cu, Hg, and As are consistently elevated as opposed to chemically zoned. The OP1 is commonly found disseminated throughout jasperoid and/or breccia matrix. In one sample, OP1 was observed rimming a presumably pre-ore sphalerite crystal (Fig. 18B).

The OP2 differs texturally from OP1, and textural variations between the iron sulfide types cannot be attributed to variations in polish because visible OP1s are commonly within micrometers of OP2s, indicating that both pyrites have undergone the same polishing. OP2s are similar in reflectivity and relief to the cores that they surround, which makes them difficult to detect petrographically (Fig. 20A), as they closely resemble pre-ore-stage pyrites. The OP2s contain As >> (Tl+Hg+Cu) > (Au+Sb) > Ag and differ chemically from OP1s in that Au and Sb are consistently associated (Fig. 20B).

The OP3s display low relief, are anhedral with an irregular “fuzzy” outer edge, and do not contain the same bright reflectivity as pre-ore-stage or stoichiometric pyrites (Fig. 21A), which makes them appear to be Au-bearing iron-sulfide minerals (Cline and Hofstra, 2000). However, EPMA data indicate that OP3 does not always contain Au

above detection. Overall, OP3s contain As >> (Tl+Hg+Cu) > ± Au > Ag ≥ ± Sb (Table 7; Fig. 21). Figure 21B shows that Tl, Cu, and Hg points, which overlie one another, increase gradually across the rim. However, the concentrations of Au and As increase abruptly within the rim (Fig. 21B) in analyses r1 and r2. The concentration of Sb is above detection in some core and some rim analyses, but does not consistently follow Cu, Tl, and Hg, indicating that the rim is zoned.

Illite

Throughout the CHBZ, Au-bearing iron-sulfide minerals are commonly surrounded by clay minerals and quartz. Illite, which is difficult to characterize by using transmitted light microscopy due to close proximity to opaque iron-sulfide minerals and blue epoxy, was confirmed by using SEM-EDS to identify equal Si and Al>O and K peaks and a small Mg peak (Fig. 22B). Other clay minerals were not identified in-situ by using SEM-EDS or optical petrography. Illite is fine grained, on the scale of a few micrometers, and often completely surrounds Au-bearing iron-sulfide minerals (Fig. 22A). The XRD data also confirm the presence of illite in Au-bearing samples (Fig. 22C). Additionally, XRD data indicate the presence of kaolinite, dickite, and montmorillonite in samples from the CHBZ that contain Au and dickite is also present in samples with undetectable Au (below 0.0001 oz/t) based on 10 foot assays (Appendix F). XRD data also suggest the presence of kaolinite, dickite, and illite in CHLZ (Appendix F). Although these clay minerals were not identified by using SEM-EDS, XRD data indicate they are common within the rocks of the CHBZ and CHLZ.

Quartz and Jasperoid

Quartz within the CHBZ was identified by its high relief relative to the surrounding minerals (Fig. 23A-B), common euhedral crystal faces in reflected light (Fig. 23B) and first order grey to white birefringence in transmitted light (Fig. 23C). Figure 23C shows an example of a replacement texture that is interpreted to represent quartz replacing calcite, forming jasperoid (Spurr, 1898); quartz is dominant along the periphery of the calcite clast and is replacing the calcite from the edges inward. Where quartz is documented replacing pre-ore-stage calcite, the calcite commonly appears dark (blue rectangles in Fig. 23C) due to concentrated carbonaceous material, increase in blue epoxy, and addition of clay and quartz as the calcite begins to dissolve. Within jasperoid, solid calcite inclusions are observed and identified by their lower relief than the surrounding quartz and their high birefringence in transmitted light (Fig. 23D). Figure 23E shows high calcite birefringence (bottom), low grey to white quartz birefringence (top), and grey quartz with high birefringence calcite solid inclusions (center left), consistent with jasperoid formation.

Quartz is commonly observed in rocks that contain elevated Au concentrations surrounding Au-bearing iron-sulfide minerals (Fig. 23A) and as non-interlocking crystals with low relief illite and Au-bearing iron-sulfide minerals between quartz crystals (Fig. 23B). Although quartz is dominant in ore grade rock, small remnant zones of original fine-grained mottled calcite from limestone deposition is commonly present as well. The 0.221 oz/t sample shown in Figure 23C displays the extent to which Paleozoic calcite can remain in a mineralized sample.

Porosity Associations

High-grade Au samples commonly exhibit a large amount of pore space, now filled with blue epoxy. Ore-stage minerals that include jasperoid, illite, and fine-grained Au-bearing iron-sulfide minerals are commonly associated with blue epoxy. Blue epoxy is visible where illite is present (Fig. 24A) because of the fine-grained thin nature of the mineral (Fig. 24A-B). Where non-interlocking jasperoid crystals are present, blue epoxy fills the open spaces of the rock, as shown within the white ovals in Figure 23C and throughout the thin section scan in Figure 23F. Illite, jasperoid and Au-bearing iron-sulfide minerals are commonly observed as pseudomorphs of pre-ore-stage radiating tremolite crystals (Fig. 24A-D), with blue epoxy pervasive through the pseudomorph (Fig. 24A).

Elongated seams of blue epoxy are commonly observed within photomicrographs of mineralized rocks (Fig. 25C, 26D, 27D). Directly adjacent and parallel to blue epoxy seams, are areas of brownish black dark material in transmitted light (Figs. 25C, 26D, 27D) which may appear jet black in reflected light (Fig. 27C). Within a seam, SEM-EDS analyses identified opaque residual carbonaceous material, along with illite, jasperoid, fine-grained, mottled calcite, and fine-grained (<1 μm) Au-bearing iron-sulfide minerals. Figure 25 shows a seam in transmitted light (C), with the dark material radiating from the region of blue epoxy, and reflected light (D), which shows the fine grained Au-bearing iron-sulfide minerals within the seam material.

Sample Transects

Figure 26 displays a sample transect shown in hand samples, thin sections, and photomicrographs that transitions from primarily recrystallized calcite (A) into rocks that

contain Au-bearing iron-sulfide minerals, jasperoid, fine-grained calcite, illite and carbonaceous material along seams (D) over 16 feet. Sample A is a limestone that contains 0.001 oz/t Au and is primarily composed of recrystallized calcite. These rocks commonly contain pre-ore-stage minerals, including, but not limited to, calcite, detrital quartz, tremolite, pyrite, and carbonaceous materials. Thin zones of dark material, primarily consisting of clay and residual pre-ore carbon, appear in sample B, located at a distance of approximately 2.5 feet from sample A, as Au concentration increases to 0.025 oz/t. The majority of the rock is still recrystallized calcite. Blue epoxy in the thin section is located adjacent to the darker areas, and in the photomicrograph jasperoid is present within these areas. As Au concentration increases to 0.312 oz/t in sample C, porosity increases significantly. Some areas are opaque due to the presence of Au-bearing iron-sulfide minerals (Fig. 26C circled). The rock is still primarily recrystallized calcite, although realgar, jasperoid, and illite are also present. Continuing along the transect to sample D, located 4.5 feet away from sample C, the hand sample decreases in induration; the amount of calcite decreases while the dark material that contains illite, carbonaceous residual material, fine-grained Au-bearing iron-sulfide minerals and non-interlocking jasperoid increases within the sample. In the thin section, low relief dark material is present in some, but not all, of the matrix that surrounds the clasts. The photomicrograph reveals an elongated region of the dark material parallel to a seam of high porosity.

Samples with higher Au concentrations (0.541 and 2.02 oz/t) than shown in Figure 26 are displayed in Figure 27 in order to characterize mineral textures and associations with increasing Au grade. As the concentration of Au increases in the limestones, elongated regions of dark material and porosity become more pervasive

throughout the sample (Fig. 27B-D). The sample contains less recrystallized calcite and significantly more jasperoid, illite, fine-grained iron-sulfide minerals, and carbonaceous material than the samples in Figure 26. In high grade (2.02 oz/t) heavily brecciated samples (Fig. 27E-H), the dark opaque material is irregularly distributed throughout the breccia matrix (Fig. 27G-H) instead of concentrated in elongated seams. Recrystallized calcite is now a minor component of the sample. The primary components of the high-grade ore are jasperoid, illite, carbonaceous material, and iron-sulfide minerals.

Breccia Associations

Gold-bearing iron-sulfide minerals are concentrated within the matrix of monolithic and polylithic brecciated rocks along clast boundaries (Fig. 28A); however, it is also common to observe strongly mineralized clasts surrounded by a less mineralized matrix (Fig. 28B-D). For example, the clasts in Figure 28A are not mineralized; instead, the bright reflective Au-bearing iron-sulfide minerals are distributed along the clast boundary. In contrast, Figure 28B shows a clast that is opaque owing to pervasive Au-bearing iron-sulfide mineralization and is more strongly mineralized than the surrounding matrix. Similarly, Figure 28C shows a cubic clast that is strongly mineralized by bright reflective Au-bearing iron-sulfide minerals and a less mineralized matrix. Figure 28D shows the extent of mineralization of the same clast under transmitted light. Above the clast, at the boundary between it and the next clast (within the drawn oval), there is a concentration of opaque carbonaceous material, illite, and fine-grained Au-bearing iron-sulfide minerals. The Au mineralization is concentrated within the clast as well as at the clast boundary with the unmineralized clast (Fig. 28C-D). Because these samples were

collected from drill core within heavily brecciated rocks, they may be mega-clasts within the breccia that contain smaller clasts and matrix.

Two samples contain clasts that are strongly Au mineralized with a halo of disseminated Au-bearing iron-sulfide minerals within the matrix surrounding the clasts, shown as the opaque material in Figure 29A. These strongly mineralized clasts are black in hand sample (Fig. 29D, circled) and thin section (Fig. 29E, circled), making some breccia samples appear to be polylithic. It is not possible to determine the composition of the original clasts due to the extent of mineralization (Fig. 29B). An LA-ICP-MS transect through the clast and surrounding mineralized halo and matrix indicates significant Au within the clast as well as in the matrix (Fig. 29C). The Au-bearing iron-sulfide minerals are concentrated within the clast; however, the matrix has sporadic Au-bearing iron-sulfide mineralization. The trace element chemistry in the clast and matrix is similar (Fig. 29C).

CHAPTER 6

LATE-ORE STAGE

Late-ore-stage is defined as the stage when ore-stage minerals (Au-bearing iron-sulfide minerals, illite, and jasperoid) are no longer being deposited throughout the majority of the system. Instead, minerals begin to precipitate that are modeled as precipitating as the system cools and collapses, such as realgar and calcite (Hofstra et al., 1991). The late-ore-stage minerals within the CHBZ, which include five types of iron-sulfide minerals, calcite, aktashite, christite, cinnabar, and realgar, are most abundant in heavily brecciated samples. Calcite and realgar, however, are pervasive throughout the entire deposit and commonly occur in both un-brecciated and brecciated samples. Textural characteristics of realgar discussed in this section are specific to the CHBZ. No late-ore-stage minerals were observed in samples from the CHLZ.

Late-ore-stage Iron-sulfide Minerals

Five iron-sulfide minerals are grouped separately from the ore-stage iron-sulfide minerals based on consistent elevated concentrations of Pb and Sb that are distinctly different from ore-stage iron-sulfide minerals, as determined by using EPMA. Additionally, inconsistent associations of Au with Tl, Hg, Cu, and As (Table 7) commonly exist. The group is classified as chemically evolved-ore-stage iron-sulfide minerals (EOP). The evolved-ore-stage marks the transition between the main-ore-stage and the late-ore-stage, and is included with the late-ore-stage system because the majority of the EOPs do not contain detectable Au, indicating that the system was no longer depositing Au within certain areas.

The EOP1 is a low relief, anhedral iron sulfide that is texturally similar to OP1s, but they rim fragmented realgar as well as pyrite (Fig. 30A-B). The EOP1s differ chemically from OP1s in that they contain As >> (Pb+Cu) ≥ (Sb+Hg±Tl) ≥ (Au±Bi) > ± Ag (Table 7; Fig. 30). The EOP2s are diagnostically anhedral with irregular fuzzy crystal boundaries and are dull tannish white in reflected light (Fig. 31A-B). Breccia zone EOP2s contain As >> (Pb+Cu) > (Sb+Hg) > (Tl+Au) > Ag (Table 7; Fig. 31A, C). The CHBZ EOP1s and EOP2s are the only evolved-ore-stage iron-sulfide minerals that commonly contain Au; however, they also contain elevated and strongly associated Pb and Sb. The CHLZ EOP2s (Fig. 31B) are texturally similar to EOP2s from CHBZ (Fig. 31A); however, the CHLZ EOP2s contain As >> Ni > (Au+Cu+Hg+Pb+Tl) > Ag > ± Sb (Table 7; Fig. 31D). The CHLZ EOP2s appear to contain high Au and Ni relative to all CHBZ ore-stage iron-sulfide minerals; however, microprobe major element totals are consistently low within CHLZ CHUE 215 246.5', ranging from 44-96 wt%, due to varying degree of oxidation as is common in CHLZ.

The EOP3s have a brownish-white color under reflected light (Fig. 32A) and are surrounded by feldspars and clays within one mineralized dike sample. These iron-sulfide minerals contain elevated As >> (Tl+Hg+Sb±Pb) >> (±Cu±Ni±Ag±Ti) with no detectable Au or Bi (Fig. 32C). The LA-ICP-MS line scan (Fig. 32B) does not reveal concentration, but does suggest that As, Tl, Hg, Sb, and Pb are relatively elevated within the EOP3. The element Cu, which is present in all other ore- and evolved-ore-stage iron-sulfide minerals, is below LA-ICP-MS detection and is significantly lower in concentration (Fig. 32) than in other ore and evolved-ore-stage iron-sulfide minerals.

The EOP4s are characteristically tan in reflected light with bright white flecks and they rim a bright reflective core (Fig. 33A). These iron-sulfide minerals contain As >> Cu > (Tl+Hg+Ni) > (Pb±Sb±Au) ≥ ± Ag. Gold in EOP4s that are surrounded by aktashite ($Cu_6Hg_3As_4S_{12}$) is consistently below EPMA detection limit (Fig. 33A and C, points r5, r6), whereas EOP4s that are surrounded by realgar and quartz contain detectable Au (Fig. 33A, C, points c1, r3). The EOP5s have a yellowish-white color in reflected light, relatively dull reflectivity, and are a circular shape with a hole at the center (Fig. 33B). EOP5s contain As >> (Pb+Cu) > (Tl+Hg+Bi) > Sb > Ag ± Ti with Au below detection limit (Fig. 33D).

Aktashite and Christite

Aktashite is an uncommon sulfosalt ($Cu_6Hg_3As_4S_{12}$) that has a postulated hydrothermal origin and has been documented at the Getchell CTGD in Nevada (Mineral Data Publishing, 2001). The mineral was identified by EPMA analysis with the calculated formula $Cu_{5.982}Hg_{2.966}As_{2.155}Zn_{0.271}S_{12}$ (Table 8). In hand sample, aktashite is steely bluish grey, anhedral (Fig. 34A), and has a reported Mohs hardness of ~3.5 (Mineral Data Publishing, 2001).

Christite ($TlHgAsS_3$) and routhierite ($Tl(Cu,Ag)(Hg, Zn)_2(As,Sb)_2S_6$) are sulfosalts with similar compositions; however, they differ in crystallography and routhierite allows Cu and other elements in its structure whereas christite does not. Christite has been reported as a hydrothermal mineral deposited during the late-ore-stage deposition of the original Carlin gold deposit, Nevada (Radtke et al., 1977). Routhierite is found in hydrothermal deposits in France and has not been reported within CTGDs (Mineral Data Publishing, 2001); however, it has been reported in the presence of

aktashite in the Hemlo deposit (Pan and Fleet, 1995; Muir, 2002). Table 8 compares the chemistry of aktashite, christite and routhierite from other deposits to the minerals sampled in this study. The CHBZ EPMA data match more closely with christite than routhierite, with the calculated formula $Tl_{0.666}Hg_{0.706}Cu_{0.168}As_{0.563}S_3$. Although the CHBZ mineral contains Cu, Cu and/or Ag concentrations are too low and there is too much Tl to satisfy the routhierite mineral formula.

X-ray diffraction analysis for sample CHUD 038 457' matches more closely with christite than routhierite (Fig. 35A). However, it is not possible to determine the mineral diffraction pattern with high confidence because minerals and clays were not separated for the analysis. There is extensive peak overlap between the unknown mineral (christite or routhierite) and realgar, and realgar is much more pervasive in samples that contain the unknown mineral. Data suggest that the unknown mineral is more likely christite than routhierite, and will be referred to as christite in the remaining portion of this thesis.

Microscopically, aktashite is most commonly observed as euhedral triangular prisms (Fig. 34B) or irregular masses in contact with sphalerite (Fig. 34C-D) and/or chalcopyrite (Fig. 34A, E-F). Aktashite completely surrounds and fills fractures in sphalerite (Fig. 34C-D). Figure 34E displays aktashite along the outer edge of chalcopyrite and along the contact between two EOP5s and chalcopyrite. Other EOP5s in this image (indicated by the circle) have open space at the contact between the EOP5 and chalcopyrite, which is also at the center of the EOP5s. Each sample that contains aktashite also contains chalcopyrite and/or sphalerite in close proximity; however, chalcopyrite and sphalerite commonly occur without aktashite (Fig. 36; Appendix D). Aktashite is also observed conforming to calcite rhombohedrons (Fig. 37A) and EOP4s

in multiple thin sections (Fig. 37A-B). Microprobe points 1, 2, 3, 4, 5 (Fig. 37B) within EOP4 surrounded by aktashite do not contain detectable Au; however, texturally similar points 7, 8, 9 within EOP4 surrounded by realgar (Fig. 37B), do contain Au. The realgar conforms to the euhedral aktashite edge (Fig. 37B). The EOP4s are very abundant within the aktashite and commonly do not exist within the minerals immediately adjacent to aktashite (Fig. 34D, 37C). EOP4s are concentrated at the contact between sphalerite and aktashite; however, they occur within the aktashite (Fig. 34D).

Christite is not common, and was only observed in one sample. In reflected light, christite resembles aktashite in that it is bluish white (Fig. 37C-F), but it can be distinguished by its deep crimson purplish red color in transmitted light. SEM images reveal a different shade of grey between aktashite and christite, with christite being brighter due to higher Hg content (Fig. 37D). Christite has a reported hardness similar to that of realgar (~2), and it has a similar relief (Fig. 37D-E). Within CHBZ, christite is always anhedral and is commonly crossed by fractures filled with realgar (Fig. 37E) or completely surrounded by realgar (Fig. 37F). Christite occurs with aktashite and realgar in the same sample. Figure 37F shows christite surrounding EOP5, a pyrite that is commonly spatially related to aktashite.

Realgar

Realgar was observed in samples from the CHBZ conforming to euhedral crystals of quartz (Fig. 37D), ore-stage iron-sulfide minerals (Fig. 37B), aktashite (Fig. 37B,D), calcite (Fig. 38A, B), and cinnabar (Fig. 38B-C). Figure 38D reveals solid realgar inclusions within calcite, which is not as common as realgar conforming to calcite

rhombohedrons. Figure 39A shows a common veinlet form of realgar located adjacent to calcite veins and filling the fractures within the limestone.

Although realgar primarily conforms to other minerals and fills in the open spaces of the breccia, fragmented realgar is obvious in some hand samples (Fig. 39B). Fragmented realgar from four thin sections, all of which are located in close proximity to each other within the hanging wall of a dike (Fig. 36), have EOP1 Au-bearing iron-sulfide rims (Fig. 39C). Two of these samples also contain the heavily Au mineralized clasts and disseminated Au mineralized halos shown in Figure 29. A LA-ICP-MS transect through one of the fragmented and EOP1 rimmed realgar clasts (Fig. 40) reveals a Au, Tl, Cu, Sb, and Bi association within the iron-sulfide rim.

CHAPTER 7

IRON-SULFIDE GEOCHEMISTRY

Iron-sulfide Spearman Rank Correlation Matrix

A Spearman rank correlation matrix (SYSTAT 13) was conducted for a matrix of 18 elements by using the EPMA data collected on all iron-sulfide minerals within CHBZ. Correlation coefficients (r) are listed in Table 9, with values > 0.4 and < -0.4 in bold in order to show strong positive and negative correlations. Gold shows a > 0.4 positive correlation with As (0.679), Tl (0.456), Cu (0.484), and a < -0.4 negative correlation with S (-0.645) and Fe (-0.529).

Ore to Evolved Ore-stage Geochemical Suites

Detailed examination of EPMA analyses of ore- and evolved ore-stage iron-sulfide minerals within eight samples from the CHBZ and one from CHLZ reveal the presence of two distinct geochemical suites within the CHBZ, referred to as the main-ore-stage and evolved-ore-stage suites. Table 10 indicates whether the sample represents the main-ore-stage or evolved-ore-stage geochemical suite, and lists each sample name, elevation, elevated trace elements, element correlation coefficients, and the iron-sulfide-type from which the EPMA data were collected. All of the EPMA data used to compile Table 10 were collected from Au-bearing iron-sulfide minerals.

Figure 41 is a matrices plot in which Au, Hg, Tl, Cu, Sb, and Pb are plotted against each other and color coded by sample. The data plotted are referred to in Table 10, and the least-squares lines are determined by using all data points in each plot. There are two categories of plots that the data produce: 1) data from each sample plot in clusters along the least-squares lines, as shown on the Tl:Hg plot; 2) data from each sample have

a range of values that generally do not plot in a cluster or trend parallel to the least-squares line, as shown in the Sb and Pb plots. Samples DC 124 1273' (lavender) and DC 114 1236.5' (purple) chemistries plot very differently. Although the two samples are close spatially (Fig. 42), they exhibit different mineral textures. For example, DC 114 1236.5' (purple) contains fragmented realgar with Au-bearing EOP1 rims while DC 124 1273' (lavender) contains realgar that fills in the open space within the breccia. Au-bearing iron-sulfide minerals within DC 124 1273' (lavender) contain high Hg and Tl regardless of Au concentration, while DC 114 1236.5' (purple) iron-sulfide minerals contain the lowest Hg and Tl concentrations of all analyzed samples (Fig. 41). Additionally, DC 114 1236.5' (purple) plots parallel to the Pb and Sb regression line while DC 124 1273' (lavender) plots horizontal, displaying a zero correlation between Pb and Sb (Fig. 41). Sample DC 124 1264' is not included in Figure 41 because Sb, Pb, Hg, and Tl are anomalously high in this sample and skew all plots containing these elements.

Three samples contain iron-sulfide minerals in which Pb and Sb correlate positively, and, thus, are referred to as the evolved ore-stage geochemical suite: DC 114 1236.5' (purple), CHUE 215 246.5' (olive green) and DC 124 1264' (yellow) (Fig. 43). Figure 43 displays the least-squares lines and the correlation coefficient (R^2) for each sample. Data from DC 114 1236.5' (purple) exhibit a positive correlation coefficient for Au:Pb (R^2=0.68), Au:Sb (R^2=0.64), and Pb:Sb (R^2=0.79) (Fig. 43). The majority of the iron-sulfide minerals selected for EPMA analysis for this sample are EOP1s and EOP2s, and include the EOP1s that rim fragmented realgar clasts (Table 10). Lower zone sample CHUE 215 246.5' (olive green) has the strongest positive correlation coefficient for Pb:Sb (R^2=0.99) (Table 10; Fig. 43); data were collected from OP3 and EOP2. DC 124

1264’ (yellow) has a strong positive correlation coefficient between Pb:Sb (R^2=0.62); however, no Au was detected in the EOP3s. All other samples contain iron-sulfide minerals with Pb:Sb and Au:Pb R^2 values between 0 and 0.34 (Table 10), and are thus included in the main ore-stage geochemical suite. CHUD 038 464’ (dark blue) is an exception. EPMA data for this sample were collected from evolved ore-stage iron-sulfide minerals; therefore, the sample is grouped within the evolved ore-stage geochemical suite (Table 10).

Scatter plots of Au versus As, Hg, Tl, Cu, Bi, Ag, Ti, Co, and Ni for each sample and the least-squares lines between them are shown in Figure 44. Gold correlates positively with As, Hg, Tl, and Cu; however, individual thin section trace-element patterns vary with respect to the least-squares line. Sample DC 124 1273’ (lavender) plots above the Au least-squares line for Hg and Tl whereas sample DC 114 1236.5’ (purple) plots below the Au least-squares line for Hg and Tl. Sample CHUE 019 485.5’ (light blue) has elevated Bi and Ag and CHUD 038 453’ (pink) has elevated Cu, Co, and Ni. Sample CHUD 038 464’ (dark blue) contains some elevated values of As, Hg, Tl, Cu, Bi, and Ag, but Au concentrations do not exceed 1220 ppm; the ratio of these trace elements to Au is relatively high.

CHAPTER 8

POST-ORE STAGE

Post-ore-stage mineralogy in the CHBZ primarily consists of calcite and supergene minerals. The Au-bearing iron-oxides in the CHBZ and CHLZ are characterized and their chemistry is described for each zone. Differences in chemistry between Au-bearing iron-sulfide minerals and Au-bearing iron-oxide minerals are described in order to properly characterize ore.

Cortez Hills Breccia Zone

Post-ore-stage mineralogy and alteration primarily consist of calcite veining and oxidation of the early sulfide-bearing rocks into the iron-oxide minerals jarosite, hematite, and goethite (Jackson et al., 2010). Calcite veins cut across rocks regardless of Au concentration. The veins are observed crosscutting pre-ore-stage minerals such as tremolite, as well as incorporating fragmented late-ore-stage mineral clasts, such as realgar, within the vein (Fig. 39D). Oxidation is pervasive throughout much of the CHBZ; different portions of the deposit are partially oxidized, fully oxidized, and/or not oxidized at all, determined by the presence of sulfide minerals in the sample. Though not the primary focus of this study, some oxidized samples were examined and observations and data are described below.

Breccia zone sample CHUD 043 376.5' is a breccia that is composed of light-colored visibly oxidized clasts and dark-colored clasts (Fig. 45A). Fine-grained calcite and jasperoid are the primary constituents of the sample. Photomicrographs from the dark-colored clasts show visible red cores with bright reddish white reflective rims (Fig. 45C) and disseminated red material adjacent to fractures (Fig 46) that resembles former

ore-stage iron-sulfide textures. Microprobe data from the cores and rims, such as those in Figure 45C, indicate the absence of sulfur and the presence of Fe, Hg, Cu, Sb, and Ni ± Au (Table 11). However, EPMA total weight percent data are low; therefore, the data are suspect. A LA-ICP-MS transect collected from the disseminated material verifies the presence of Au as well as elevated As, Tl, Sb, Pb, and Bi; however, S does not rise at any location along the transect line and Cu is not detected (Fig. 46).

Some samples within CHBZ are heavily oxidized and have a greenish brown tint, indicating arsenate (Fig. 45B). The highly oxidized rocks of the CHBZ do not contain textures that resemble ore-stage iron-sulfide minerals present in the refractory rock, but instead contain a Au alloy. EPMA data indicate that the Au alloy contains a high percent of Hg (3.6 wt %) as well as elevated Tl and Cu (Table 11).

Cortez Hills Lower Zone

Throughout the CHLZ, the rock is primarily dark grey silty carbonate with a common red iron-oxide staining that appears primarily on fractures. Jasperoid, fine-grained calcite, clays, Au-bearing iron-sulfide minerals, and Au-bearing iron-oxide minerals are present in mineralized samples. Photomicrographs reveal reddish-yellow iron-oxide minerals throughout some samples (Fig. 47B), not just along fractures. The iron-oxide minerals maintain the rim-core texture (Fig. 47B) and are also disseminated throughout the samples (Fig. 48A), resembling former ore-stage iron-sulfide textures. The iron-oxide rim and disseminated material commonly host Au within the CHLZ (Fig. 47-48). The LA-ICP-MS transects through both types of iron-oxide reveal that Au, As, Fe, Sb, Pb, and Bi are elevated, but S, Cu, Tl and Hg are not.

CHAPTER 9

INTERPRETATION AND DISCUSSION

Mineral Paragenesis

The interpreted CHBZ mineral paragenesis includes the earliest minerals that precipitated during the Paleozoic (Fig. 49), followed by pre-ore-stage minerals that formed during contact metamorphism related to emplacement of Mesozoic intrusions. During the Eocene, the pre-ore-stage minerals reacted with the Carlin ore-fluids, enhancing fluid-rock interaction, which resulted in the deposition of ore-stage iron-sulfide minerals, jasperoid, and illite. After the majority of the Au-bearing iron-sulfide minerals were deposited, evolved ore-stage iron-sulfide minerals with low to undetectable Au and elevated Pb and Sb began to precipitate contemporaneously with the first late-ore-stage minerals. The evolved-ore-stage encompasses all of the minerals that precipitated contemporaneously with the evolved-ore-stage iron-sulfide minerals. Some of these minerals, such as realgar, continued to form after precipitation of evolved-ore-stage iron-sulfide minerals, and also represent the main phase of the late-ore-stage system. The CTGD ore-stage, evolved-ore-stage, and late-ore-stage minerals were variably overprinted by later, low temperature oxidation.

Pre-ore-stage event

The earliest minerals include calcite, quartz, and diagenetic pyrite, and are interpreted to have been deposited in the Paleozoic. Fine-grained mottled calcite, later recrystallized, is the primary mineral comprising the carbonate host rocks that were deposited in the Silurian and Devonian. The host rocks also contain detrital quartz (Fig. 11E) (Harry Cook, Barrick Internal Report, 2008). PO1 pyrite trace element chemistry,

which includes Ni, Pb, Co, and Ag, is consistent with diagenetic pyrite chemistries of other CTGDs (Large et al., 2009), suggesting that PO1 pyrites likely formed during diagenesis of the host carbonate rocks in the Paleozoic (Fig. 49). PO1 pyrites are observed rimmed by Au-bearing iron-sulfide minerals, which also indicate that they precipitated during the pre-ore stage.

Euhedral and subhedral PO2 pyrites that are commonly elevated in As, Sn, and Sb, do not contain the typical diagenetic suite of trace metals (Ni, Co, Pb, Ag) nor do they resemble the texture of the anhedral PO1 pyrites, suggesting they did not form at the same time or from the same processes as the PO1 pyrites. PO2 pyrites typically have the largest and most prominent Au-bearing iron-sulfide rims, indicating that they are pre-ore-stage pyrites and were reactive or more available for reaction with the Carlin ore fluid than the other pre-ore-stage pyrites. The relative timing of the PO2 pyrites to the other pre-ore-stage pyrites and the origin of the PO2 pyrites is undetermined.

Tremolite, chalcopyrite, sphalerite, and PO3 pyrite did not form as a result of the CTGD fluid as they are commonly observed in rocks with undetectable to negligible Au, As, Tl, Hg, and Cu. In two samples that do contain detectable Au, PO3 pyrite and sphalerite have Au-bearing iron-sulfide rims, indicating that they are pre-ore stage. The mineral suite has been interpreted to be intrusion-related in other CTGDs (Cline, 2001), and is also the interpretation of this study. The current thesis study does not recognize intrusion-related minerals preferentially associated with the Voodoo Fault as Venendaal (2007) describes. Henry and Muntean (2012) interpret a 104Ma quartz monzonite intrusive located approximately 4 km southwest of Cortez Hills to be the cause of contact metamorphism of the Paleozoic host rocks.

Relative timing relationships for some of the intrusion-related pre-ore-stage minerals in the CHBZ have been determined in this study (Fig. 49). Tremolite is interpreted to have formed early, prior to PO3 pyrite, sphalerite, and chalcopyrite; chalcopyrite was the latest of these minerals to form. PO3 pyrite and chalcopyrite relationships, such as the puzzle piece texture (Fig. 12E), may indicate dissolution of the wispy PO3 pyrite and chalcopyrite replacement. The chalcopyrite disease displayed in Figure 15B indicates chalcopyrite replacement of sphalerite as well (Barton and Bethke, 1987).

The relative timing relationship of euhedral quartz to other minerals is elusive. Islands of PO3 pyrite surrounded by quartz are consistent with PO3 pyrite precipitation before quartz (Fig. 16B), though PO3 pyrite that overgrew euhedral quartz is present as well (Fig. 16C). There are no crosscutting relationships between quartz with chalcopyrite and sphalerite. Quartz may be part of the early Carlin fluid and/or the last of the intrusion-related mineralogical sequence, and possibly also formed at both times.

Ore-stage event

Microprobe data have shown that CHBZ ore-stage iron-sulfide minerals (OP) consistently contain Au, Tl, Hg, Cu, and As. The elements Sb, Bi, and Ag do not consistently correlate with Au, but are commonly detected in the CHBZ ore-stage iron-sulfide minerals. Of these elements, Bi is not commonly elevated in other CTGD Au-bearing iron-sulfide minerals.

Petrography has shown that ore-stage iron-sulfide minerals are commonly completely surrounded by illite and jasperoidal quartz, strongly suggesting they are coeval with ore deposition. Textures indicate that the ore fluid precipitated Au-bearing

iron-sulfide minerals, jasperoid, and illite as decarbonatization removed carbonate minerals. Decarbonatization, silicification, and sulfidation are spatially coincident and have been determined to be contemporaneous at other CTGDs (Cline et al., 2005).

Late-ore-stage event

The minerals aktashite and christite are composed of ore-stage elements, except Au, which is interpreted to indicate that these minerals precipitated from the late-ore-stage fluid while it still contained sufficient Tl, Cu, Hg, As, and S. This chemistry, along with textures, signifies a very close temporal relationship between aktashite, christite, and evolved ore-stage iron-sulfide minerals. The textural and spatial relationships between aktashite and chalcopyrite signify replacement of chalcopyrite by aktashite (Fig. 34E-F). Chalcopyrite provided Cu and Fe required to form aktashite while the Carlin ore fluid provided Hg, As, and S. Textures indicate that EOP5s replaced chalcopyrite from the center outwards (Fig. 34C, E). Although aktashite replaced chalcopyrite, it also precipitated in open space, as evidenced by local euhedral tetragonal crystal faces. Realgar precipitated after aktashite, christite, and euhedral calcite, as it conforms to and crosscuts euhedral crystal faces of the latter three minerals, but does not replace them. Realgar conforms to Au-bearing iron-sulfide minerals (Fig. 37B) and calcite rhombohedrons (Fig. 38A) throughout the majority of the CHBZ, consistent with the interpretation of realgar as a late-ore-stage mineral in other well studied CTGDs (Cline et al., 2005), and as a mineral that precipitated during ore system cooling and collapse (Hofstra et al., 1991).

The relative timing relationship between late-ore-stage realgar and euhedral calcite is opposite of most other well studied CTGDs (Figs. 2, 49) and may indicate

differences in the late-ore-stage fluid chemical evolution compared to how it was modeled by Hofstra et al. (1991). Additionally, the presence of abundant original Paleozoic calcite within high grade rocks (Fig. 23C) indicates that the ore fluid that mineralized the CHBZ may not have been as acidic or the same temperature as other Carlin ore fluids. These differences may have played a role in the timing relationship between the realgar and crystalline calcite precipitation. An additional possibility for the remaining Paleozoic calcite is that the carbonate host rocks lacked permeability and the ore fluid did not access all of the calcite.

Evolved ore-stage event

The evolved ore-stage event was the transitional phase between the ore stage and the late-ore stage and is manifested by the presence of anomalous iron-sulfide minerals and their textural relationships with late-ore-stage minerals. The presence of Au-bearing iron-sulfide rims (EOP1) on fragmented realgar clasts played a key role in distinguishing the transitional phase. Realgar at other CTGDs is recognized as characterizing the late-ore stage; however, at Cortez Hills there is evidence of realgar that both post- and pre-dates Au deposition. As realgar precipitates during ore-system cooling and collapse, the EOP1s that rim realgar also must have precipitated during or following system collapse. These relationships reveal a period of time within the CHBZ, referred to as the evolved-ore-stage event, during which realgar, aktashite, christite, and Au-bearing iron-sulfide minerals were precipitating contemporaneously, probably in different portions of the deposit.

These observations provide insight into the collapse of Carlin-type ore systems. The EOPs are consistently spatially associated with late-ore-stage realgar and/or aktashite

and some contain Au, though concentrations are low. The EOP1s are surrounded by illite and jasperoid (Fig. 30A-B), indicating that main-ore-stage alteration was still forming at the beginning of the evolved-ore stage (Fig. 49). Some minerals are part of both the evolved and late-ore stages; however, Au-bearing iron-sulfide minerals, illite, and/or jasperoid ceased to form during the late-ore-stage owing to changes in temperature and chemistry as the system finally collapsed (Fig. 49).

Post-ore-stage event

Post-ore-stage minerals primarily consist of calcite veining and oxidation minerals including goethite, hematite, jarosite, and arsenate (Jackson et al., 2010). The coarsely crystalline calcite veins precipitated after the ore fluid had completely dissipated, which is evident by the presence of calcite veins with realgar clasts within them and because the veins crosscut mineralization and brecciation. Highly oxidized rocks contain visible gold alloys, indicating that the remobilized Au became concentrated after it was released by the oxidation of pyrite. In partially oxidized rocks, Au remains where it was deposited in former iron-sulfide minerals, a common relationship in the CHLZ. Although the Au remains within the location of the former Au-bearing iron-sulfide mineral, other pathfinder elements including Tl, Hg, Cu, and As appear much more mobile because they no longer correlate with Au within the secondary Au-bearing iron-oxide minerals. Other elements, however, such as Sb, Bi, and Pb, better correlate with Au within CHBZ partially oxidized samples, and should be examined as pathfinder elements within partially oxidized rocks.

Geochemical Suites

Two distinct geochemical suites of iron-sulfide minerals are interpreted based on differences in Pb and Sb concentrations and associated Au, and are referred to as the evolved- and main-ore-stage geochemical suites. The main-ore-stage fluid represents the Carlin fluid at the time the majority of the Au-bearing iron-sulfide minerals precipitated. The evolved ore-stage suite is interpreted to represent the chemistry of the Carlin fluid at the time the last Carlin related iron-sulfide minerals precipitated. At this time, the Cortez Hills system was beginning to collapse and precipitate typical CTGD late-ore-stage minerals on the system periphery while Au-bearing iron-sulfide minerals were precipitating in other regions of the deposit.

The evolved ore-stage fluid chemistry is represented by the EOPs previously described. The evolved-ore-stage fluid contained elevated and positively correlated Sb and Pb relative to the main-ore-stage fluid (Tables 7, 10). Emsbo et al. (2003) reports a similar increase in Sb in the ore fluid through time at the Meikle deposit, indicated by increased Sb in late-ore-stage pyrite and the deposition of late-ore-stage stibnite. The authors interpreted the late-ore-stage increase in Sb to be a result of decreasing solubility as the system cooled. Muntean et al. (2011) document an increase in Sb from the inner (early) rim to the middle of the rim in a zoned Au-bearing iron-sulfide mineral from the Getchell deposit. The current study also recognizes an increase in the concentration of Sb through time owing to changes in solubility that occurred with cooling.

There are two possibilities for the elevated and positively correlated Pb in the CHBZ evolved-ore-stage iron-sulfide minerals. 1) Similar to Sb, Pb may have become insoluble as the system cooled, thus, precipitating in higher concentrations with time.

Unlike Sb, an increase in the concentration of Pb through time within Au-bearing iron sulfide minerals has not been documented in other well studied CTGDs. 2) Lead was added to the ore-stage fluid by fluid-rock interaction with Neoproterozoic and Cambrian clastic rocks as documented by Tosdal et al. (2003) in ore-stage pyrites at the Getchell and Turquoise Ridge deposits.

The presence of Hg- and Tl-rich minerals aktashite and christite suggest elevated Hg and Tl in the ore fluid during the evolved-ore stage. Additionally, Hg and Tl remain present in all of the evolved-ore-stage iron-sulfide minerals. However, there is variation in the correlation of Hg and Tl with Au and/or Sb and Pb in the evolved ore-stage iron sulfide minerals. The precipitation of aktashite and christite may control the concentration of Hg and Tl in the evolved-ore-stage fluid at a given location and time.

This study reveals the first definitive documentation of precipitation of a typical late-ore-stage mineral, realgar, after precipitation of Au-bearing iron-sulfide minerals, thus, making the timing relationships between ore-stage and late-ore-stage minerals more complex than previously documented. The evolved ore-stage fluid indicates the spatial and temporal complexity of the chemical evolution of the fluid.

Breccia Formation

Transects through host rocks that transition from negligible to high Au concentrations were examined (Figs. 26-27) in order to determine the relationship between brecciation and mineralization. Carbonate rocks transition from primarily recrystallized calcite into rocks that contain Au-bearing iron-sulfide minerals, jasperoid, fine-grained calcite, illite and carbonaceous material along seams. The seams only occur in mineralized rocks, which signify that they are a result of the alteration caused by the

ore fluid that formed the Cortez Hills CTGD. The seams are associated with high porosity and Au mineralization, and are interpreted to be a result of dissolution and residual enrichment of insoluble carbonate rock and Au-bearing iron sulfide minerals.

Paragenetic and textural observations demonstrate that these dissolution seams represent ore fluid pathways through carbonate host rocks, and intense fluid-rock interaction along these seams ultimately removed significant rock mass and resulted in brecciation. Figure 50 illustrates processes that caused the formation of the dissolution seams and ultimately brecciation. The ore fluid likely took advantage of the porosity along the pre-ore Voodoo fault (Fig. 50A) (Venendaal, 2007) and pervasively altered and mineralized the areas adjacent to the fault by removing silicate and carbonate minerals and adding ore-stage alteration and Au-bearing iron-sulfide minerals (Fig. 50B). Dissolution of large volumes of carbonate rock along and adjacent to the Voodoo fault created open space by removing abundant rock mass (Fig. 50B), which concentrated insoluble materials and ore-stage minerals within the seams (Fig. 50C). The dissolution created the space that caused collapse breccia formation (Fig. 50C). In areas containing heterolithic brecciation and the most intense dissolution, the dissolution seams are all that remain of a much larger volume of rock, and the seams contain insoluble materials from an originally much greater volume of rock. With increasing grade the seams become less linear and more patchy. Such areas comprise the most heavily brecciated and mineralized core of the CHBZ that grades outward into a low-grade mineralized crackle breccia on the periphery of the breccia zone.

Late-ore-stage realgar precipitated in open space throughout the breccia, commonly conforming to euhedral crystal faces of calcite and aktashite and chemically

cementing zones of intense fracturing and high porosity. This signifies that brecciation terminated before most of the realgar precipitated within the CHBZ, thus, allowing realgar to cement the breccia. The region of the CHBZ that contains fragmented realgar clasts indicates that localized brecciation continued after some realgar precipitation. The rimming of the fragmented realgar with Au-bearing iron-sulfide minerals indicates that Au was still being transported by the fluid after localized brecciation. These textures are consistent with local contemporaneous brecciation and mineralization.

The consistent association between fragmented realgar and the presence of Au-bearing rims on realgar clasts indicates that the same process that fragmented the realgar also allowed the ore fluid to be reintroduced to previously mineralized rocks (Fig. 51). The four samples that contain the EOP1s are located in the footwall of, and directly adjacent to, a dike, and many of the dikes within CHBZ fill faults (Jackson et al., 2010). Hypotheses for the formation of EOP1s that rim realgar include: 1) reactivation of a fault fragmented the realgar, reduced local pressure, and allowed Au-bearing evolved ore-stage fluid to encounter the evolved-ore-stage realgar (Fig. 51), or 2) a second, later Carlin-type ore fluid interacted with previously-formed late-ore-stage rocks. As there is no other evidence for a later pulse of ore fluid, the first hypothesis better explains why the EOP1s rim fragmented realgar at a single locality.

CHAPTER 10

CONCLUSIONS

The primary focus of this study was to determine if the Cortez Hills Breccia Zone (CHBZ) contains mineral assemblages, alteration, and paragenetic relationships that resemble other well studied CTGDs. The data collected indicate that the CHBZ refractory ore exhibits the following mineral paragenesis (Fig. 49). 1) Diagenetic pyrite was deposited in passive margin carbonate rocks. 2) A pre-ore suite of minerals associated with low-grade contact metamorphism includes pyrite, sphalerite, chalcopyrite, and tremolite. 3) Ore-stage ore and alteration minerals include illite, jasperoid, and Au- and trace element-rich iron-sulfide minerals. 4) Hg- and Tl-rich minerals including aktashite ($Cu_6Hg_3As_4S_{12}$) and christite ($TlHgAsS_3$) precipitated during a late-ore-stage directly following the precipitation of the vast majority of the Au-bearing iron-sulfide minerals. 5) Late- to post-ore-stage minerals include realgar and calcite and are associated with cooling and collapse of the hydrothermal system. The mineral paragenesis completed as a result of this study closely resembles the paragenesis completed for the CTGDs along the Getchell trend and the Goldstrike deposit (Groff et al., 1997; Cline and Hofstra, 2000; Almeida et al., 2010); however the current study recognizes an evolved ore-stage mineral assemblage that is transitional between the ore-stage and late-ore-stage mineral events.

The evolved ore-stage refers to the period of time when the system began to cool and collapse; it is the transition between the main-ore stage and the late-ore stage. The evolved ore-stage iron-sulfide minerals contain elevated Sb and Pb and typically inconsistent associations of Au with Tl, Hg, Cu, and As. During the evolved ore-stage

event, realgar, aktashite, christite and Au-bearing iron-sulfide minerals precipitated simultaneously at different localities within the deposit, resulting in local formation of realgar with Au-bearing iron-sulfide rims.

The secondary goal of this study was to determine if Au deposition occurred contemporaneously with brecciation. Transects through host rocks that transition from negligible to high Au concentrations exhibit increasing alteration from primarily recrystallized calcite into rocks that contain Au-bearing iron-sulfide minerals, illite, jasperoid, fine-grained calcite and insoluble carbonaceous material concentrated in dissolution seams. Paragenetic and textural observations suggest that the dissolution seams represent ore fluid pathways through the carbonate host rocks, and intense fluid-rock interaction along these seams ultimately resulted in significant decrease in rock mass and resulting brecciation. Although silicification occurred with Au mineralization, porosity increased because of the non-interlocking texture of the jasperoid, which contributed to the formation of soft, non-cohesive rock and aided in collapse brecciation. The process by which this occurred began with contemporaneous sulfidation, decarbonatization, and silicification of the host rock by the Carlin ore fluid. This resulted in the precipitation of Au-bearing iron-sulfide minerals and the alteration of host rocks to form illite, and jasperoid, along with intense dissolution of carbonate and silicate minerals by the ore fluid (Fig. 50).

Future Work

The oxidation of the minerals aktashite and christite should be studied, as these minerals are unique to the CHBZ. The Cortez Hills deposit contains native mercury in specific localities, and the source of the native mercury is undetermined. The oxidation

of these minerals may release the Hg from the prior sulfide bond, allowing it to concentrate as native Hg, conceptually similar to the concentration of Au alloy in strongly oxidized rocks.

The Cortez Hills Lower Zone partially oxidized ore should be studied in detail to determine which elements best correlate with Au within Au-bearing iron-oxide minerals. These data should be compared to whole rock geochemistry. This thesis study suggests that partially oxidized rocks may have Au path finder elements that are different from sulfide-bearing and fully oxidized rocks. Soil sampling is a common exploration technique for CTGDs, and, because soil samples are commonly oxidized, it may enhance exploration techniques to fully understanding the element correlations in a partially oxidized CTGD.

Lastly, the dike that is adjacent to the fragmented and rimmed realgar clasts should be studied and dated. This dike may constrain the age of Carlin-type mineralization as it crosscuts mineralized rocks through the majority of the CHBZ, but is also mineralized on its periphery in other portions of the deposit. The crosscutting relationships of the dike may provide insight into the age of brecciation, the main- and evolved-ore-stage events.

APPENDIX A

TABLES

Table 1. List of acronyms

CTGD	Carlin-type gold deposit
CHBZ	Cortez Hills Breccia Zone
CHLZ	Cortez Hills Lower Zone
RMT	Roberts Mountains Thrust
UNLV	University of Nevada, Las Vegas
EPMA	Electron Probe Microanalyzer
XRD	X-ray diffraction
SEM	Scanning electron microscope
CL	Cathodoluminescence
LA-ICP-MS	Laser ablation inductively-coupled plasma mass spectrometry
MDL	Method detection limit
PO	Pre-ore
OP	Ore-stage iron-sulfide
EOP	Evolved-ore-stage iron-sulfide

Table 2. Probe conditions

20 kV, 10 nA, 1-2 µm				
	1	2	3	4
MAJORS	TAP	PETH	LIF	TAP
	As	Ca	Fe	As
	Si	S		
Run Time (min)	2	2	1	1

20 kV, 100 nA, 1-2 µm				
	1	2	3	4
TRACE	TAP	PETH	LIF	TAP
	Zn	Hg	Ti	Zn
	Se	Ag	Co	Se
	Si	Te	Ni	
		Sb	Cu	
		Mo	Au	
		Sn	Tl	
		W	Bi	
		Pb		
Run Time (min)	3	9	21	2

Table modified from Muntean et al. (2011).

Instrument: JEOL-8900 Electron Probe Microanalyzer.

Table 3. X-ray line, spectrometer, peak data, and minimum detection limit (MDL) for the suite of elements used for EPMA analysis at the Cortez Hills deposit

Element	X-ray	Spectrometer	Crystal	Peak (mm)	Back[H+] (mm)	Back [L-] (mm)	Peak (sec)	Back (sec)	MDL (ppm)	MDL (cps)	standard
Si	Kα	SP1	TAP	77.435	2.25	2.25	30	15	49		MAC-Wollastonite
S	Kα	SP2	PETH	172.089	5.00	5.00	30	15	1,493		MAC-FeS_2
Ca	Kα	SP2	PETH	108.100	2.80	2.80	30	15	465		MAC-Wollastonite
Fe	Kα	SP3	LIF	134.709	4.00	2.00	30	15	558		MAC-FeS_2
As	Lα	SP1 & SP4	TAP	105.145	5.00	5.00	30	15	310		MAC-Aresenic
Ti	Kα	SP3	LIF	191.192	1.50	1.50	30	15	197	9.4	SMH-Ilmenite
Co	Kα	SP3	LIF	124.506	5.00	5.00	30	15	32	8.6	GLR-Co
Ni	Kα	SP3	LIF	115.308	4.50	4.50	30	15	163	9.4	GLR-Ni
Cu	Kα	SP3	LIF	107.174	2.80	2.80	30	15	186	10.5	MAC-Chalcopyrite
Zn	Lα	SP1 & SP4	TAP	133.266	5.00	5.00	30	15	176	5.5	MAC-ZnS
Se	Lα	SP1 & SP4	TAP	97.705	2.75	5.00	30	15	89	7.5	CMI-Se
Mo	Lβ	SP2	PETH	165.869	1.00	1.250	30	15	282	8	GLR-Mo
Ag	Lβ	SP2	PETH	133.285	2.00	2.00	30	15	97	13.1	CMI-Ag
Sn	Lβ	SP2	PETH	115.669	1.50	1.50	30	15	145	9.4	CM1-Sn
Sb	Lβ	SP2	PETH	110.634	4.00	4.00	30	15	111	19	CM1-Sb
Te	Lβ	SP2	PETH	105.058	3.75	3.75	30	15	130	20.2	CM2-PbTe
W	Mα	SP2	PETH	223.570	3.00	3.00	30	15	375	3.1	CM1-W
Au	Lα	SP3	LIF	88.741	4.00	2.80	270	135	91	4.5	GLR-Au
Hg	Mα	SP2	PETH	180.815	2.40	2.40	120	60	97	3.9	CM2-HgS
Tl	Lα	SP3	LIF	83.915	1.20	0.98	120	60	426	6.7	CM2-TlBr
Pb	Mα	SP2	PETH	169.249	5.50	3.00	30	15	387	4.1	MAC-PbS
Bi	Lα	SP3	LIF	78.642	5.00	5.00	120	60	373	9.9	CM1-Bi

Table modified from Muntean et al. (2011)

Instrument: JEOL-8900 Electron Probe Microanalyzer.

Abbreviations: Kα = K alpha-line x ray; Lα = L alpha-line x ray; Lβ = L alpha-line x ray; Mα = M alpha-line x ray; SP = spectrometer; TAP = Thallium acid phthalate; PETH = high Pentaerythritol; LiF = Lithium fluoride; Back[H+] = high background; Back[L-] = low background; MDL: method detection limit; MAC, SMH, GLR, CM1, CM2 = standard blocks.

Table 4. X-Ray Diffraction settings

Configuration	Sample Spinner
Scan axis	Gonio
Scan mode	Continuous
Start angle	5
End angle	75.998
Step size	0.0041778
Time per step	17.780
Scan speed	0.029842
Number of steps	16994
Sample disk diameter	27 mm
Total time	40:53

Instrument information: PANalytical X'PERT Pro X-ray Diffraction Spectrometer

Table 5. LA-ICP-MS conditions

Laser System		**ICP-MS**	
Wavelength	193 nm	rF Power	1400 W
Spot Size	5 µm	Carrier Gas (He)	1.0 l/min
Pulse Frequency	3 Hz (spots) 5 Hz (lines/maps)	Makeup Gas (Ar)	0.6 l/min
Scan Speed	1 µm/sec		
Energy Density	~5 J/cm^2		

Instrument information: Photon Machines Analyte G2 LA system (193 nm, 4 ns Excimer laser) coupled to a PerkinElmer DRC-e Inductively Coupled Plasma Mass Spectrometer.

Table 6. Pre ore-stage pyrite classification by description, chemistry and associated minerals

Pyrite type	Appearance in reflected light microscopy	Elevated Chemistry (probe data)	Spatially Associated Minerals	Int. Process of Formation
PO1	Anhedral, textured pyrite with a yellowish tint.	Ni, Pb, Co ± Ag in interior ± Au, Hg, Cu, Tl, Sb, Ni, Co in rim	Fine grained mottled calcite, medium to coarse grained recrystallized calcite. Rarely has a Au, Hg, Cu, Tl, Sb, Ni, Co enriched iron-sulfide rim with similar relief as the PO1 pyrite.	Diagenetic
PO2	Bright white, subhedral, high relief, with good-excellent polish	As, Sb, Sn ± Au, Tl, Hg, Cu, As rich rim	Fine grained mottled calcite, quartz, and illite. Commonly has a low relief yellowish white Au, As, Tl, Cu, Hg enriched iron-sulfide rim.	Undetermined
PO3	Irregular anhedral pyrite masses. Contains linearly aligned pore spaces, hundreds of microns in size	n.a.	Chalcopyrite, tremolite, quartz, sphalerite, calcite	Metamorphic

Abbreviations: n.a. = not analyzed, PO = pre ore, Int. = interpreted

Table 7. Ore- and evolved-ore-stage iron-sulfide minerals differentiated by petrographic characteristics and chemistry

Name	Appearance in reflected light	Chemistry	Other characteristics	Spatially associated minerals
OP1	Bright yellowish white, low relief, anhedral, disseminated and/or rimming pyrite cores	As >> (Tl+Hg+Cu) > (Au±Sb) > ± Ag, Bi, Ti. No Au:Pb correlation	Hardness of 2-3. >1 to 50 µm	realgar, sphalerite, mottled calcite, illite, quartz
OP2	Bright white, typical pyrite relief and reflectivity, anhedral	As >> (Tl+Hg+Cu) > (Au+Sb) > Ag ± Bi, W, No Au:Pb correlation	Irregular masses	mottled calcite, illite, quartz
OP3	Light brownish yellow, uneven relief, anhedral, poor polish, clusters without pyrite cores	As >> (Tl+Hg+Cu) > ± Au > Ag ≥ ± Sb, ± Bi, W No Au:Pb correlation Elevated Bi	2 to 30 µm	mottled calcite, illite, quartz
EOP1	Bright yellowish white, low relief, anhedral, disseminated and/or rimming pyrite or realgar cores	As >> (Pb+Cu) ≥ (Sb+Hg±Tl) ≥ (Au±Bi) > ± Ag	Texturally similar to OP1	commonly rim realgar
EOP2	Dull tannish white to pinkish white, low relief, anhedral fuzzy rims	As >> (Pb+Cu) > (Sb+Hg) > (Tl+Au) > Ag + elevated Ni and Au within CHLZ	None	iron-oxide, mottled calcite, illite, quartz
EOP3	Brownish-white rimming a brighter whitish tan pyrite core, subhedral	As >> (Tl+Hg+Sb±Pb) >> (±Cu±Ni±Ag±Ti) No Au	Located within a dike	feldspar, illite
EOP4	Tan with bright white flecks, irregular ratty texture	As >> Cu > (Tl+Hg+Ni) > (Pb±Sb±Au) ≥ ± Ag	Rarely contains Au	aktashite, realgar, illite, quartz
EOP5	Dull yellowish-white circular doughnut shape with dark browns holes at the center, relatively low reflectivity	As >> (Pb+Cu) > (Tl+Hg+Bi) > Sb > Ag ± Ti No Ni or Au	Rarely observed with aktashite or chalcopyrite core, but commonly surrounded by these minerals.	aktashite, chalcopyrite, quartz

Abbreviations: OP = ore-stage iron-sulfide, EOP = evolved ore-stage iron-sulfide.

Table 8. EPMA weight percent data for aktashite, routhierite and christite element compositions within CHBZ and mineral type localities

Element	Aktashite (CHBZ)	Aktashite (Russia)	Christite (CHBZ)	Routhierite (France)	Christite (Carlin mine, NV)
As	10.21	18.20	9.76	13.2	13.1
S	24.33	23.80	22.27	19.6	16.6
Zn	1.12		0.20	2.0	
Hg	37.62	32.54	32.80	34.7	35.1
Cu	24.04	23.38	2.47	3.9	
Sb	0.27	2.55	0.36	2.6	
Tl			31.50	20.4	35.2
total	97.59	100.47	99.36	96.40	100.00

Aktashite and christite data from Mineral Data Publishing (2001).
Only the elements that comprise the mineral chemical formulas are listed, see Appendix E for other elements.

Table 9. Spearman rank correlation matrix of 18 elements.

	As	S	Fe	Zn	Hg	Au	Se	Pb	Tl	W	Bi	Cu	Sb	Ni	Sn	Co	Ag
S	**-0.893**																
Fe	**-0.868**	**0.848**															
Zn	-0.042	0.050	-0.015														
Hg	**0.751**	**-0.640**	**-0.790**	0.043													
Au	**0.679**	**-0.645**	**-0.529**	-0.153	**0.442**												
Se	-0.329	0.252	0.261	0.040	-0.192	-0.252											
Pb	-0.108	0.154	0.025	0.043	0.014	-0.259	0.253										
Tl	**0.718**	**-0.604**	**-0.728**	-0.023	**0.934**	**0.456**	-0.230	-0.108									
W	-0.154	0.189	0.228	-0.017	-0.203	-0.156	0.221	0.143	-0.230								
Bi	-0.225	0.182	0.155	-0.002	-0.073	-0.110	0.307	**0.531**	-0.180	0.235							
Cu	**0.524**	**-0.483**	**-0.476**	0.159	**0.495**	**0.484**	-0.035	-0.074	**0.425**	-0.044	0.131						
Sb	**0.602**	**-0.444**	**-0.491**	-0.085	**0.606**	0.358	-0.301	0.126	**0.613**	-0.131	-0.197	0.074					
Ni	-0.167	0.105	0.033	0.047	-0.088	-0.028	0.187	-0.060	-0.120	-0.067	0.000	0.173	**-0.443**				
Sn	-0.206	0.267	0.185	0.120	-0.137	-0.255	0.070	0.094	-0.180	0.164	0.000	0.003	-0.017	0.010			
Co	**-0.493**	**0.436**	**0.457**	0.114	-0.353	-0.259	0.258	0.005	-0.374	0.130	0.039	-0.167	**-0.474**	**0.428**	0.023		
Ag	0.244	-0.293	-0.308	0.049	0.392	0.246	0.074	0.086	0.343	0.003	**0.429**	**0.459**	-0.042	0.088	-0.125	-0.078	
Ti	0.092	-0.109	-0.091	0.041	-0.009	0.098	-0.050	0.108	-0.021	0.031	0.079	0.144	-0.026	0.052	-0.061	-0.048	0.081

EPMA data collected on all iron-sulfides within CHBZ. Values >0.4 and <-0.4 in bold.

Table 10. Elevated trace element chemistry and elevation within the deposit by thin section

Thin section	Elevation (feet)	Elevated trace elements (EPMA)	Element correlations (Pb,Sb,Au)	# pts. (EPMA)	Pyrite types (EPMA)	Minerals present in sample
Main ore-stage						
DC 124 1273’	4790’	Sb, Hg, Tl, Au, Cu, As High Tl/Au and Hg/Au ratios	Au:Sb R^2=0.52 Au:Pb R^2=0.01 Pb:Sb R^2=0.01	23	OP1, OP2	realgar, sphalerite
CHUE 019 485.5'	4314’	Pb, Bi, Ag, Hg, Tl, Au, Cu, As, ±Ti, Ni, Co	Au:Sb R^2=0.04 Au:Pb R^2=0.00 Pb:Sb R^2=0.00	26	OP1, OP3	realgar
CHUD 038 453’	4339’	Ni, Co, Hg, Tl, Au, Cu, As, ±Ag	Au:Sb R^2=0.00 Au:Pb R^2=0.00 Pb:Sb R^2=0.01	7	OP1, EOP4	aktashite, titanium oxide pyrrhotite
CHUD 038 457’	4338’	Hg, Tl, Au, Cu, As, ±Ni, Co	Au:Sb R^2=0.20 Au:Pb R^2=0.30 Pb:Sb R^2=0.21	5	OP1, EOP4	aktashite, realgar
Evolved ore-stage						
CHUD 038 464’	4333’	Sb, Pb, Bi, Hg, Tl, Au, Cu, As, ±Ag High element/Au ratios	Au:Sb R^2=0.08 Au:Pb R^2=0.11 Pb:Sb R^2=0.00	11	EOP4, EOP5	aktashite, christite, sphalerite
DC 114 1236.5’	4830’	Sb, Pb, Bi, Hg, Tl, Au, Cu, As, low Tl/Au and Hg/Au ratios,	Au:Sb R^2=0.64 Au:Pb R^2=0.68 Pb:Sb R^2=0.79	21	EOP1, EOP2	realgar and pyrite with Au-bearing iron-sulfide rims
DC 124 1264’	4800	Anomalously high Sb, Pb, Hg, Tl, As, Au below detection.	Pb:Sb R^2=0.62	6	EOP3	feldspar
CHUE 215 246.5’ (CHLZ)	4081’	Sb, Pb, Ni, Co, Ag, Hg, Tl, Au, Cu, As	Au:Sb R^2=0.54 Au:Pb R^2=0.65 Pb:Sb R^2=0.99	3	OP3, EOP2	none
Oxidized						
CHUD 043 376.5’	4483’	Sb, [Hg ± Au]	Au:Sb R^2=0.49 Au:Pb R^2=0.34 Pb:Sb R^2=0.03	3	Oxidized iron-sulfides	

All data in this table were acquired from EPMA analyses of Au-bearing iron-sulfide minerals, with the exception of sample DC-124-1264’, which contains EOP3 data that do not contain Au (see EOP3 description in text).
All samples contain illite, quartz, and calcite.
Samples are listed in the order of greatest to least confidence of being interpreted as main-ore stage.
Abbreviations: pts. = points plotted in Figures 41-44.

Table 11. EPMA element weight percent and totals for select Au-bearing iron oxides.

Sample ID	As	S	Fe	Si	Zn	Hg	Au	Pb	Tl	Bi	Cu	Sb	Ni	Co	Ti	Totals
CHUD043_376.5a_unk1	2.78	0.03	45.93	3.85	0.067	0.250	0.000	0.064	0.021	0.018	0.157	0.266	0.138	0.084	0.102	54.41
CHUD043_376.5a_unk2	1.72	0.03	45.39	4.44	0.057	0.210	0.190	0.063	0.009	0.011	0.120	0.251	0.127	0.085	0.105	53.20
CHUD043_376.5a_r1	2.26	0.03	39.31	10.70	0.047	0.162	0.000	0.052	0.004	0.024	0.126	0.271	0.131	0.078	0.090	53.62
CHUD043_376.5a_1	2.54	0.01	49.41	3.31	0.066	0.381	0.000	0.035	0.000	0.000	0.133	0.316	0.120	0.077	0.079	56.89
CHUD043_376.5a_2	2.59	0.01	48.48	3.92	0.087	0.427	0.000	0.030	0.000	0.012	0.165	0.253	0.109	0.076	0.079	56.70
CHUD043_376.5a_3	2.41	0.01	51.54	3.29	0.071	0.284	0.000	0.029	0.000	0.000	0.159	0.344	0.137	0.081	0.106	58.93
CHUD043_376.5a_4	2.89	0.01	53.27	0.90	0.075	0.372	0.000	0.035	0.000	0.035	0.172	0.228	0.130	0.106	0.059	58.79
CHUD043_376.5b_unk1	1.70	0.01	45.13	3.47	0.068	0.334	0.000	0.051	0.000	0.000	0.060	0.300	0.069	0.073	0.087	51.61
CHUD043_376.5b_unk2	1.97	0.01	46.38	3.25	0.070	0.300	0.000	0.045	0.021	0.014	0.054	0.330	0.081	0.084	0.103	52.97
CHUD043_376.5b_unk3	1.53	0.00	37.38	6.87	0.053	0.255	0.000	0.032	0.000	0.000	0.042	0.238	0.057	0.055	0.064	46.77
CHUD043_376.5b_unk4	1.56	0.01	40.21	9.87	0.057	0.356	0.051	0.061	0.007	0.000	0.041	0.192	0.059	0.062	0.061	52.80
CHUD043_376.5b_unk5	1.16	0.01	38.05	15.87	0.037	0.214	0.000	0.046	0.000	0.024	0.050	0.250	0.049	0.077	0.080	56.10
CHUD043_376.5b_unk6	5.23	0.03	23.55	10.91	0.066	0.188	0.045	0.027	0.000	0.000	0.029	0.233	0.061	0.036	0.085	41.40
CHUD046_238a_Au1	0.06	0.04	0.39	0.17	0.000	3.613	95.137	0.000	0.400	0.000	0.117	0.011	0.000	0.000	0.007	100.38

Not all elements analyzed are represented here. See Appendix E for full element suite and compositions.

APPENDIX B

FIGURES

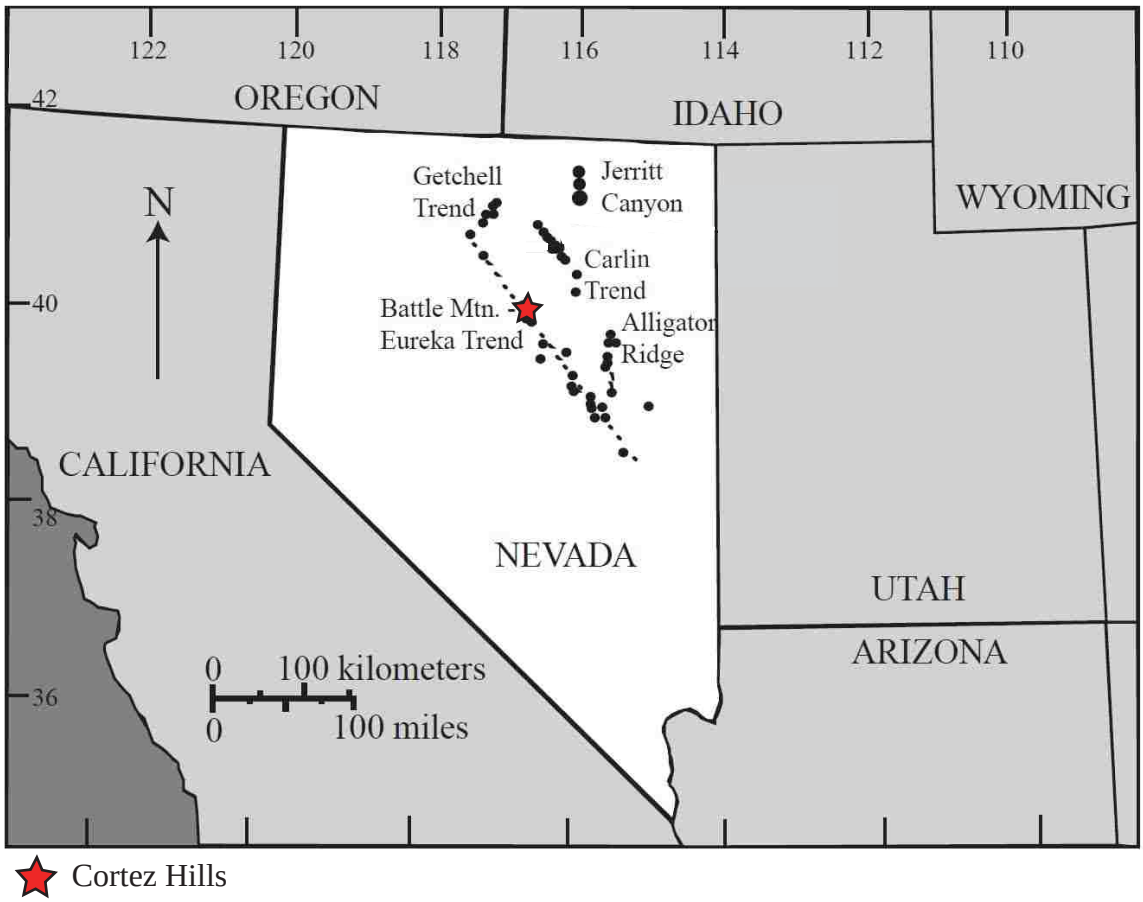

Figure 1. Regional setting of the Getchell, Carlin, and Battle Mountain-Eureka trends in Nevada, western United States. Location of the Cortez district (red star). Modified from Lubben (2004).

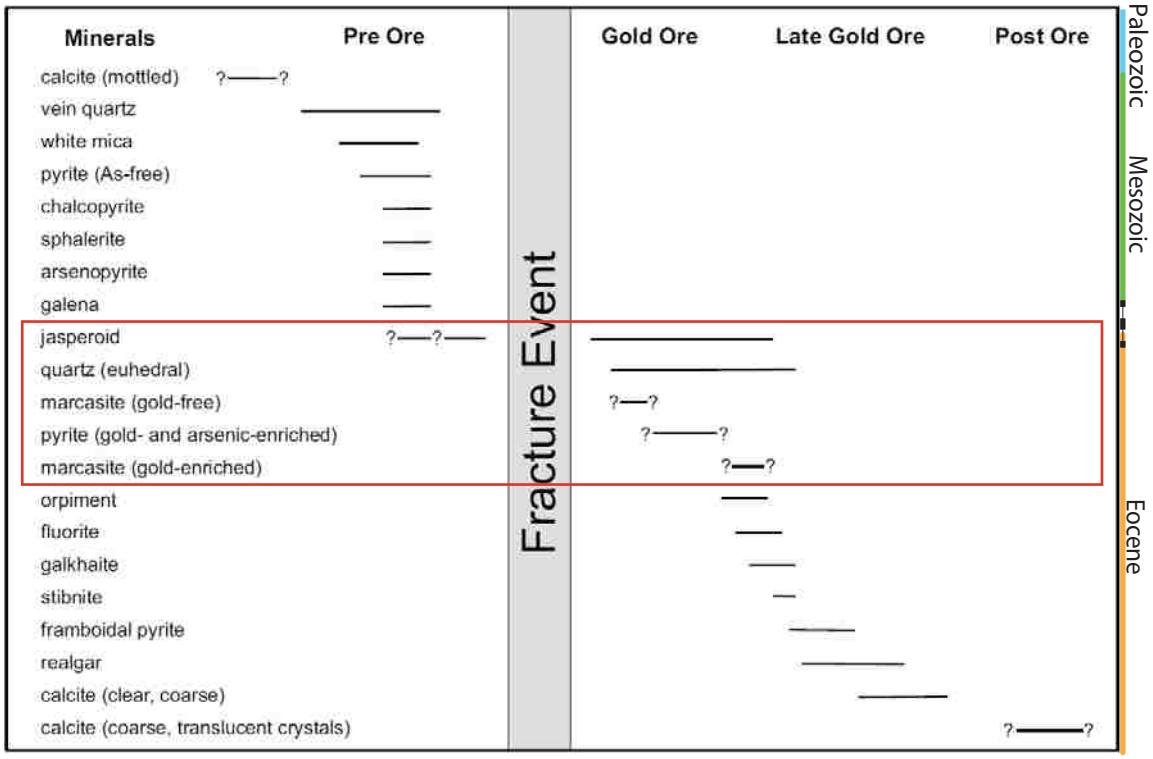

Figure 2. Mineral paragenesis of the Getchell deposit modified from Cline (2001). Paleozoic minerals are associated with deposition of the host rocks, Mesozoic minerals are associated with the 92 Ma Osgood stock, and Eocene minerals are associated with Carlin-type mineralization. The red box indicates the ore-stage alteration mineralogy.

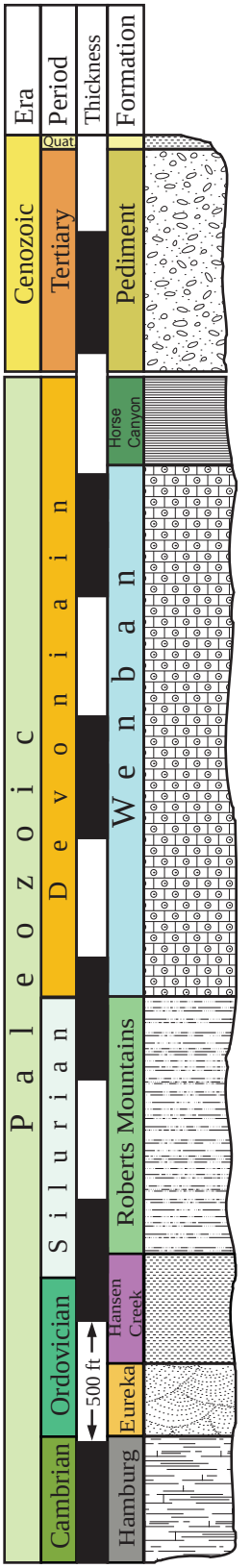

Unit Descriptions:

Quaternary Alluvium - Sedimentary fill (~50 ft thick).

Tertiary Pediment Deposit (informal) -
Siltstone & limestone clast-rich colluvium containing tuffaceous material (~950 ft. thick).

Devonian Horse Canyon Formation -
Siltstones, mudstones, claystones & cherts (300 ft. thick).

Devonian Wenban Formation -
Fine-grained silty & muddy limestones containing fossils and debris flows (~2100 ft. thick).

Silurian Roberts Mountains Formation -
Thin-bedded, silty limestones containing burrowing, fossils and black lenses (~1100 ft. thick).

Ordovician Hansen Creek Formation -
Dolomite & limestone marble (~500 ft. thick).

Ordovician Eureka Quartzite -
Tan to white quartzite with some cross-bedding (~400 ft. thick).

Cambrian Hamburg Formation -
Dolomite with some burrowing (~2000 ft thick).

Figure 3. Stratigraphic column of the Cortez window modified from Harry Cook, Barrick Internal Report (2008), Jackson et al. (2010), and L.P. Anderson, Barrick Cortez GeoServices, pers. comm. (2012).

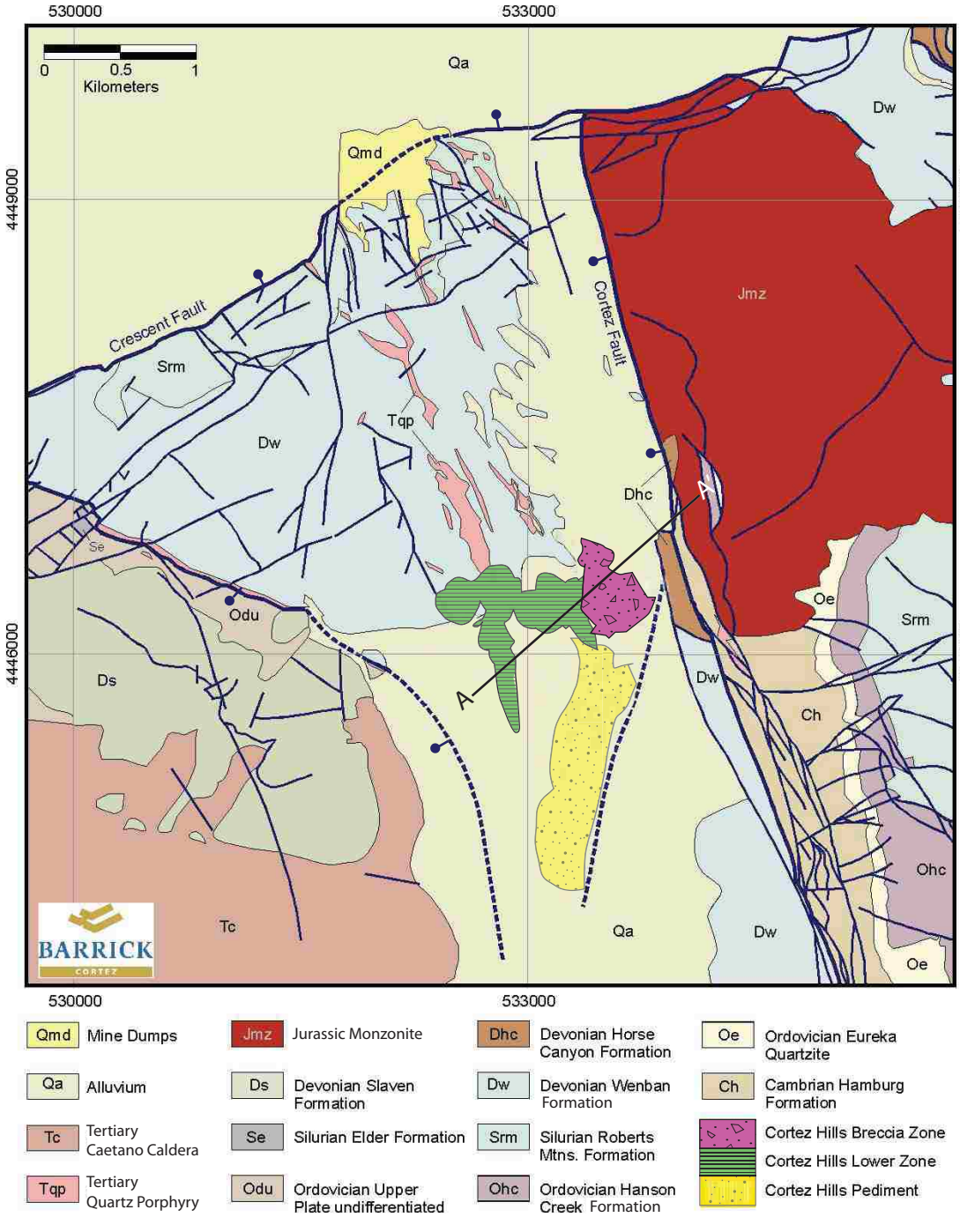

Figure 4. Geologic map of the Cortez Hills area indicating the surface projection of the Cortez Hills Breccia Zone (purple), Cortez Hills Lower Zone (green), and the Pediment Deposit (yellow). A-A' (black line) marks the location of the cross section in Figure 5. Blue lines indicate fault, with a blue circle on the down-dropped stratigraphy. Modified from Jackson et al. (2010).

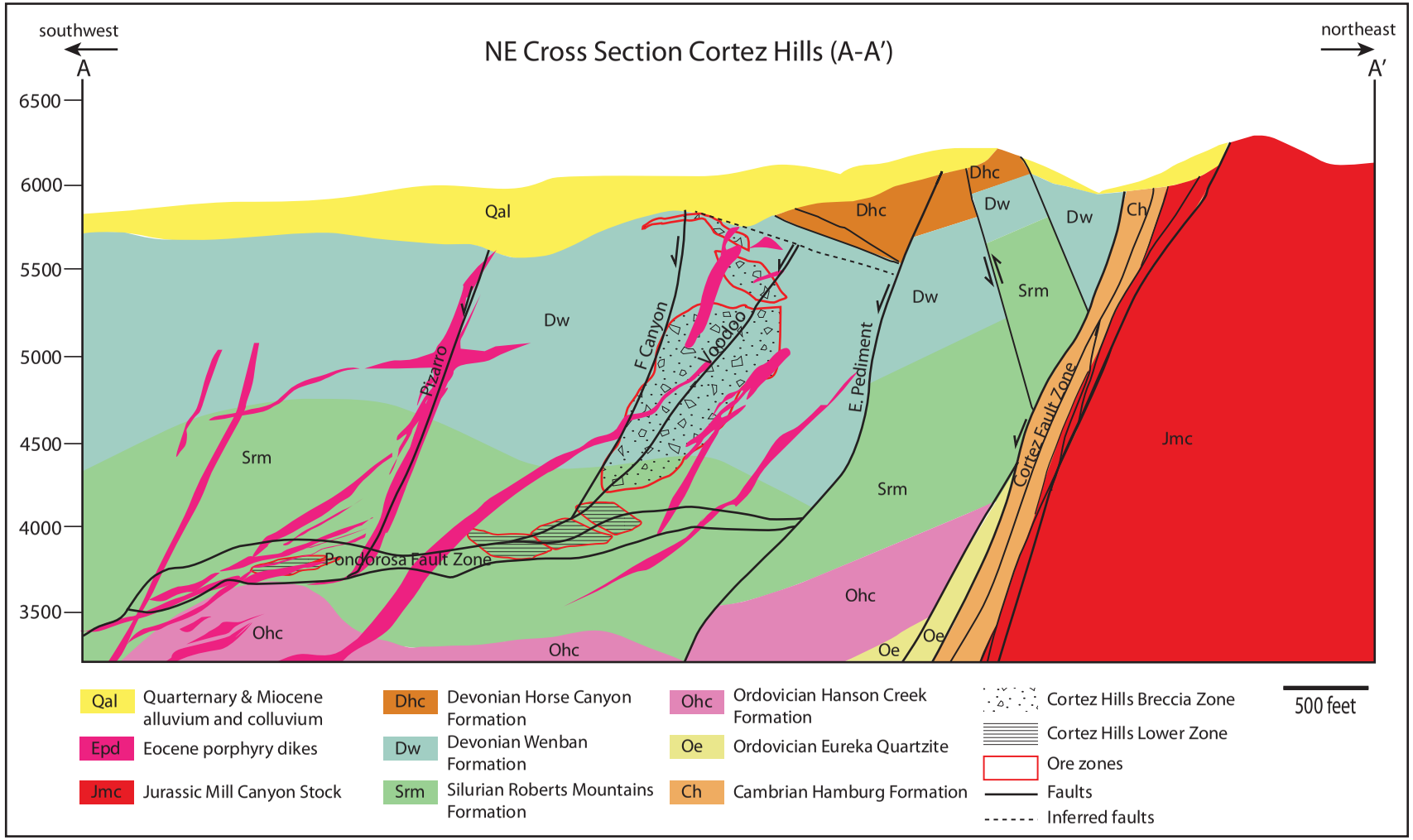

Figure 5. Simplified geologic cross section of location A-A' displayed in Figure 4. Ore bodies and stratigraphic contacts are projected as much as 50' behind and in front of the cross section line. Drill hole locations are projected as much as 200' behind and in front of the cross section line in order to display all sampled drill hole locations on one cross section. Many small scale structures and stratigraphic offsets are not shown due to scale of map. Elevations are above sea level.

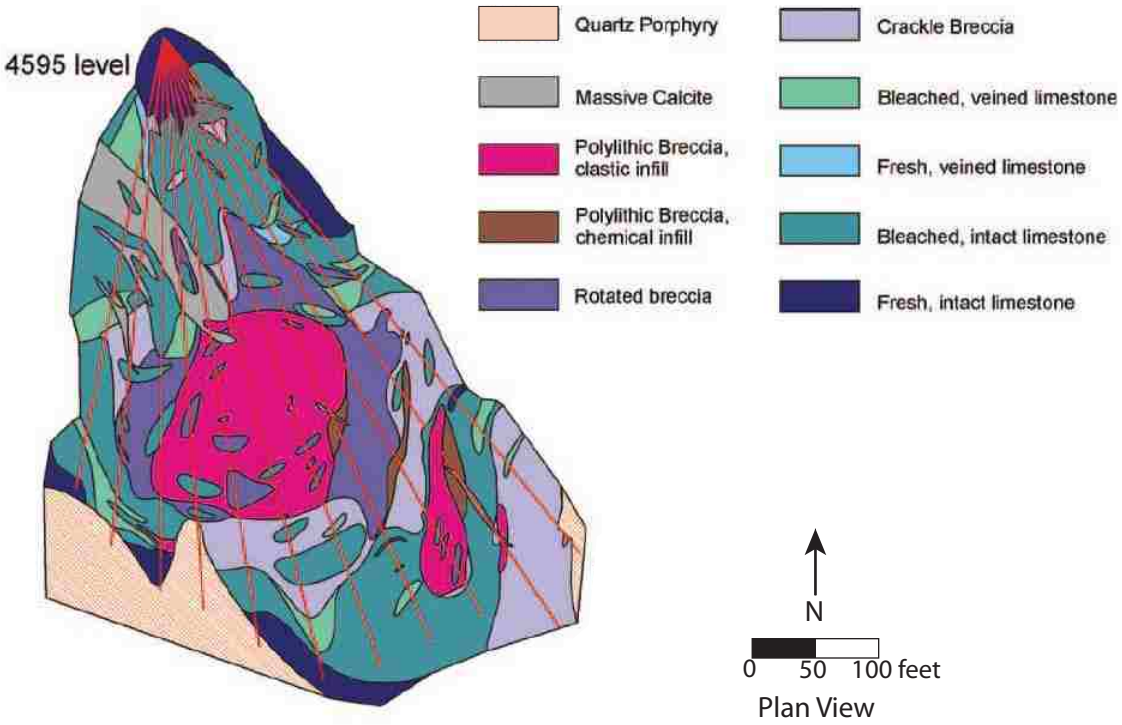

Figure 6. Plan view map of breccia architecture modeled from drill hole petrography from the 4595 level drill fan. Orange lines represent drill hole locations. The polylithic breccia core grades into a rotated breccia, which then grades into a crackle breccia and various limestone units. Modified from Jackson et al. (2010).

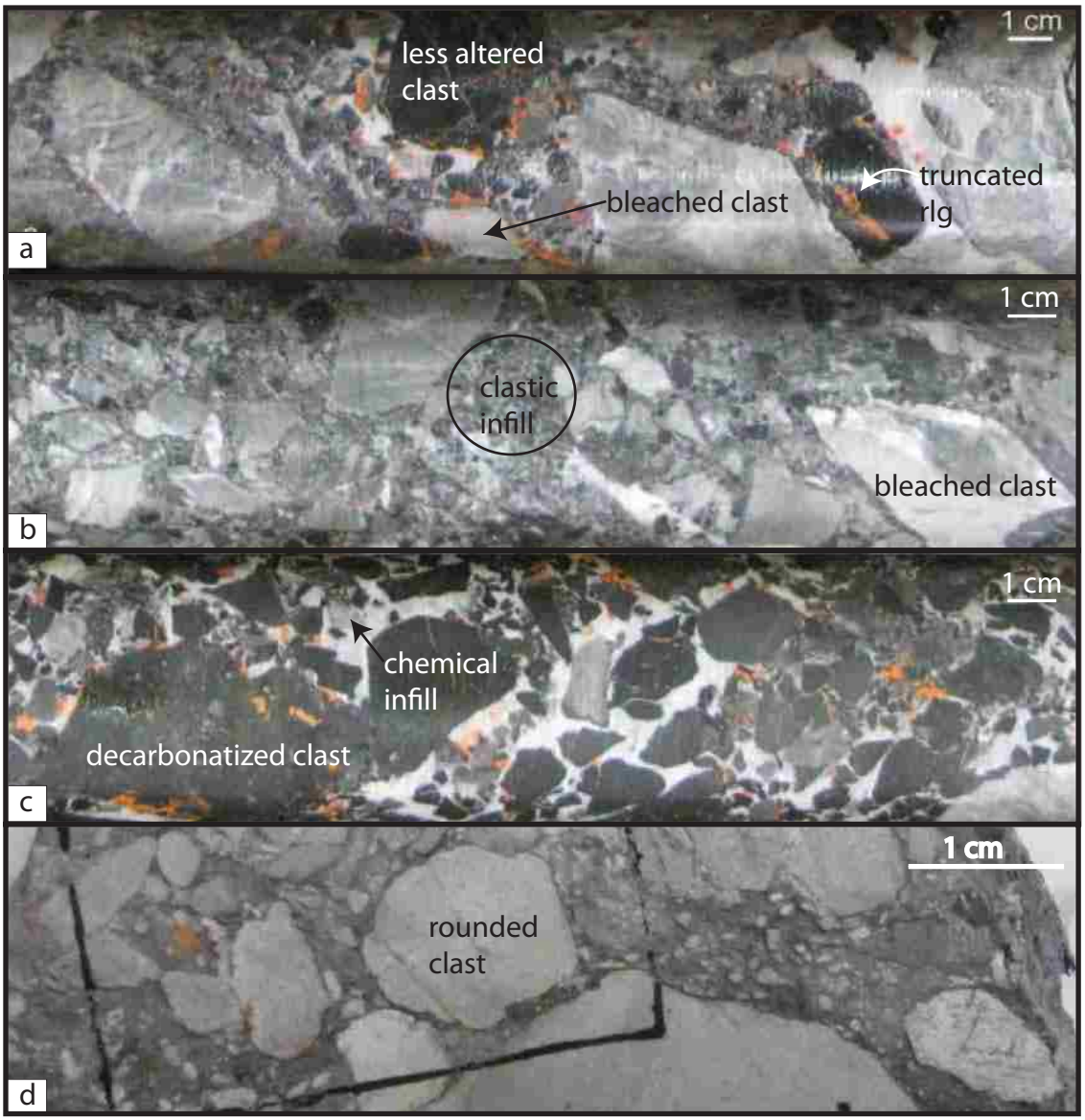

Figure 7. Photographs of polylithic breccia that contains a) bleached clasts, visually unaltered clasts, and realgar veinlets (orange) truncated at clast margins, b) recrystallized and bleached clasts and clastic infilled matrix, c) decarbonatized and bleached clasts with a dominantly calcite and realgar chemical infill matrix (a-c Modified from Jackson et al. (2010)), and d) sub rounded clasts that consist primarily of recrystallized calcite.

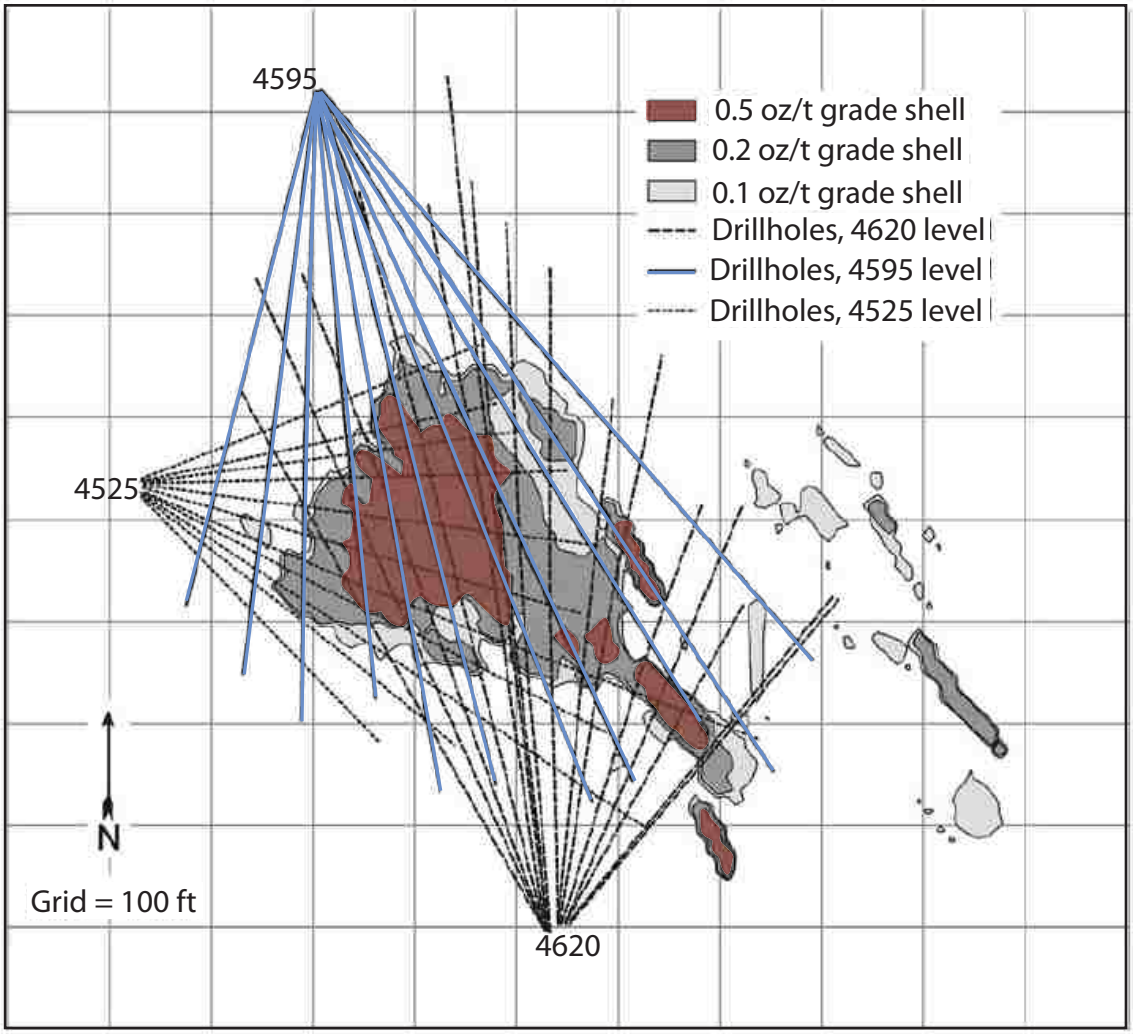

Figure 8. Plan view map displaying modeled grade shells from the 4595 level. Black lines indicate projected drill hole locations of three drill fans, and the blue lines indicate the 4595 level drill fan. This plan view map coincides with Figure 6. Modified from Jackson et al. (2010).

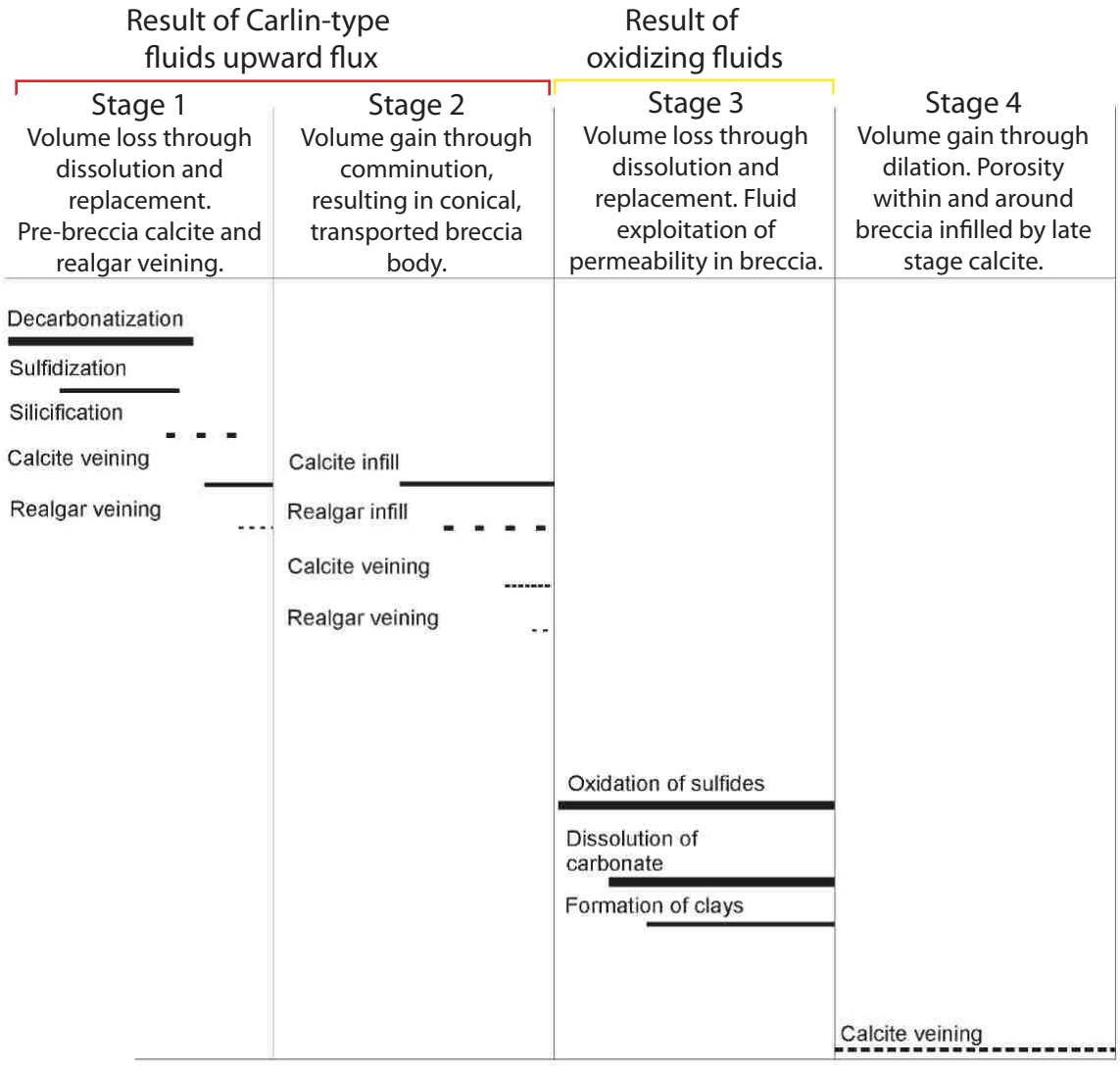

Figure 9. The sequence of events reported in Jackson et al. (2010) that resulted in the Cortez Hills Breccia Zone. Stage 1) the upward flux of Carlin-type fluid caused replacement mineralization and pre-breccia realgar and calcite veining. Stage 2) the upward flux of Carlin-type fluid cause the "transported", conical shaped, polylithic breccia, and thus, the dominant architecture of the breccia body. Stage 3) oxidizing fluids reacted with the pyrite to produce acid, which increased porosity and open space. Stage 4) late-stage calcite veins infilled the porosity within the breccia. Vertical spacing indicates time lapse between events. Modified from Jackson et al. (2010).

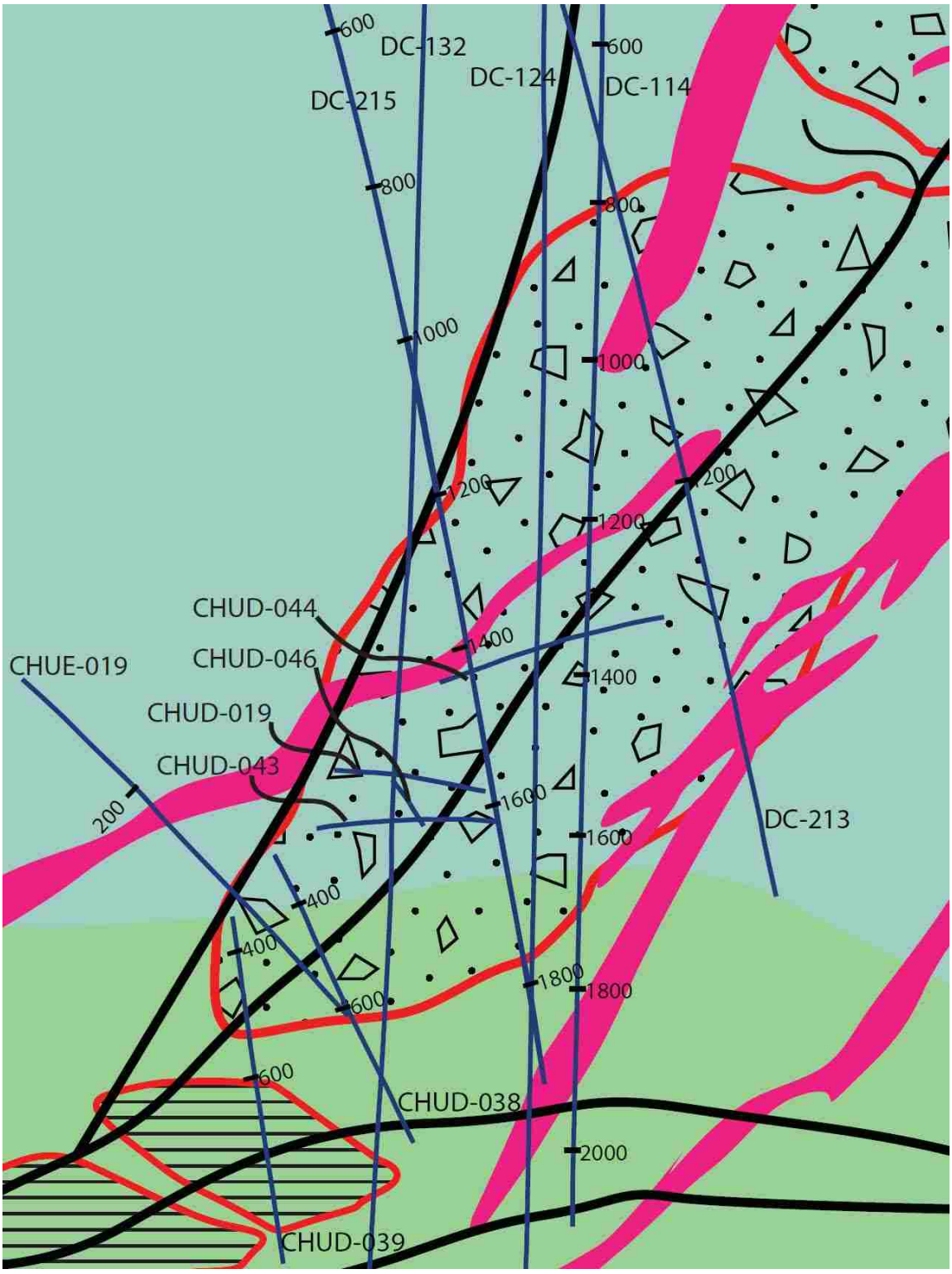

Figure 10. Magnified view of Figure 5 simplified cross section that displays the names and locations of each drill hole from which samples were collected for this study. See Figure 5 for legend.

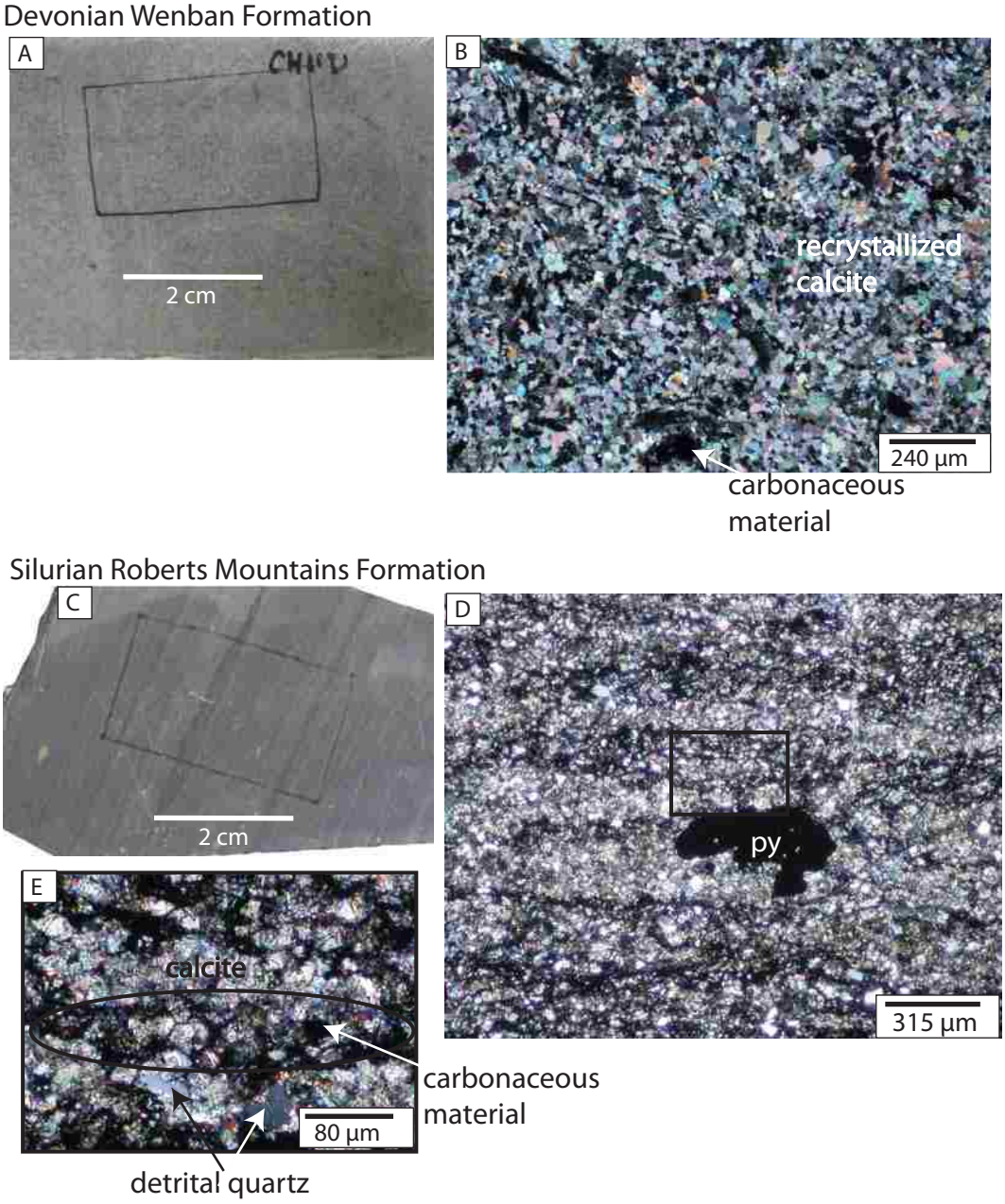

Figure 11. Hand sample (A) and crossed-polarized transmitted light photomicrograph (B) of a Devonian Wenban limestone sample. Hand sample (C) and crossed-polarized transmitted light photomicrograph (D, E) of a Silurian Roberts Mountains limestone sample; (E) is a magnified view of the black square in (D). Abbreviations: py = pyrite.

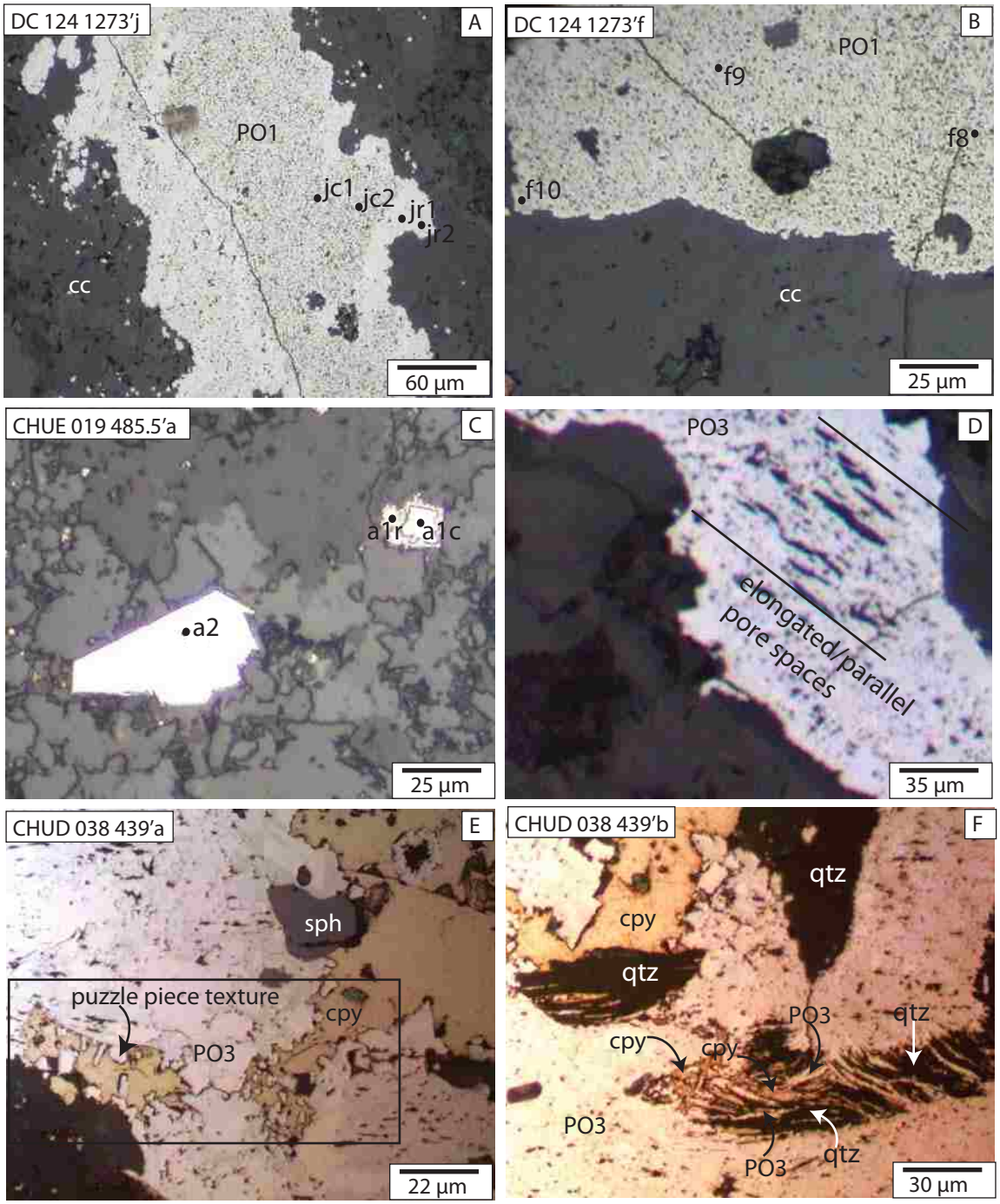

Figure 12. Photomicrographs of pre-ore-stage minerals under reflected light. (A-C) PO1 pyrites (A, B) and PO2 pyrites (C) with EPMA point locations indicated by small black dots. D) Elongated PO3 pyrite with pore spaces parallel to each other. PO3 and chalcopyrite exhibit an interlocking puzzle-piece texture (E) and wispy texture (F). Abbreviations: cc = calcite; sph = sphalerite; cpy = chalcopyrite; qtz -= quartz.

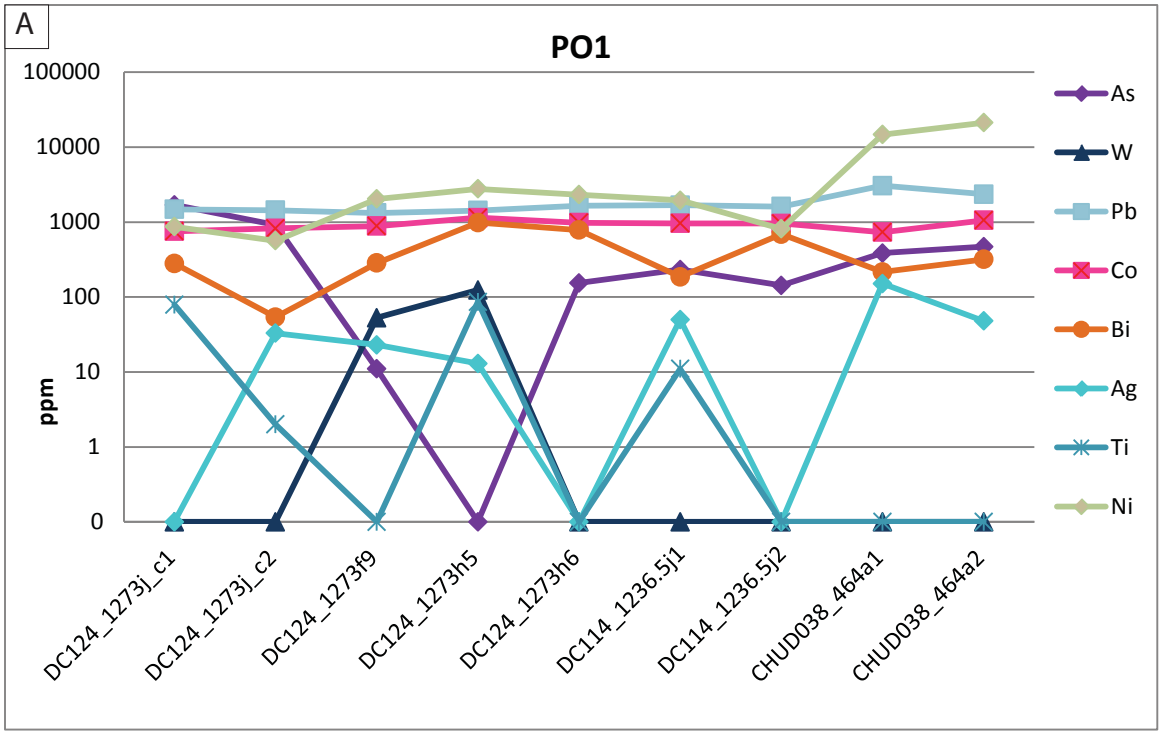

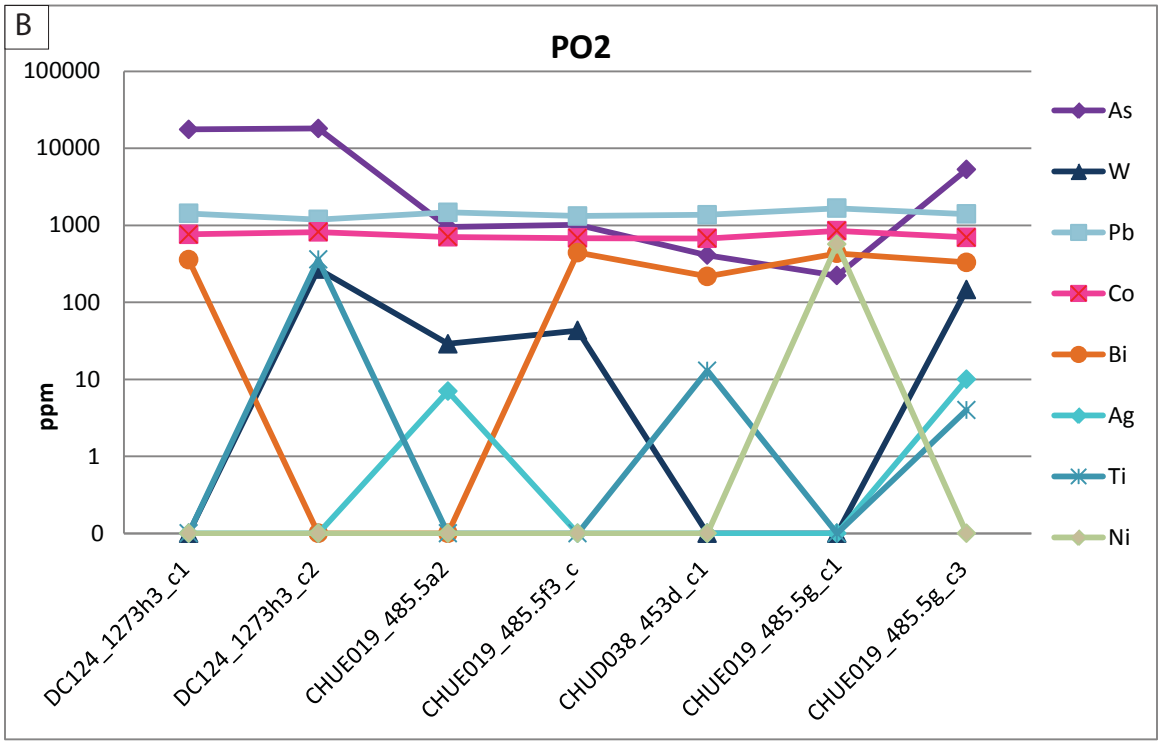

Figure 13. EPMA concentrations of PO1 pyrites (A) and PO2 pyrites (B). Each plot contains data points from different PO pyrite crystals within 3 different samples. All data plotted are collected from PO pyrites.

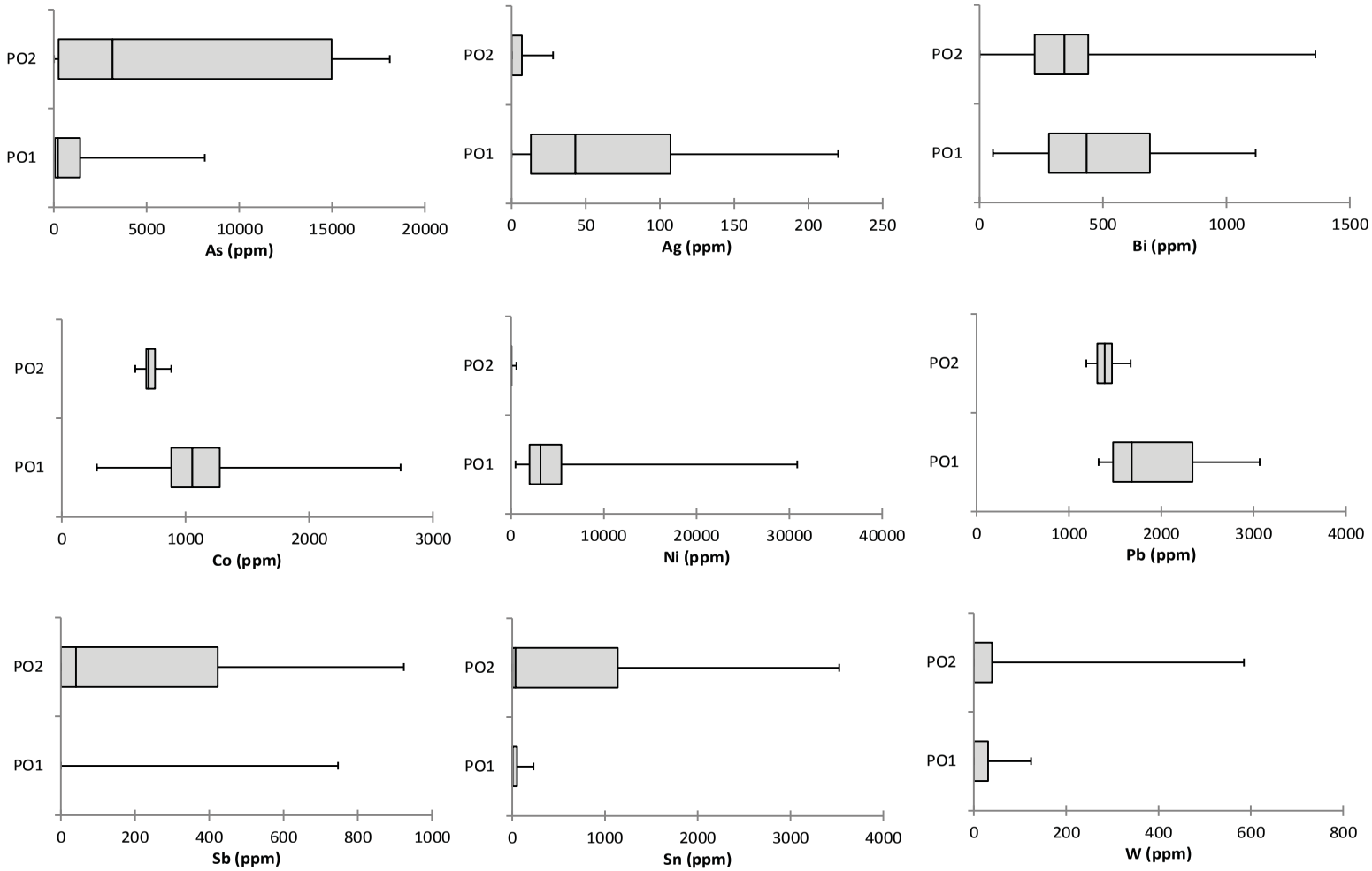

Figure 14. Box and whisker diagrams for As, Ag, Bi, Co, Ni, Pb, Sb, Sn, and W. EPMA data for PO1 (n = 21) and PO2 (n = 14) pyrites are plotted. The center vertical line indicates the median value; the total box shows the values that 50% of the data plot within. The horizontal black lines indicate the minimum (left) and maximum (right) values for each element.

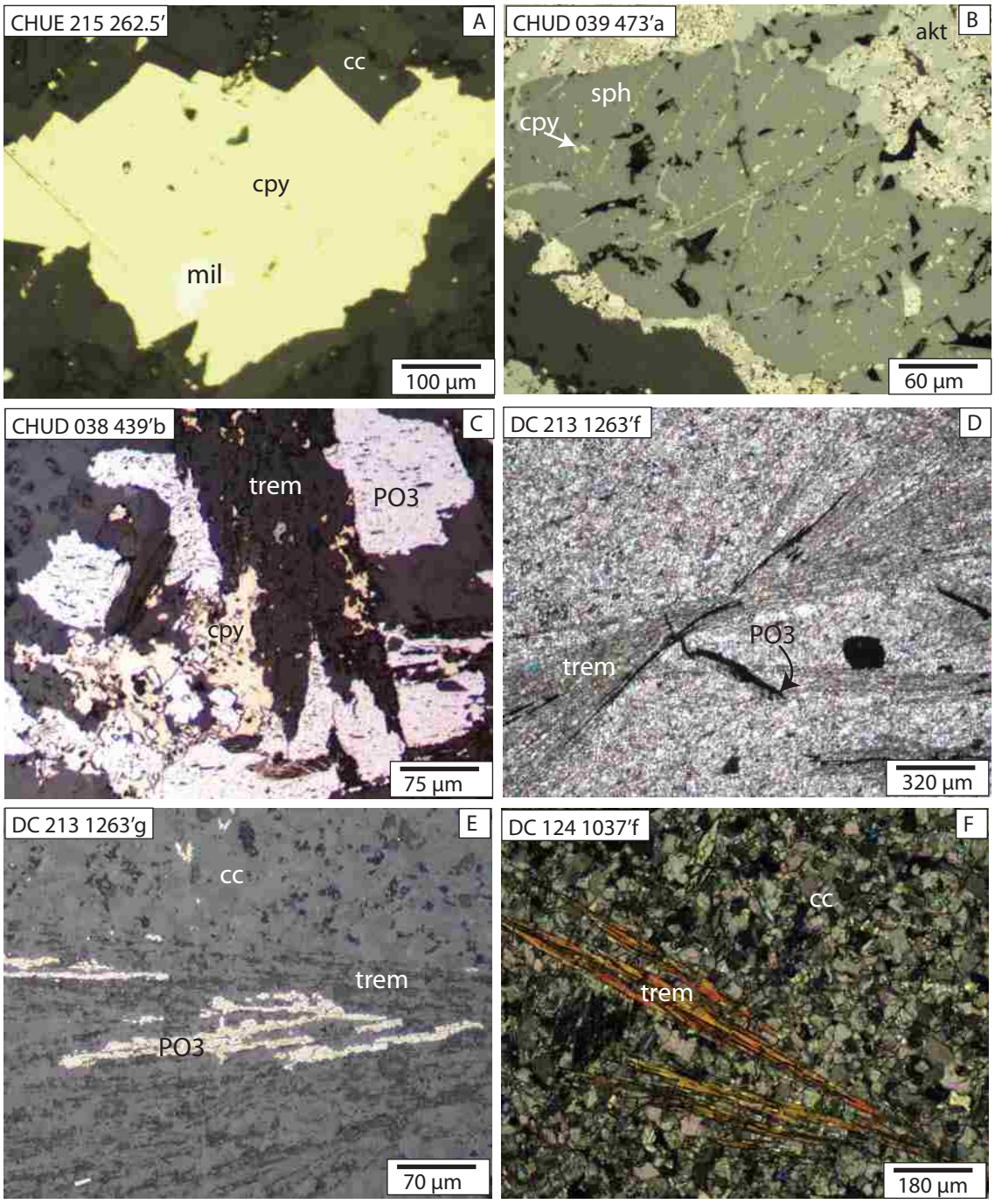

Figure 15. Photomicrographs of pre-ore-stage minerals. A) Chalcopyrite conforming to calcite rhombohedrons and millerite. B) Sphalerite with chalcopyrite inclusions under reflected light. C) PO3 pyrite and chalcopyrite crystals conforming to a tremolite crystal under reflected light. D, E) Radiating tremolite crystals with elongated PO3 pyrites incorporated within the tremolite structure, all surrounded by recrystallized calcite under crossed-polarized transmitted light (D) and reflected light (E). F) Elongated tremolite crystal surrounded by recrystallized calcite within a carbonate that does not contain detectable Au under crossed-polarized transmitted light. Abbreviations: cc = calcite; sph = sphalerite; cpy = chalcopyrite; akt = aktashite; trem = tremolite; mil = millerite.

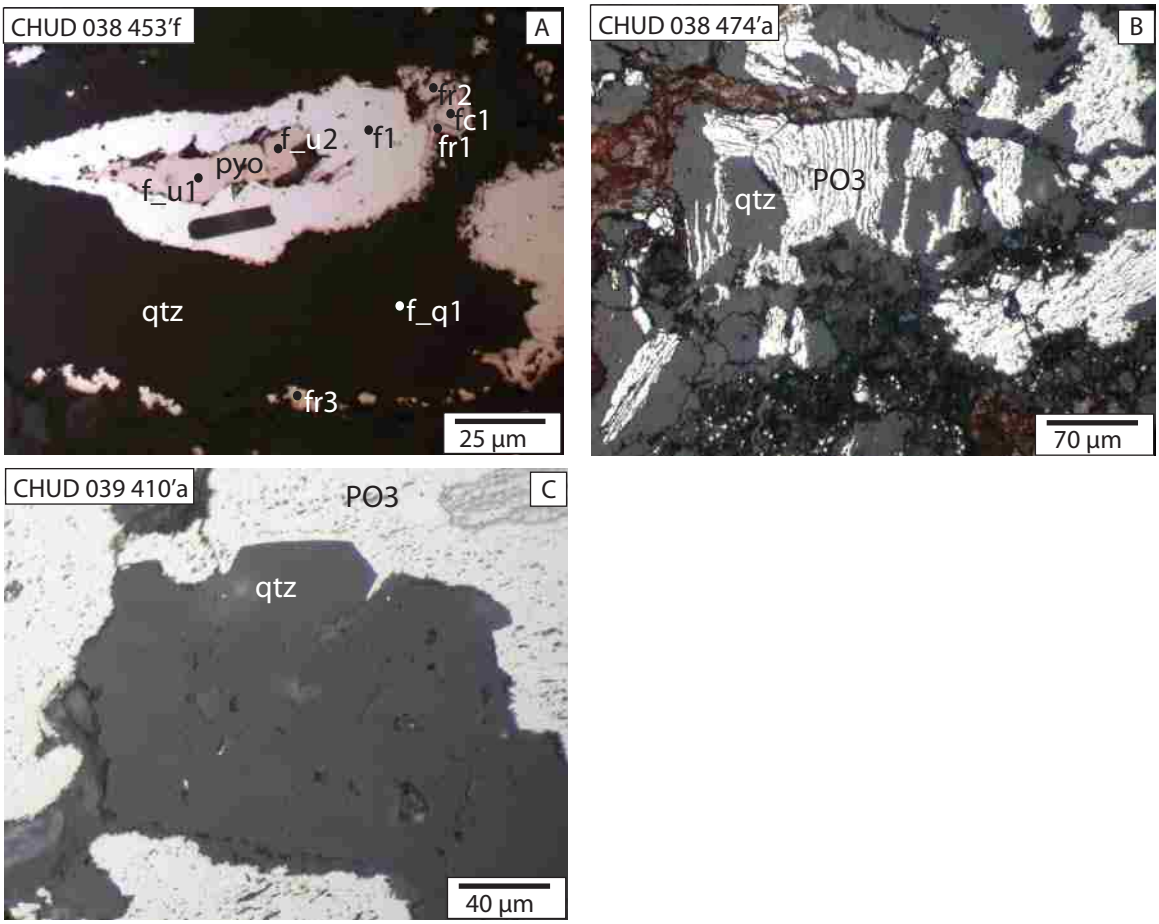

Figure 16. Photomicrographs of pyrrhotite (pink) surrounded by a pre-ore-stage pyrite (A), pre-ore-stage quartz and PO3 pyrite displaying a zebra-like texture (B), and PO3 pyrite conforming to euhedral quartz (C) under reflected light. Abbreviations: pyo = pyrrhotite; qtz = quartz.

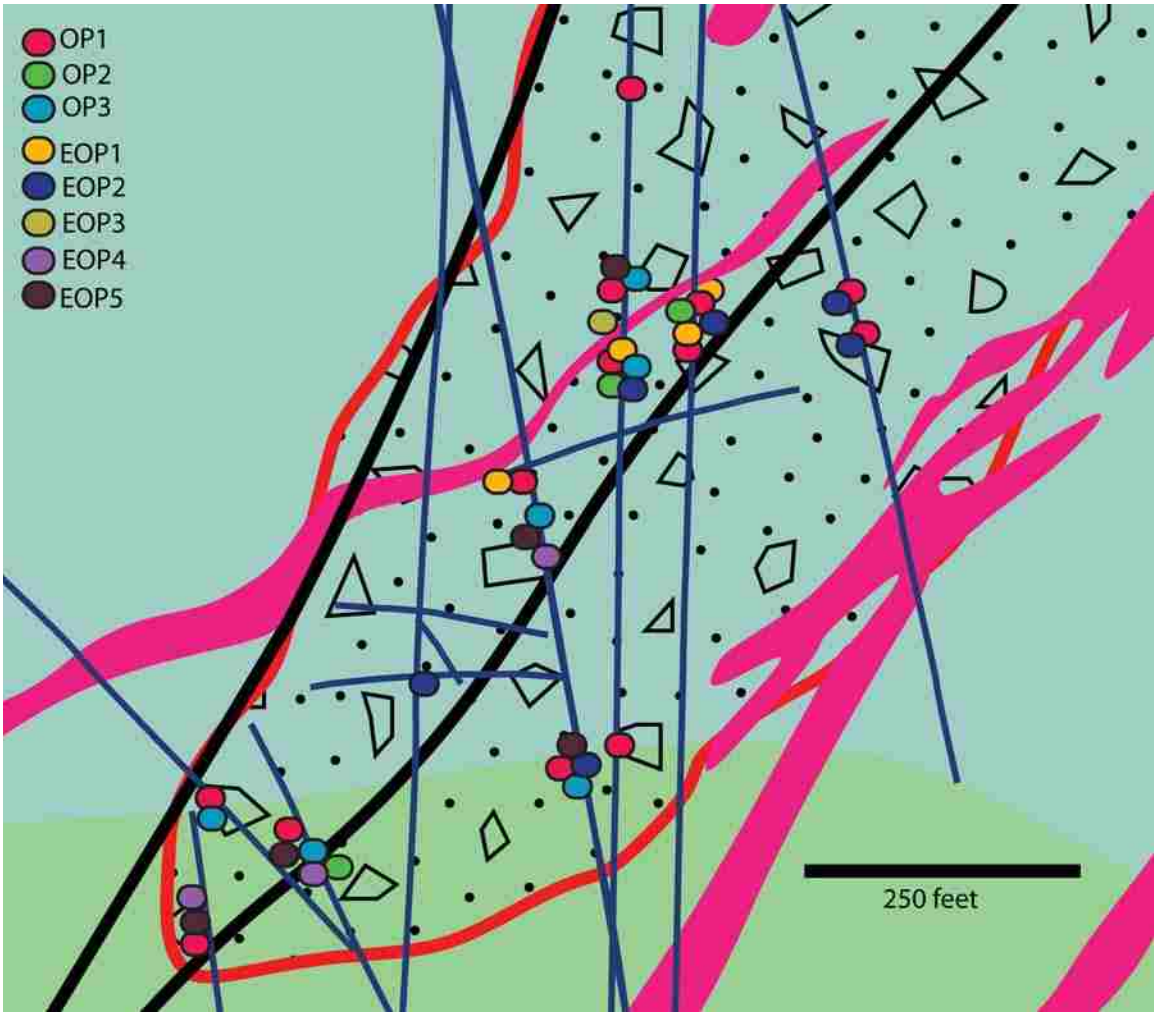

Figure 17. Magnified view of the NE simplified cross section shown in Figure 5. Section displays the location of the ore-stage and evolved ore-stage iron-sulfide minerals in the CHBZ described in Table 7. Some samples contain multiple types of iron-sulfide minerals, indicated by the clusters of symbols. Dark blue lines indicate sampled drill hole locations.

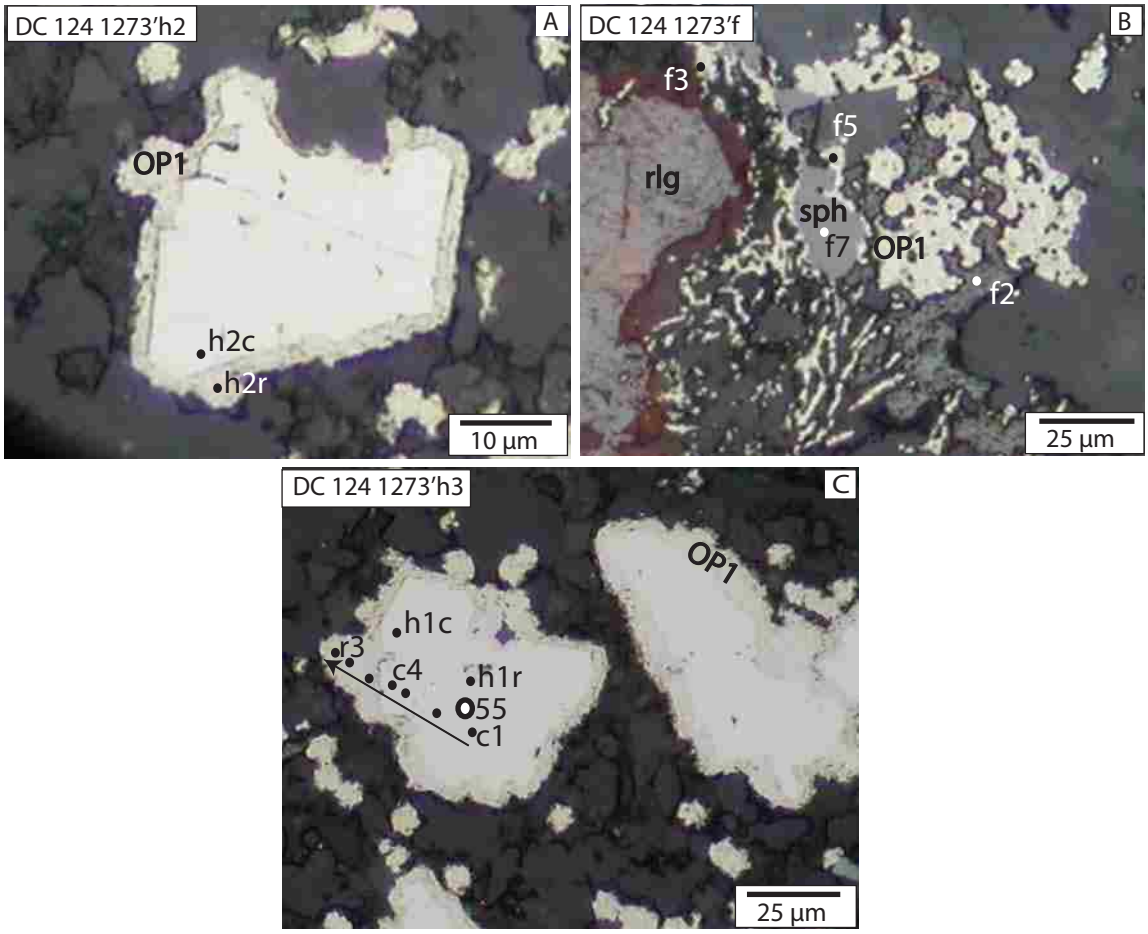

Figure 18. A-C) Photomicrographs of OP1 rimming a sphalerite crystal (B) as well as typical OP1 occurrences rimming pyrite cores (A,C) under reflected light. EPMA locations are indicated by small black solid circles and LA-ICP-MS analysis locations are indicated by large open circles. EPMA data from image C are plotted in ppm on the spider diagram (D). Cu plots behind Hg for most points; Bi is undetectable at points c2, c3, r1, r2, and r3. All points that begin with "r" (rim) are OP1 points. Abbreviations: rlg = realgar; sph = sphalerite.

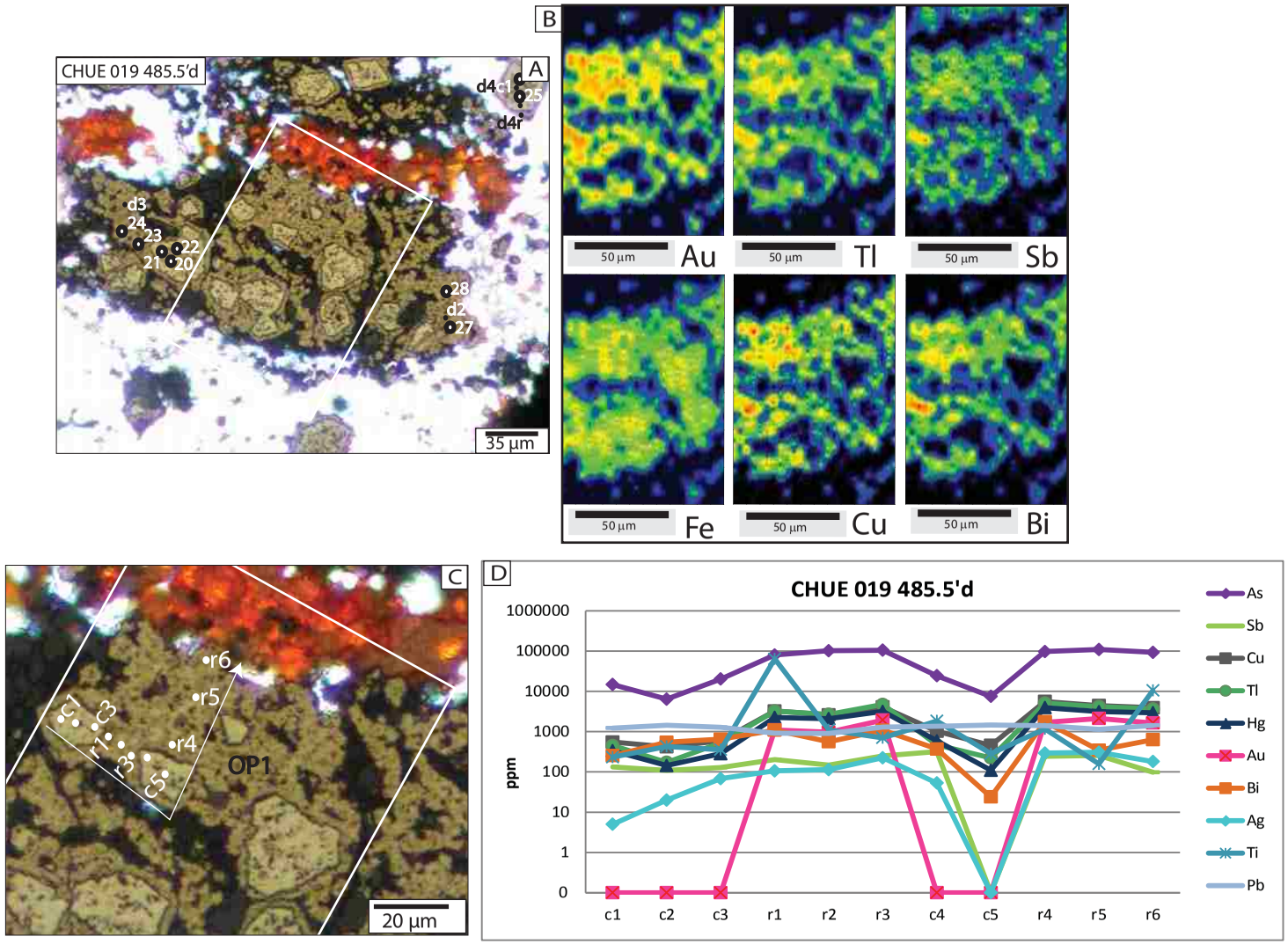

Figure 19. A, C) Photomicrograph of OP1 under partial transmitted and partial reflected light. A) White box indicates the region of LA-ICP-MS maps (B). C) White dots indicate the locations of EPMA data plotted on the spider diagram in ppm (D). Hg, Tl, and Cu points overlap. All points that begin with "r" (rim) are OP1 points.

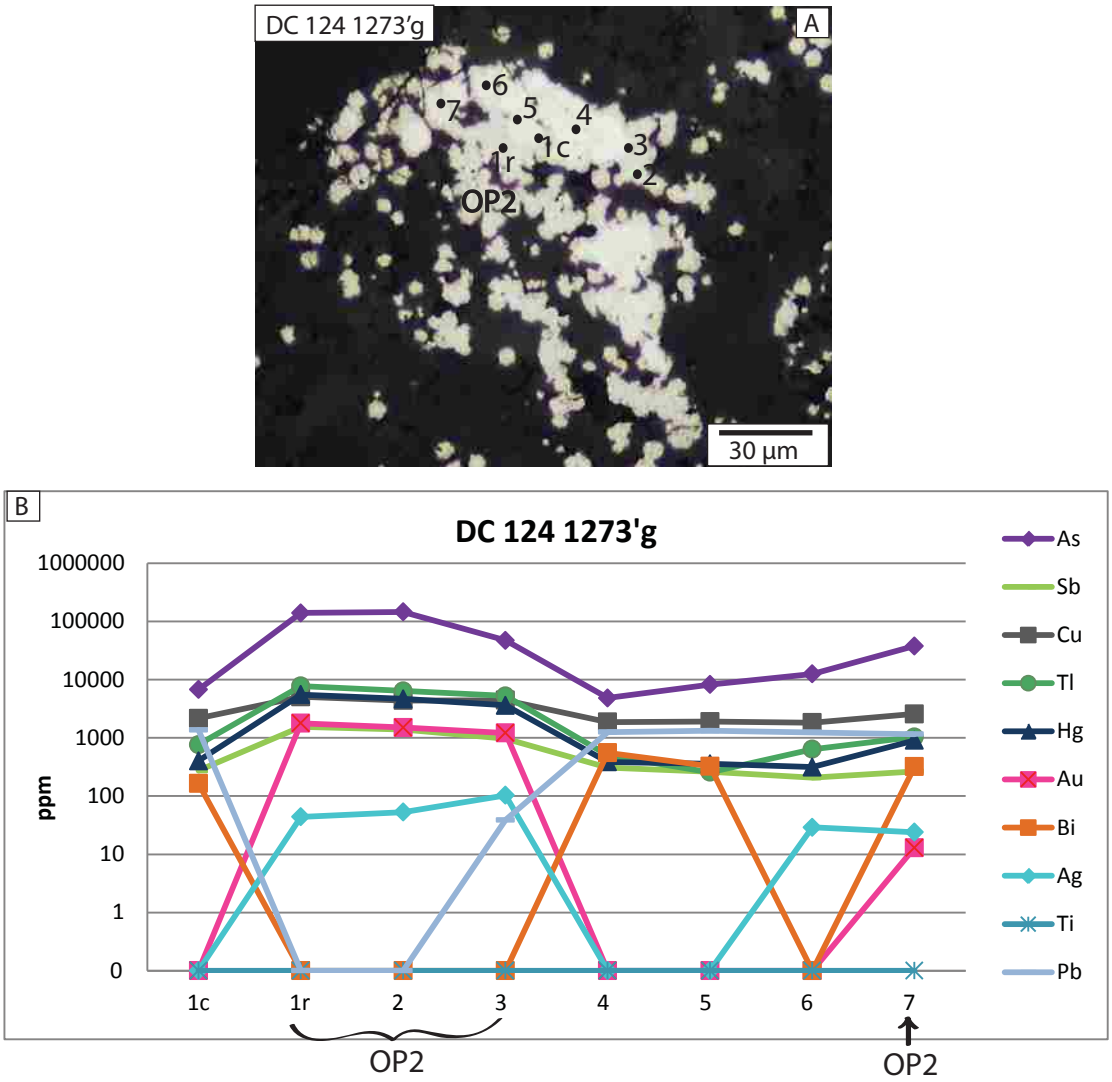

Figure 20. A) Photomicrograph of OP2 under reflected light with black dots indicating EPMA locations. B) EPMA data are plotted on the spider diagram in ppm.

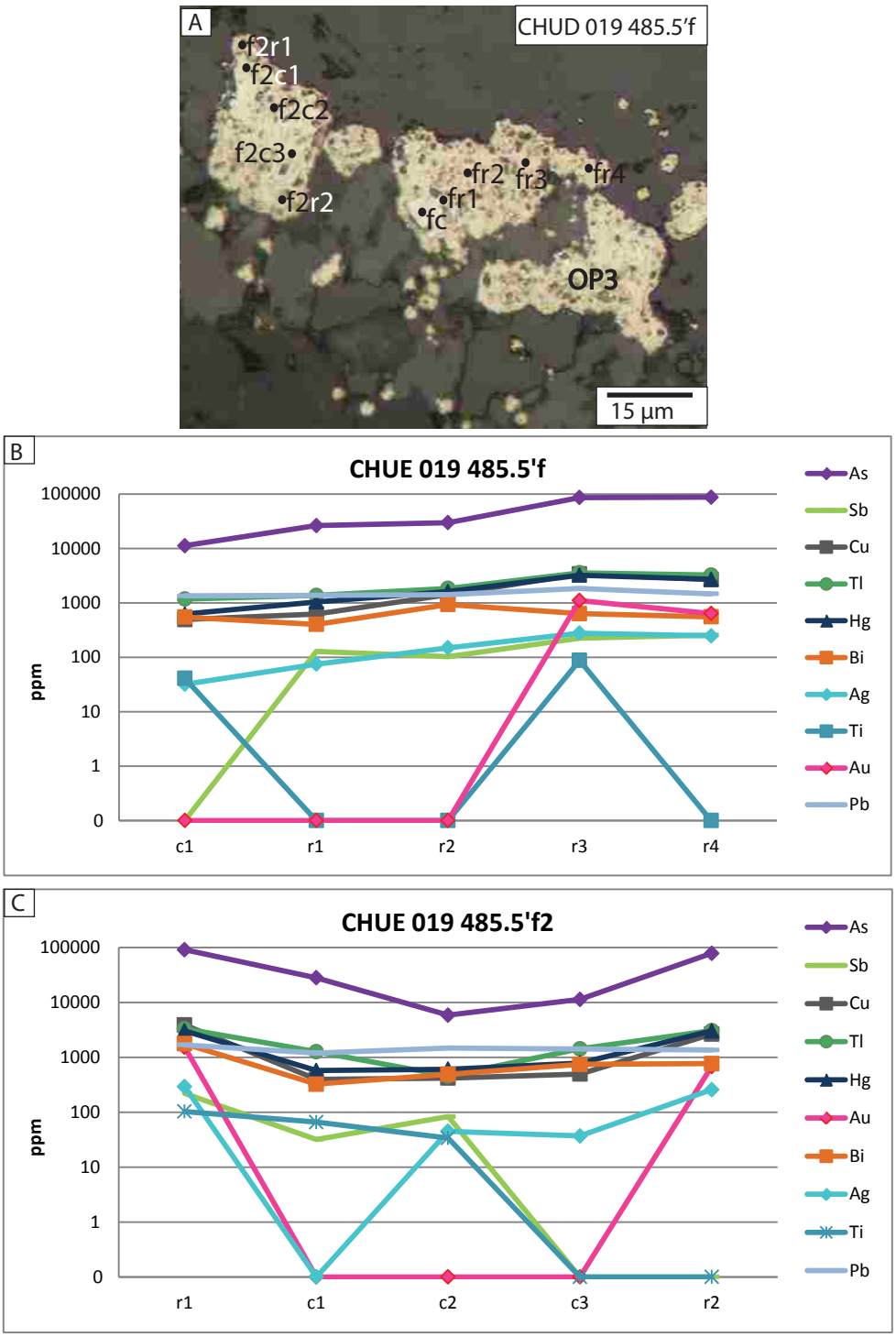

Figure 21. A) Photomicrograph of OP3 under reflected light with dots indicating EPMA locations on two crystals. B, C) EPMA data are plotted on the spider diagram in ppm. Cu, Tl, and Hg points overlap, with Cu at the back. All points that begin with "r" (rim) are located within OP3s.

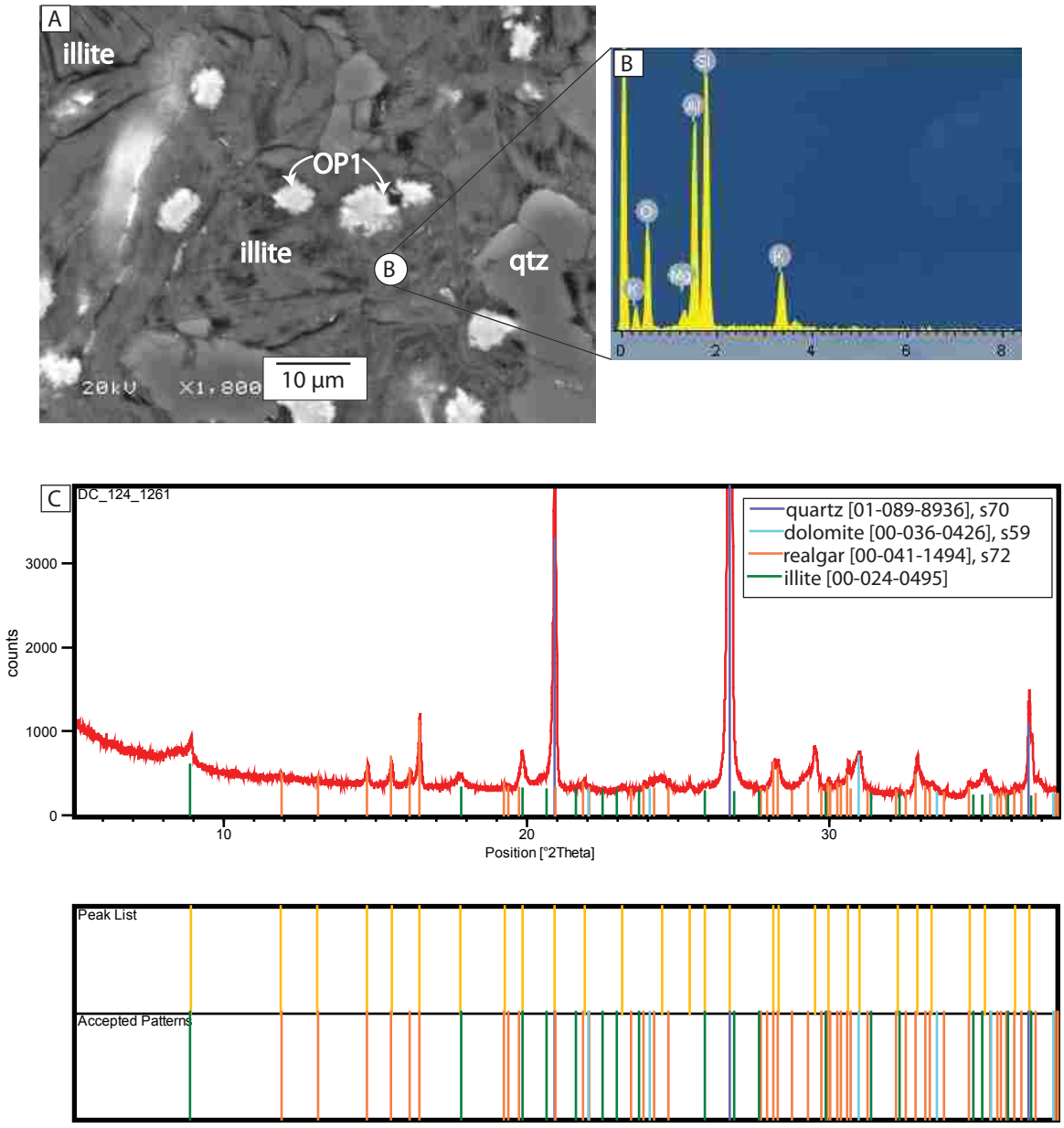

Figure 22. A) Secondary electron image of illite and OP1. B) SEM-EDS detected elements from point B shown in (A). C) XRD pattern for sample DC 124 1261', indicating the sample contains illite, dolomite, realgar, and quartz.

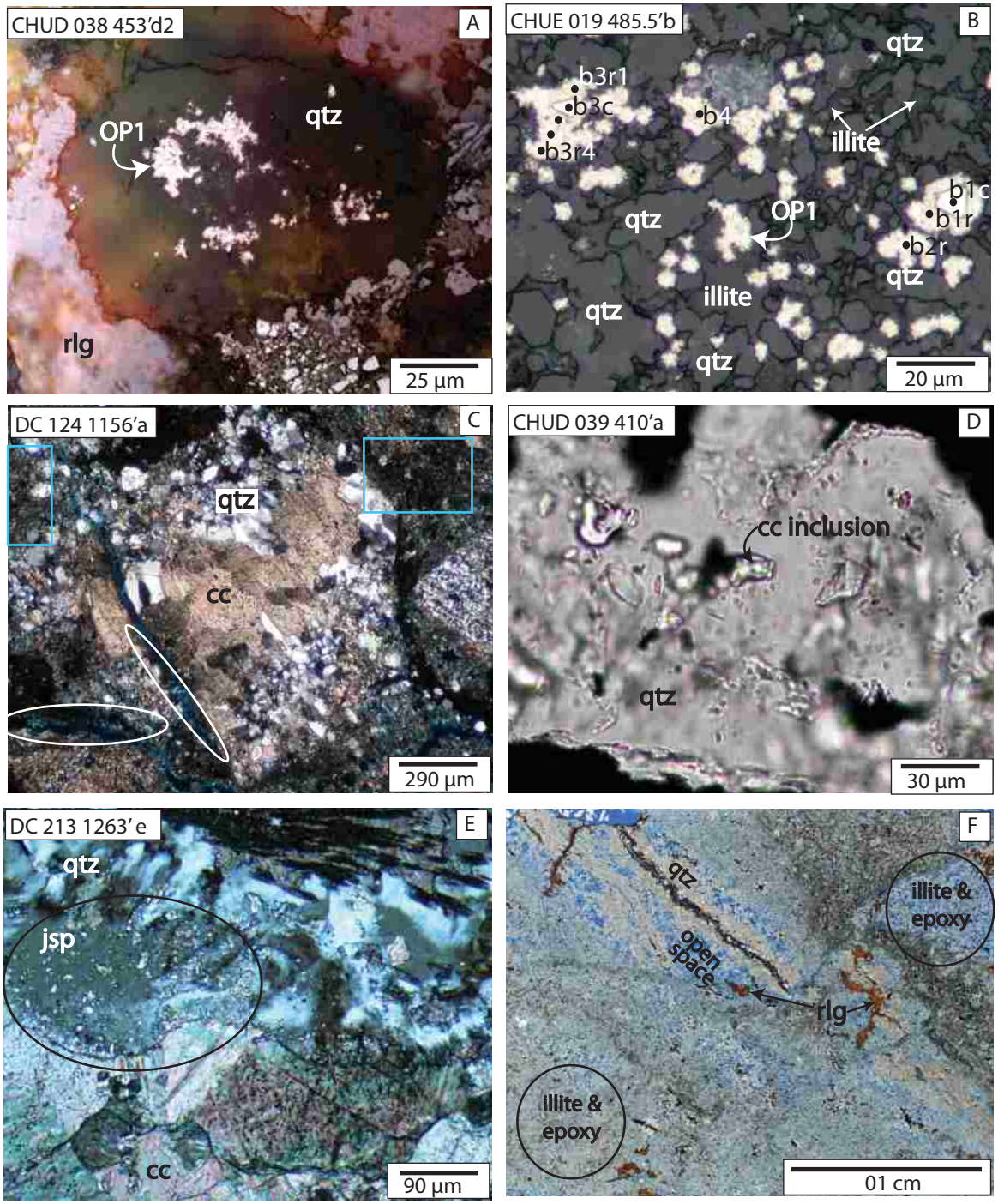

Figure 23. A, B) Photomicrographs of quartz and Au-bearing iron-sulfide minerals under reflected light. Photomicrograph of the alteration of calcite into jasperoid under crossed-polarized transmitted light (C, E) and plane-polarized transmitted light (D). C) White circles indicate zones of high porosity (blue epoxy); blue rectangles indicate dark mottled calcite as it is dissolved and replaced. F) Scan of a thin section that displays porosity as blue epoxy

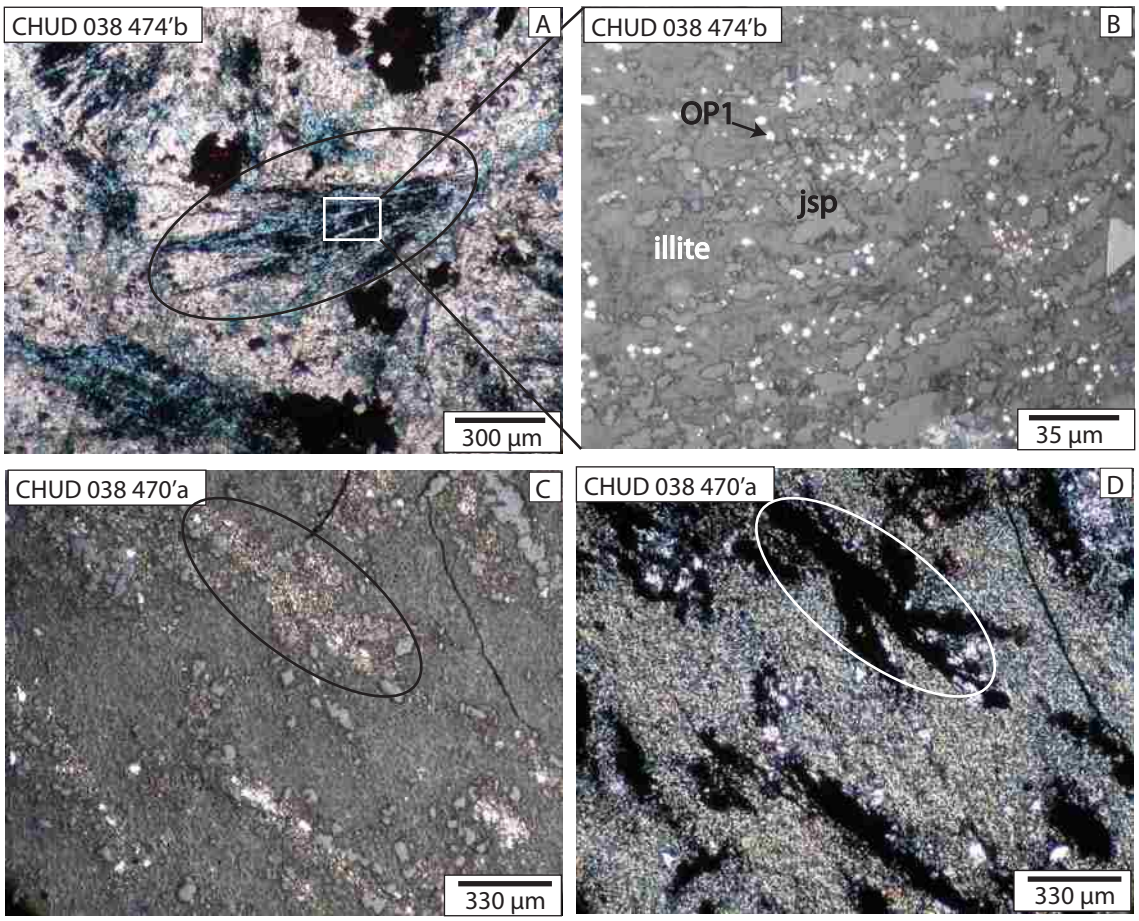

Figure 24. A) Photomicrograph of ore-stage mineralogy (illite, jasperoid, Au-bearing iron-sulfide minerals) replacing tremolite under plane-polarized transmitted light. B) A magnified image of the area within the rectangle shown in A under reflected light. C, D) Au-bearing iron-sulfide minerals pseudomorphing tremolite under reflected light (C) and crossed-polarized transmitted light (D).

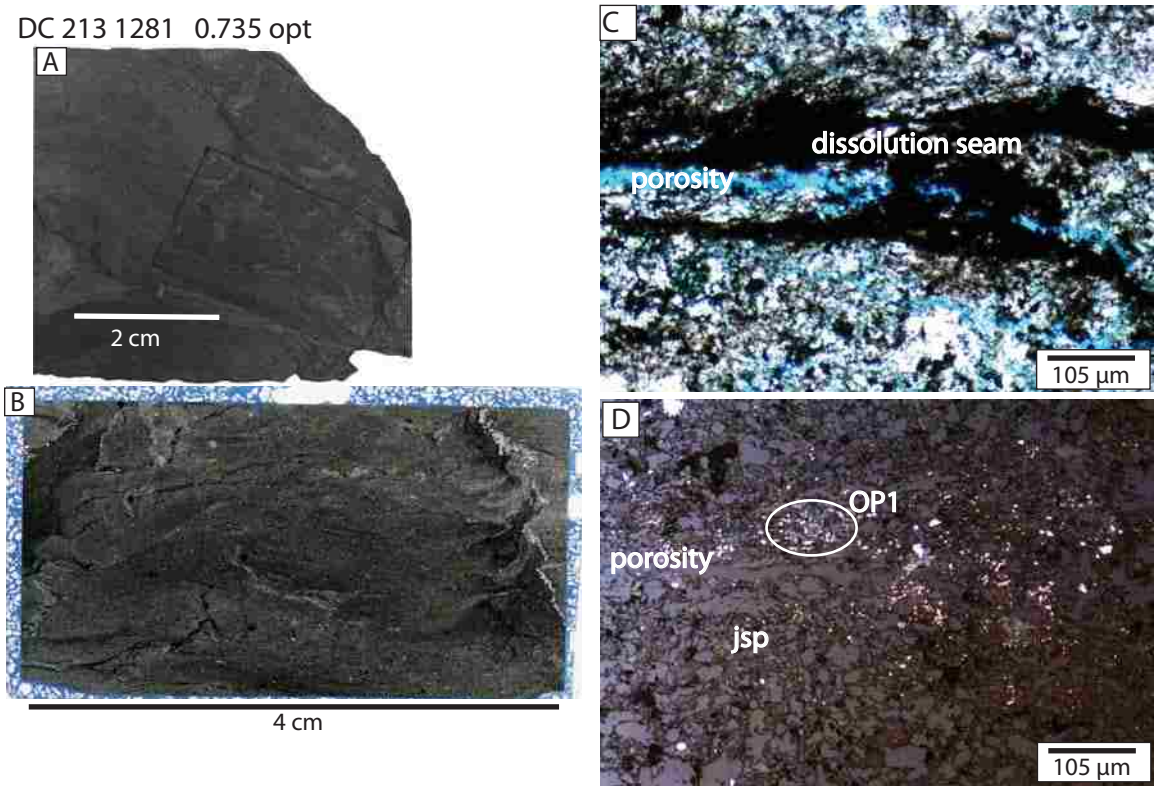

Figure 25. Hand sample (A) and section (B) that transmitted crossed-polarized (C) and reflected (B) light photomicrographs were taken from. C, D) The same area displaying a zone of high porosity (blue epoxy) with a seam of carbonaceous material (C) and Au-bearing iron-sulfide minerals (D) radiating from the center. Abbreviations: jsp = jasperoid.

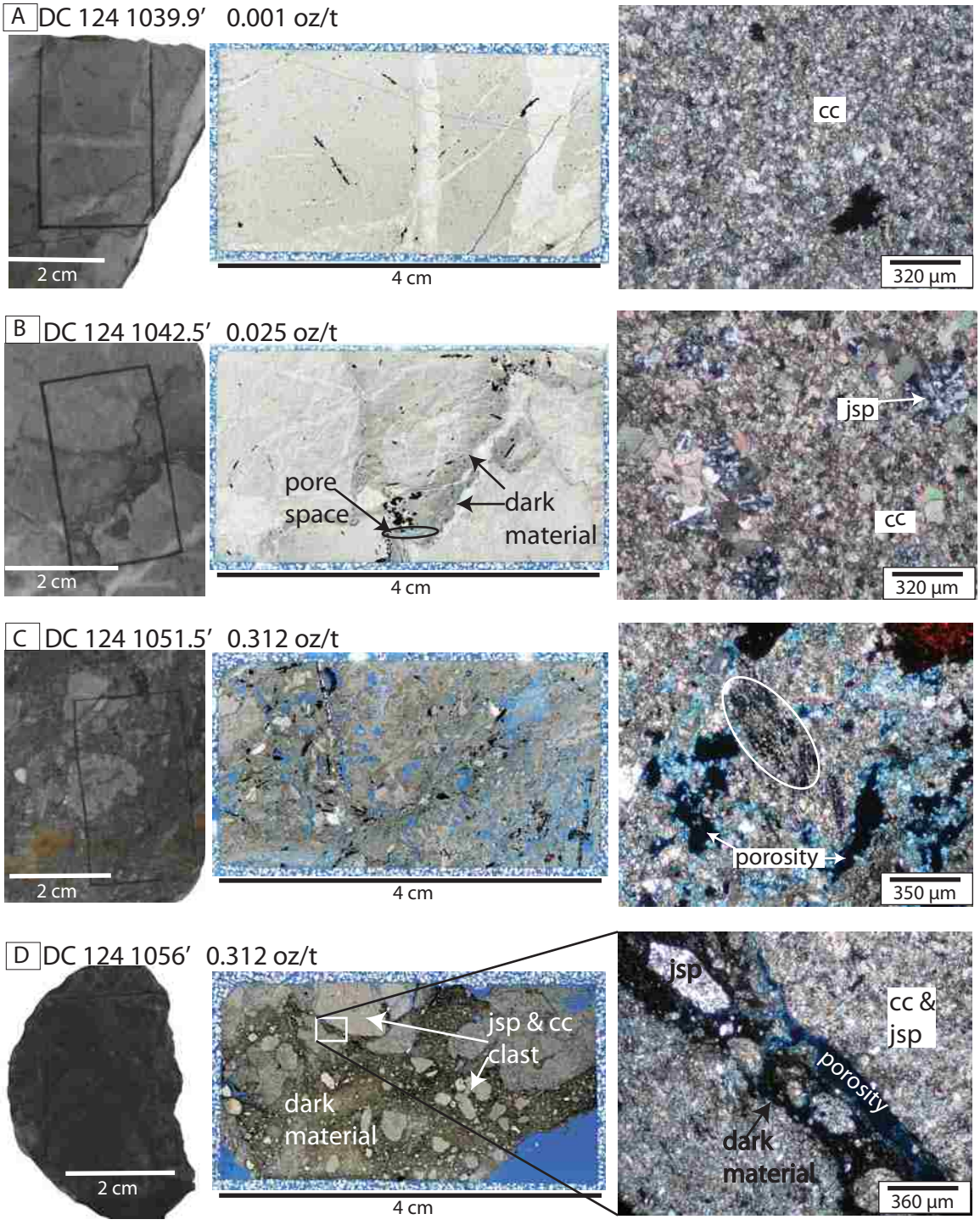

Figure 26. Hand samples (left), thin sections (center) and photomicrographs under crossed-polarized transmitted light (right) for four different rocks that are located along a ~16 foot transect within drill hole DC 124. The samples increase in Au concentration and porosity from rock A to D.

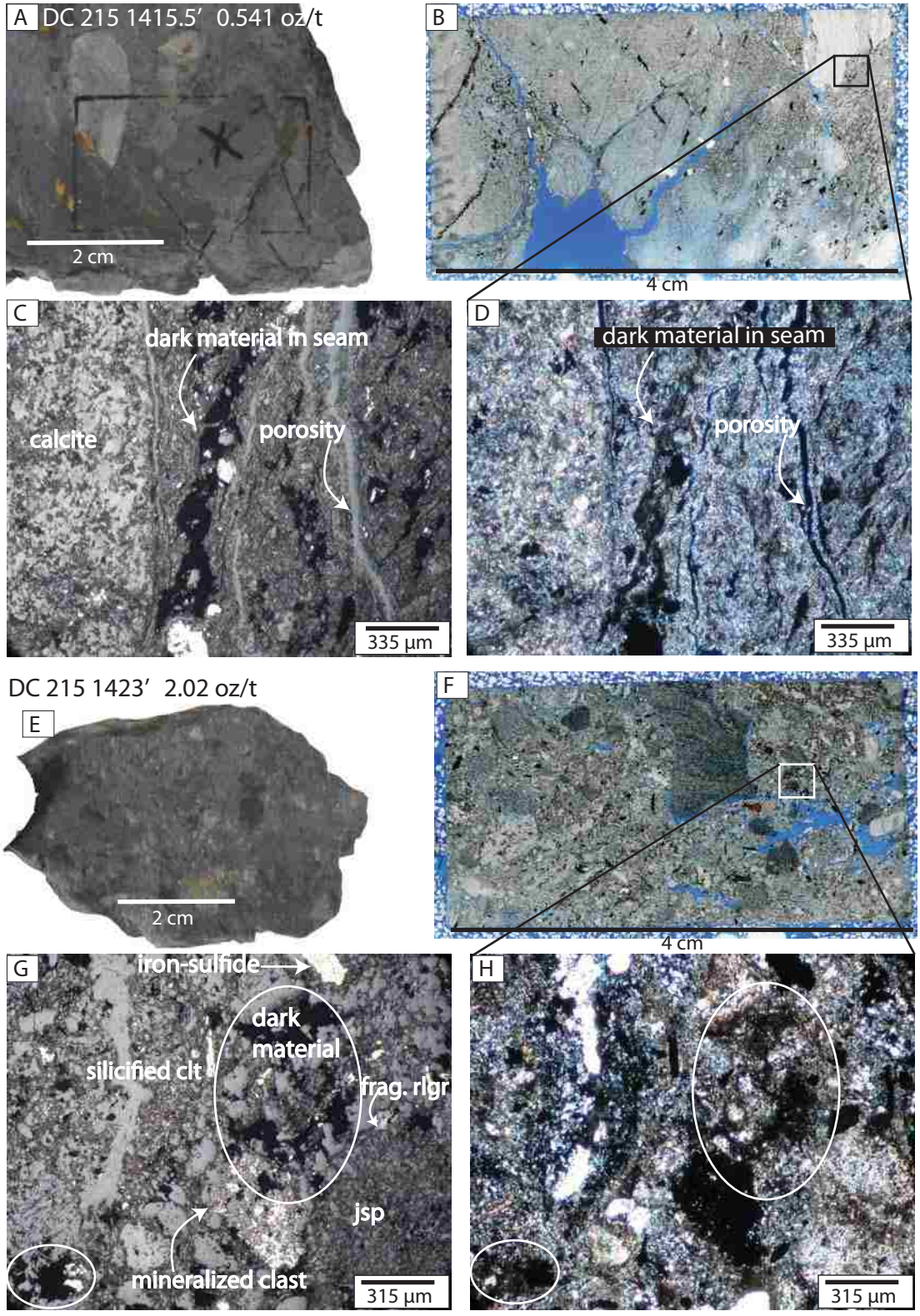

Figure 27. Hand samples (A, E), thin sections (B, F), photomicrographs under reflected light (C, G) and crossed-polarized transmitted light (D, H) for two samples separated by 7.5 feet. C and D display the same area; G and H display the same area. The samples increase in Au concentration and degree of brecciation from sample DC 215 1415.5' to DC 214 1423'. Dark material is composed of carbon, fine-grained Au-bearing iron-sulfide and clay minerals, and jasperoid.

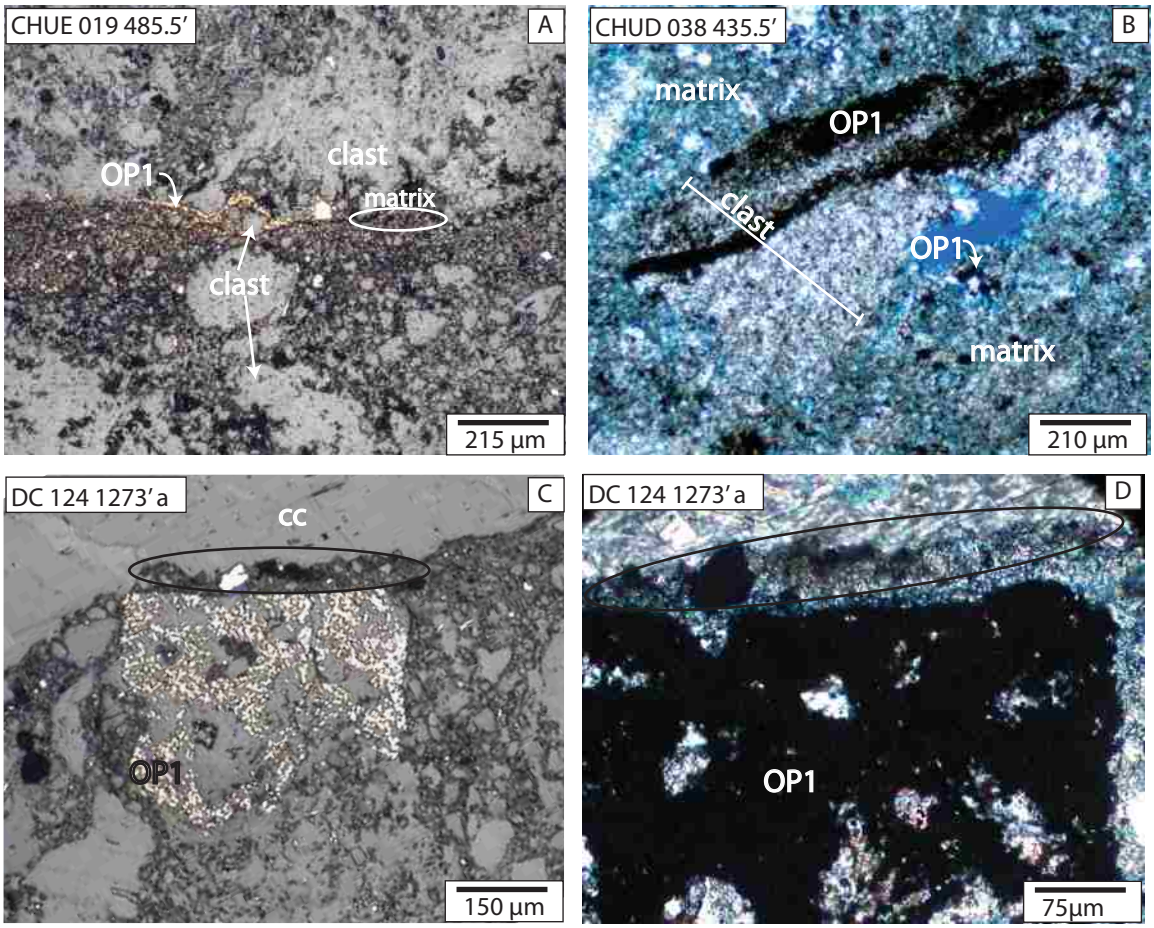

Figure 28. Photomicrographs displaying Au-bearing iron-sulfide minerals within the matrix (A) and clasts (B-D) in heavily brecciated rocks under reflected light (A, C) and crossed-polarized transmitted light (B, D). C, D) The black oval indicates an area that is opaque owing to fine grained Au-bearing iron-sulfides, illite, jasperoid, and carbonaceous material. The material is concentrated adjacent to an unaltered limestone clast.

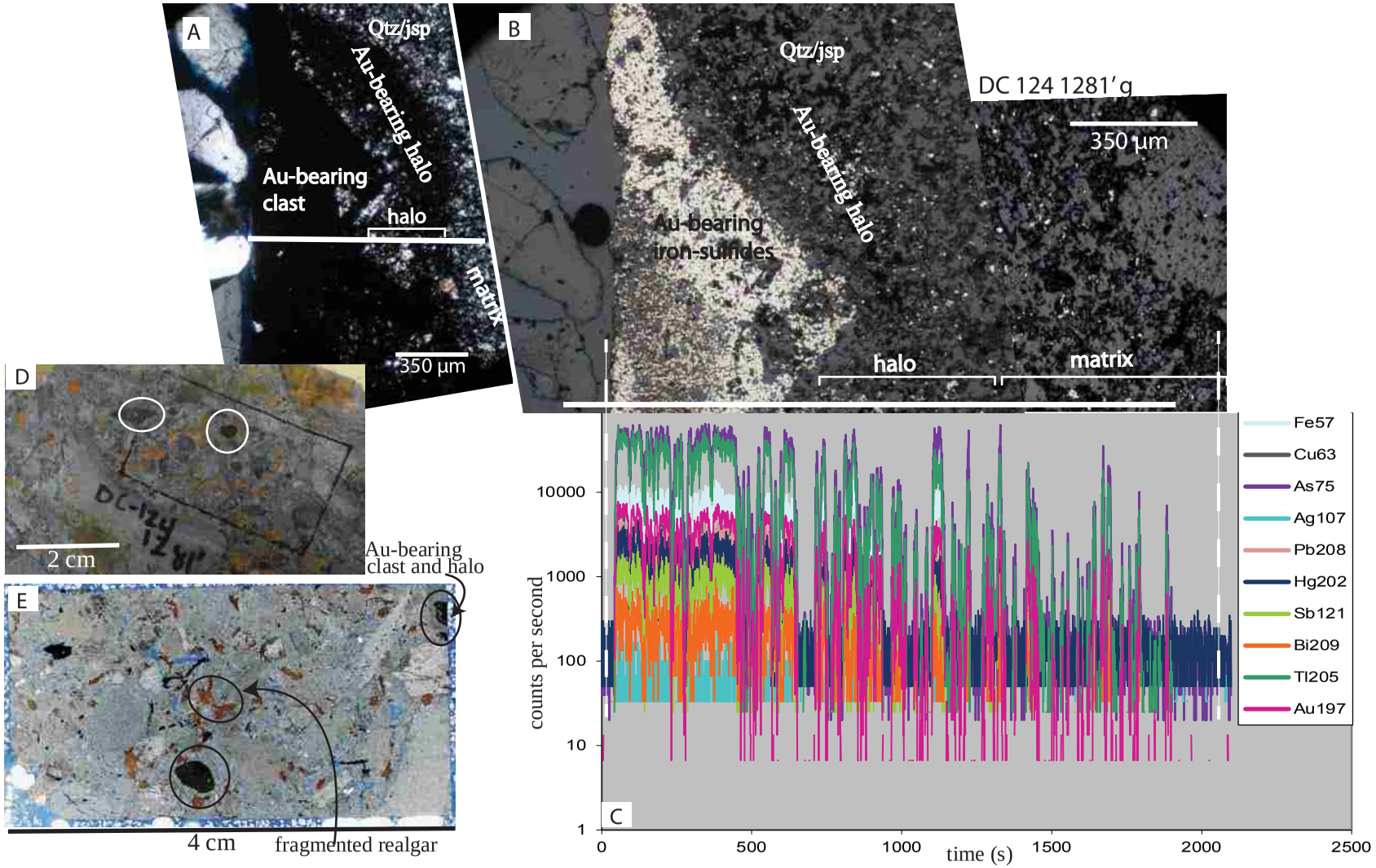

Figure 29. Photomicrograph of a pyrite with a Au-bearing iron-sulfide enriched halo surrounding it under cross-polarized transmitted light (A) and reflected light (B) with white lines indicating the path of ablation for LA-ICP-MS analysis. C) LA-ICP-MS data collected along the line is show in B. Hand sample (D) and thin section (E) with the heavily mineralized clasts circled.

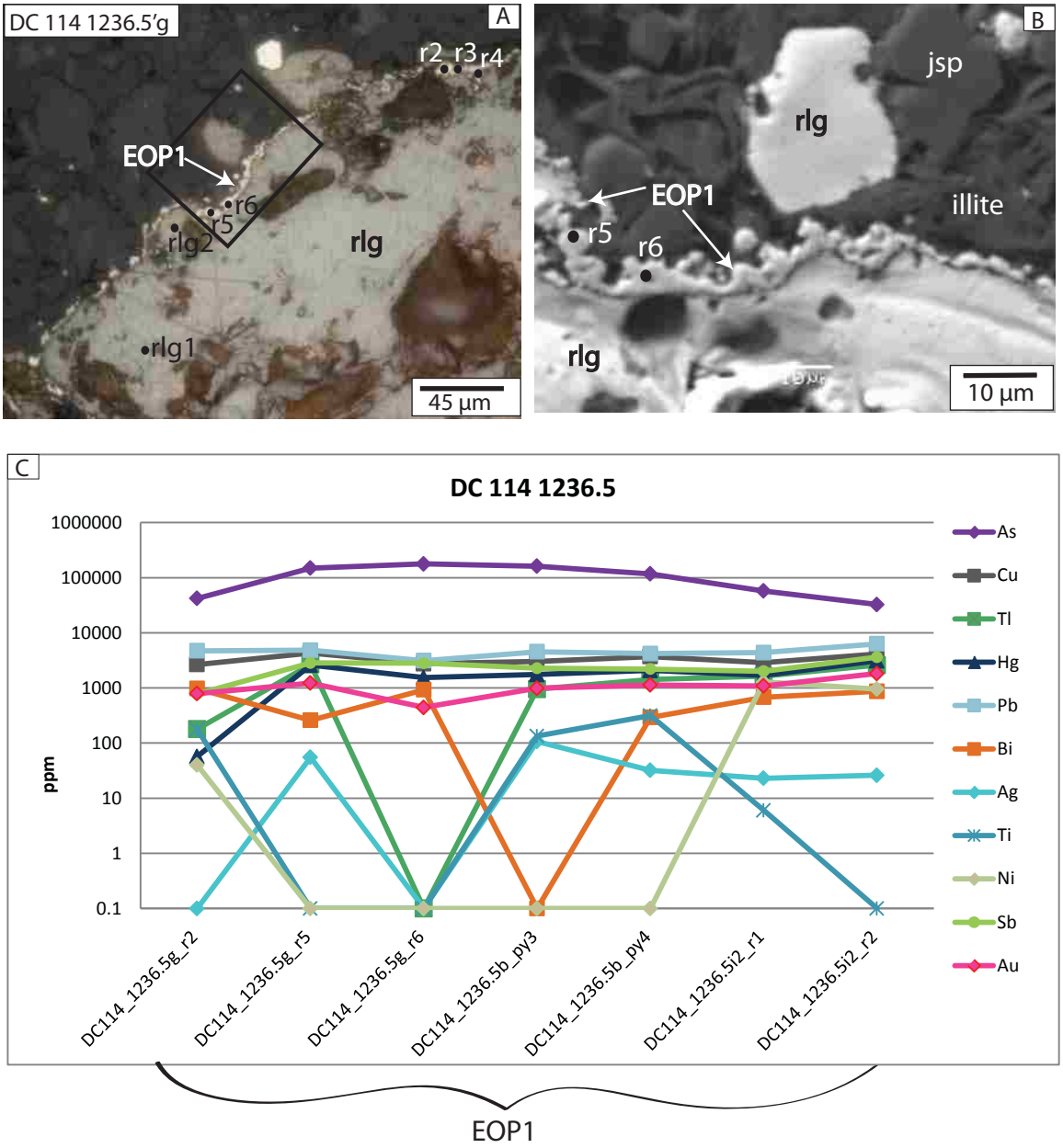

Figure 30. A) Photomicrograph of EOP1 under reflected light with dots indicating EPMA locations. B) SEM image of rectangular area in (A). C) EPMA data are plotted on the spider diagram in ppm; all data plotted are collected from EOP1s. Only the point locations that begin with DC 114 1235.5g are shown in A, B. All other point locations are shown in Appendix H.

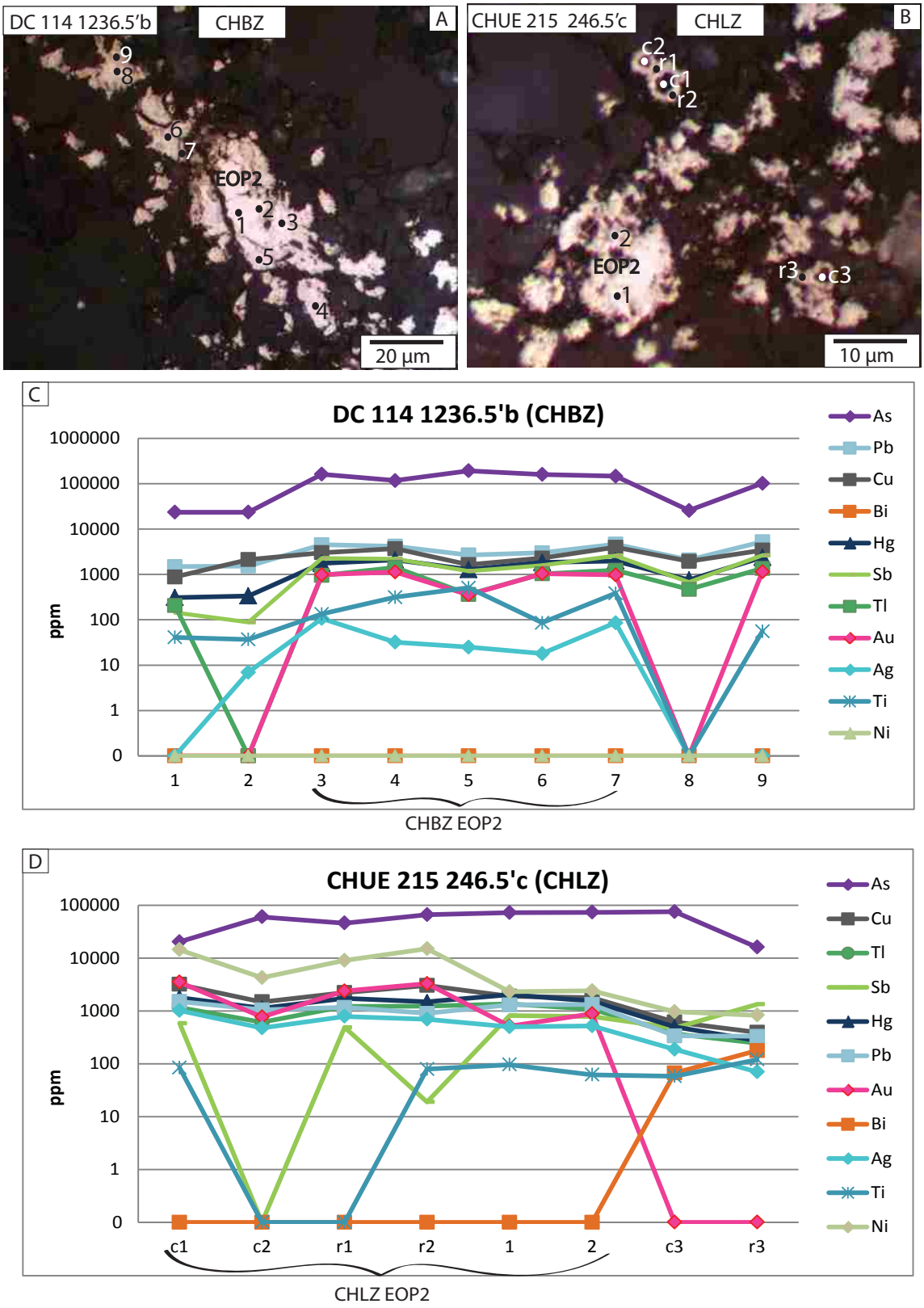

Figure 31. Photomicrographs of EOP2s from CHBZ (A) and CHLZ (B) under reflected light with dots indicating EPMA locations. EPMA data are plotted on the spider diagram in ppm for CHBZ (C) and CHLZ (D). C) Sb and Hg values overlap. D) Au, Pb, Tl, Hg, Cu, and Ag values plot similarly.

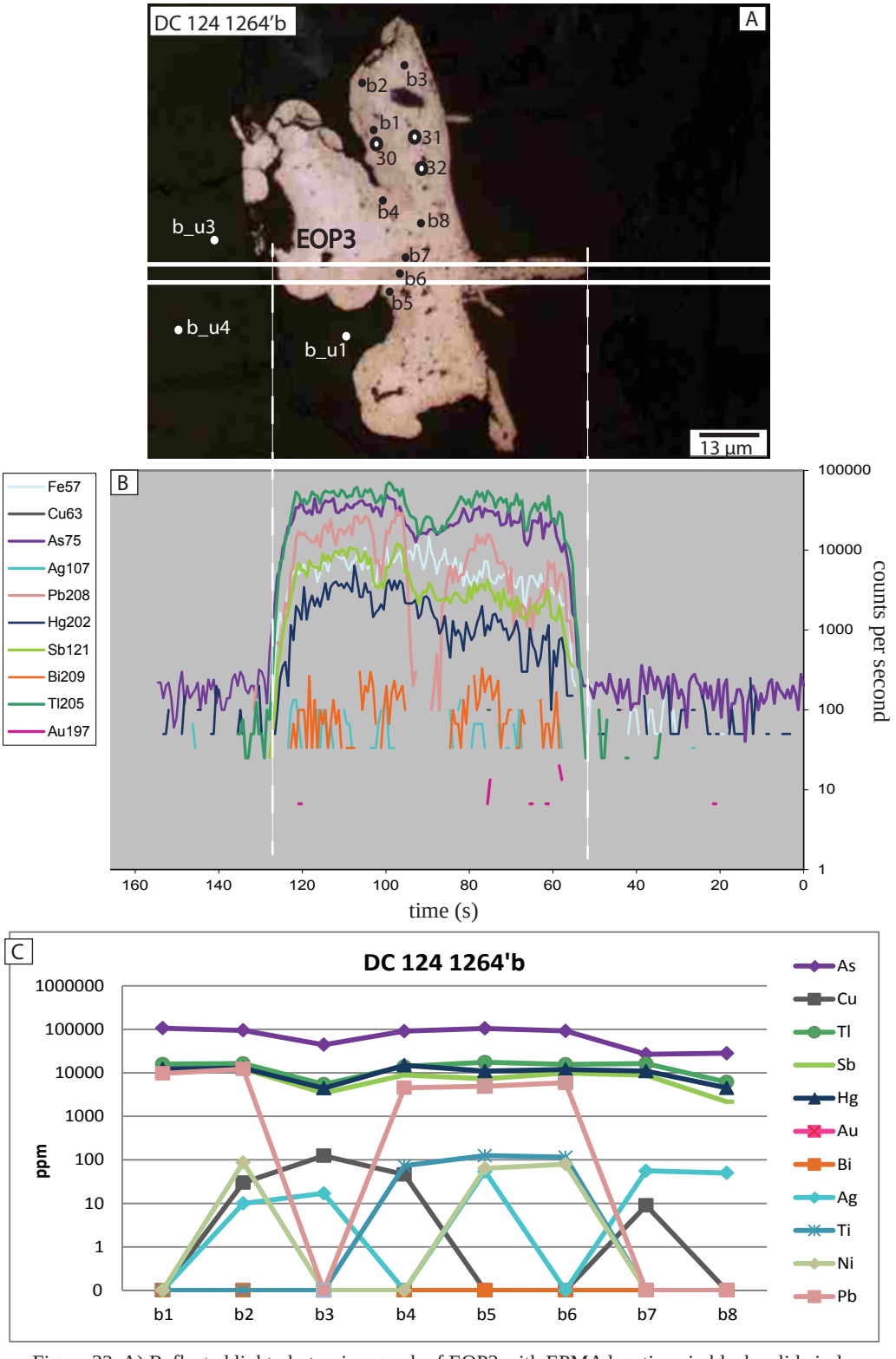

Figure 32. A) Reflected light photomicrograph of EOP3 with EPMA locations in black solid circles and LA-ICP-MS analyses locations in larger black open circles. The two parallel solid white lines indicate the LA-ICP-MS path and the area that was ablated (B). The two vertical dashed white lines indicate how the locations on the photomicrograph correlate on the LA-ICP-MS data. LA-ICP-MS data indicate elevated As, Tl, Hg, Sb, and Pb, and undetectable Cu. C) EPMA data are plotted on the spider diagram in ppm. Au and Bi were not detected. Tl, Hg, and Sb values overlap.

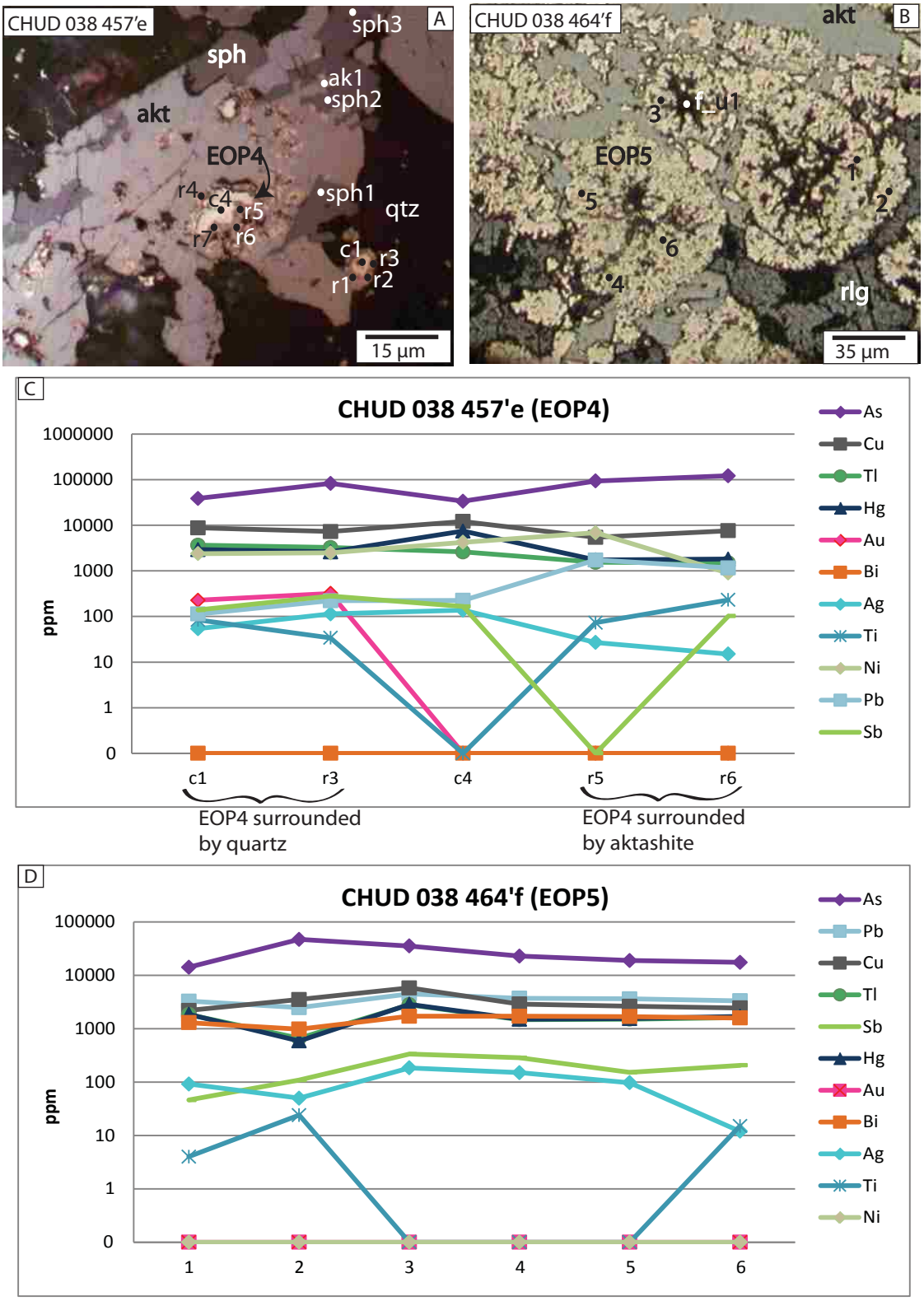

Figure 33. Photomicrograph of EOP4 (A) and EOP5 (B) under reflected light with dots indicating EPMA locations on multiple crystals. C, D) EPMA data are plotted on the spider diagrams in ppm for EOP4 (C) and EOP5 (D). C) Sb, Au, and Pb values overlap for points c1 and r3. Au and Bi were not detected for points c4, r5, and r6. D) Au is not detected and Tl, Hg, and Bi values overlap for most points. Abbreviations: akt = aktashite; qtz = quartz; sph = sphalerite; rlg = realgar.

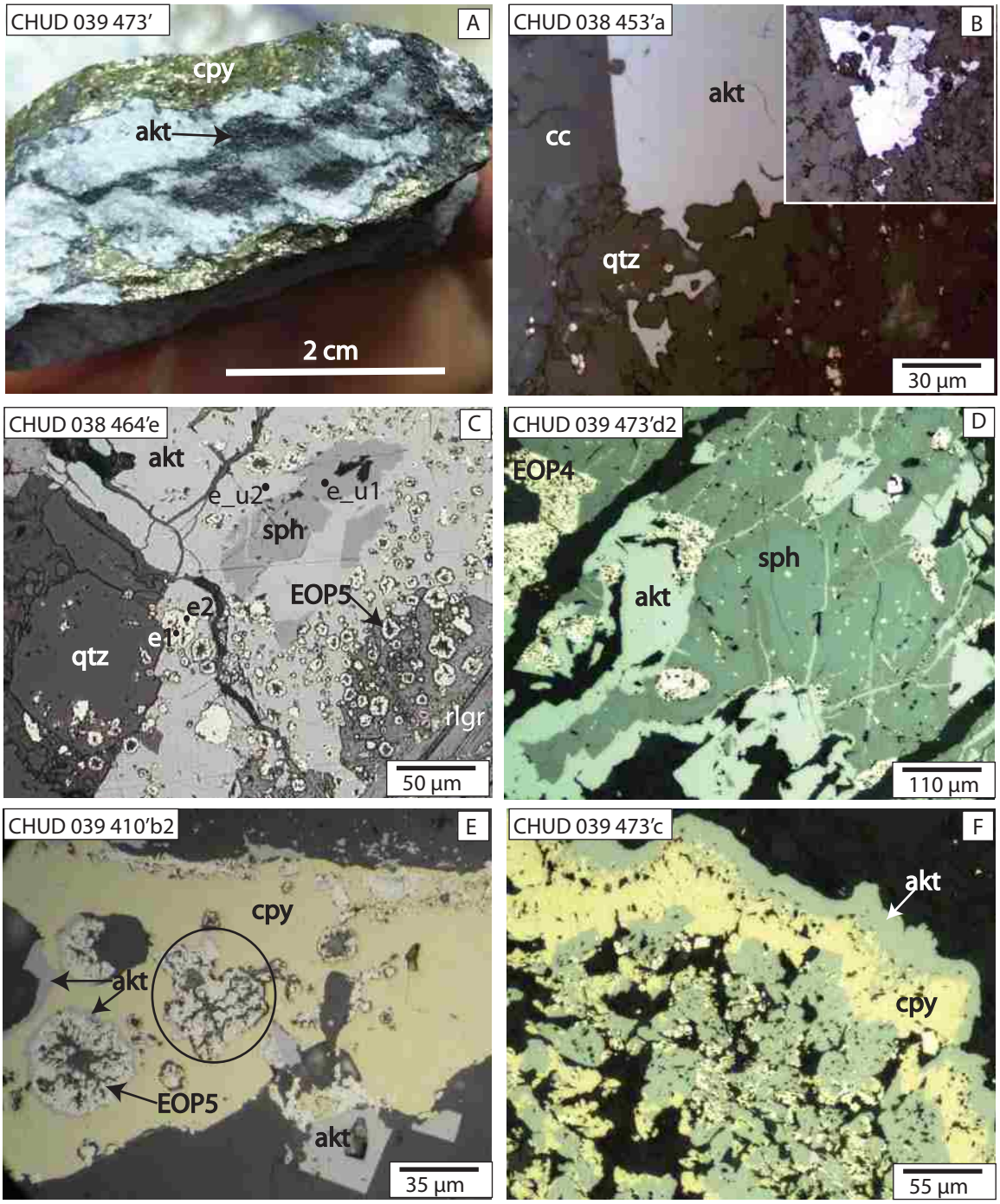

Figure 34. A) Hand sample containing aktashite and chalcopyrite. Reflected light photomicrographs of aktashite and quartz (B), aktashite, sphalerite, and EOP5 (C), aktashite, sphalerite and EOP4 (D), aktashite, chalcopyrite and EOP5 (E), and aktashite and chalcopyrite (F). Abbreviations: akt = aktashite; qtz = quartz; sph = sphalerite; cpy = chalcopyrite; cc = calcite.

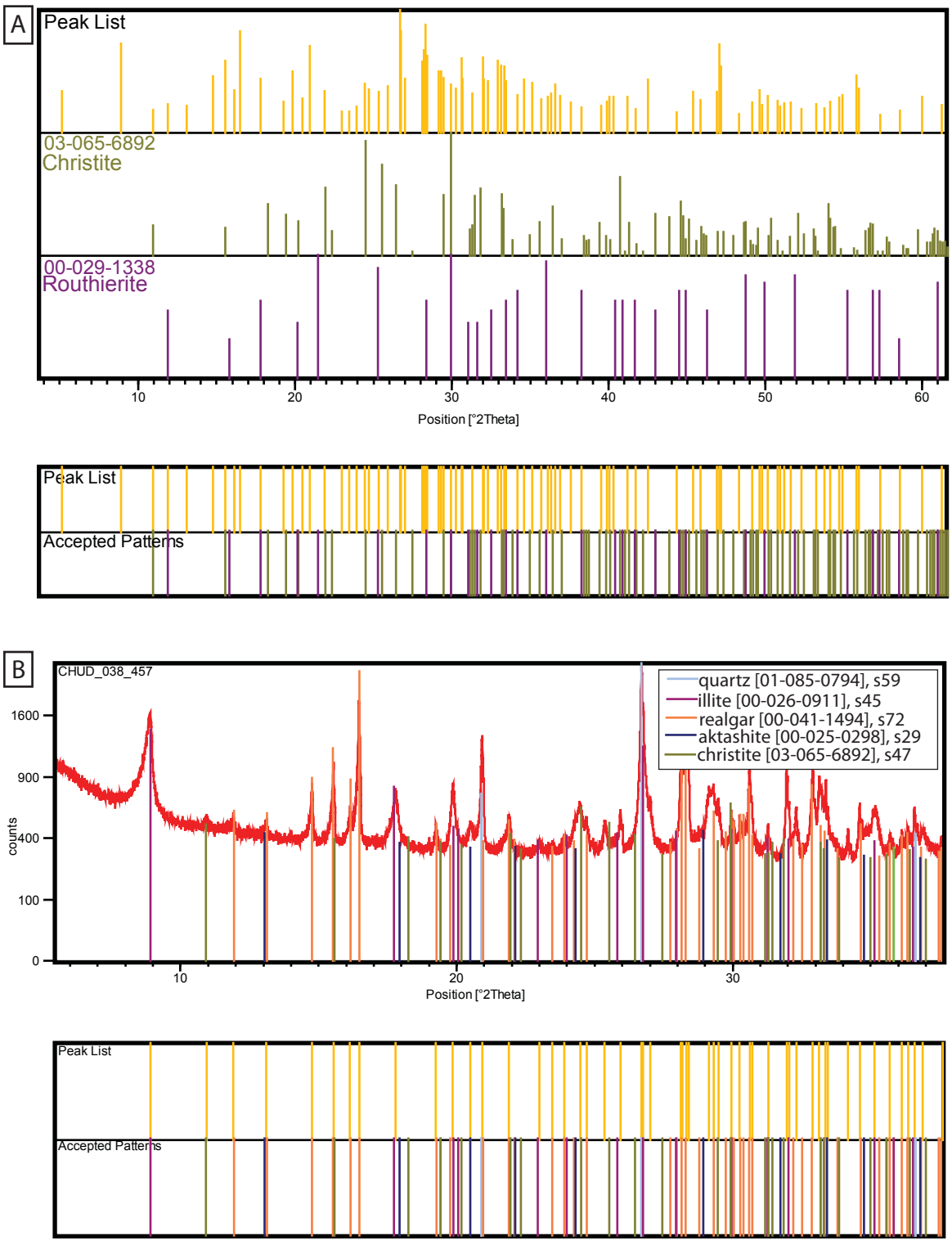

Figure 35. XRD data for sample CHUD 038 457'. A) Whole rock sample, routhierite, and christite peak lists and accepted patterns. B) Whole rock sample XRD pattern displaying the accepted mineral peaks.

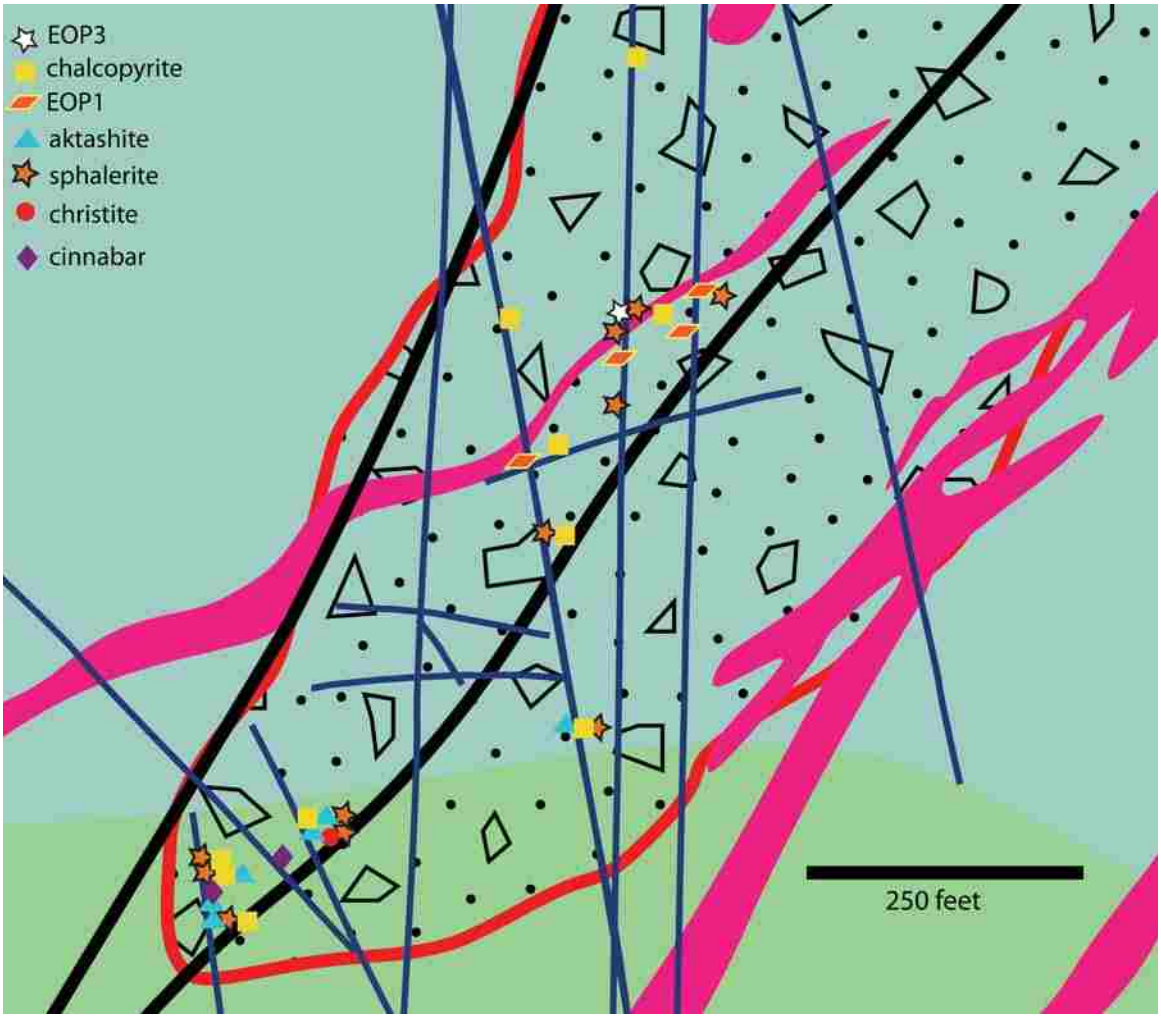

Figure 36. Magnified view of NE simplified cross section from Figure 5 that displays the locations of the minerals chalcopyrite, aktashite, sphalerite, christite, cinnabar, EOP1, and EOP3. Dark blue lines indicate sampled drill hole locations.

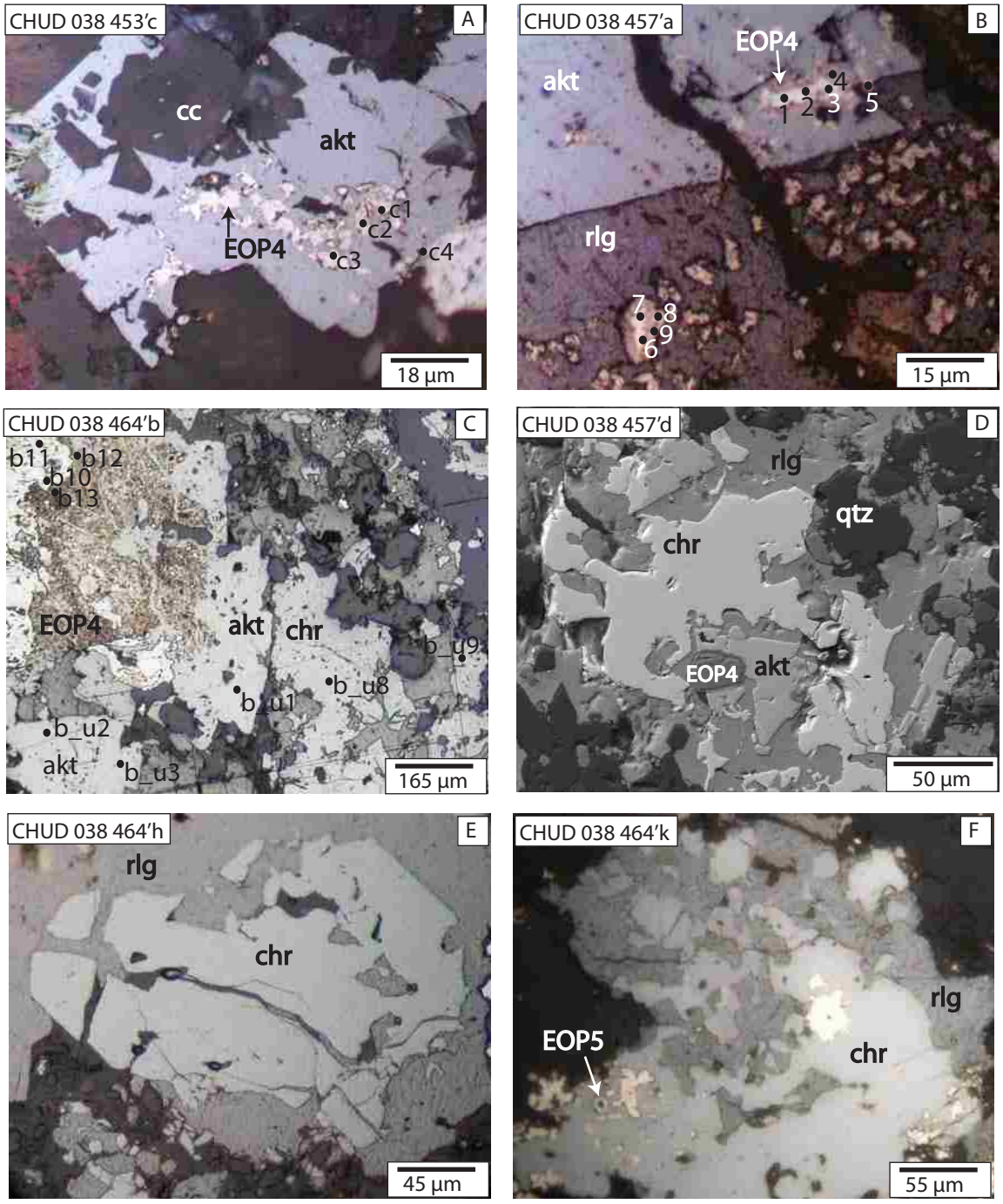

Figure 37. (A-C, E-F) Photomicrographs of late-ore-stage minerals under reflected light. A) Aktashite conforming to calcite rhombohedrons and EOP4. B) Aktashite surrounding EOP4; realgar conforming to aktashite crystal edge and also surrounding Au-bearing EOP4. C) Aktashite in contact with christite and surrounding abundant EOP4s. D) Secondary electron image of EOP4, aktashite, christite, and realgar. E) Christite crosscut by realgar. F) Christite surrounding EOP5 and realgar surrounding christite. Abbreviations: akt = aktashite; chr = christite; qtz = quartz; cc = calcite; rlg = realgar.

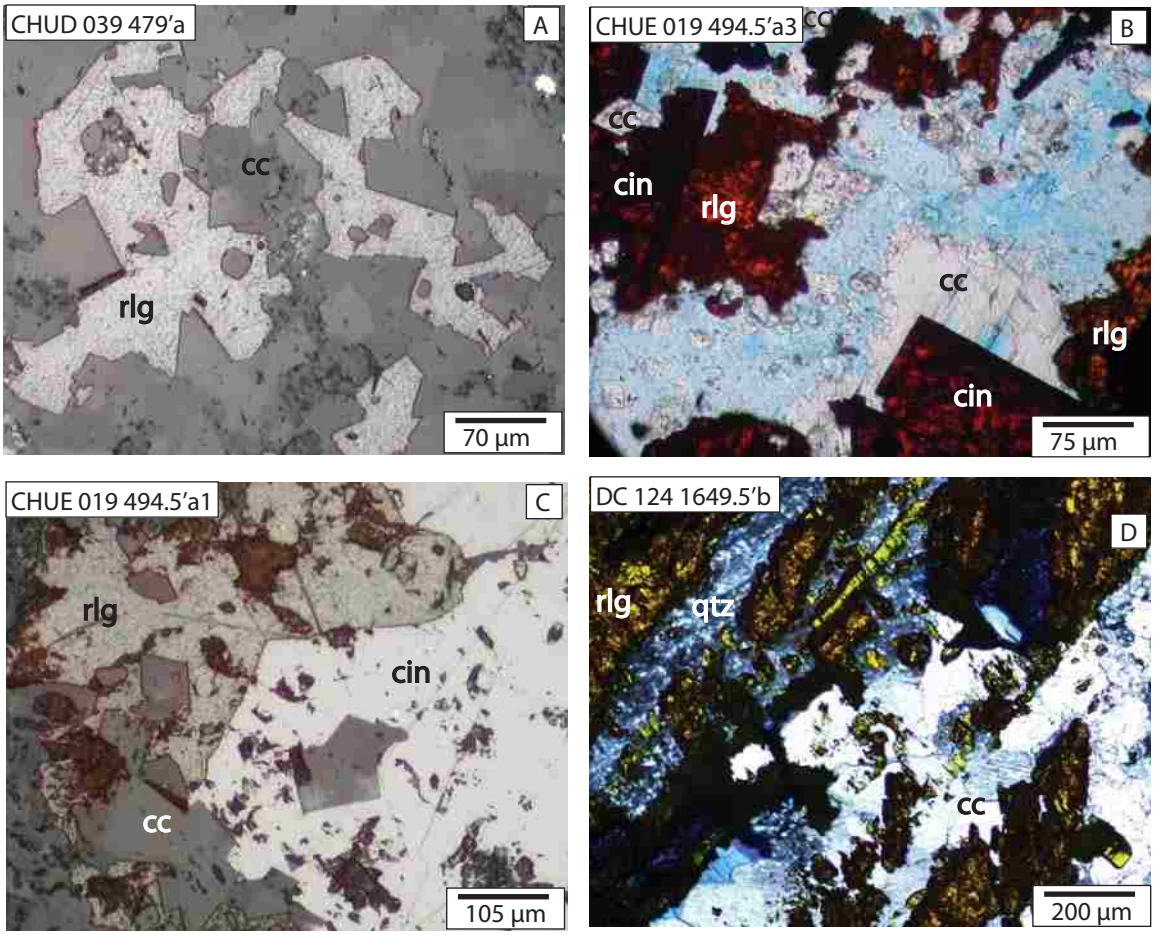

Figure 38. Photomicrographs of realgar and associated late-ore-stage minerals under reflected light (A,C), plane-polarized (B) and cross-polarized (D) transmitted light. A) Realgar surrounded by calcite rhombohedrons. B) Calcite conforming to euhedral cinnabar and realgar in the bottom right of the image. C) Realgar conforming to cinnabar; cinnabar and realgar conforming to calcite rhombohedrons. D) Solid realgar inclusions within calcite. Abbreviations: cc = calcite; rlg = realgar; cin = cinnabar; qtz = quartz.

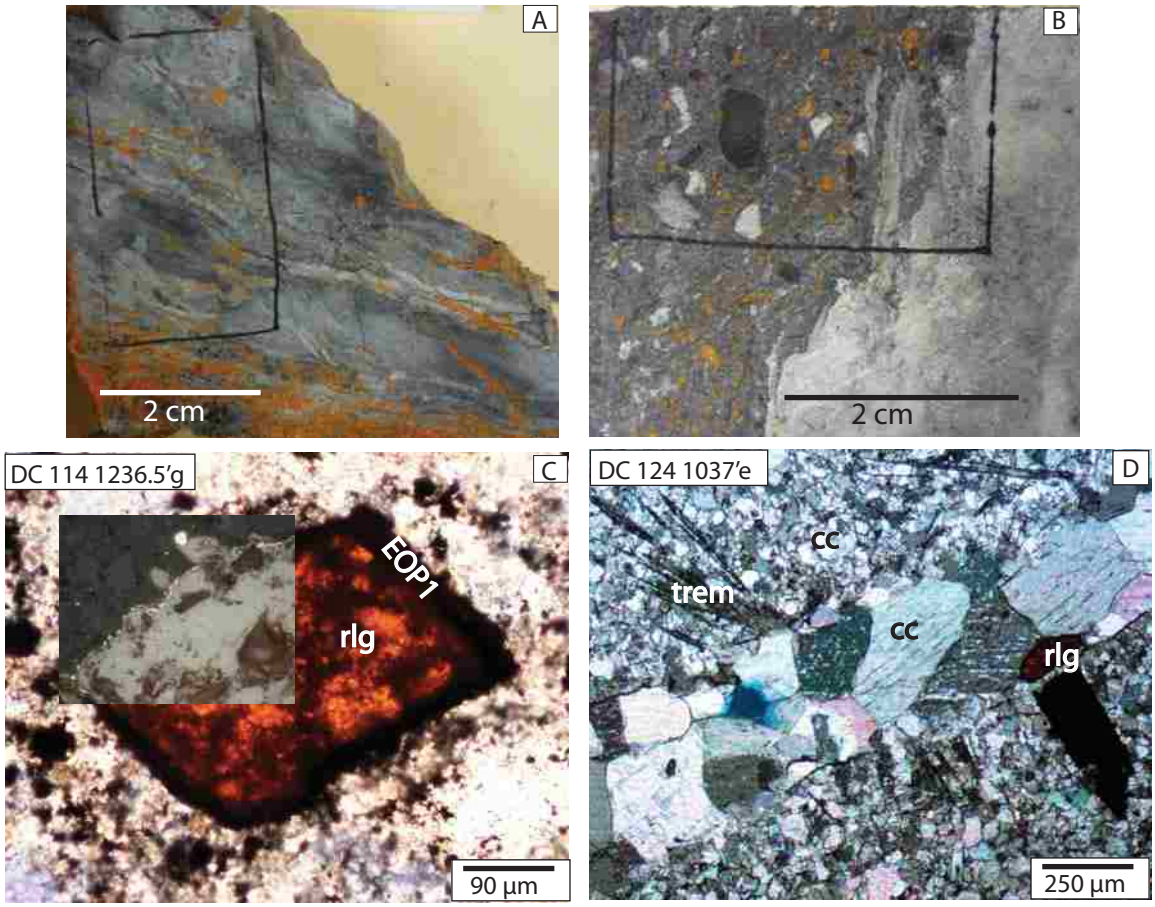

Figure 39. A) Whole rock sample that contains realgar and calcite veinlets along fractures. B) Whole rock sample that contains fragmented realgar. C) Photomicrographs of fragmented realgar with an Au-bearing iron sulfide rim under plane-polarized transmitted light (C) and reflected light (small grey square within C). D) Cross-polarized transmitted light photomicrograph of a calcite vein with a realgar fragment; the vein cross cuts recrystallized calcite and tremolite. Abbreviations: cc = calcite; rlg = realgar; trem = tremolite.

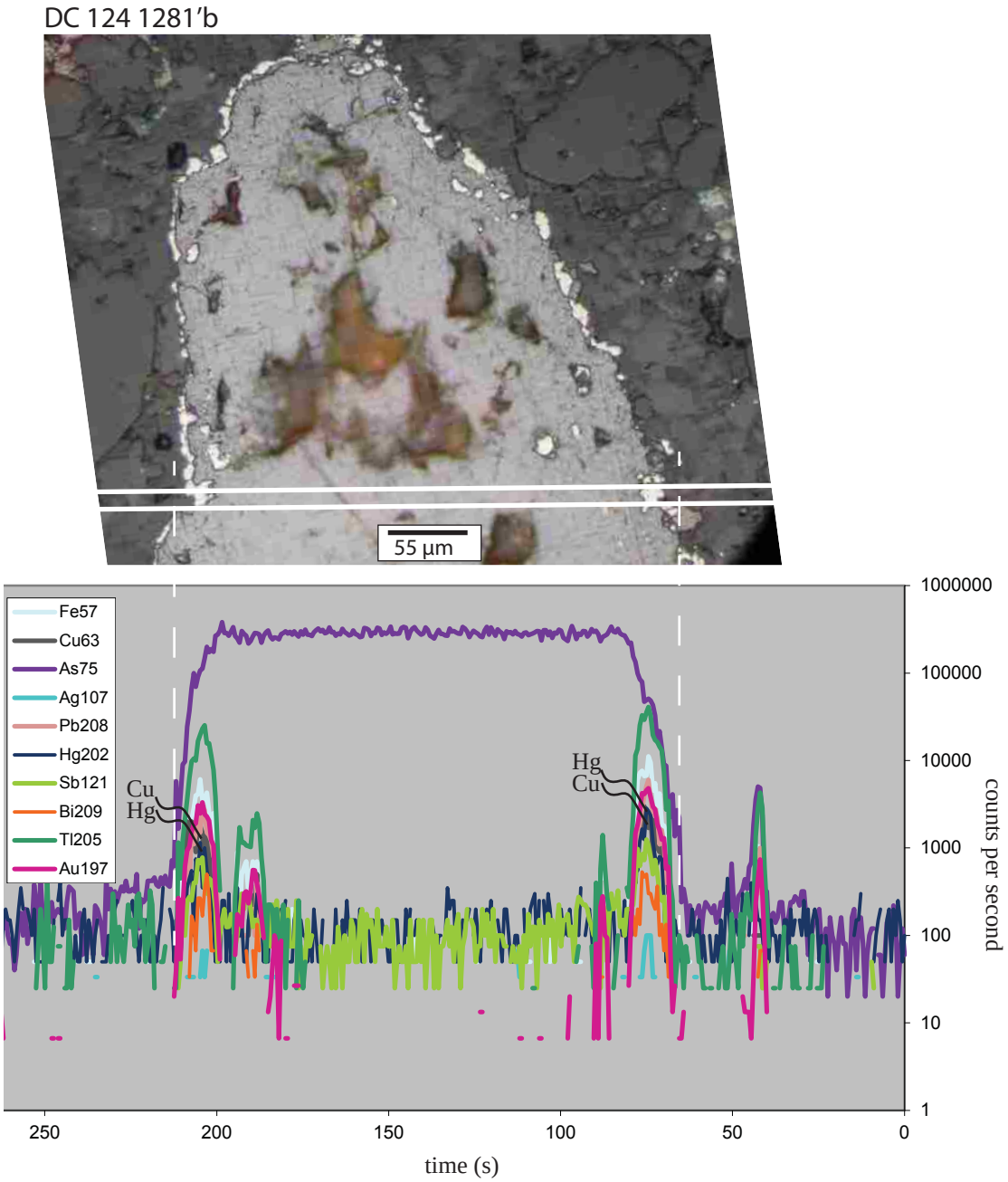

Figure 40. Photomicrograph of a realgar crystal with a Au-bearing iron-sulfide (EOP1) rim under reflected light. The two parallel solid white lines indicate the location of the LA-ICP-MS path and the area that was ablated. The dashed white lines indicate how the photomicrograph correlates with the LA-ICP-MS data.

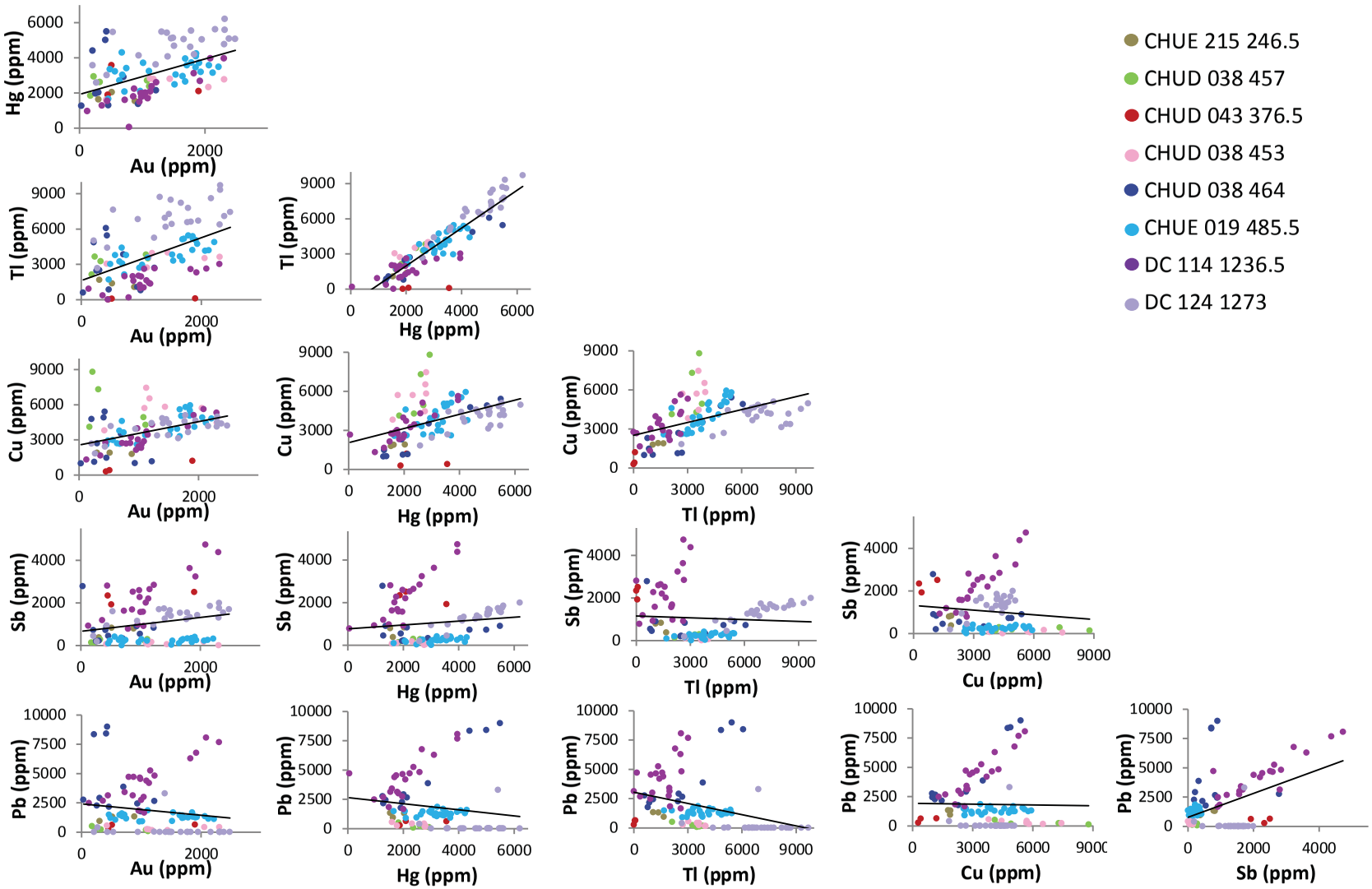

Figure 41. Scatter plots of Au, Hg, Tl, Cu, Sb, and Pb versus each other for all EPMA data collected on Au-bearing iron-sulfide minerals. The best fit correlation lines are calculated for all data points in each plot. Each color represents a sample.

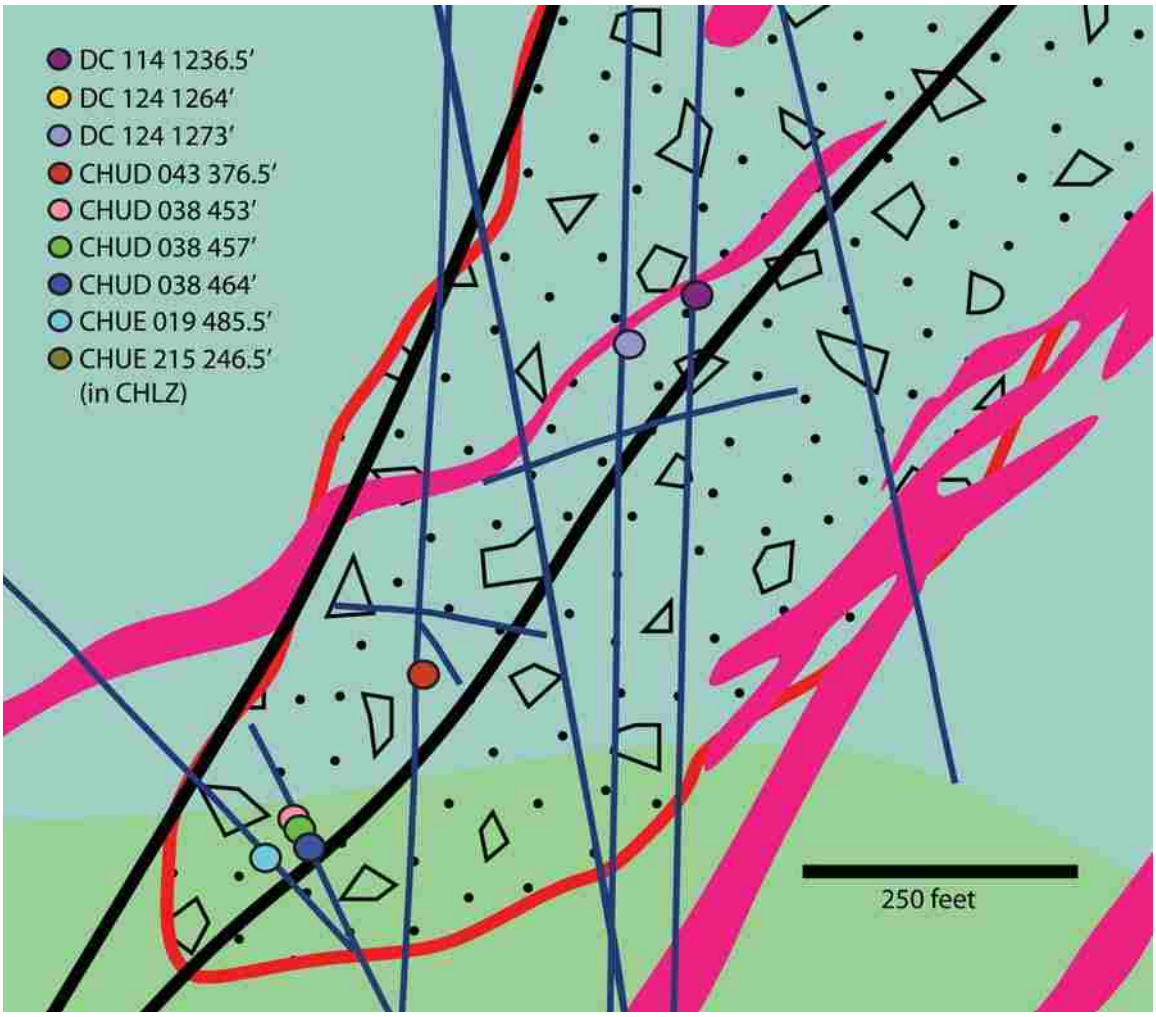

Figure 42. Magnified view of NE simplified cross section in Figure 5 that displays the location of eight thin sections within the CHBZ that were analyzed by using EPMA. Dark blue lines indicate sampled drill hole locations.

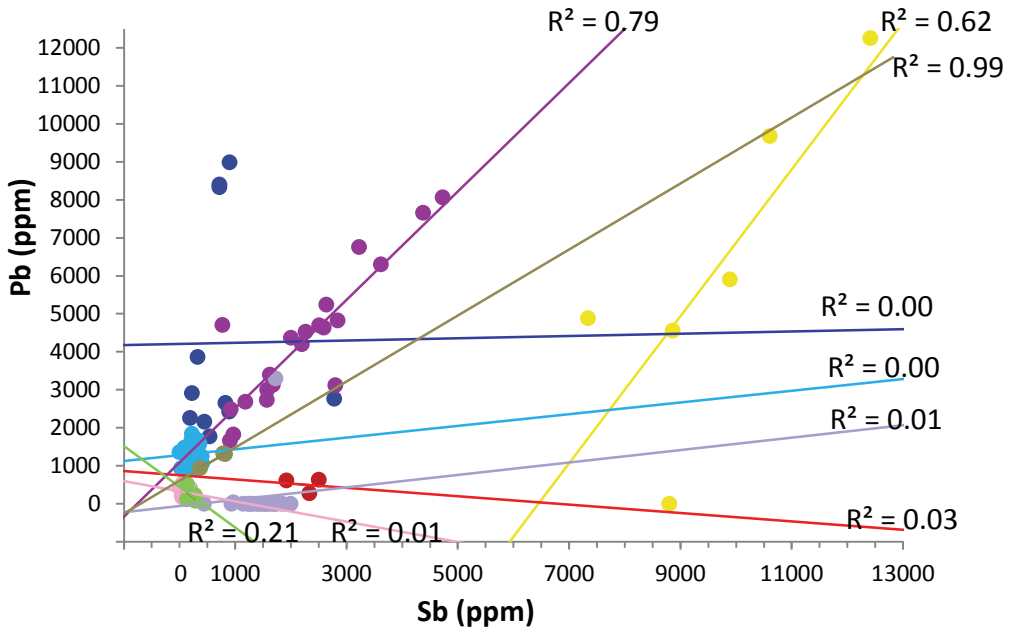

Thin section	Pb:Sb	Au:Pb	Au:Sb
CHUD 038 453'	0.01	0.00	0.00
CHUD 038 457'	0.21	0.30	0.20
CHUD 038 464'	0.00	0.11	0.08
CHUD 043 376.5'	0.03	0.34	0.49
CHUE 019 485.5'	0.00	0.00	0.04
CHUE 215 246.5'	0.99	0.65	0.54
DC 114 1236.5'	0.79	0.68	0.64
DC 124 1264'	0.62	0.00	0.00
DC 124 1273'	0.01	0.01	0.52

Figure 43. Scatter plot of Pb vs. Sb for all EPMA data collected on ore- and evolved-ore-stage iron-sulfide minerals. Each color represents a sample. Best fit correlation lines are plotted for each sample.

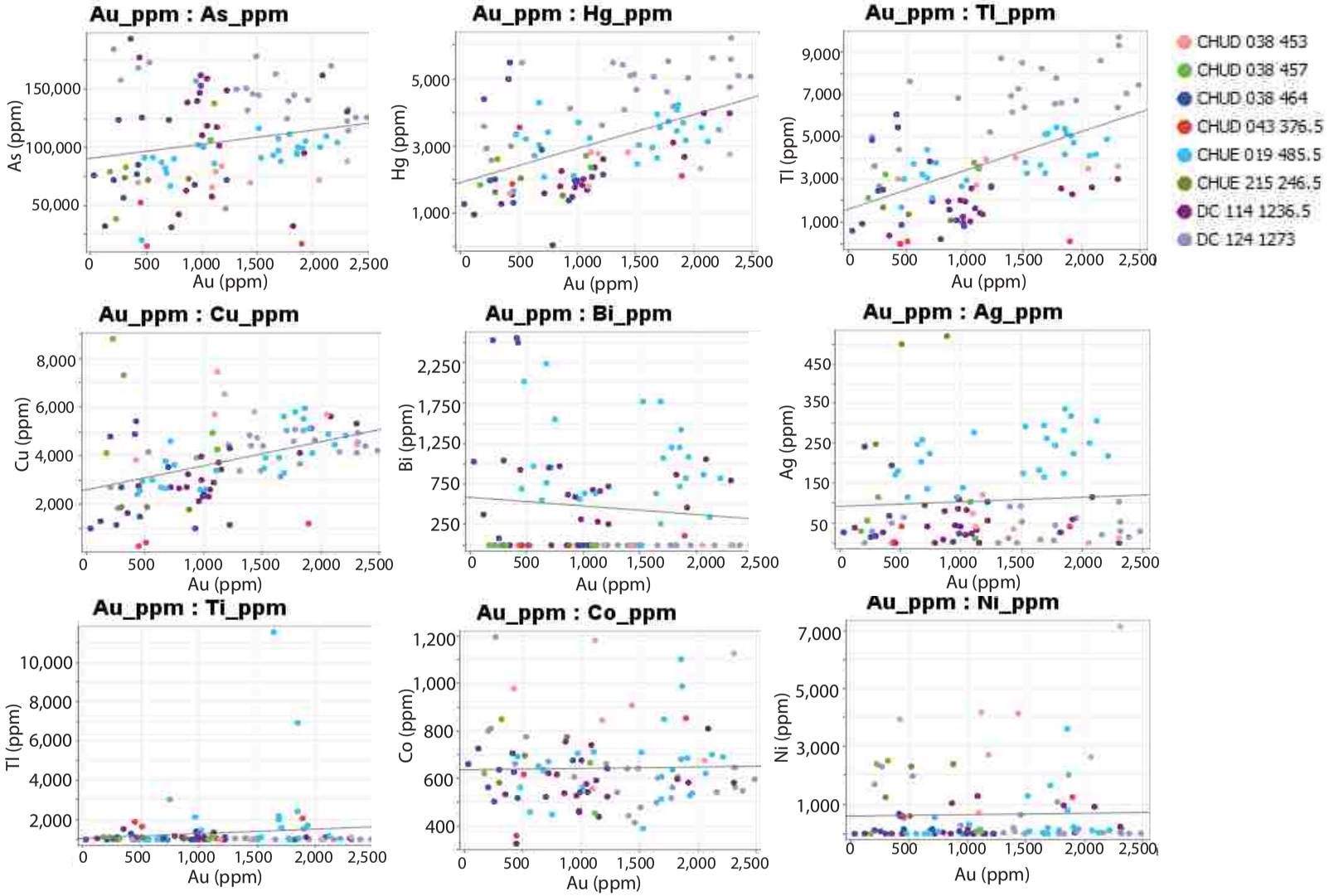

Figure 44. Scatter plots of Au versus As, Hg, Tl, Cu, Bi, Ag, Ti, Co, and Ni for all EPMA data collected from Au-bearing iron-sulfide minerals. All data in each plot are used to determine the best fit correlation lines. Each color represents a sample.

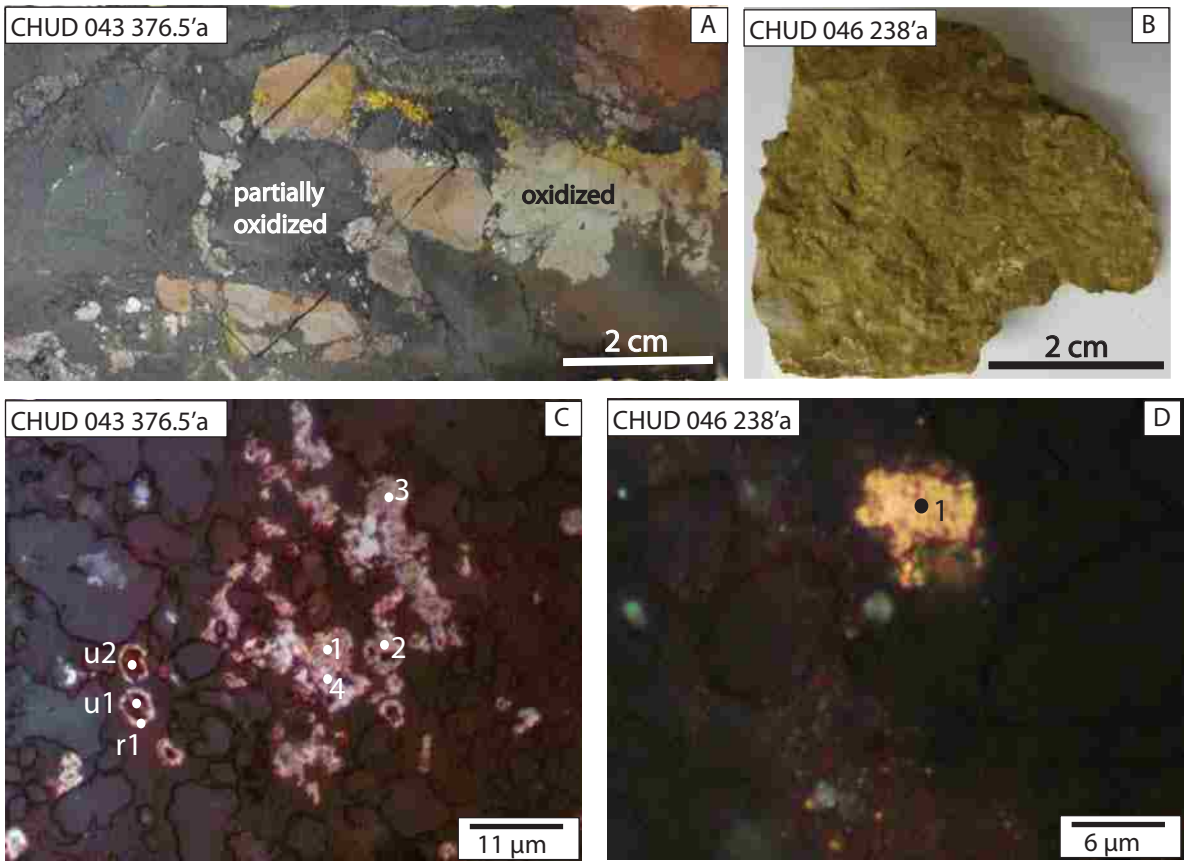

Figure 45. Whole rock samples of partially oxidized (A) and fully oxidized (B) samples from the CHBZ. Photomicrographs of Au-bearing iron-oxide minerals (C) and a Au alloy (D).

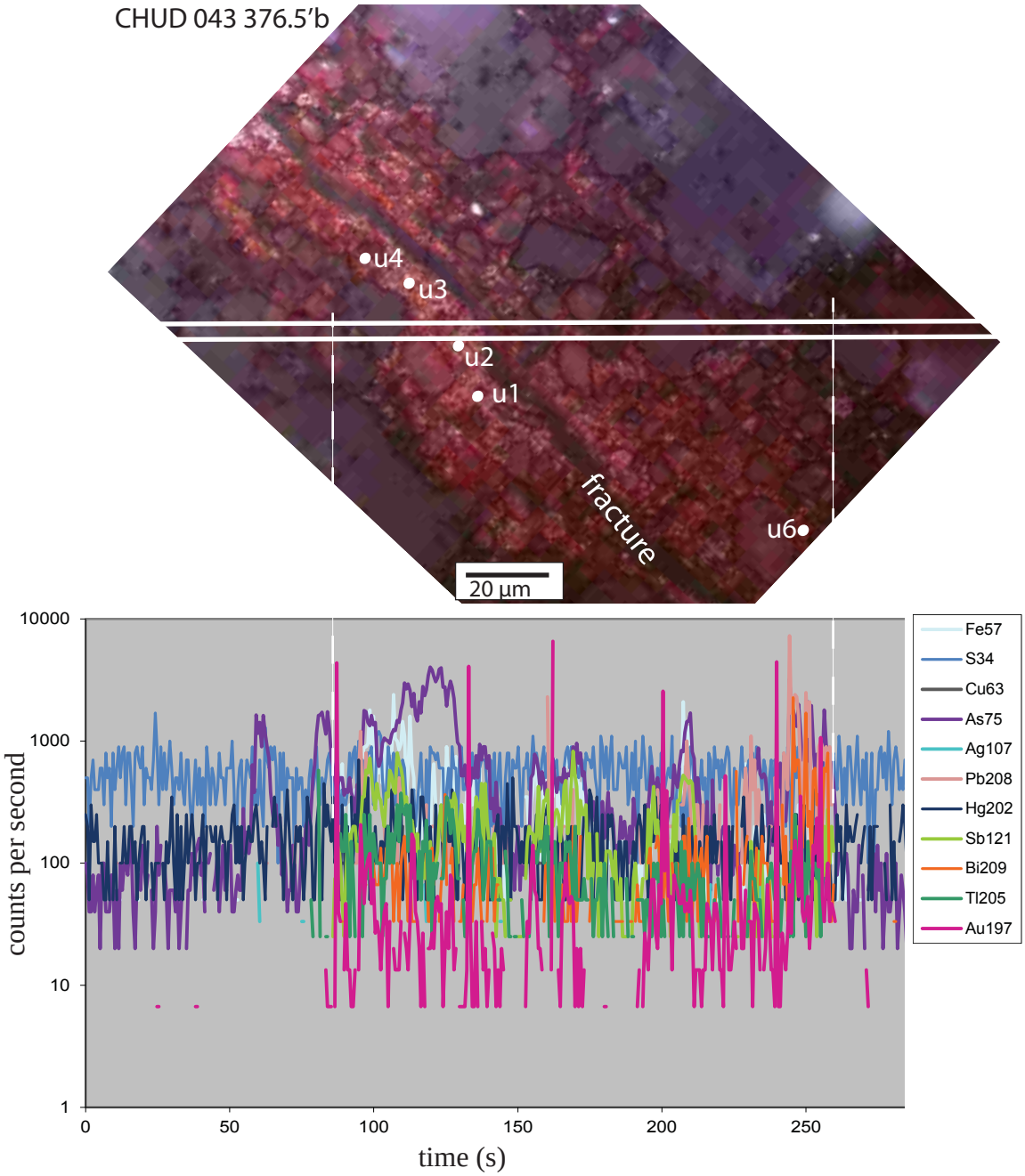

Figure 46. Photomicrograph of disseminated Au-bearing iron-oxide under reflected light. The two parallel solid white lines indicate the transect of the LA-ICP-MS path and the area that was ablated; these data are displayed in the plot below as counts per second on the y axis and time (s) on the x axis. The dashed white lines indicate where the photomicrograph correlates with the LA-ICP-MS data.

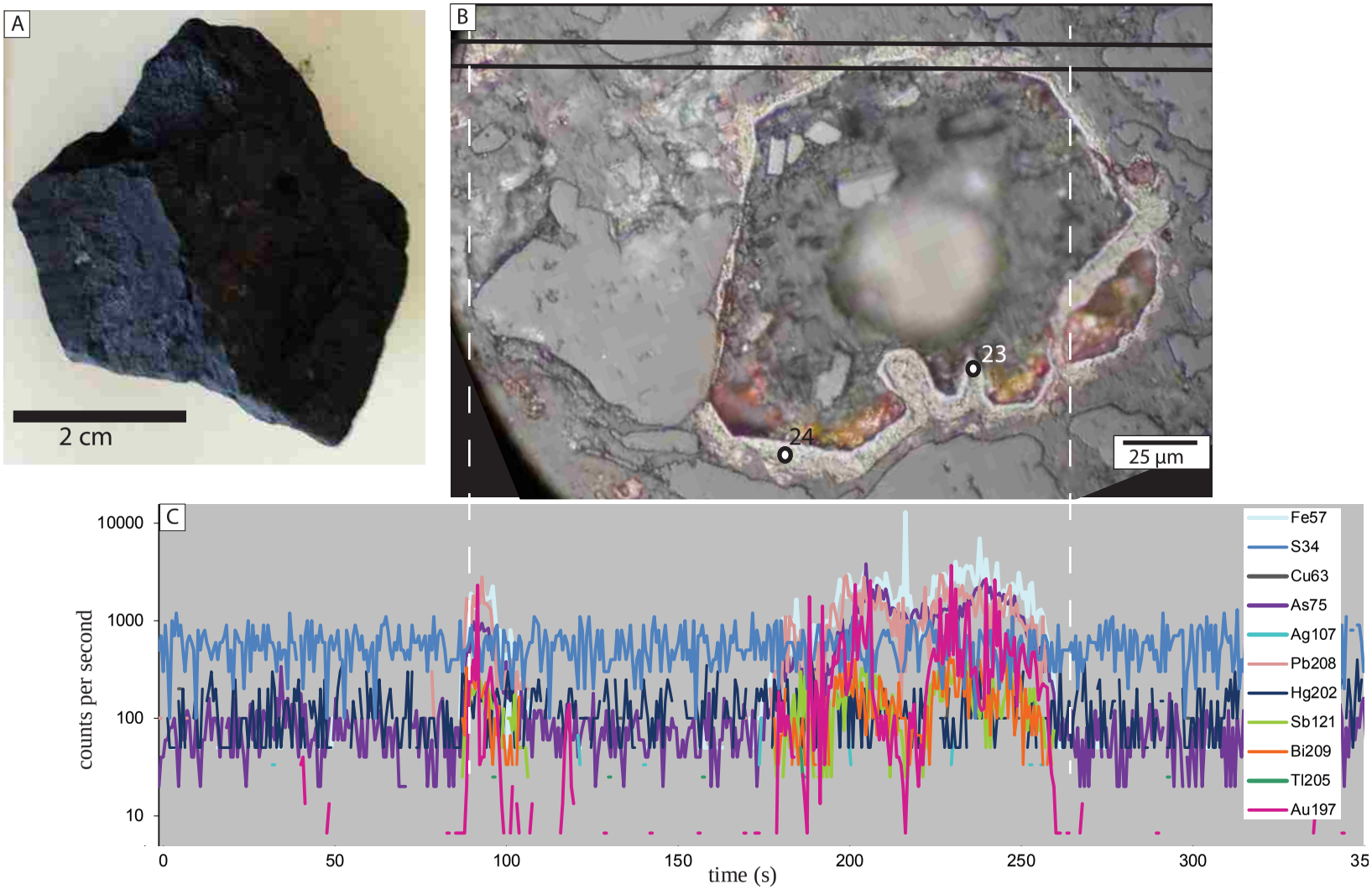

Figure 47. Whole rock sample (A) and reflected light photomicrograph of a Au-bearing iron-oxide rim (B). The two parallel black lines indicate the transect of the LA-ICP-MS path and the area that was ablated; these data are displayed in the plot below as counts on the y axis. The dashed white lines indicate where the photomicrograph correlates with the LA-ICP-MS data. The center of B is out of focus due to variation in relief from the other mineral surfaces.

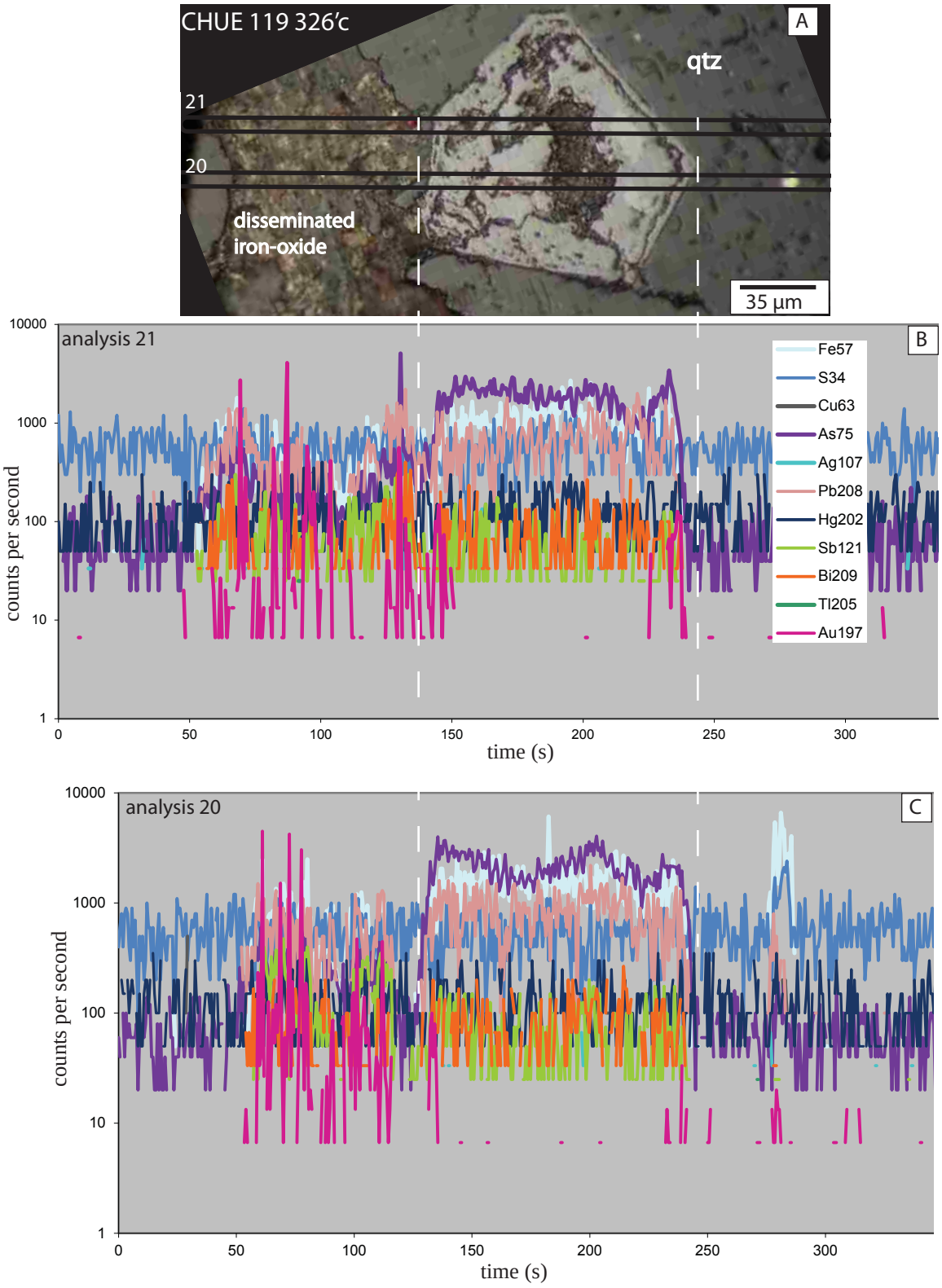

Figure 48. Photomicrograph of disseminated Au-bearing iron oxide material from CHLZ under reflected light. The two parallel black lines indicate the transect of the LA-ICP-MS path and the area that was ablated; these data are displayed in the plot below as counts on the y axis. The dashed white lines indicate how the photomicrograph correlates with the LA-ICP-MS data. Abbreviations: qtz = quartz

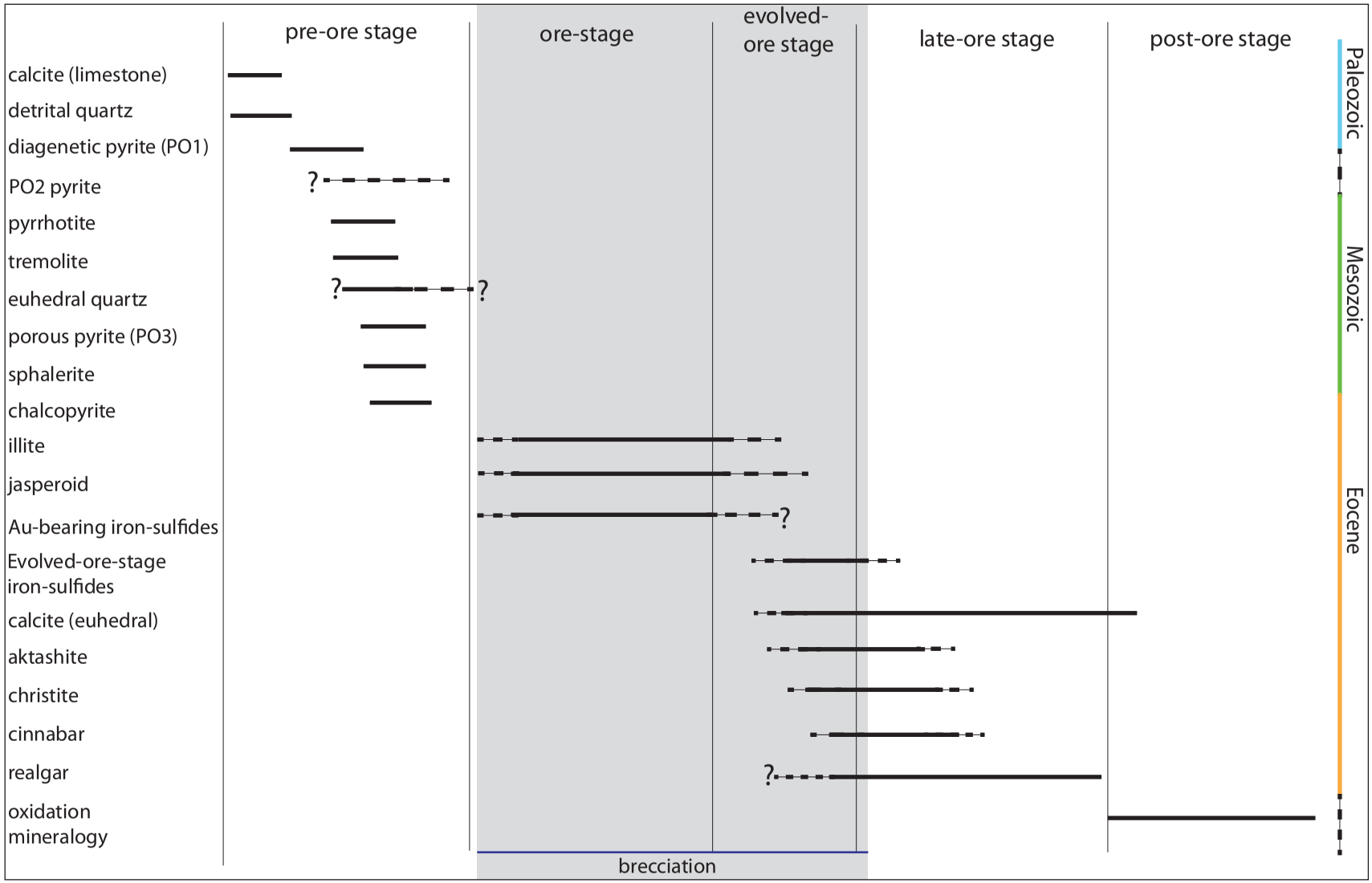

Figure 49. Paragenesis of the CHBZ displaying minerals in the pre-ore, ore-, evolved-ore-, and late-ore-stages.

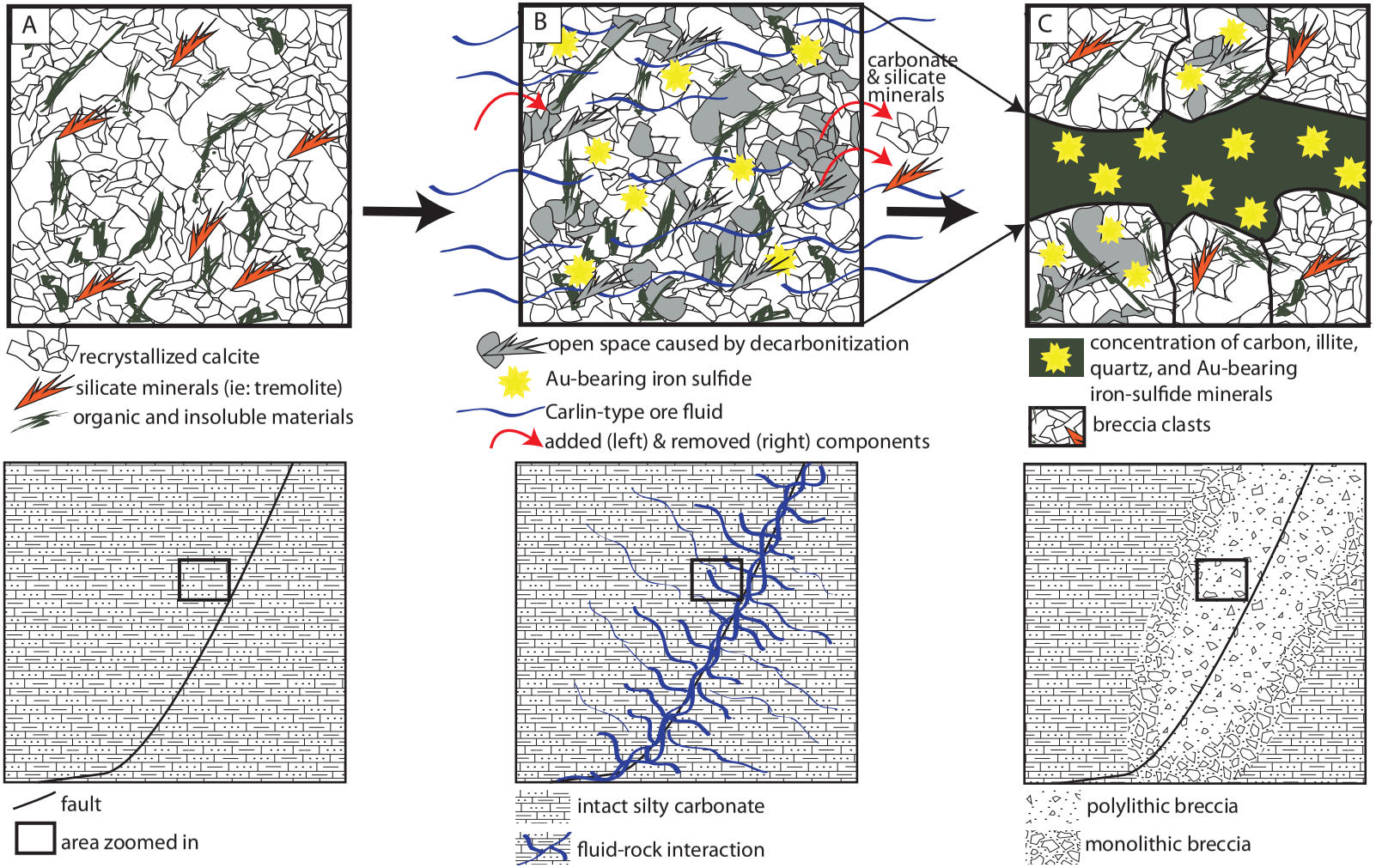

Figure 50. Schematic diagram illustrating how the Carlin ore fluid caused brecciation within the CHBZ. A) The pre-ore-stage host rocks contain recrystallized calcite, insoluble carbonaceous materials, and other pre-ore-stage minerals, including tremolite. B) The ore fluid took advantage of the porosity of the pre-ore Voodoo fault as a conduit to ascend, along the way dissolving reactive carbonate and silicate minerals. C) Dissolution created open space by removing abundant rocks mass, which concentrated insoluble materials and Au-bearing iron-sulfides within dissolution seams, ultimately leading to the collapse breccia formation. Clasts of rock that are unaltered by the Carlin fluid as well as mineralized clasts of the polylithic breccia surround mineralized seams.

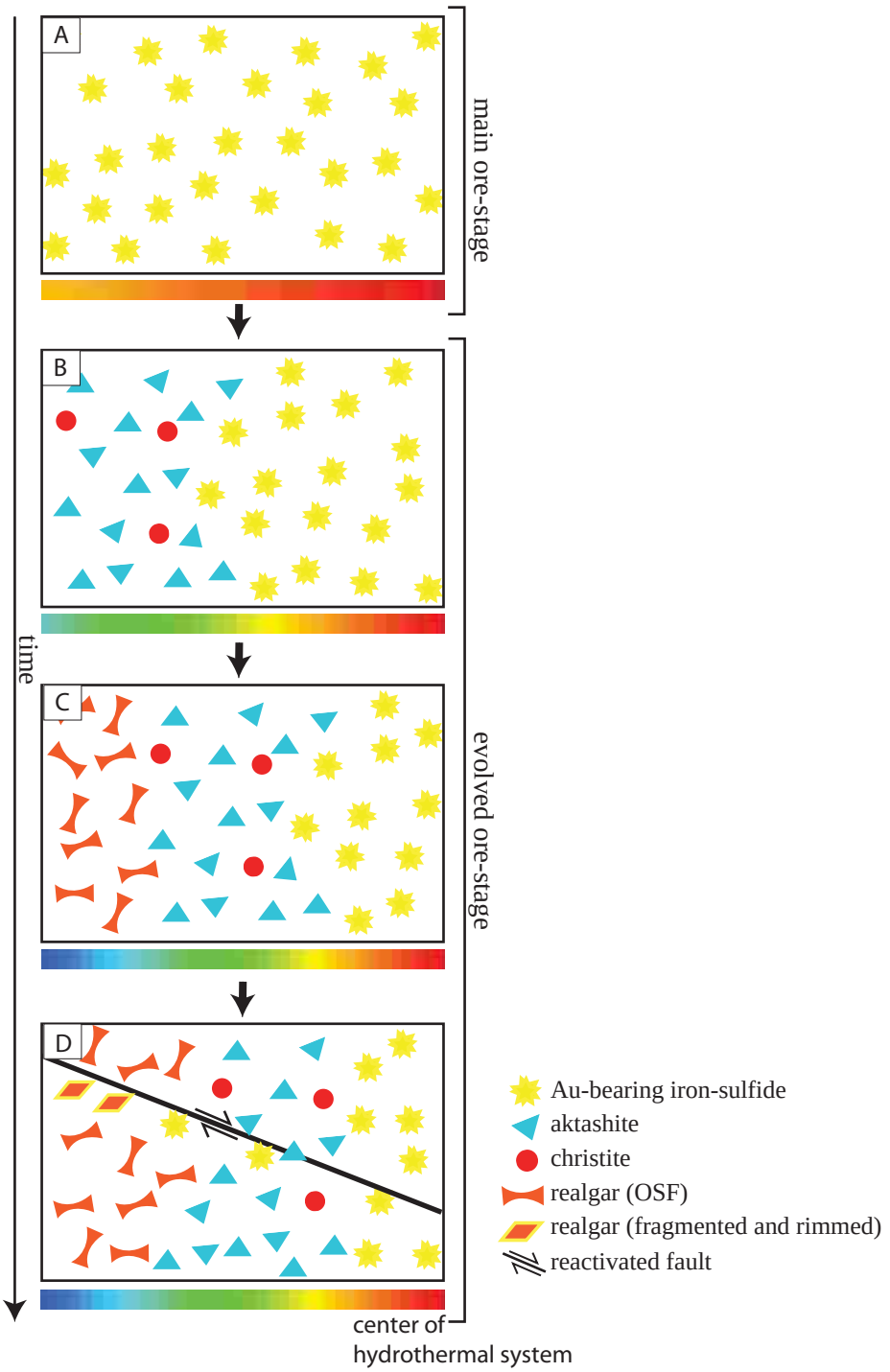

Figure 51. Cartoon displaying an interpretation of the formation of Au-bearing iron-sulfide rims on fragmented realgar. The boxes show the minerals that precipitated through time as the system cooled. The minerals displayed do not replace each other. This figure assumes that the hottest portion of the deposit is to the right, indicated by red on the color scale. A) When the Carlin ore system is at its peak temperature, Au-bearing iron-sulfide minerals precipitated. B) As the system began to cool and collapse, aktashite and christite were deposited in the cooler portions of the deposit while evolved ore-stage iron-sulfides precipitated closer to the heat source. C) As cooling continued, realgar began to precipitate on the periphery. D) At some point in time pressure was released, possibly owing to reactivation along a fault, which fragmented realgar and allowed the evolved ore-stage fluid to again access a region containing evolved-ore-stage and late-ore-stage minerals.

APPENDIX C

SAMPLES COLLECTED

All samples collected for this study are listed here and include three hundred and seventy samples from thirteen drill holes through the CHBZ and forty samples from three drill holes through the CHLZ. For each sample, this appendix lists the drill hole footage and Au assay (oz/t). Additionally, an X indicates if a thin section was made from the sample and which analytical techniques, if any, were performed on the sample.

Appendix C. Samples Collected

Hole ID & Zone	Footage	Au (oz/t)	Thin Section	EPMA	LA-ICP-MS	XRD	SEM CL	SEM
CHUD-019	266	5.24	x					x
CHBZ	288	8.44	x					
	324	7.11	x					
CHUD-038	430	0.386						
CHBZ	435.5	1.605	x					
	439	0.378	x					
	444	1.045						
	447	0.742						
	453	1.915	x	x			x	
	457	4.16	x	x		x		x
	464	3.07	x	x				
	470	5.83	x					
	474	2.37	x					
	478	2.65						
	482	2.65						
	490	1.22						
	495	0.223						
	504.5	0.208						
	513	0.343						
	532	0.0724						
CHUD-039	400.5	0.0836	x					
CHBZ	410	0.192	x				x	
	421	0.324	x					
	433	1.11	x					
	442	0.973						
	451	1.39	x					
	457	1.88	x					
	463	1.54	x					
	468	1.405	x		x			
	473	0.457	x					
	479	0.307	x					
	498	0.629	x					
	501	0.048	x					
CHUD-043	313.5	0.0267						
CHBZ	331	0.275						
	337	0.579						
	339	4.35						
	343	5.28						
	350	3.14						

Hole ID & Zone	Footage	Au (oz/t)	Thin Section	EPMA	LA-ICP-MS	XRD	SEM CL	SEM
CHUD-043	353	6.32						
cont.	374	5.86						
	376.5	5.25	x	x	x			
	382	7.12	x					
	383.5	7.12						
	388	0.661						
	393	3.05						
	401.5	3.32						
	404	3.32						
	417	3.46						
	432	0.985						
	443	0.513						
CHUD-044	217.5	0.0003	x					
CHBZ	220	0.125	x					
	222	0.125	x					
	223	0.125						
	226.5	0.331						
	231	0.451	x					
	234	0.451	x					
	237	0.0093	x					
	241.5	0.0013						
	247.5	0.0003						
	251	0.0471						
	255.5	0.379						
	263	0.204						
	265.5	0.006						
	270	0.106						
	275	0.0014						
	303	0.0003	x			x		
	306.5	0.519						
	307.5	0.519	x					
	308-309	0.519						
	322	0.029						
	324.5	2.63						
	333	2.3						
	352	4.42						
	358.5	4.63						
	360	1.765						
	365	5.94						
	377	5.83	x					

Hole ID & Zone	Footage	Au (oz/t)	Thin Section	EPMA	LA-ICP-MS	XRD	SEM CL	SEM
CHUD-044	383	2.71						
cont.	385	4.24						
	391	5.45						
	393	5.45	x					
	396.5	2.7						
	410	0.151						
	419	3.38						
	419.5	3.38						
	425	4.15						
	431	4.34						
	435	3.49						
	444.1	0.815						
	448	0.815						
	453	0.131						
	458.5	0.983						
	461	3.33						
	469.1	2.3						
	476	3.73						
	501	5.02						
	505	4.43						
	508.5	4.43						
	511	5.26						
	518.9	0.344						
	525	0.839						
	542	2.15						
	546	0.929						
	551	0.51						
	554.1	0.301						
	564.5	0.0587						
	572	0.0543						
	578	0.265						
	583	0.112						
	586	0.169						
	590	0.0037						
	592	0.0037						
CHUD-046	168	0.0163						
CHBZ	185	0.0989						
	202.5	0.729						
	207-210	0.103						
	210-212	0.103						

Hole ID & Zone	Footage	Au (oz/t)	Thin Section	EPMA	LA-ICP-MS	XRD	SEM CL	SEM
CHUD-046	214.5	7.49						
cont.	218	5.75						
	226	5.18	x					
	227-232	3.99						
	232.5	7.19						
	234-236	7.19						
	236.5	7.19						
	237-240	30.5	x	x		x		
	240-242	30.5						
	244	6.66						
	245.5	6.66						
	247-249	5.17						
	249-252	5.17						
	252-254	12.35						
	254.5	12.35						
	255.5	12.35						
	257.5	0.983						
	262.5-265	0.194	x					
	270	2.56						
	276	6.24						
	280.5	7.32	x					
	283	4.83	x			x		
	285	4.83	x					
	288	5.47						
	289-292	5.47						
CHUE-019	438.5	3.48	x					
CHBZ	469.5	3.69	x					
	485.5	1.67	x	x	x			x
	494.5	1.785	x					x
CHUE-119	285	0.0001						
CHLZ	293	0.0009						
	298	0.0009						
	304	0.147						
	308	0.147						
	310.5	0.147						
	313	0.386	x					
	316	0.386						
	317.2	0.804						
	317-322	0.804						
	324.5-326.5	1.67	x		x			

Hole ID & Zone	Footage	Au (oz/t)	Thin Section	EPMA	LA-ICP-MS	XRD	SEM CL	SEM
CHUE-119	327-328	1.75						
cont.	329-331	1.75						
CHUE-126	308-309	1.045	x					
CHLZ	309.5-311	1.045	x					
	311-313	0.506	x					
	313.5	0.506	x					
	314.5-315	0.506						
	315-316	0.016						
	317	0.016	x					
	318	0.016						
	319	0.016	x					
	322.5	0.016	x					
	324	0.0004						
	326	0.0004	x					
	328	0.0004						
	331	0.0004	x					
CHUE-215	241.5	0.83						
CHLZ	243.5	0.83						
	245	1.195	x			x		
	246.5	1.195	x	x	x		x	x
	247	1.195						
	248.5	1.195	x					
	250	0.377						
	252	0.377	x					
	254-257	0.056	x					
	258	0.056						
	259.5	0.0008	x					
	262.5	0.0008	x	x		x		
	273	0.0003						
DC-114	1187	0.007						
CHBZ	1192	0.333						
	1220	0.252						
	1226	0.337						
	1236.5	0.845	x	x	x		x	x
	1252	0.656						
	1261	0.884	x					
	1270	0.884						
	1276.5	0.362						
	1277.5	0.362	x					
	1294	0.052	x					

Hole ID & Zone	Footage	Au (oz/t)	Thin Section	EPMA	LA-ICP-MS	XRD	SEM CL	SEM
DC-114	1314.5	0.284						
cont.	1358	1.635						
	1378	1.604						
	1406	0.257	x					
DC-124	1002	0.001						
CHBZ	1013	0.001						
	1029	0.001						
	1037	0.001	x			x		
	1039.9	0.001	x					
	1042.5	0.025	x					
	1043	0.025						
	1046	0.025						
	1049	0.025						
	1050.5	0.312						
	1051.5	0.312	x					
	1056	0.312	x					
	1060.5	0.082	x					
	1066	0.083	x					
	1088.5	0.329						
	1104	0.258						
	1112	0.238						
	1143	0.122						
	1156	0.221	x					
	1162.5	0.131						
	1186	0.329						
	1194	0.192						
	1196	0.192						
	1222	0.001						
	1252	0.464						
	1257	0.464	x					
	1261	2.166	x			x		
	1264	2.166	x	x	x			x
	1267	2.166						
	1268	2.166						
	1273	3.094	x	x	x			
	1276.5	3.094	x					
	1281	1.205	x		x			
	1282.5-1284	1.205						
	1289.5	1.205						
	1291	0.809						

Hole ID & Zone	Footage	Au (oz/t)	Thin Section	EPMA	LA-ICP-MS	XRD	SEM CL	SEM
DC-124	1293	0.809						
cont.	1303	1.802						
	1305.5	1.802	x					
	1311	1.034						
	1315	1.034						
	1325.5	1.241						
	1347	2.876						
	1351.5	2.191						
	1356	2.191						
	1370-1373	3.236						
	1388-1390	0.283						
	1397	0.091	x					
	1402.5	0.378	x					
	1408.5	0.378	x					
	1423	3.747	x					
	1431.5	4.63						
	1465	0.336						
	1474	0.198						
	1522	0.293						
	1649.5	0.479	x					
	1653	0.199						
	1658	0.199						
	1667	0.202	x					
DC-132	1489	0.142						
CHBZ	1502	1.194						
	1507	1.194						
	1518	2.236						
	1535	0.899						
	1538	0.8						
	1548	3.568						
	1564.5	0.958						
	1587	2.262						
	1597.5	2.57						
	1606	1.584						
	1614	4.066	x					
	1620	4.066						
	1625	3.006						
	1641	0.102						
DC-213	1258	0.0107	x					
CHBZ	1260.5	0.0565						

Hole ID & Zone	Footage	Au (oz/t)	Thin Section	EPMA	LA-ICP-MS	XRD	SEM CL	SEM
DC-213	1263	0.0565	x			x		
cont.	1267	0.2512						
	1270	0.2512	x					
	1274	0.2512						
	1278	0.2512	x					
	1281	0.735	x			x		x
	1283	0.735						
	1286	0.229	x					
	1319.5	2.58	x					
	1370.5	0.512						
	1373	0.512						
	1374	0.512						
	1376	0.147						
	1384	0.002						
	1386	0.0014						
	1389.5	0.0014						
DC-215	1212.5	0.0001	x					
CHBZ	1221	0.008	x					
	1226	0.223	x					
	1264	0.0262						
	1266	0.0261						
	1270.5	0.0261						
	1276.5	0.0982						
	1281	0.0982						
	1283.5	0.205	x					
	1285.5	0.205						
	1290	0.289						
	1293.5	0.289	x					
	1296	0.322	x					
	1316	0.433	x			x		
	1318	0.433	x					
	1320.1	0.0811	x					
	1322	0.0811	x					
	1328	0.366						
	1338	0.643						
	1350.5	0.49						
	1360	0.27						
	1369	0.0028						
	1409	1.12						
	1415.5	0.541	x					

Hole ID & Zone	Footage	Au (oz/t)	Thin Section	EPMA	LA-ICP-MS	XRD	SEM CL	SEM
DC-215	1423	2.02	x					
cont.	1425	2.02						
	1434	5.76						
	1444	4.6						
	1457	4.57						
	1462	5.6						
	1468	1.375						
	1474	4.73						
	1483	6.56						
	1493	4.56	x					
	1497	4.6	x		x			x
	1508	5.77						
	1510-1515	10.2						
	1515.5	5.44						
	1531.5	6.1						
	1541	2.98						
	1544	0.998						
	1557	3.3						
	1564	4.12						
	1569	2.02	x	x		x		
	1578	0.562						
	1586	0.377						
	1591.5	0.23						
	1596.5	0.119						
	1601	0.0064						
	1647	0.007						
	1653	0.0884						
	1658.5	0.381						
	1667	0.065	x					
	1669	0.065	x					
	1672.5	0.0919	x					
	1674	0.0919						
	1675	0.0919						
	1677	1.805	x					
	1678.5	1.805	x					x
	1680	0.645						
ODC-048	1548	0.235						
CHBZ	1550	4.16						
	1554	0.369						
	1556.5	0.221						

Hole ID & Zone	Footage	Au (oz/t)	Thin Section	EPMA	LA-ICP-MS	XRD	SEM CL	SEM
ODC-048	1567.5	3.35						
cont.	1572.5	6.37						
	1578	5.46						
	1584	3.07						
	1593	5.25						
	1603	4.36						
	1608	4.6						
	1615	2.42						
	1617	2.42						
	1625	1.385						
	1639	2.15						
	1654.5	4.53	x					
	1658	5.26	x					
	1659.5	5.26						
	1683	0.0874						

APPENDIX D

DOCUMENTED MINERAL LOCATIONS FOR 46 SAMPLES

Detailed optical petrography notes were taken on forty-six samples. This appendix lists the Au assay (oz/t) and the minerals of interest observed in each sample. These minerals include ore-stage iron-sulfide (OP), evolved-ore-stage iron-sulfide (EOP), pre-ore-stage pyrite (PO), chalcopyrite (cpy), sphalerite (sph), pyrrhotite (pyo), titanium-oxide (TiO), aktashite (akt), christite (chr), cinnabar (cin). The sample ID name consists of the drill hole followed by the footage that the sample was collected at within the drill hole.

Appendix D. Documented Mineral Locations for 46 samples

Sample ID	Au (oz/t)	OP1	OP2	OP3	EOP1	EOP2	EOP3	EOP4	EOP5	PO1	PO2	PO3	cpy	sph	pyo	TiO	akt	chr	cin
CHUD 038 435.5'	1.605	x																	
CHUD 038 439'	0.378	x				x			x			x	x	x					
CHUD 038 453'	1.915	x						x	x		x				x	x	x		
CHUD 038 457'	4.16							x	x					x			x	x	
CHUD 038 464'	3.07	x		x				x	x	x	x	x		x			x	x	
CHUD 038 470'	5.83	x						x	x										
CHUD 038 474'	2.37	x										x							
CHUD 039 410'	0.192								x			x	x	x			x		
CHUD 039 421'	0.324							x	x								x		
CHUD 039 451'	1.39	x						x			x								x
CHUD 039 457'	1.88	x						x	x								x		
CHUD 039 468'	1.405	x								x	x								
CHUD 039 473'	0.457							x	x				x	x			x		
CHUD 039 501'	0.048										x		x	x					
CHUD 043 376.5'	5.25					x													
CHUD 044 303'	0.0003											x	x						
CHUE 019 485.5'	1.67	x	x																
CHUE 019 494.5'	1.785	x																	x
CHUE 119 326'	1.67					x													
CHUE 126 308'	1.045					x													
CHUE 215 262.5'	0.0008												x						
DC 114 1236.5'	0.845	x		x	x	x								x					
DC 114 1261'	0.884	x									x								
DC 114 1277.5'	0.362	x			x														

Sample ID	Au (oz/t)	OP1	OP2	OP3	EOP1	EOP2	EOP3	EOP4	EOP5	PO1	PO2	PO3	cpy	sph	pyo	TiO	akt	chr	cin
DC 124 1037'	0.001											x	x						
DC 124 1042.5'	0.025										x	x							
DC 124 1056'	0.312	x																	
DC 124 1261'	2.166	x	x						x	x		x							
DC 124 1264'	2.166						x												
DC 124 1273'	3.094	x	x	x		x				x	x			x					
DC 124 1281'	1.205	x			x					x									
DC 124 1649.5'	0.479	x																	
DC 213 1258'	0.0107										x								
DC 213 1263'	0.0565										x	x							
DC 213 1270'	0.2512										x								
DC 213 1278'	0.2512	x									x								
DC 213 1281'	0.735	x				x													
DC 213 1319.5'	2.58	x				x					x	x							
DC 215 1316'	0.433											x	x						
DC 215 1415.5'	0.541											x							
DC 215 1423'	2.02	x			x					x		x							
DC 215 1493'	4.56		x						x		x		x	x					
DC 215 1497'	4.6		x					x											
DC 215 1675'	0.0919								x			x	x	x			x		
DC 215 1677'	1.805	x				x							x	x			x		
DC 215 1678'	1.805	x	x			x													

Abbreviations: OP = ore-stage iron-sulfide; EOP = evolved-ore-stage iron-sulfide; PO = pre-ore-stage pyrite; cpy = chalcopyrite; sph = sphalerite; pyo = pyrrhotite; TiO = titanium oxide mineral; akt = aktashite; chr = christite; cin = cinnabar.

APPENDIX E

EPMA DATA

A JEOL-8900 Electron Probe Microanalyzer (EPMA) at University of Nevada Las Vegas (UNLV) Electron Microanalysis and Imaging Laboratory (EMiL) was used to collect EPMA data from twelve samples. The elements Ca, Si, S, Fe, and As were calibrated and measured as major elemental components, whereas Au, Hg, Ag, Pb, Tl, Sb, Cu, Bi, Zn, Ni, W, Co, Sn, Te, Se, Ti, and Mo were calibrated and measured as trace elements. Two analyses were performed iteratively for each point, one for the major elements and one for trace elements, so that the beam current can be modified to optimize for the full range of elements of interest (see Methods). This appendix lists the measured weight percent of each element at each EPMA location. The EPMA point name consists of the drill hole (ie. DC124), footage (ie. 1273), photomicrograph shown in Appendix H (ie. h), and spot within photomicrograph (ie. c1).

Appendix E. Electron Probe Microanalysis

EPMA point name	As	S	Fe	Si	Ca	Au	Hg	Ag	Pb	Tl	Sb	Cu
CHUD038_453b2_1	8.25	42.36	37.19	0.12	0.40	0.142	0.152	0.003	0.036	0.217	0.012	0.347
CHUD038_453b2_c1	0.13	53.44	45.45	0.04	0.56	0.000	0.037	0.000	0.129	0.005	0.000	0.000
CHUD038_453b2_r1	9.16	42.25	37.00	0.08	0.89	0.130	0.242	0.000	0.040	0.341	0.001	0.412
CHUD038_453b2_r2	7.94	37.53	32.31	0.07	6.85	0.104	0.270	0.009	0.020	0.287	0.000	0.353
CHUD038_453b2_r3	8.66	46.98	39.96	0.03	0.63	0.188	0.266	0.004	0.024	0.363	0.008	0.473
CHUD038_453b2_unk1	0.01	0.03	0.07	0.39	0.74	0.145	0.000	0.004	0.000	0.009	0.001	0.002
CHUD038_453b2_unk2	0.05	0.16	0.15	0.68	0.57	0.131	0.000	0.000	0.000	0.000	0.002	0.008
CHUD038_453c1	2.83	48.22	36.89	0.13	0.01	0.000	3.797	0.004	0.044	0.166	0.006	2.777
CHUD038_453c2	4.93	48.62	41.04	0.04	0.01	0.000	2.207	0.000	0.009	0.277	0.017	2.261
CHUD038_453c3	5.61	48.89	41.88	0.03	0.01	0.000	1.562	0.014	0.039	0.248	0.007	2.105
CHUD038_453c4	9.49	44.83	39.33	0.06	0.01	0.000	2.888	0.000	0.023	0.251	0.006	1.753
CHUD038_453d_akt1	10.33	24.44	1.47	0.13	0.00	0.000	37.353	0.060	0.000	0.000	0.298	23.935
CHUD038_453d_akt2	10.53	24.07	1.37	0.10	0.00	0.000	36.310	0.052	0.000	0.000	0.363	24.811
CHUD038_453d_c1	0.04	53.88	46.42	0.02	0.00	0.000	0.005	0.000	0.137	0.006	0.000	0.058
CHUD038_453d_r1	7.56	47.64	41.98	0.07	0.02	0.008	1.902	0.010	0.000	0.417	0.033	1.449
CHUD038_453d_r2	7.35	46.89	41.88	0.14	0.05	0.000	2.376	0.009	0.001	0.352	0.045	2.372
CHUD038_453d2_1	7.90	46.89	40.70	0.24	0.11	0.112	0.280	0.004	0.022	0.360	0.004	0.744
CHUD038_453d2_2	8.86	45.55	39.35	0.43	0.14	0.231	0.276	0.001	0.042	0.362	0.000	0.445
CHUD038_453d2_3	8.38	46.41	40.87	0.30	0.17	0.118	0.278	0.012	0.017	0.395	0.016	0.652
CHUD038_453d2_4	4.54	36.73	32.04	12.53	0.33	0.139	0.240	0.000	0.032	0.265	0.002	0.656
CHUD038_453d2_5	6.55	44.54	37.15	3.86	0.02	0.110	0.178	0.007	0.024	0.272	0.010	0.570
CHUD038_453d2_unk1	0.15	54.07	44.83	0.20	0.01	0.000	0.008	0.000	0.153	0.000	0.000	0.010
CHUD038_453f_c1	0.22	52.55	45.88	0.55	0.03	0.000	0.000	0.000	0.157	0.037	0.000	0.037
CHUD038_453f_qtz1	0.00	0.01	0.12	39.73	0.00	0.000	0.000	0.000	0.006	0.013	0.001	0.000
CHUD038_453f_r1	7.15	45.47	39.21	1.53	0.11	0.206	0.232	0.000	0.042	0.352	0.017	0.570
CHUD038_453f_r2	7.01	48.88	42.00	0.11	0.08	0.043	0.159	0.000	0.054	0.304	0.007	0.380
CHUD038_453f_r3	6.99	40.94	35.63	5.59	0.47	0.144	0.280	0.003	0.016	0.399	0.006	0.582

EPMA point name	Bi	Zn	Ni	W	Co	Sn	Te	Se	Ti	Mo	Totals
CHUD038_453b2_1	0.000	0.000	0.153	0.232	0.056	0.006	0.000	0.005	10.635	0.000	100.32
CHUD038_453b2_c1	0.008	0.000	0.328	0.000	0.068	0.000	0.000	0.026	0.407	0.000	100.63
CHUD038_453b2_r1	0.000	0.002	0.471	0.081	0.065	0.004	0.000	0.009	4.005	0.000	95.18
CHUD038_453b2_r2	0.000	0.000	0.463	0.000	0.074	0.000	0.000	0.001	0.512	0.000	86.79
CHUD038_453b2_r3	0.000	0.011	0.201	0.022	0.077	0.011	0.000	0.000	1.327	0.000	99.24
CHUD038_453b2_unk1	0.008	0.004	0.000	1.512	0.000	0.010	0.000	0.016	54.236	0.005	57.18
CHUD038_453b2_unk2	0.000	0.000	0.013	0.951	0.000	0.004	0.000	0.031	48.862	0.009	51.62
CHUD038_453c1	0.000	0.043	0.000	0.000	0.054	0.011	0.000	0.007	0.000	0.000	94.98
CHUD038_453c2	0.000	0.069	0.137	0.009	0.065	0.014	0.000	0.007	0.000	0.000	99.73
CHUD038_453c3	0.000	0.027	0.180	0.000	0.071	0.004	0.000	0.000	0.002	0.000	100.68
CHUD038_453c4	0.000	0.080	0.562	0.000	0.086	0.010	0.000	0.000	0.000	0.000	99.37
CHUD038_453d_akt1	0.000	0.951	0.000	0.000	0.012	0.000	0.000	0.005	0.000	0.003	98.99
CHUD038_453d_akt2	0.000	1.012	0.000	0.000	0.013	0.006	0.000	0.004	0.000	0.005	98.65
CHUD038_453d_c1	0.022	0.003	0.000	0.000	0.068	0.005	0.000	0.003	0.001	0.000	100.66
CHUD038_453d_r1	0.000	0.016	0.361	0.000	0.073	0.000	0.000	0.000	0.008	0.000	101.55
CHUD038_453d_r2	0.000	0.033	0.370	0.000	0.059	0.000	0.000	0.005	0.018	0.000	101.95
CHUD038_453d2_1	0.000	0.000	0.417	0.000	0.118	0.005	0.000	0.004	0.011	0.000	97.92
CHUD038_453d2_2	0.000	0.003	0.713	0.000	0.113	0.000	0.000	0.001	0.011	0.000	96.54
CHUD038_453d2_3	0.000	0.002	0.271	0.000	0.084	0.000	0.000	0.005	0.000	0.000	97.98
CHUD038_453d2_4	0.000	0.000	0.359	0.000	0.097	0.007	0.000	0.002	0.006	0.000	87.98
CHUD038_453d2_5	0.000	0.000	0.073	0.000	0.056	0.008	0.000	0.006	0.003	0.000	93.43
CHUD038_453d2_unk1	0.066	0.007	0.793	0.000	0.100	0.002	0.000	0.002	0.007	0.000	100.40
CHUD038_453f_c1	0.023	0.000	0.016	0.000	0.070	0.005	0.000	0.005	0.000	0.000	99.58
CHUD038_453f_qtz1	0.003	0.000	0.007	0.000	0.000	0.004	0.000	0.000	0.002	0.000	39.89
CHUD038_453f_r1	0.000	0.000	0.263	0.000	0.067	0.003	0.000	0.005	0.000	0.000	95.23
CHUD038_453f_r2	0.000	0.001	0.395	0.000	0.098	0.003	0.000	0.007	0.000	0.000	99.54
CHUD038_453f_r3	0.000	0.009	0.413	0.000	0.091	0.005	0.000	0.000	0.000	0.000	91.57

EPMA point name	As	S	Fe	Si	Ca	Au	Hg	Ag	Pb	Tl	Sb	Cu
CHUD038_453f_unk1	0.03	39.96	59.75	0.09	0.00	0.000	0.000	0.011	0.118	0.000	0.000	0.003
CHUD038_453f_unk2	0.04	39.59	59.62	0.11	0.00	0.000	0.000	0.002	0.117	0.000	0.006	0.004
CHUD038_453f1	0.01	53.26	45.01	0.03	0.01	0.000	0.007	0.003	0.132	0.013	0.000	0.000
CHUD038_453G_akt1	10.63	24.37	1.52	0.09	0.05	0.000	38.331	0.070	0.000	0.000	0.033	24.176
CHUD038_453G_py1	5.54	46.61	38.73	0.08	0.09	0.000	0.721	0.001	0.076	0.274	0.000	0.824
CHUD038_457a_1	1.52	51.81	45.04	0.01	0.00	0.000	0.134	0.000	0.145	0.098	0.000	0.625
CHUD038_457a_2	2.20	50.73	44.29	0.01	0.00	0.000	0.121	0.002	0.113	0.123	0.000	0.572
CHUD038_457a_3	10.56	43.13	38.59	0.03	0.01	0.000	0.166	0.004	0.131	0.124	0.000	0.584
CHUD038_457a_4	11.15	41.67	36.22	0.05	0.01	0.000	0.362	0.008	0.040	0.234	0.017	0.861
CHUD038_457a_5	12.50	32.74	20.25	0.06	0.00	0.000	6.475	0.003	0.000	0.140	0.025	4.989
CHUD038_457a_6	5.19	48.74	42.28	0.05	0.00	0.000	0.134	0.005	0.091	0.122	0.018	0.316
CHUD038_457a_7	7.91	45.12	38.45	0.12	0.00	0.018	0.183	0.003	0.051	0.214	0.014	0.411
CHUD038_457a_8	13.80	43.09	34.21	0.23	0.01	0.112	0.236	0.001	0.007	0.349	0.029	0.427
CHUD038_457a_9	10.66	43.68	37.76	0.13	0.00	0.108	0.270	0.010	0.018	0.381	0.018	0.492
CHUD038_457d_c1	0.40	53.29	45.83	0.02	0.00	0.000	0.093	0.005	0.119	0.149	0.000	0.259
CHUD038_457d_c2	2.78	51.69	42.52	0.03	0.02	0.000	0.212	0.009	0.099	0.195	0.000	0.461
CHUD038_457d_c3	4.05	48.61	42.57	0.02	0.03	0.000	0.259	0.005	0.071	0.246	0.006	0.502
CHUD038_457d_r1	22.33	38.80	30.14	0.15	0.10	0.000	0.408	0.019	0.000	0.601	0.009	0.680
CHUD038_457d_r2	28.21	36.13	22.81	0.21	0.08	0.000	1.569	0.009	0.000	2.244	0.064	3.072
CHUD038_457d_r3	12.59	36.51	26.89	0.10	0.06	0.000	6.613	0.006	0.000	0.656	0.025	7.030
CHUD038_457d_r4	12.00	38.24	32.20	0.13	0.12	0.000	3.257	0.001	0.000	1.805	0.020	3.127
CHUD038_457d_r5	11.72	37.63	32.24	0.13	0.15	0.000	3.357	0.008	0.000	0.307	0.007	3.413
CHUD038_457e_akt1	10.23	24.33	0.73	0.05	0.00	0.399	2.716	0.002	0.031	0.000	0.000	1.451
CHUD038_457e_c1	3.86	49.91	40.61	0.12	0.01	0.023	0.293	0.005	0.011	0.365	0.014	0.880
CHUD038_457e_c4	3.37	50.08	41.48	0.01	0.00	0.000	0.746	0.014	0.023	0.260	0.017	1.213
CHUD038_457e_r1	11.79	39.20	36.68	0.15	0.37	0.000	39.563	0.056	0.000	0.000	0.236	23.850
CHUD038_457e_r2	11.04	33.18	27.62	2.55	0.12	0.005	0.637	0.010	0.011	0.303	0.012	0.942

EPMA point name	Bi	Zn	Ni	W	Co	Sn	Te	Se	Ti	Mo	Totals
CHUD038_453f_unk1	0.053	0.000	0.000	0.000	0.087	0.003	0.000	0.018	0.000	0.000	100.13
CHUD038_453f_unk2	0.045	0.012	0.000	0.000	0.101	0.000	0.000	0.018	0.005	0.000	99.66
CHUD038_453f1	0.044	0.000	0.326	0.003	0.095	0.008	0.000	0.030	0.000	0.000	98.97
CHUD038_453G_akt1	0.000	1.106	0.000	0.000	0.015	0.129	0.000	0.000	0.000	0.010	100.53
CHUD038_453G_py1	0.000	0.519	1.701	0.000	0.630	0.011	0.000	0.015	0.009	0.000	95.83
CHUD038_457a_1	0.002	0.007	0.294	0.012	0.080	0.007	0.000	0.003	0.000	0.000	99.78
CHUD038_457a_2	0.000	0.000	0.212	0.006	0.074	0.003	0.000	0.006	0.002	0.000	98.46
CHUD038_457a_3	0.000	0.002	0.133	0.026	0.073	0.013	0.000	0.004	0.000	0.000	93.57
CHUD038_457a_4	0.000	0.012	0.102	0.000	0.053	0.014	0.000	0.007	0.008	0.000	90.83
CHUD038_457a_5	0.000	0.183	0.002	0.000	0.056	0.006	0.000	0.000	0.001	0.000	77.42
CHUD038_457a_6	0.016	0.000	0.058	0.000	0.062	0.007	0.000	0.003	0.000	0.000	97.09
CHUD038_457a_7	0.000	0.000	0.000	0.002	0.062	0.006	0.000	0.003	0.010	0.000	92.59
CHUD038_457a_8	0.000	0.000	0.004	0.000	0.045	0.000	0.000	0.000	0.008	0.000	92.55
CHUD038_457a_9	0.000	0.000	0.006	0.000	0.066	0.006	0.000	0.002	0.000	0.000	93.60
CHUD038_457d_c1	0.008	0.008	0.177	0.014	0.077	0.007	0.000	0.002	0.000	0.000	100.46
CHUD038_457d_c2	0.000	0.005	0.374	0.000	0.080	0.007	0.000	0.005	0.003	0.000	98.49
CHUD038_457d_c3	0.000	0.000	0.435	0.002	0.074	0.005	0.000	0.003	0.000	0.000	96.90
CHUD038_457d_r1	0.000	0.007	0.615	0.000	0.062	0.006	0.000	0.002	0.000	0.000	93.93
CHUD038_457d_r2	0.000	0.610	0.201	0.000	0.063	0.003	0.000	0.004	0.001	0.000	95.28
CHUD038_457d_r3	0.000	0.073	0.174	0.000	0.049	0.009	0.000	0.000	0.000	0.000	90.79
CHUD038_457d_r4	0.000	0.142	0.211	0.010	0.055	0.000	0.000	0.001	0.000	0.000	91.32
CHUD038_457d_r5	0.000	0.068	0.171	0.000	0.061	0.000	0.000	0.005	0.000	0.000	89.27
CHUD038_457e_akt1	0.011	151.751	0.002	0.000	0.066	0.066	0.000	0.010	0.013	0.000	191.86
CHUD038_457e_c1	0.000	0.012	0.239	0.000	0.081	0.005	0.000	0.000	0.008	0.000	96.45
CHUD038_457e_c4	0.000	0.049	0.423	0.000	0.072	0.013	0.000	0.000	0.000	0.000	97.77
CHUD038_457e_r1	0.000	1.059	0.002	0.000	0.018	0.005	0.000	0.000	0.000	0.000	152.98
CHUD038_457e_r2	0.000	0.002	0.293	0.000	0.107	0.000	0.000	0.002	0.007	0.000	76.85

EPMA point name	As	S	Fe	Si	Ca	Au	Hg	Ag	Pb	Tl	Sb	Cu
CHUD038_457e_r3	8.26	44.57	40.07	0.36	0.13	0.032	0.261	0.011	0.022	0.326	0.028	0.730
CHUD038_457e_r4	10.64	38.81	38.32	0.13	0.03	0.000	37.761	0.069	0.000	0.000	0.054	23.801
CHUD038_457e_r5	9.37	43.49	40.09	0.07	0.02	0.000	0.175	0.003	0.173	0.155	0.000	0.545
CHUD038_457e_r6	12.17	41.16	38.51	0.06	0.03	0.000	0.181	0.002	0.117	0.150	0.010	0.760
CHUD038_457e_r7	10.57	42.24	38.23	0.07	0.02	0.000	0.273	0.010	0.088	0.143	0.006	0.876
CHUD038_457e_sph1	0.01	25.97	5.40	0.02	0.01	0.000	15.836	0.028	0.000	0.000	0.022	12.413
CHUD038_457e_sph2	0.02	26.04	5.34	0.01	0.01	0.000	21.762	0.031	0.000	0.000	0.024	15.687
CHUD038_457e_sph3	0.00	25.97	5.74	0.03	0.01	0.308	0.683	0.002	0.038	0.000	0.036	0.573
CHUD038_457f2_c1	8.90	44.00	38.54	0.82	0.82	0.000	0.288	0.009	0.000	0.433	0.019	0.796
CHUD038_457f2_r1	11.09	39.76	35.08	1.51	0.79	0.059	0.251	0.001	0.000	0.370	0.013	0.645
CHUD038_457f2_r2	11.49	39.31	34.95	3.28	0.89	0.000	0.138	0.003	0.000	0.226	0.033	0.514
CHUD038_464a_unk1	10.21	24.33	0.33	0.07	0.00	0.000	37.623	0.090	0.000	0.000	0.266	25.043
CHUD038_464a_unk2	9.76	22.27	0.18	0.07	0.00	0.000	32.795	0.107	0.000	31.498	0.355	2.471
CHUD038_464a1	0.04	51.39	42.45	0.20	0.83	0.000	0.039	0.015	0.307	0.006	0.000	0.000
CHUD038_464a10	4.38	47.03	40.83	0.06	0.05	0.000	0.196	0.014	0.577	0.146	0.023	0.204
CHUD038_464a11	4.48	51.52	41.96	0.02	0.01	0.000	0.184	0.006	0.341	0.090	0.008	0.147
CHUD038_464a2	0.05	53.61	44.53	0.08	0.01	0.000	0.034	0.005	0.236	0.000	0.000	0.000
CHUD038_464a3	0.81	49.25	39.84	0.57	0.09	0.000	0.507	0.022	0.297	0.066	0.000	0.000
CHUD038_464a4	0.59	49.16	41.03	2.48	0.08	0.000	0.051	0.020	0.185	0.081	0.000	0.716
CHUD038_464a5	0.69	48.42	38.90	8.81	0.03	0.000	0.094	0.021	0.241	0.088	0.000	0.117
CHUD038_464a6	2.78	43.84	37.97	5.54	0.13	0.000	0.208	0.018	0.456	0.175	0.000	0.190
CHUD038_464a7	3.97	46.44	40.21	0.65	0.22	0.000	0.204	0.014	0.520	0.183	0.000	0.166
CHUD038_464a8	2.35	50.26	42.81	0.79	0.13	0.000	0.172	0.011	0.378	0.155	0.001	0.133
CHUD038_464a9	2.67	50.89	43.71	0.01	0.01	0.000	0.191	0.029	0.405	0.165	0.016	0.429
CHUD038_464b_unk1	10.48	24.90	0.00	0.05	0.00	0.000	39.110	0.098	0.000	0.000	0.052	24.055
CHUD038_464b_unk2	10.26	24.36	0.10	0.05	0.00	0.000	38.655	0.118	0.000	0.000	0.081	24.022
CHUD038_464b_unk3	9.98	24.16	0.10	0.04	0.00	0.000	39.791	0.108	0.000	0.000	0.039	24.403

EPMA point name	Bi	Zn	Ni	W	Co	Sn	Te	Se	Ti	Mo	Totals
CHUD038_457e_r3	0.000	0.018	0.249	0.000	0.085	0.013	0.000	0.000	0.003	0.000	95.18
CHUD038_457e_r4	0.000	1.145	0.018	0.000	0.024	0.021	0.000	0.000	0.000	0.000	150.83
CHUD038_457e_r5	0.000	0.009	0.686	0.021	0.082	0.000	0.000	0.001	0.007	0.000	94.88
CHUD038_457e_r6	0.000	0.036	0.089	0.005	0.062	0.010	0.000	0.002	0.023	0.000	93.37
CHUD038_457e_r7	0.000	0.006	0.181	0.000	0.073	0.000	0.000	0.004	0.013	0.000	92.80
CHUD038_457e_sph1	0.000	81.834	0.040	0.078	0.048	0.125	0.000	0.012	3.334	0.000	145.18
CHUD038_457e_sph2	0.000	82.751	0.009	0.000	0.027	0.247	0.000	0.000	0.000	0.000	151.96
CHUD038_457e_sph3	0.000	105.172	0.003	0.000	0.049	0.136	0.000	0.016	0.001	0.000	138.77
CHUD038_457f2_c1	0.000	0.000	0.239	0.000	0.057	0.000	0.000	0.000	0.007	0.000	94.94
CHUD038_457f2_r1	0.000	0.003	0.169	0.000	0.051	0.002	0.000	0.000	0.003	0.000	89.80
CHUD038_457f2_r2	0.000	0.035	0.136	0.000	0.039	0.000	0.000	0.000	0.014	0.000	91.06
CHUD038_464a_unk1	0.000	1.116	0.000	0.000	0.018	0.007	0.000	0.009	0.020	0.013	99.15
CHUD038_464a_unk2	0.000	0.203	0.000	0.282	0.011	0.000	0.000	0.001	0.000	0.000	100.01
CHUD038_464a1	0.022	0.010	1.474	0.000	0.073	0.000	0.000	0.000	0.000	0.000	96.86
CHUD038_464a10	0.204	0.005	0.264	0.102	0.060	0.016	0.000	0.007	0.005	0.000	94.18
CHUD038_464a11	0.078	0.013	0.191	0.036	0.060	0.013	0.000	0.001	0.008	0.000	99.17
CHUD038_464a2	0.032	0.027	2.115	0.000	0.106	0.001	0.011	0.003	0.000	0.000	100.84
CHUD038_464a3	0.112	0.000	3.085	0.000	0.204	0.000	0.013	0.003	0.000	0.000	94.88
CHUD038_464a4	0.064	0.007	0.318	0.000	0.061	0.019	0.000	0.017	0.005	0.000	94.88
CHUD038_464a5	0.081	0.000	0.713	0.000	0.028	0.023	0.001	0.015	0.009	0.000	98.28
CHUD038_464a6	0.181	0.006	0.482	0.000	0.062	0.010	0.000	0.015	0.007	0.000	92.07
CHUD038_464a7	0.184	0.000	0.677	0.013	0.073	0.008	0.000	0.009	0.000	0.000	93.54
CHUD038_464a8	0.116	0.013	0.514	0.000	0.065	0.018	0.000	0.011	0.010	0.000	97.93
CHUD038_464a9	0.100	0.025	0.043	0.010	0.074	0.012	0.000	0.019	0.005	0.000	98.81
CHUD038_464b_unk1	0.000	1.254	0.000	0.004	0.013	0.003	0.000	0.001	0.006	0.006	100.04
CHUD038_464b_unk2	0.000	1.111	0.000	0.014	0.000	0.000	0.000	0.000	0.000	0.000	98.77
CHUD038_464b_unk3	0.000	1.009	0.000	0.000	0.023	0.000	0.000	0.000	0.000	0.000	99.65

EPMA point name	As	S	Fe	Si	Ca	Au	Hg	Ag	Pb	Tl	Sb	Cu
CHUD038_464b_unk4	0.01	26.92	8.60	0.01	0.02	0.617	0.052	0.000	0.111	0.000	0.000	0.311
CHUD038_464b_unk5	0.00	27.36	7.97	0.00	0.01	0.627	0.027	0.005	0.105	0.000	0.000	0.473
CHUD038_464b_unk6	3.79	35.30	31.97	3.11	0.07	0.000	0.284	0.012	0.668	0.269	0.058	0.824
CHUD038_464b_unk8	9.67	21.64	0.09	0.10	0.00	0.000	13.734	0.013	0.000	28.365	0.066	8.053
CHUD038_464b_unk9	10.66	23.66	0.14	0.06	0.00	0.000	31.331	0.064	0.000	27.557	0.121	3.257
CHUD038_464b1	0.02	53.92	46.25	0.01	0.01	0.000	0.000	0.011	0.212	0.011	0.000	0.023
CHUD038_464b10	0.12	53.61	44.93	0.01	0.00	0.000	0.017	0.009	0.223	0.006	0.000	0.096
CHUD038_464b11	0.00	53.98	46.80	0.01	0.00	0.000	0.001	0.003	0.141	0.016	0.000	0.000
CHUD038_464b12	7.24	42.92	31.00	0.03	0.00	0.000	9.170	0.036	0.627	0.000	0.058	7.265
CHUD038_464b13	6.88	41.36	27.53	0.04	0.01	0.000	16.123	0.053	0.278	0.000	0.025	12.104
CHUD038_464b2	0.02	53.90	45.88	0.02	0.01	0.000	0.006	0.004	0.227	0.013	0.000	0.064
CHUD038_464b3	0.28	54.31	46.13	0.02	0.00	0.000	0.073	0.015	0.256	0.059	0.000	0.134
CHUD038_464b4	4.36	50.01	43.68	0.02	0.00	0.000	0.122	0.011	0.547	0.098	0.031	0.399
CHUD038_464b5	1.63	52.46	44.94	0.01	0.01	0.000	0.175	0.012	0.368	0.161	0.019	0.261
CHUD038_464b7	3.42	50.28	43.33	0.04	0.01	0.000	0.415	0.016	0.623	0.242	0.044	0.784
CHUD038_464c_c1	4.72	48.88	41.77	0.06	0.01	0.000	0.151	0.000	0.375	0.047	0.022	0.211
CHUD038_464c_c13	7.66	47.96	38.91	0.11	0.03	0.000	0.536	0.009	0.970	0.599	0.088	0.522
CHUD038_464c_c14	7.17	48.12	40.19	0.09	0.04	0.021	0.440	0.024	0.833	0.486	0.072	0.476
CHUD038_464c_c2	2.19	51.40	43.72	0.03	0.02	0.000	0.078	0.001	0.287	0.042	0.006	0.082
CHUD038_464c_c3	3.42	50.53	43.32	0.04	0.01	0.000	0.076	0.007	0.264	0.085	0.005	0.119
CHUD038_464c_r1	10.97	38.40	35.09	2.80	0.11	0.093	0.266	0.007	0.377	0.344	0.070	0.335
CHUD038_464c_r10	10.14	39.21	34.66	1.82	0.17	0.104	0.380	0.011	0.573	0.464	0.057	0.450
CHUD038_464c_r11	8.73	47.19	38.23	0.11	0.05	0.000	0.574	0.019	0.972	0.730	0.099	0.553
CHUD038_464c_r12	8.36	47.68	39.05	0.10	0.04	0.000	0.532	0.017	0.865	0.639	0.095	0.520
CHUD038_464c_r2	8.74	46.87	38.61	0.15	0.02	0.000	0.540	0.018	0.876	0.663	0.085	0.574
CHUD038_464c_r3	8.94	47.38	39.64	0.41	0.02	0.000	0.533	0.013	0.822	0.593	0.082	0.563
CHUD038_464c_r4	7.39	47.56	40.11	0.13	0.02	0.000	0.461	0.012	0.789	0.511	0.076	0.484

EPMA point name	Bi	Zn	Ni	W	Co	Sn	Te	Se	Ti	Mo	Totals
CHUD038_464b_unk4	0.000	151.037	0.011	0.000	0.066	0.000	0.000	0.006	0.010	0.105	187.88
CHUD038_464b_unk5	0.084	150.295	0.000	0.000	0.047	0.000	0.000	0.008	0.000	0.111	187.13
CHUD038_464b_unk6	0.411	0.013	0.000	0.000	0.064	0.003	0.000	0.010	0.009	0.000	76.87
CHUD038_464b_unk8	0.000	0.234	0.000	0.052	0.002	0.009	0.000	0.042	0.000	0.000	82.07
CHUD038_464b_unk9	0.000	0.845	0.008	0.050	0.021	0.003	0.005	0.005	0.001	0.000	97.78
CHUD038_464b1	0.043	0.000	0.395	0.012	0.146	0.003	0.000	0.002	0.000	0.000	101.06
CHUD038_464b10	0.064	0.000	0.543	0.009	0.274	0.008	0.000	0.029	0.000	0.000	99.94
CHUD038_464b11	0.034	0.000	0.047	0.000	0.123	0.001	0.000	0.000	0.000	0.000	101.16
CHUD038_464b12	0.089	0.596	0.093	0.029	0.058	0.036	0.000	0.003	0.001	0.000	99.25
CHUD038_464b13	0.000	1.064	0.000	0.016	0.049	0.153	0.000	0.013	0.000	0.000	105.70
CHUD038_464b2	0.041	0.009	0.845	0.000	0.133	0.005	0.000	0.006	0.000	0.000	101.18
CHUD038_464b3	0.068	0.011	0.202	0.000	0.156	0.000	0.000	0.000	0.006	0.000	101.72
CHUD038_464b4	0.314	0.003	0.006	0.005	0.057	0.005	0.000	0.003	0.017	0.000	99.69
CHUD038_464b5	0.210	0.051	0.000	0.011	0.067	0.013	0.000	0.019	0.000	0.000	100.40
CHUD038_464b7	0.341	0.038	0.000	0.008	0.061	0.016	0.000	0.017	0.008	0.000	99.70
CHUD038_464c_c1	0.090	0.001	0.009	0.000	0.062	0.000	0.000	0.011	0.000	0.000	96.42
CHUD038_464c_c13	0.241	0.003	0.007	0.014	0.067	0.005	0.000	0.000	0.000	0.000	97.72
CHUD038_464c_c14	0.253	0.000	0.009	0.004	0.056	0.002	0.000	0.005	0.000	0.000	98.29
CHUD038_464c_c2	0.079	0.011	0.005	0.000	0.068	0.000	0.000	0.009	0.000	0.000	98.03
CHUD038_464c_c3	0.061	0.003	0.000	0.011	0.066	0.000	0.000	0.007	0.000	0.000	98.03
CHUD038_464c_r1	0.089	0.004	0.021	0.000	0.048	0.007	0.000	0.002	0.017	0.000	89.05
CHUD038_464c_r10	0.188	0.000	0.029	0.000	0.047	0.008	0.000	0.006	0.016	0.000	88.33
CHUD038_464c_r11	0.259	0.007	0.000	0.024	0.060	0.002	0.000	0.008	0.000	0.000	97.62
CHUD038_464c_r12	0.244	0.000	0.000	0.000	0.049	0.000	0.000	0.003	0.004	0.000	98.21
CHUD038_464c_r2	0.284	0.002	0.020	0.000	0.060	0.003	0.000	0.004	0.000	0.000	97.51
CHUD038_464c_r3	0.234	0.000	0.009	0.000	0.053	0.001	0.000	0.000	0.012	0.000	99.30
CHUD038_464c_r4	0.266	0.000	0.001	0.006	0.062	0.000	0.000	0.005	0.000	0.000	97.89

EPMA point name	As	S	Fe	Si	Ca	Au	Hg	Ag	Pb	Tl	Sb	Cu
CHUD038_464c_r5	9.51	46.95	38.80	0.04	0.01	0.000	0.387	0.004	0.788	0.524	0.079	0.412
CHUD038_464c_r6	8.99	47.44	39.17	0.03	0.01	0.000	0.521	0.013	0.992	0.668	0.082	0.493
CHUD038_464c_r7	8.65	47.66	38.27	0.05	0.01	0.000	0.500	0.015	0.962	0.636	0.088	0.472
CHUD038_464c_r8	8.49	47.05	39.17	0.08	0.01	0.000	0.511	0.015	0.865	0.611	0.078	0.498
CHUD038_464c_r9	9.47	40.50	34.81	1.80	0.12	0.077	0.511	0.007	0.738	0.571	0.085	0.520
CHUD038_464c1	7.10	47.55	39.42	0.25	0.05	0.000	0.075	0.000	0.204	0.029	0.006	0.078
CHUD038_464c10	0.32	53.67	45.75	0.09	0.14	0.000	0.019	0.002	0.190	0.006	0.104	0.010
CHUD038_464c11	9.54	31.81	33.41	1.88	0.41	0.036	0.297	0.011	0.387	0.317	0.046	0.366
CHUD038_464c12	15.33	38.30	35.98	3.41	0.28	0.099	0.191	0.002	0.177	0.078	0.054	0.229
CHUD038_464c13	7.18	45.08	41.21	0.04	0.18	0.122	0.214	0.010	0.265	0.269	0.083	0.115
CHUD038_464c14	6.79	44.32	42.11	0.04	0.08	0.093	0.137	0.000	0.242	0.108	0.090	0.100
CHUD038_464c15	15.56	35.41	34.75	0.29	0.58	0.080	0.225	0.002	0.188	0.169	0.040	0.268
CHUD038_464c16	0.01	54.20	46.54	0.03	0.02	0.000	0.049	0.007	0.237	0.083	0.000	0.124
CHUD038_464c17	9.06	47.33	38.91	0.05	0.06	0.000	0.585	0.020	0.927	0.726	0.092	0.531
CHUD038_464c2	5.66	49.54	43.64	0.19	0.06	0.030	0.202	0.002	0.291	0.250	0.022	0.268
CHUD038_464c2_c1	0.01	53.85	46.02	0.04	0.10	0.000	0.017	0.005	0.154	0.000	0.000	0.000
CHUD038_464c2_r1	8.52	45.05	37.35	0.25	0.09	0.043	0.549	0.019	0.898	0.544	0.090	0.540
CHUD038_464c2_r2	7.72	45.36	37.57	0.22	0.11	0.041	0.500	0.007	0.840	0.607	0.072	0.490
CHUD038_464c3	12.39	41.40	38.02	0.93	0.15	0.070	0.290	0.010	0.386	0.383	0.033	0.351
CHUD038_464c4	3.60	50.27	44.29	0.12	0.18	0.000	0.020	0.007	0.152	0.012	0.000	0.041
CHUD038_464c5	12.40	44.86	40.35	0.33	0.07	0.025	0.196	0.001	0.226	0.246	0.019	0.112
CHUD038_464c6	7.62	46.73	41.84	0.06	0.02	0.003	0.126	0.003	0.276	0.059	0.278	0.098
CHUD038_464c7	12.59	43.05	39.85	0.12	0.18	0.046	0.129	0.000	0.215	0.086	0.045	0.147
CHUD038_464c8	0.92	53.14	44.99	0.09	0.05	0.000	0.062	0.002	0.148	0.110	0.065	0.086
CHUD038_464c9	1.05	53.49	45.22	0.12	0.06	0.000	0.091	0.004	0.252	0.064	0.086	0.193
CHUD038_464d1	4.61	45.13	38.46	0.04	0.39	0.000	0.357	0.019	0.951	0.245	0.047	0.478
CHUD038_464d2	4.10	47.16	41.56	0.03	0.30	0.000	0.285	0.017	0.745	0.138	0.032	0.369

EPMA point name	Bi	Zn	Ni	W	Co	Sn	Te	Se	Ti	Mo	Totals
CHUD038_464c_r5	0.265	0.000	0.005	0.003	0.060	0.000	0.000	0.004	0.008	0.000	97.85
CHUD038_464c_r6	0.338	0.000	0.000	0.000	0.064	0.003	0.000	0.000	0.000	0.000	98.82
CHUD038_464c_r7	0.300	0.009	0.000	0.000	0.064	0.002	0.000	0.000	0.015	0.000	97.70
CHUD038_464c_r8	0.277	0.011	0.000	0.000	0.061	0.001	0.000	0.003	0.002	0.000	97.74
CHUD038_464c_r9	0.201	0.000	0.037	0.000	0.067	0.000	0.000	0.000	0.004	0.000	89.51
CHUD038_464c1	0.047	0.006	0.000	0.162	0.062	0.011	0.000	0.002	0.006	0.000	95.05
CHUD038_464c10	0.032	0.000	0.009	0.027	0.072	0.000	0.000	0.007	0.015	0.000	100.47
CHUD038_464c11	0.151	0.000	0.007	0.000	0.052	0.000	0.000	0.002	0.000	0.000	78.73
CHUD038_464c12	0.000	0.000	0.000	0.103	0.054	0.012	0.000	0.000	0.029	0.000	94.33
CHUD038_464c13	0.072	0.000	0.000	1.271	0.064	0.004	0.000	0.031	0.008	0.000	96.22
CHUD038_464c14	0.059	0.000	0.006	1.015	0.068	0.006	0.000	0.020	0.000	0.000	95.28
CHUD038_464c15	0.000	0.000	0.004	0.052	0.058	0.000	0.000	0.000	0.004	0.000	87.67
CHUD038_464c16	0.023	0.000	0.024	0.000	0.067	0.006	0.000	0.014	0.014	0.000	101.46
CHUD038_464c17	0.276	0.005	0.000	0.000	0.054	0.001	0.000	0.001	0.002	0.000	98.63
CHUD038_464c2	0.105	0.000	0.000	0.051	0.064	0.000	0.000	0.001	0.011	0.000	100.37
CHUD038_464c2_c1	0.012	0.008	0.535	0.000	0.128	0.004	0.000	0.001	0.006	0.000	100.90
CHUD038_464c2_r1	0.250	0.000	0.058	0.010	0.063	0.007	0.000	0.000	0.010	0.000	94.34
CHUD038_464c2_r2	0.255	0.002	0.068	0.000	0.071	0.002	0.000	0.006	0.027	0.000	93.97
CHUD038_464c3	0.095	0.001	0.014	0.000	0.052	0.001	0.000	0.002	0.006	0.000	94.59
CHUD038_464c4	0.053	0.005	0.000	0.035	0.056	0.007	0.000	0.000	0.007	0.000	98.86
CHUD038_464c5	0.008	0.000	0.005	0.000	0.050	0.004	0.000	0.004	0.002	0.000	98.91
CHUD038_464c6	0.102	0.000	0.000	0.500	0.066	0.004	0.000	0.012	0.000	0.000	97.80
CHUD038_464c7	0.000	0.006	0.014	0.297	0.052	0.000	0.000	0.003	0.008	0.000	96.84
CHUD038_464c8	0.000	0.002	0.000	0.011	0.069	0.044	0.000	0.000	0.011	0.000	99.80
CHUD038_464c9	0.029	0.006	0.003	0.000	0.069	0.176	0.000	0.000	0.007	0.000	100.92
CHUD038_464d1	0.386	0.431	0.018	0.098	0.078	0.007	0.000	0.007	0.004	0.000	91.75
CHUD038_464d2	0.250	0.600	0.010	0.058	0.083	0.016	0.000	0.012	0.000	0.000	95.76

EPMA point name	As	S	Fe	Si	Ca	Au	Hg	Ag	Pb	Tl	Sb	Cu
CHUD038_464d3	2.16	52.31	45.20	0.02	0.00	0.000	0.096	0.000	0.202	0.081	0.000	0.889
CHUD038_464d4	2.04	51.54	43.60	0.02	0.00	0.000	5.678	0.014	0.145	0.062	0.004	4.172
CHUD038_464e_unk1	0.00	27.24	9.55	0.00	0.01	0.559	0.029	0.000	0.101	0.000	0.000	0.508
CHUD038_464e_unk2	10.24	24.45	0.37	0.05	0.00	0.000	38.662	0.094	0.000	0.000	0.157	24.850
CHUD038_464e1	3.01	51.74	43.81	0.02	0.00	0.000	0.231	0.014	0.393	0.183	0.030	0.618
CHUD038_464e2	2.23	52.35	44.03	0.01	0.01	0.000	0.236	0.026	0.415	0.175	0.008	0.669
CHUD038_464f_unk1	3.81	26.41	31.07	2.06	0.05	0.000	0.305	0.009	0.483	0.260	0.044	0.577
CHUD038_464f1	1.41	52.77	45.57	0.01	0.00	0.000	0.186	0.009	0.327	0.184	0.005	0.220
CHUD038_464f2	4.70	50.23	44.14	0.01	0.00	0.000	0.059	0.005	0.248	0.066	0.011	0.351
CHUD038_464f3	3.54	51.15	43.93	0.02	0.00	0.000	0.286	0.018	0.448	0.280	0.034	0.581
CHUD038_464f4	2.28	51.85	45.15	0.01	0.00	0.000	0.150	0.015	0.372	0.148	0.029	0.290
CHUD038_464f5	1.89	52.32	45.15	0.01	0.00	0.000	0.155	0.010	0.362	0.151	0.015	0.262
CHUD038_464f6	1.74	52.71	45.46	0.03	0.00	0.000	0.170	0.001	0.333	0.162	0.021	0.244
CHUD043_376.5a_1	2.54	0.01	49.41	3.31	0.37	0.000	0.381	0.009	0.035	0.000	0.316	0.133
CHUD043_376.5a_2	2.59	0.01	48.48	3.92	0.42	0.000	0.427	0.006	0.030	0.000	0.253	0.165
CHUD043_376.5a_3	2.41	0.01	51.54	3.29	0.41	0.000	0.284	0.000	0.029	0.000	0.344	0.159
CHUD043_376.5a_4	2.89	0.01	53.27	0.90	0.47	0.000	0.372	0.001	0.035	0.000	0.228	0.172
CHUD043_376.5a_r1	2.26	0.03	39.31	10.70	0.30	0.000	0.162	0.004	0.052	0.004	0.271	0.126
CHUD043_376.5a_unk1	2.78	0.03	45.93	3.85	0.60	0.000	0.250	0.006	0.064	0.021	0.266	0.157
CHUD043_376.5a_unk2	1.72	0.03	45.39	4.44	0.35	0.190	0.210	0.004	0.063	0.009	0.251	0.120
CHUD043_376.5b_unk1	1.70	0.01	45.13	3.47	0.19	0.000	0.334	0.000	0.051	0.000	0.300	0.060
CHUD043_376.5b_unk2	1.97	0.01	46.38	3.25	0.19	0.000	0.300	0.009	0.045	0.021	0.330	0.054
CHUD043_376.5b_unk3	1.53	0.00	37.38	6.87	0.15	0.000	0.255	0.004	0.032	0.000	0.238	0.042
CHUD043_376.5b_unk4	1.56	0.01	40.21	9.87	0.17	0.051	0.356	0.004	0.061	0.007	0.192	0.041
CHUD043_376.5b_unk5	1.16	0.01	38.05	15.87	0.14	0.000	0.214	0.002	0.046	0.000	0.250	0.050
CHUD043_376.5b_unk6	5.23	0.03	23.55	10.91	0.89	0.045	0.188	0.000	0.027	0.000	0.233	0.029
CHUD046_238a_Au1	0.06	0.04	0.39	0.17	0.05	95.137	3.613	0.375	0.000	0.400	0.011	0.117

EPMA point name	Bi	Zn	Ni	W	Co	Sn	Te	Se	Ti	Mo	Totals
CHUD038_464d3	0.038	0.029	0.006	0.000	0.067	0.004	0.000	0.014	0.018	0.000	101.13
CHUD038_464d4	0.000	0.318	0.000	0.000	0.054	0.029	0.000	0.020	0.000	0.000	107.69
CHUD038_464e_unk1	0.078	142.038	0.008	0.000	0.046	0.000	0.000	0.033	0.010	0.114	180.32
CHUD038_464e_unk2	0.000	1.133	0.001	0.000	0.037	0.000	0.000	0.000	0.000	0.000	100.04
CHUD038_464e1	0.099	0.051	0.039	0.010	0.065	0.022	0.000	0.025	0.009	0.000	100.37
CHUD038_464e2	0.143	0.013	0.042	0.009	0.063	0.018	0.000	0.029	0.003	0.000	100.47
CHUD038_464f_unk1	0.191	0.004	0.000	0.000	0.051	0.011	0.000	0.002	0.016	0.000	65.35
CHUD038_464f1	0.130	0.011	0.000	0.009	0.077	0.015	0.000	0.029	0.000	0.000	100.97
CHUD038_464f2	0.098	0.011	0.000	0.000	0.076	0.000	0.000	0.003	0.002	0.000	100.02
CHUD038_464f3	0.171	0.009	0.000	0.000	0.067	0.007	0.000	0.012	0.000	0.000	100.55
CHUD038_464f4	0.171	0.003	0.000	0.028	0.070	0.017	0.000	0.011	0.000	0.000	100.60
CHUD038_464f5	0.169	0.005	0.000	0.009	0.057	0.018	0.000	0.014	0.000	0.000	100.60
CHUD038_464f6	0.159	0.000	0.000	0.019	0.071	0.021	0.000	0.023	0.002	0.000	101.16
CHUD043_376.5a_1	0.000	0.066	0.120	0.000	0.077	0.013	0.000	0.001	0.079	0.022	56.89
CHUD043_376.5a_2	0.012	0.087	0.109	0.000	0.076	0.013	0.000	0.000	0.079	0.022	56.70
CHUD043_376.5a_3	0.000	0.071	0.137	0.000	0.081	0.019	0.000	0.003	0.106	0.024	58.93
CHUD043_376.5a_4	0.035	0.075	0.130	0.000	0.106	0.005	0.000	0.000	0.059	0.038	58.79
CHUD043_376.5a_r1	0.024	0.047	0.131	0.000	0.078	0.005	0.000	0.000	0.090	0.031	53.62
CHUD043_376.5a_unk1	0.018	0.067	0.138	0.000	0.084	0.014	0.000	0.001	0.102	0.031	54.41
CHUD043_376.5a_unk2	0.011	0.057	0.127	0.000	0.085	0.012	0.000	0.003	0.105	0.022	53.20
CHUD043_376.5b_unk1	0.000	0.068	0.069	0.000	0.073	0.012	0.000	0.000	0.087	0.048	51.61
CHUD043_376.5b_unk2	0.014	0.070	0.081	0.000	0.084	0.018	0.000	0.002	0.103	0.037	52.97
CHUD043_376.5b_unk3	0.000	0.053	0.057	0.000	0.055	0.007	0.000	0.002	0.064	0.034	46.77
CHUD043_376.5b_unk4	0.000	0.057	0.059	0.000	0.062	0.010	0.000	0.002	0.061	0.009	52.80
CHUD043_376.5b_unk5	0.024	0.037	0.049	0.000	0.077	0.011	0.000	0.001	0.080	0.022	56.10
CHUD043_376.5b_unk6	0.000	0.066	0.061	0.000	0.036	0.000	0.000	0.000	0.085	0.030	41.40
CHUD046_238a_Au1	0.000	0.000	0.000	0.000	0.000	0.000	0.000	0.002	0.007	0.000	100.38

EPMA point name	As	S	Fe	Si	Ca	Au	Hg	Ag	Pb	Tl	Sb	Cu
CHUE019_485.5a1_c	0.06	52.45	44.83	0.42	0.26	0.000	0.013	0.000	0.152	0.023	0.000	0.013
CHUE019_485.5a1_r	11.61	44.72	39.73	0.07	0.71	0.152	0.248	0.018	0.093	0.382	0.003	0.346
CHUE019_485.5a2	0.10	53.53	46.45	0.02	0.07	0.000	0.000	0.001	0.148	0.007	0.000	0.000
CHUE019_485.5b1_c	1.25	52.84	44.92	0.10	0.02	0.000	0.061	0.000	0.144	0.080	0.021	0.249
CHUE019_485.5b1_r	10.77	45.30	40.40	0.36	0.08	0.169	0.264	0.017	0.120	0.331	0.023	0.330
CHUE019_485.5b2_r	10.04	41.95	36.94	1.76	0.15	0.102	0.370	0.014	0.093	0.295	0.029	0.261
CHUE019_485.5b3_c	6.65	47.41	39.86	0.09	0.03	0.072	0.207	0.013	0.147	0.212	0.020	0.459
CHUE019_485.5b3_r1	10.02	44.46	38.89	0.17	0.13	0.186	0.423	0.034	0.130	0.515	0.015	0.593
CHUE019_485.5b3_r2	10.05	45.10	40.14	0.17	0.08	0.206	0.356	0.025	0.134	0.413	0.022	0.489
CHUE019_485.5b3_r3	10.40	45.40	40.49	0.13	0.02	0.222	0.347	0.022	0.111	0.488	0.031	0.482
CHUE019_485.5b3_r4	9.96	45.16	38.29	0.19	0.04	0.191	0.371	0.032	0.124	0.505	0.040	0.512
CHUE019_485.5b4	9.41	43.53	37.74	1.26	0.02	0.185	0.408	0.028	0.155	0.538	0.034	0.551
CHUE019_485.5d_c1	1.48	52.21	45.65	0.05	0.01	0.000	0.034	0.001	0.123	0.045	0.013	0.055
CHUE019_485.5d_c2	0.64	52.64	45.00	0.03	0.00	0.000	0.014	0.002	0.144	0.017	0.011	0.042
CHUE019_485.5d_c3	2.03	52.14	45.16	0.04	0.01	0.000	0.028	0.007	0.128	0.053	0.013	0.059
CHUE019_485.5d_c4	2.43	50.67	45.11	0.30	0.00	0.000	0.059	0.005	0.136	0.047	0.032	0.102
CHUE019_485.5d_c5	0.75	52.94	46.18	0.03	0.01	0.000	0.011	0.000	0.145	0.022	0.000	0.046
CHUE019_485.5d_r1	7.99	38.16	34.17	0.10	1.01	0.110	0.225	0.011	0.091	0.323	0.020	0.325
CHUE019_485.5d_r2	10.19	43.37	38.81	0.28	0.95	0.097	0.210	0.011	0.090	0.269	0.015	0.260
CHUE019_485.5d_r3	10.52	45.27	40.44	0.17	0.03	0.193	0.318	0.022	0.129	0.472	0.025	0.410
CHUE019_485.5d_r4	9.75	45.39	39.48	0.31	0.16	0.169	0.395	0.029	0.141	0.511	0.024	0.559
CHUE019_485.5d_r5	10.97	44.75	40.64	0.12	0.08	0.212	0.314	0.031	0.114	0.419	0.026	0.444
CHUE019_485.5d_r6	9.29	42.54	38.12	0.56	0.53	0.165	0.295	0.018	0.143	0.366	0.010	0.391
CHUE019_485.5d2	9.50	46.16	39.96	0.07	0.63	0.185	0.344	0.018	0.167	0.420	0.033	0.504
CHUE019_485.5d3	8.81	45.66	40.52	0.05	0.03	0.171	0.356	0.026	0.125	0.517	0.029	0.504
CHUE019_485.5d4_c1	1.64	51.67	44.46	0.04	0.00	0.000	0.025	0.006	0.127	0.009	0.008	0.038
CHUE019_485.5d4_c2	1.47	51.89	45.43	0.05	0.01	0.000	0.030	0.005	0.109	0.068	0.020	0.063

EPMA point name	Bi	Zn	Ni	W	Co	Sn	Te	Se	Ti	Mo	Totals
CHUE019_485.5a1_c	0.003	0.000	0.016	0.000	0.073	0.003	0.000	0.001	0.005	0.000	98.32
CHUE019_485.5a1_r	0.000	0.000	0.129	0.005	0.071	0.005	0.000	0.000	0.006	0.000	98.30
CHUE019_485.5a2	0.000	0.003	0.000	0.003	0.071	0.002	0.000	0.072	0.000	0.000	100.48
CHUE019_485.5b1_c	0.035	0.000	0.038	0.000	0.062	0.201	0.000	0.000	0.005	0.000	100.02
CHUE019_485.5b1_r	0.026	0.000	0.018	0.000	0.060	0.001	0.000	0.001	0.097	0.000	98.37
CHUE019_485.5b2_r	0.064	0.000	0.030	0.000	0.056	0.006	0.000	0.001	0.043	0.000	92.21
CHUE019_485.5b3_c	0.095	0.000	0.054	0.000	0.067	0.102	0.000	0.001	0.005	0.000	95.49
CHUE019_485.5b3_r1	0.143	0.000	0.202	0.000	0.099	0.000	0.000	0.012	0.005	0.000	96.02
CHUE019_485.5b3_r2	0.087	0.006	0.009	0.000	0.062	0.002	0.000	0.005	0.000	0.000	97.37
CHUE019_485.5b3_r3	0.082	0.008	0.009	0.008	0.069	0.000	0.000	0.004	0.001	0.000	98.33
CHUE019_485.5b3_r4	0.083	0.000	0.021	0.002	0.069	0.000	0.000	0.003	0.052	0.000	95.64
CHUE019_485.5b4	0.120	0.000	0.081	0.000	0.068	0.000	0.000	0.003	0.590	0.000	94.72
CHUE019_485.5d_c1	0.025	0.011	0.000	0.020	0.059	0.018	0.000	0.001	0.023	0.000	99.83
CHUE019_485.5d_c2	0.054	0.003	0.000	0.001	0.066	0.010	0.000	0.000	0.043	0.000	98.73
CHUE019_485.5d_c3	0.065	0.000	0.000	0.019	0.066	0.006	0.000	0.000	0.036	0.000	99.87
CHUE019_485.5d_c4	0.037	0.000	0.000	0.000	0.068	0.030	0.000	0.001	0.185	0.000	99.21
CHUE019_485.5d_c5	0.002	0.000	0.002	0.034	0.078	0.006	0.000	0.000	0.028	0.000	100.28
CHUE019_485.5d_r1	0.109	0.022	0.006	0.031	0.048	0.000	0.000	0.005	6.381	0.000	89.14
CHUE019_485.5d_r2	0.056	0.022	0.000	0.000	0.070	0.000	0.000	0.001	0.111	0.000	94.81
CHUE019_485.5d_r3	0.109	0.000	0.006	0.000	0.053	0.000	0.000	0.000	0.070	0.000	98.23
CHUE019_485.5d_r4	0.177	0.000	0.000	0.000	0.051	0.000	0.000	0.004	0.117	0.000	97.27
CHUE019_485.5d_r5	0.035	0.000	0.003	0.003	0.070	0.008	0.000	0.005	0.016	0.000	98.26
CHUE019_485.5d_r6	0.063	0.009	0.001	0.000	0.050	0.000	0.000	0.000	1.051	0.000	93.61
CHUE019_485.5d2	0.072	0.000	0.361	0.017	0.110	0.000	0.000	0.000	0.141	0.000	98.68
CHUE019_485.5d3	0.107	0.000	0.164	0.000	0.085	0.000	0.000	0.003	0.059	0.000	97.22
CHUE019_485.5d4_c1	0.081	0.000	0.000	0.005	0.066	0.010	0.000	0.004	0.000	0.000	98.19
CHUE019_485.5d4_c2	0.017	0.022	0.000	0.000	0.055	0.022	0.000	0.006	0.000	0.000	99.26

EPMA point name	As	S	Fe	Si	Ca	Au	Hg	Ag	Pb	Tl	Sb	Cu
CHUE019_485.5d4_r	11.12	44.76	39.71	0.15	0.02	0.178	0.372	0.024	0.125	0.544	0.033	0.578
CHUE019_485.5f_c	1.12	51.67	44.21	0.48	0.15	0.000	0.062	0.003	0.134	0.117	0.000	0.049
CHUE019_485.5f_r1	2.63	48.98	42.40	0.76	0.25	0.000	0.104	0.008	0.138	0.137	0.013	0.063
CHUE019_485.5f_r2	2.98	47.65	40.16	1.10	0.29	0.000	0.161	0.015	0.142	0.185	0.010	0.142
CHUE019_485.5f_r3	8.63	45.26	39.45	0.27	0.41	0.111	0.323	0.028	0.184	0.356	0.022	0.339
CHUE019_485.5f_r4	8.76	45.78	39.59	0.67	0.10	0.064	0.271	0.025	0.146	0.324	0.026	0.268
CHUE019_485.5f2_c1	2.81	49.96	43.30	0.66	0.09	0.000	0.057	0.000	0.120	0.127	0.003	0.040
CHUE019_485.5f2_c2	0.59	51.12	43.22	0.76	0.08	0.000	0.061	0.005	0.148	0.046	0.008	0.042
CHUE019_485.5f2_c3	1.13	50.34	42.61	0.96	0.14	0.000	0.079	0.004	0.142	0.143	0.000	0.050
CHUE019_485.5f2_r1	9.08	43.74	38.27	2.87	0.60	0.153	0.303	0.029	0.168	0.331	0.022	0.389
CHUE019_485.5f2_r2	7.81	43.23	37.90	0.20	2.21	0.068	0.302	0.026	0.136	0.305	0.000	0.264
CHUE019_485.5f3_c	0.10	53.40	44.08	0.01	0.01	0.000	0.005	0.000	0.132	0.000	0.000	0.009
CHUE019_485.5g_c1	0.02	53.65	46.05	0.03	0.02	0.000	0.006	0.000	0.167	0.013	0.000	0.003
CHUE019_485.5g_c2	2.04	51.12	44.11	0.03	0.02	0.046	0.166	0.017	0.147	0.169	0.009	0.255
CHUE019_485.5g_c3	0.53	53.03	46.31	0.01	0.00	0.000	0.001	0.001	0.141	0.014	0.000	0.011
CHUE019_485.5g_r1	8.22	46.82	41.32	0.22	0.02	0.068	0.430	0.020	0.158	0.440	0.036	0.377
CHUE019_485.5g_r2	9.01	41.86	37.46	2.91	0.05	0.075	0.340	0.022	0.115	0.378	0.025	0.362
CHUE019_485.5g_r3	9.16	43.27	38.72	1.43	0.04	0.048	0.335	0.018	0.121	0.302	0.022	0.294
CHUE019_485.5g2	9.14	45.22	40.31	0.96	0.13	0.056	0.322	0.011	0.106	0.376	0.041	0.296
CHUE019_485.5g4	0.18	12.38	1.39	11.83	14.33	0.000	0.004	0.002	0.014	0.002	0.000	0.003
CHUE019_485.5g5	0.23	9.77	1.84	10.33	13.85	0.000	0.011	0.000	0.005	0.016	0.000	0.000
CHUE215_246.5c_1	7.23	46.33	41.54	0.05	0.05	0.052	0.203	0.050	0.131	0.137	0.082	0.189
CHUE215_246.5c_2	7.33	42.50	40.75	0.33	0.21	0.088	0.153	0.052	0.132	0.108	0.079	0.179
CHUE215_246.5c_c1	2.03	21.48	37.14	0.77	0.67	0.349	0.179	0.102	0.151	0.116	0.059	0.316
CHUE215_246.5c_c2	6.02	32.77	31.09	2.94	4.86	0.077	0.113	0.047	0.105	0.061	0.000	0.148
CHUE215_246.5c_c3	7.52	36.98	36.19	6.85	0.69	0.000	0.050	0.019	0.034	0.037	0.047	0.062
CHUE215_246.5c_r1	4.59	34.87	33.08	4.19	1.31	0.238	0.173	0.079	0.117	0.122	0.049	0.221

EPMA point name	Bi	Zn	Ni	W	Co	Sn	Te	Se	Ti	Mo	Totals
CHUE019_485.5d4_r	0.121	0.000	0.013	0.004	0.064	0.011	0.000	0.003	0.000	0.000	97.84
CHUE019_485.5f_c	0.055	0.000	0.004	0.000	0.058	0.002	0.000	0.000	0.004	0.000	98.12
CHUE019_485.5f_r1	0.040	0.008	0.000	0.000	0.082	0.007	0.000	0.000	0.000	0.000	95.61
CHUE019_485.5f_r2	0.093	0.004	0.003	0.000	0.064	0.000	0.000	0.001	0.000	0.000	93.00
CHUE019_485.5f_r3	0.064	0.001	0.013	0.000	0.071	0.002	0.000	0.006	0.009	0.000	95.54
CHUE019_485.5f_r4	0.055	0.013	0.000	0.000	0.065	0.001	0.000	0.000	0.000	0.000	96.16
CHUE019_485.5f2_c1	0.033	0.000	0.000	0.000	0.071	0.000	0.000	0.004	0.007	0.000	97.27
CHUE019_485.5f2_c2	0.049	0.021	0.000	0.000	0.071	0.001	0.000	0.000	0.003	0.000	96.23
CHUE019_485.5f2_c3	0.074	0.000	0.007	0.000	0.066	0.000	0.000	0.004	0.000	0.000	95.75
CHUE019_485.5f2_r1	0.177	0.004	0.006	0.000	0.039	0.003	0.000	0.002	0.010	0.000	96.20
CHUE019_485.5f2_r2	0.077	0.010	0.000	0.000	0.063	0.002	0.000	0.001	0.000	0.000	92.61
CHUE019_485.5f3_c	0.044	0.001	0.000	0.004	0.068	0.000	0.000	0.151	0.000	0.000	98.01
CHUE019_485.5g_c1	0.043	0.002	0.057	0.000	0.085	0.000	0.000	0.000	0.000	0.000	100.15
CHUE019_485.5g_c2	0.069	0.005	0.052	0.013	0.069	0.002	0.000	0.003	0.001	0.005	98.35
CHUE019_485.5g_c3	0.033	0.000	0.000	0.015	0.070	0.000	0.000	0.002	0.000	0.000	100.17
CHUE019_485.5g_r1	0.224	0.005	0.013	0.000	0.064	0.001	0.000	0.005	0.007	0.000	98.45
CHUE019_485.5g_r2	0.155	0.000	0.007	0.000	0.045	0.000	0.000	0.007	0.203	0.000	93.03
CHUE019_485.5g_r3	0.202	0.000	0.000	0.000	0.056	0.001	0.000	0.005	0.000	0.000	94.02
CHUE019_485.5g2	0.097	0.000	0.000	0.000	0.046	0.000	0.000	0.006	0.000	0.000	97.12
CHUE019_485.5g4	0.021	0.008	0.000	0.000	0.010	0.002	0.000	0.000	0.002	0.000	40.18
CHUE019_485.5g5	0.077	0.028	0.000	0.000	0.004	0.002	0.000	0.000	0.009	0.011	36.19
CHUE215_246.5c_1	0.000	0.000	0.231	0.005	0.070	0.004	0.002	0.009	0.010	0.000	96.37
CHUE215_246.5c_2	0.000	0.000	0.240	0.000	0.078	0.001	0.000	0.000	0.006	0.000	92.24
CHUE215_246.5c_c1	0.000	0.000	1.434	0.000	0.096	0.000	0.000	0.004	0.008	0.000	64.90
CHUE215_246.5c_c2	0.000	0.002	0.425	0.000	0.040	0.000	0.000	0.000	0.000	0.000	78.68
CHUE215_246.5c_c3	0.007	0.002	0.097	0.000	0.027	0.000	0.000	0.000	0.006	0.000	88.60
CHUE215_246.5c_r1	0.000	0.005	0.903	0.000	0.062	0.012	0.000	0.000	0.000	0.000	80.03

EPMA point name	As	S	Fe	Si	Ca	Au	Hg	Ag	Pb	Tl	Sb	Cu
CHUE215_246.5c_r2	6.60	35.79	36.08	0.75	0.90	0.328	0.149	0.070	0.090	0.123	0.002	0.302
CHUE215_246.5c_r3	1.60	11.88	16.37	13.69	0.17	0.000	0.028	0.007	0.033	0.025	0.134	0.039
CHUE215_246.5d_c1	0.00	53.84	46.33	0.02	0.01	0.000	0.000	0.003	0.154	0.000	0.000	0.000
CHUE215_246.5d_c2	0.00	54.94	47.86	0.02	0.01	0.000	0.003	0.000	0.130	0.017	0.008	0.000
CHUE215_246.5d_r1	0.26	51.89	44.27	0.44	0.04	0.000	0.018	0.017	0.143	0.000	0.000	0.000
CHUE215_246.5d_r2	0.17	49.93	42.57	1.02	0.07	0.000	0.019	0.007	0.141	0.026	0.024	0.000
CHUE215_246.5d_r3	2.08	48.27	43.03	0.78	0.21	0.000	0.093	0.028	0.118	0.118	0.035	0.128
CHUE215_246.5d_r4	0.09	52.77	45.54	0.28	0.08	0.000	0.012	0.012	0.151	0.000	0.009	0.001
CHUE215_246.5e_unk1	0.00	0.57	0.00	37.96	0.29	0.000	0.000	0.000	0.000	0.001	0.000	0.000
CHUE215_246.5e_unk2	0.10	0.31	0.32	2.16	18.65	0.000	0.000	0.004	0.000	0.000	0.000	0.013
CHUE215_246.5f_c1	0.00	54.15	46.55	0.02	0.02	0.000	0.000	0.001	0.141	0.000	0.000	0.009
CHUE215_246.5f_r1	5.91	48.96	42.01	0.04	0.49	0.000	0.264	0.025	0.049	0.302	0.041	0.242
CHUE215_246.5f_r2	7.37	46.53	42.25	0.03	0.23	0.030	0.163	0.025	0.094	0.167	0.037	0.189
CHUE215_262.5b_unk1	0.00	27.91	2.21	0.01	0.65	0.000	0.000	0.003	0.077	0.119	0.000	0.000
CHUE215_262.5b_unk2	0.00	36.47	13.56	0.01	0.78	0.000	0.000	0.003	0.124	0.000	0.000	0.000
CHUE215_262.5b_unk3	0.00	33.72	2.91	0.02	0.53	0.000	0.002	0.001	0.121	0.000	0.000	0.000
CHUE215_262.5b_unk4	0.00	27.90	2.42	0.02	0.73	0.000	0.001	0.000	0.088	0.005	0.000	0.000
DC114_1236.5b_1	2.36	51.83	45.55	0.03	0.02	0.000	0.031	0.000	0.149	0.021	0.014	0.088
DC114_1236.5b_2	2.36	52.18	44.73	0.04	0.02	0.000	0.034	0.001	0.153	0.000	0.009	0.213
DC114_1236.5b_3	16.18	37.84	35.44	2.84	0.03	0.099	0.176	0.011	0.452	0.095	0.227	0.301
DC114_1236.5b_4	11.71	43.78	39.71	0.24	0.04	0.113	0.208	0.003	0.419	0.143	0.220	0.371
DC114_1236.5b_5	19.31	38.62	39.56	0.09	0.01	0.036	0.128	0.003	0.268	0.036	0.119	0.164
DC114_1236.5b_6	15.95	41.06	38.76	0.04	0.09	0.104	0.183	0.002	0.300	0.103	0.158	0.230
DC114_1236.5b_7	14.67	40.87	36.23	0.38	0.10	0.098	0.198	0.009	0.464	0.123	0.259	0.397
DC114_1236.5b_8	2.56	51.90	45.77	0.06	0.07	0.000	0.076	0.000	0.209	0.047	0.067	0.194
DC114_1236.5b_9	10.18	43.85	37.27	0.19	0.28	0.115	0.238	0.000	0.524	0.135	0.264	0.344
DC114_1236.5g_r2	4.21	39.11	49.63	0.64	0.19	0.079	0.006	0.000	0.471	0.018	0.078	0.266

EPMA point name	Bi	Zn	Ni	W	Co	Sn	Te	Se	Ti	Mo	Totals
CHUE215_246.5c_r2	0.000	0.000	1.501	0.000	0.101	0.001	0.007	0.000	0.008	0.000	82.80
CHUE215_246.5c_r3	0.018	0.000	0.083	0.000	0.020	0.006	0.000	0.000	0.012	0.000	44.11
CHUE215_246.5d_c1	0.104	0.000	0.009	0.000	0.069	0.000	0.000	0.017	0.000	0.000	100.56
CHUE215_246.5d_c2	0.024	0.000	0.034	0.000	0.072	0.000	0.000	0.023	0.000	0.000	103.15
CHUE215_246.5d_r1	0.035	0.000	0.505	0.000	0.079	0.006	0.000	0.000	0.009	0.000	97.71
CHUE215_246.5d_r2	0.043	0.008	0.274	0.000	0.074	0.000	0.000	0.000	0.000	0.000	94.38
CHUE215_246.5d_r3	0.043	0.000	0.251	0.000	0.065	0.000	0.000	0.003	0.000	0.000	95.24
CHUE215_246.5d_r4	0.030	0.000	0.200	0.000	0.070	0.000	0.000	0.000	0.000	0.000	99.24
CHUE215_246.5e_unk1	0.032	0.000	0.004	0.000	0.004	0.000	0.000	0.000	0.005	0.049	38.91
CHUE215_246.5e_unk2	0.009	0.007	0.000	0.000	0.003	0.000	0.000	0.000	0.000	0.134	21.70
CHUE215_246.5f_c1	0.039	0.000	0.000	0.000	0.065	0.001	0.000	0.033	0.001	0.000	101.03
CHUE215_246.5f_r1	0.000	0.009	0.074	0.000	0.064	0.005	0.000	0.001	0.002	0.000	98.48
CHUE215_246.5f_r2	0.000	0.000	0.124	0.000	0.058	0.000	0.000	0.005	0.000	0.000	97.31
CHUE215_262.5b_unk1	0.146	0.000	62.040	0.000	0.724	0.000	0.632	0.032	0.000	0.000	94.56
CHUE215_262.5b_unk2	0.021	0.000	32.931	0.000	11.822	0.000	0.322	0.049	0.008	0.000	96.10
CHUE215_262.5b_unk3	0.049	0.000	56.586	0.001	0.961	0.000	0.569	0.047	0.003	0.000	95.52
CHUE215_262.5b_unk4	0.006	0.000	63.776	0.000	0.802	0.000	0.669	0.035	0.000	0.000	96.45
DC114_1236.5b_1	0.000	0.005	0.000	0.013	0.062	0.037	0.000	0.000	0.004	0.000	100.21
DC114_1236.5b_2	0.000	0.000	0.000	0.000	0.069	0.035	0.000	0.005	0.004	0.000	99.85
DC114_1236.5b_3	0.000	0.006	0.000	0.000	0.046	0.000	0.000	0.000	0.013	0.000	93.77
DC114_1236.5b_4	0.029	0.000	0.000	0.000	0.059	0.018	0.000	0.000	0.032	0.000	97.08
DC114_1236.5b_5	0.000	0.000	0.000	0.000	0.053	0.000	0.000	0.000	0.051	0.000	98.45
DC114_1236.5b_6	0.000	0.000	0.000	0.006	0.057	0.011	0.000	0.000	0.009	0.000	97.07
DC114_1236.5b_7	0.031	0.006	0.000	0.000	0.046	0.000	0.000	0.000	0.038	0.000	93.92
DC114_1236.5b_8	0.037	0.000	0.000	0.000	0.058	0.031	0.000	0.002	0.000	0.000	101.09
DC114_1236.5b_9	0.067	0.004	0.000	0.000	0.044	0.002	0.000	0.006	0.006	0.000	93.51
DC114_1236.5g_r2	0.098	0.001	0.004	0.000	0.062	0.000	0.000	0.000	0.018	0.000	94.89

EPMA point name	As	S	Fe	Si	Ca	Au	Hg	Ag	Pb	Tl	Sb	Cu
DC114_1236.5g_r3	10.50	33.80	38.78	1.85	0.32	0.054	0.017	0.005	0.424	0.052	0.101	0.343
DC114_1236.5g_r4	14.59	33.68	31.15	2.48	0.18	0.109	0.192	0.005	0.441	0.113	0.220	0.340
DC114_1236.5g_r5	14.92	40.37	35.73	1.09	0.07	0.123	0.259	0.006	0.482	0.266	0.284	0.430
DC114_1236.5g_r6	17.76	40.96	36.80	0.13	0.12	0.044	0.154	0.000	0.312	0.000	0.280	0.276
DC114_1236.5g_rlgr1	67.42	31.49	0.07	0.04	0.00	0.050	0.006	0.000	0.015	0.000	0.003	0.016
DC114_1236.5g_rlgr2	64.17	31.15	0.39	0.12	0.04	0.000	0.061	0.000	0.085	0.000	0.190	0.102
DC114_1236.5g_rlgr3	67.23	31.94	0.28	0.09	0.04	0.011	0.045	0.000	0.011	0.000	0.040	0.006
DC114_1236.5g_rlgr4	65.61	31.77	0.06	0.06	0.00	0.000	0.001	0.000	0.006	0.000	0.011	0.011
DC114_1236.5g_rlgr5	59.12	33.67	0.03	0.08	0.01	0.019	0.007	0.000	0.003	0.000	0.000	0.042
DC114_1236.5g_rlgr6	59.87	33.11	0.01	0.18	0.03	0.635	0.019	0.005	0.009	0.151	0.000	0.003
DC114_1236.5h_1	3.23	50.54	44.78	0.19	0.02	0.013	0.096	0.004	0.249	0.092	0.092	0.131
DC114_1236.5h_2	6.29	49.54	43.46	0.34	0.01	0.086	0.179	0.001	0.313	0.199	0.168	0.271
DC114_1236.5h_3	9.51	46.24	39.55	0.06	0.02	0.192	0.267	0.006	0.675	0.231	0.323	0.510
DC114_1236.5i2_c1	0.94	53.05	44.66	0.02	0.03	0.000	0.038	0.004	0.137	0.013	0.000	0.022
DC114_1236.5i2_c2	0.71	53.20	45.71	0.02	0.04	0.000	0.028	0.000	0.121	0.038	0.006	0.064
DC114_1236.5i2_c3	0.73	52.40	45.83	0.02	0.03	0.000	0.024	0.000	0.138	0.014	0.006	0.051
DC114_1236.5i2_c4	1.49	53.01	45.11	0.03	0.05	0.000	0.024	0.000	0.125	0.017	0.000	0.063
DC114_1236.5i2_r1	5.73	50.29	43.13	0.07	0.03	0.109	0.168	0.002	0.437	0.164	0.201	0.287
DC114_1236.5i2_r2	3.26	51.97	42.91	0.09	0.05	0.182	0.311	0.003	0.629	0.259	0.362	0.412
DC114_1236.5i2_r3	13.10	45.06	38.24	0.12	0.05	0.230	0.396	0.000	0.766	0.302	0.438	0.530
DC114_1236.5i2_r4	16.17	41.48	35.27	0.13	0.04	0.208	0.396	0.012	0.806	0.263	0.473	0.562
DC114_1236.5i2_r5	13.84	44.03	37.15	0.06	0.06	0.087	0.224	0.008	0.470	0.159	0.251	0.321
DC114_1236.5j1	0.02	53.51	46.33	0.08	0.07	0.000	0.001	0.005	0.168	0.019	0.002	0.000
DC114_1236.5j2	0.01	53.63	46.50	0.06	0.00	0.000	0.009	0.000	0.161	0.005	0.000	0.006
DC114_1236.5j_sph1	0.00	27.05	9.09	0.01	0.04	0.777	0.032	0.000	0.083	0.000	0.000	0.068
DC114_1236.5j_sph2	0.05	26.91	8.60	0.01	0.06	0.793	0.023	0.000	0.104	0.018	0.001	0.038
DC114_1236.5j_sph3	0.00	25.59	8.54	0.08	0.06	0.668	0.007	0.007	0.083	0.000	0.000	0.585

EPMA point name	Bi	Zn	Ni	W	Co	Sn	Te	Se	Ti	Mo	Totals
DC114_1236.5g_r3	0.011	0.001	0.014	0.000	0.053	0.000	0.000	0.000	0.000	0.000	86.33
DC114_1236.5g_r4	0.046	0.000	0.008	0.000	0.046	0.000	0.000	0.000	0.011	0.000	83.61
DC114_1236.5g_r5	0.026	0.020	0.000	0.000	0.052	0.003	0.000	0.000	0.000	0.000	94.13
DC114_1236.5g_r6	0.093	0.000	0.000	0.012	0.033	0.006	0.000	0.000	0.000	0.000	96.98
DC114_1236.5g_rlgr1	0.000	0.012	0.000	0.000	0.000	0.000	0.000	0.000	0.006	0.000	99.13
DC114_1236.5g_rlgr2	0.000	0.007	0.004	0.000	0.007	0.000	0.000	0.000	0.006	0.000	96.33
DC114_1236.5g_rlgr3	0.000	0.421	0.000	0.001	0.004	0.002	0.000	0.000	0.002	0.000	100.13
DC114_1236.5g_rlgr4	0.118	0.018	0.007	0.000	0.000	0.007	0.000	0.000	0.002	0.000	97.68
DC114_1236.5g_rlgr5	0.164	0.002	0.021	0.004	0.000	0.006	0.000	0.000	0.000	0.000	93.19
DC114_1236.5g_rlgr6	0.000	0.156	0.014	0.003	0.001	0.000	0.000	0.000	0.003	0.000	94.19
DC114_1236.5h_1	0.038	0.009	0.000	0.089	0.073	0.002	0.000	0.005	0.006	0.000	99.66
DC114_1236.5h_2	0.000	0.000	0.000	0.000	0.054	0.002	0.000	0.000	0.009	0.000	100.92
DC114_1236.5h_3	0.046	0.018	0.002	0.000	0.058	0.006	0.000	0.006	0.008	0.000	97.72
DC114_1236.5i2_c1	0.051	0.005	0.634	0.000	0.121	0.215	0.000	0.002	0.004	0.000	99.94
DC114_1236.5i2_c2	0.035	0.001	0.110	0.000	0.057	0.188	0.000	0.006	0.005	0.000	100.34
DC114_1236.5i2_c3	0.045	0.000	0.044	0.000	0.061	0.202	0.000	0.000	0.005	0.000	99.59
DC114_1236.5i2_c4	0.033	0.004	0.339	0.012	0.072	0.111	0.000	0.002	0.000	0.000	100.48
DC114_1236.5i2_r1	0.068	0.000	0.128	0.000	0.074	0.073	0.000	0.000	0.001	0.000	100.97
DC114_1236.5i2_r2	0.087	0.000	0.096	0.000	0.059	0.042	0.000	0.004	0.000	0.000	100.72
DC114_1236.5i2_r3	0.080	0.007	0.022	0.000	0.058	0.009	0.000	0.000	0.005	0.000	99.40
DC114_1236.5i2_r4	0.106	0.000	0.090	0.005	0.081	0.007	0.000	0.000	0.008	0.000	96.11
DC114_1236.5i2_r5	0.062	0.000	0.103	0.000	0.076	0.091	0.000	0.003	0.005	0.000	97.00
DC114_1236.5j_marc1	0.019	0.000	0.196	0.000	0.096	0.002	0.000	0.009	0.001	0.000	100.53
DC114_1236.5j_marc2	0.069	0.000	0.081	0.000	0.096	0.000	0.000	0.009	0.000	0.000	100.65
DC114_1236.5j_sph1	0.040	151.493	0.000	0.000	0.014	0.005	0.000	0.029	0.009	0.000	188.75
DC114_1236.5j_sph2	0.077	153.300	0.005	0.000	0.023	0.004	0.000	0.016	0.000	0.000	190.03
DC114_1236.5j_sph3	0.049	129.584	0.000	0.000	0.024	0.009	0.000	0.029	0.000	0.000	165.31

EPMA point name	As	S	Fe	Si	Ca	Au	Hg	Ag	Pb	Tl	Sb	Cu
DC114_1236.5j_sph4	0.01	34.11	7.23	0.01	0.06	0.736	0.038	0.007	0.061	0.000	0.000	0.035
DC114_1236.5j_sph5	0.00	34.91	7.60	0.01	0.07	0.769	0.000	0.004	0.051	0.062	0.011	0.078
DC114_1236.5j_sph6	0.01	34.16	9.31	0.02	0.02	0.747	0.073	0.006	0.070	0.003	0.000	0.462
DC114_1236.5j_sph7	0.00	33.93	7.41	0.00	0.14	0.763	0.009	0.000	0.080	0.020	0.000	0.003
DC114_1236.5j_sph8	0.04	34.08	8.12	0.01	0.03	0.766	0.000	0.000	0.074	0.000	0.000	0.000
DC114_1236.5k_1	0.61	53.58	46.08	0.01	0.01	0.000	0.023	0.000	0.192	0.027	0.003	0.000
DC114_1236.5k_2	3.10	50.54	44.37	0.19	0.05	0.072	0.159	0.004	0.340	0.197	0.162	0.271
DC114_1236.5k_3	11.06	45.65	41.11	0.15	0.05	0.100	0.197	0.004	0.273	0.195	0.157	0.243
DC114_1236.5k_4	0.18	53.98	46.85	0.03	0.01	0.000	0.011	0.001	0.125	0.000	0.000	0.000
DC114_1236.5k_unk1	4.43	38.60	35.55	0.03	0.49	0.000	0.092	0.000	0.267	0.057	0.099	0.175
DC114_1236.5k_unk2	4.66	37.91	35.95	0.07	0.54	0.000	0.095	0.002	0.281	0.073	0.108	0.179
DC114_1236.5k_unk3	4.26	35.39	33.41	0.06	0.47	0.000	0.073	0.003	0.245	0.061	0.087	0.156
DC114_1236.5k2_1	0.03	53.74	44.36	0.10	0.01	0.000	0.000	0.000	0.123	0.000	0.000	0.007
DC114_1236.5k2_2	3.26	51.67	46.16	0.03	0.06	0.000	0.091	0.000	0.226	0.101	0.085	0.333
DC114_1236.5k2_3	14.01	42.57	40.84	0.03	0.11	0.096	0.149	0.004	0.182	0.203	0.097	0.213
DC114_1236.5k2_4	0.31	42.92	36.81	0.02	8.75	0.000	0.006	0.000	0.127	0.000	0.000	0.004
DC114_1236.5k2_5	0.01	53.52	45.85	0.01	0.99	0.000	0.000	0.000	0.133	0.000	0.000	0.000
DC114_1236.5k2_6	11.86	44.30	41.32	0.08	0.05	0.105	0.201	0.008	0.166	0.260	0.091	0.260
DC124_1264a_py1	3.41	49.97	42.95	0.28	0.00	0.000	0.101	0.003	0.335	0.176	0.076	0.000
DC124_1264a_py2	5.16	45.45	39.08	3.03	0.03	0.000	0.180	0.000	0.000	0.595	0.163	0.000
DC124_1264a10	9.71	45.31	39.45	0.70	0.01	0.000	0.096	0.004	0.000	0.198	0.162	0.000
DC124_1264a11	3.76	47.88	43.71	0.65	0.03	0.021	0.022	0.000	0.000	0.034	0.122	0.010
DC124_1264a12	9.63	42.93	33.88	2.08	0.03	0.000	0.503	0.001	1.002	0.483	0.183	0.017
DC124_1264a3	4.12	49.75	43.07	0.30	0.00	0.000	0.265	0.006	0.054	0.808	0.195	0.000
DC124_1264a4	4.66	46.78	38.91	2.61	0.19	0.000	0.344	0.007	0.118	1.190	0.230	0.000
DC124_1264a5	4.60	49.88	41.95	0.61	0.00	0.000	0.429	0.000	0.918	0.733	0.217	0.009
DC124_1264a6	8.26	46.56	39.37	0.86	0.02	0.000	0.689	0.002	0.684	1.063	0.278	0.000

EPMA point name	Bi	Zn	Ni	W	Co	Sn	Te	Se	Ti	Mo	Totals
DC114_1236.5j_sph4	0.048	58.058	0.000	0.001	0.031	0.000	0.000	0.015	0.012	0.000	100.46
DC114_1236.5j_sph5	0.000	59.780	0.002	0.070	0.015	0.005	0.000	0.009	0.068	0.000	103.52
DC114_1236.5j_sph6	0.051	55.670	0.001	0.016	0.023	0.004	0.000	0.006	0.002	0.000	100.65
DC114_1236.5j_sph7	0.034	57.374	0.000	0.021	0.023	0.000	0.000	0.009	0.002	0.000	99.82
DC114_1236.5j_sph8	0.085	57.303	0.000	0.000	0.016	0.008	0.000	0.003	0.007	0.000	100.54
DC114_1236.5k_1	0.055	0.003	0.046	0.014	0.056	0.007	0.000	0.003	0.000	0.000	100.72
DC114_1236.5k_2	0.000	0.000	0.000	0.000	0.062	0.004	0.000	0.001	0.000	0.000	99.52
DC114_1236.5k_3	0.000	0.000	0.013	0.000	0.068	0.000	0.000	0.006	0.000	0.000	99.28
DC114_1236.5k_4	0.000	0.011	0.037	0.000	0.089	0.001	0.000	0.008	0.004	0.000	101.34
DC114_1236.5k_unk1	0.058	0.000	0.002	0.000	0.062	0.000	0.000	0.002	0.000	0.000	79.90
DC114_1236.5k_unk2	0.052	0.000	0.002	0.000	0.058	0.004	0.000	0.000	0.011	0.000	80.00
DC114_1236.5k_unk3	0.047	0.000	0.000	0.014	0.053	0.000	0.000	0.003	0.000	0.000	74.34
DC114_1236.5k2_1	0.004	0.002	0.000	0.000	0.069	0.007	0.000	0.000	0.011	0.000	98.47
DC114_1236.5k2_2	0.026	0.000	0.099	0.000	0.059	0.009	0.000	0.006	0.008	0.000	102.22
DC114_1236.5k2_3	0.000	0.000	0.000	0.000	0.053	0.001	0.000	0.001	0.000	0.000	98.56
DC114_1236.5k2_4	0.031	0.000	0.008	0.000	0.059	0.000	0.000	0.000	0.014	0.000	89.05
DC114_1236.5k2_5	0.028	0.000	0.037	0.007	0.066	0.000	0.000	0.006	0.000	0.000	100.66
DC114_1236.5k2_6	0.000	0.002	0.000	0.000	0.054	0.000	0.000	0.007	0.000	0.000	98.77
DC124_1264a_py1	0.020	0.008	0.005	0.000	0.068	0.004	0.000	0.000	0.010	0.000	97.42
DC124_1264a_py2	0.000	0.000	0.000	0.000	0.029	0.000	0.000	0.000	0.006	0.000	93.72
DC124_1264a10	0.000	0.000	0.000	0.000	0.013	0.001	0.000	0.000	0.000	0.000	95.66
DC124_1264a11	0.000	0.000	0.002	0.000	0.006	0.000	0.000	0.000	0.000	0.000	96.25
DC124_1264a12	0.000	0.000	0.000	0.000	0.085	0.003	0.000	0.007	0.006	0.000	90.84
DC124_1264a3	0.000	0.003	0.009	0.000	0.023	0.007	0.000	0.000	0.000	0.000	98.62
DC124_1264a4	0.000	0.000	0.001	0.000	0.039	0.006	0.000	0.000	0.000	0.000	95.09
DC124_1264a5	0.000	0.000	0.000	0.000	0.099	0.002	0.000	0.008	0.016	0.000	99.48
DC124_1264a6	0.000	0.001	0.000	0.000	0.066	0.005	0.000	0.002	0.000	0.000	97.86

EPMA point name	As	S	Fe	Si	Ca	Au	Hg	Ag	Pb	Tl	Sb	Cu
DC124_1264a7	6.13	27.25	20.39	14.35	0.10	0.000	0.399	0.002	0.150	1.342	0.311	0.000
DC124_1264a8	7.34	36.02	27.56	10.45	0.02	0.000	0.111	0.000	0.000	0.494	0.161	0.000
DC124_1264a9	2.81	50.55	44.30	0.13	0.00	0.000	0.213	0.000	0.929	0.359	0.194	0.018
DC124_1264b_unk1	0.08	0.10	1.17	18.74	1.12	0.000	0.007	0.000	0.004	0.015	0.007	0.007
DC124_1264b_unk2	0.00	0.01	0.09	22.58	0.00	0.000	0.005	0.000	0.006	0.008	0.000	0.000
DC124_1264b_unk3	0.00	0.00	0.06	22.28	0.00	0.000	0.000	0.000	0.000	0.003	0.112	0.007
DC124_1264b_unk4	0.00	0.00	0.05	22.47	0.00	0.008	0.000	0.000	0.004	0.000	0.098	0.000
DC124_1264b1	10.65	45.99	36.32	0.24	0.00	0.000	1.235	0.000	0.968	1.592	1.061	0.000
DC124_1264b2	9.45	45.28	36.57	0.43	0.00	0.000	1.286	0.001	1.225	1.638	1.242	0.003
DC124_1264b2_c1	1.73	52.27	44.50	0.04	0.00	0.000	0.056	0.003	0.058	0.220	0.214	0.000
DC124_1264b2_c2	2.93	51.30	43.78	0.02	0.00	0.000	0.384	0.000	0.000	0.504	0.179	0.007
DC124_1264b2_c3	4.83	49.18	41.75	0.08	0.00	0.000	0.308	0.003	0.000	0.435	0.273	0.000
DC124_1264b2_r1	10.11	46.52	36.49	0.28	0.00	0.000	1.014	0.000	1.057	1.454	0.804	0.000
DC124_1264b2_r2	9.54	45.48	36.78	0.46	0.00	0.000	1.197	0.001	1.164	1.400	1.147	0.000
DC124_1264b2_r3	8.57	48.58	39.57	0.27	0.03	0.000	0.479	0.009	0.000	1.275	0.361	0.000
DC124_1264b2_r4	10.31	45.52	36.32	0.40	0.00	0.000	1.038	0.000	1.035	1.629	0.862	0.000
DC124_1264b3	4.43	49.45	42.51	0.07	0.00	0.000	0.443	0.002	0.000	0.546	0.343	0.012
DC124_1264b4	9.10	45.67	36.85	0.26	0.00	0.000	1.493	0.000	0.455	1.402	0.886	0.005
DC124_1264b5	10.51	46.48	36.00	0.43	0.11	0.000	1.093	0.005	0.488	1.763	0.734	0.000
DC124_1264b6	9.20	45.95	36.96	0.42	0.00	0.000	1.198	0.000	0.590	1.563	0.989	0.000
DC124_1264b7	2.67	51.31	44.44	0.10	0.00	0.000	1.099	0.006	0.000	1.625	0.880	0.001
DC124_1264b8	2.82	51.71	45.17	0.04	0.00	0.000	0.452	0.005	0.000	0.616	0.216	0.000
DC124_1273a_rim	14.99	43.06	39.26	0.14	0.01	0.131	0.548	0.000	0.000	0.870	0.170	0.336
DC124_1273a2	17.04	41.75	37.38	0.25	0.03	0.216	0.561	0.002	0.000	0.860	0.185	0.416
DC124_1273a3	0.02	0.04	0.49	16.26	0.00	0.000	0.000	0.000	0.000	0.009	0.058	0.000
DC124_1273a4	17.81	40.16	37.35	0.25	0.07	0.149	0.513	0.009	0.000	0.847	0.165	0.338
DC124_1273a5	14.50	43.27	37.87	0.50	0.01	0.183	0.419	0.003	0.000	0.661	0.132	0.365

EPMA point name	Bi	Zn	Ni	W	Co	Sn	Te	Se	Ti	Mo	Totals
DC124_1264a7	0.000	0.000	0.000	0.000	0.053	0.001	0.000	0.000	0.000	0.000	70.49
DC124_1264a8	0.000	0.000	0.000	0.000	0.030	0.000	0.000	0.000	0.000	0.000	82.18
DC124_1264a9	0.000	0.001	0.017	0.000	0.147	0.000	0.000	0.000	0.000	0.000	99.67
DC124_1264b_unk1	0.002	0.004	0.006	0.000	0.000	0.003	0.000	0.000	0.020	0.013	21.29
DC124_1264b_unk2	0.001	0.014	0.000	0.000	0.001	0.000	0.000	0.000	0.008	0.000	22.73
DC124_1264b_unk3	0.003	0.000	0.000	0.000	0.002	0.000	0.000	0.000	0.000	0.000	22.48
DC124_1264b_unk4	0.000	0.000	0.002	0.000	0.005	0.000	0.000	0.000	0.000	0.000	22.64
DC124_1264b1	0.000	0.016	0.000	0.000	0.063	0.004	0.000	0.000	0.000	0.000	98.14
DC124_1264b2	0.000	0.000	0.009	0.000	0.048	0.014	0.000	0.007	0.000	0.000	97.21
DC124_1264b2_c1	0.000	0.000	0.000	0.019	0.066	0.003	0.000	0.000	0.001	0.000	99.18
DC124_1264b2_c2	0.000	0.009	0.000	0.000	0.074	0.000	0.000	0.000	0.008	0.000	99.20
DC124_1264b2_c3	0.000	0.000	0.000	0.015	0.057	0.007	0.000	0.005	0.010	0.000	96.95
DC124_1264b2_r1	0.000	0.001	0.009	0.000	0.064	0.011	0.000	0.003	0.000	0.000	97.82
DC124_1264b2_r2	0.000	0.000	0.003	0.000	0.058	0.006	0.000	0.003	0.000	0.000	97.25
DC124_1264b2_r3	0.000	0.000	0.000	0.000	0.055	0.000	0.000	0.000	0.005	0.000	99.21
DC124_1264b2_r4	0.000	0.000	0.000	0.000	0.049	0.006	0.000	0.004	0.000	0.000	97.17
DC124_1264b3	0.000	0.004	0.000	0.000	0.076	0.001	0.000	0.000	0.000	0.000	97.89
DC124_1264b4	0.000	3.540	0.000	0.000	0.060	0.012	0.000	0.002	0.007	0.000	99.73
DC124_1264b5	0.000	0.014	0.006	0.000	0.066	0.006	0.000	0.002	0.013	0.000	97.73
DC124_1264b6	0.000	0.013	0.008	0.000	0.049	0.006	0.000	0.000	0.012	0.000	96.94
DC124_1264b7	0.000	0.000	0.000	0.000	0.054	0.010	0.000	0.000	0.000	0.000	102.20
DC124_1264b8	0.000	0.000	0.000	0.003	0.061	0.000	0.000	0.001	0.000	0.000	101.09
DC124_1273a_rim	0.000	0.010	0.002	0.000	0.054	0.000	0.000	0.000	0.001	0.000	99.59
DC124_1273a2	0.000	0.001	0.001	0.000	0.054	0.009	0.000	0.000	0.000	0.000	98.75
DC124_1273a3	0.015	0.000	0.000	0.000	0.002	0.000	0.000	0.000	0.006	0.000	16.90
DC124_1273a4	0.000	0.004	0.000	0.000	0.064	0.000	0.000	0.000	0.006	0.000	97.74
DC124_1273a5	0.000	0.000	0.000	0.000	0.061	0.002	0.000	0.000	0.000	0.000	97.98

EPMA point name	As	S	Fe	Si	Ca	Au	Hg	Ag	Pb	Tl	Sb	Cu
DC124_1273a6	16.33	40.69	37.99	0.12	0.01	0.166	0.504	0.001	0.000	0.822	0.153	0.313
DC124_1273b1	16.82	40.81	39.77	0.10	0.02	0.043	0.301	0.005	0.000	0.439	0.093	0.242
DC124_1273c	15.05	42.58	37.70	0.08	0.29	0.140	0.542	0.001	0.329	0.692	0.173	0.484
DC124_1273d1_c	1.31	52.87	44.48	0.15	0.05	0.000	0.078	0.000	0.116	0.102	0.020	0.356
DC124_1273d1_r	14.59	43.52	38.19	0.46	0.04	0.146	0.509	0.000	0.000	0.726	0.147	0.474
DC124_1273d2_c	0.82	52.82	45.25	0.14	0.03	0.000	0.055	0.004	0.179	0.021	0.009	0.443
DC124_1273d2_r	12.49	39.53	34.48	1.56	0.23	0.177	0.461	0.001	0.000	0.655	0.123	0.458
DC124_1273d3_r	17.27	40.44	36.70	0.13	0.04	0.053	0.547	0.006	0.000	0.763	0.160	0.416
DC124_1273e	6.70	49.95	41.95	0.03	0.64	0.000	0.066	0.003	0.132	0.000	0.014	0.051
DC124_1273f10	15.67	41.54	38.33	0.22	0.14	0.094	0.413	0.004	0.000	0.683	0.114	0.392
DC124_1273f2	63.08	32.25	4.87	0.24	0.03	0.000	0.030	0.000	0.057	0.000	0.058	0.061
DC124_1273f3_r	13.20	38.70	34.25	2.32	0.20	0.141	0.406	0.009	0.000	0.617	0.125	0.441
DC124_1273f4_r	14.07	44.19	38.10	0.51	0.19	0.195	0.503	0.006	0.000	0.670	0.142	0.464
DC124_1273f5_r	9.24	40.43	31.92	0.04	0.73	0.150	0.676	0.005	0.000	0.695	0.126	0.529
DC124_1273f6_c	15.76	41.60	38.35	0.19	0.08	0.027	0.259	0.003	0.040	0.267	0.019	0.183
DC124_1273f6_r	18.43	39.90	37.98	0.09	0.13	0.021	0.357	0.000	0.000	0.501	0.044	0.267
DC124_1273f7	0.02	25.45	2.90	0.02	0.03	0.727	0.555	0.027	0.167	0.204	0.015	0.614
DC124_1273f8	2.50	50.81	44.28	0.03	0.00	0.000	0.100	0.000	0.132	0.118	0.044	0.005
DC124_1273f9	0.00	52.40	46.24	0.02	0.00	0.000	0.052	0.002	0.132	0.024	0.000	0.000
DC124_1273g1_c	0.68	53.99	46.54	0.03	0.05	0.000	0.040	0.000	0.137	0.076	0.027	0.216
DC124_1273g1_r	14.01	42.53	38.22	0.29	0.06	0.178	0.553	0.004	0.000	0.778	0.154	0.508
DC124_1273g2	14.52	42.32	37.70	0.14	0.08	0.151	0.466	0.005	0.000	0.642	0.139	0.439
DC124_1273g3	4.72	50.21	43.71	0.04	0.07	0.122	0.361	0.010	0.004	0.524	0.097	0.442
DC124_1273g4	0.48	53.26	46.19	0.03	0.05	0.000	0.039	0.000	0.126	0.051	0.031	0.187
DC124_1273g5	0.82	51.98	43.86	0.09	0.04	0.000	0.036	0.000	0.133	0.026	0.026	0.191
DC124_1273g6	1.26	52.60	45.54	0.02	0.08	0.000	0.031	0.003	0.124	0.064	0.021	0.183
DC124_1273g7	3.77	50.55	44.31	0.03	0.09	0.001	0.091	0.002	0.116	0.104	0.027	0.257

EPMA point name	Bi	Zn	Ni	W	Co	Sn	Te	Se	Ti	Mo	Totals
DC124_1273a6	0.000	0.003	0.000	0.000	0.060	0.006	0.000	0.000	0.000	0.000	97.17
DC124_1273b1	0.000	0.000	0.000	0.012	0.066	0.000	0.000	0.000	0.000	0.000	98.72
DC124_1273c	0.000	0.006	0.018	0.000	0.064	0.000	0.000	0.000	0.006	0.000	98.15
DC124_1273d1_c	0.004	0.010	0.020	0.000	0.070	0.133	0.000	0.002	0.000	0.000	99.77
DC124_1273d1_r	0.000	0.017	0.063	0.000	0.041	0.004	0.000	0.005	0.000	0.000	98.94
DC124_1273d2_c	0.000	0.016	0.054	0.000	0.066	0.190	0.000	0.004	0.015	0.000	100.13
DC124_1273d2_r	0.000	0.001	0.108	0.000	0.052	0.000	0.000	0.004	0.005	0.000	90.35
DC124_1273d3_r	0.000	0.020	0.197	0.000	0.077	0.017	0.000	0.000	0.000	0.000	96.84
DC124_1273e	0.049	0.009	0.000	0.000	0.064	0.002	0.000	0.000	0.000	0.000	99.66
DC124_1273f10	0.000	0.005	0.028	0.000	0.060	0.006	0.000	0.000	0.000	0.000	97.70
DC124_1273f2	0.000	0.036	0.000	0.000	0.007	0.000	0.000	0.000	0.000	0.000	100.72
DC124_1273f3_r	0.000	0.000	0.007	0.000	0.044	0.000	0.000	0.000	0.003	0.000	90.46
DC124_1273f4_r	0.000	0.000	0.014	0.000	0.054	0.000	0.000	0.000	0.000	0.000	99.11
DC124_1273f5_r	0.000	5.890	0.022	0.000	0.041	0.001	0.000	0.004	0.003	0.000	90.51
DC124_1273f6_c	0.000	0.000	0.230	0.000	0.119	0.006	0.000	0.000	0.000	0.000	97.13
DC124_1273f6_r	0.000	0.001	0.168	0.000	0.080	0.009	0.000	0.000	0.006	0.000	97.98
DC124_1273f7	0.000	202.498	0.000	0.000	0.003	0.046	0.000	0.107	0.006	0.144	233.53
DC124_1273f8	0.017	0.000	0.787	0.017	0.214	0.000	0.000	0.032	0.006	0.000	99.09
DC124_1273f9	0.029	0.000	0.204	0.005	0.089	0.000	0.000	0.019	0.000	0.000	99.22
DC124_1273g1_c	0.017	0.002	0.000	0.000	0.059	0.205	0.000	0.000	0.000	0.000	102.06
DC124_1273g1_r	0.000	0.004	0.000	0.007	0.056	0.000	0.000	0.001	0.000	0.000	97.35
DC124_1273g2	0.000	0.007	0.002	0.000	0.048	0.000	0.000	0.000	0.000	0.000	96.66
DC124_1273g3	0.000	0.008	0.000	0.000	0.066	0.093	0.000	0.000	0.000	0.000	100.48
DC124_1273g4	0.056	0.002	0.000	0.024	0.070	0.259	0.000	0.000	0.000	0.000	100.86
DC124_1273g5	0.033	0.007	0.000	0.000	0.061	0.212	0.000	0.000	0.000	0.000	97.52
DC124_1273g6	0.000	0.000	0.041	0.000	0.071	0.094	0.000	0.007	0.000	0.000	100.14
DC124_1273g7	0.032	0.000	0.010	0.009	0.067	0.179	0.000	0.000	0.000	0.000	99.64

EPMA point name	As	S	Fe	Si	Ca	Au	Hg	Ag	Pb	Tl	Sb	Cu
DC124_1273h1_c	1.03	52.93	45.29	0.04	0.02	0.000	0.046	0.000	0.128	0.051	0.045	0.054
DC124_1273h1_r	12.55	43.87	38.40	0.29	0.07	0.238	0.509	0.002	0.000	0.708	0.154	0.438
DC124_1273h2_c	0.61	52.97	45.86	0.05	0.01	0.000	0.050	0.003	0.119	0.053	0.092	0.030
DC124_1273h2_r	11.40	45.98	37.29	0.13	0.01	0.232	0.620	0.005	0.000	0.969	0.199	0.495
DC124_1273h3_c1	1.76	52.45	45.94	0.04	0.02	0.000	0.030	0.000	0.143	0.000	0.035	0.049
DC124_1273h3_c2	1.81	53.75	46.63	0.05	0.03	0.000	0.019	0.000	0.119	0.092	0.045	0.014
DC124_1273h3_c3	1.65	52.73	44.60	0.06	0.03	0.000	0.029	0.000	0.162	0.046	0.054	0.078
DC124_1273h3_c4	1.66	52.36	45.49	0.05	0.01	0.000	0.037	0.000	0.133	0.000	0.035	0.015
DC124_1273h3_r1	13.24	43.43	37.57	0.10	0.04	0.231	0.557	0.003	0.000	0.930	0.176	0.453
DC124_1273h3_r2	12.60	43.71	38.01	0.30	0.06	0.248	0.507	0.003	0.000	0.743	0.170	0.421
DC124_1273h3_r3	12.22	42.88	37.50	0.41	0.06	0.231	0.475	0.010	0.000	0.637	0.130	0.412
DC124_1273h5	0.00	54.01	46.51	0.01	0.02	0.000	0.000	0.001	0.142	0.008	0.000	0.000
DC124_1273h6	0.02	53.69	47.01	0.10	0.04	0.000	0.001	0.000	0.165	0.000	0.003	0.000
DC124_1273h7	0.00	53.40	46.46	0.11	0.04	0.000	0.006	0.000	0.162	0.000	0.000	0.000
DC124_1273j_c1	0.17	52.54	45.58	0.04	0.02	0.000	0.049	0.000	0.148	0.062	0.026	0.020
DC124_1273j_c2	0.09	53.44	46.59	0.03	0.01	0.000	0.053	0.003	0.144	0.065	0.042	0.011
DC124_1273j_r1	0.00	53.84	46.45	0.03	0.04	0.000	0.000	0.000	0.168	0.021	0.000	0.000
DC124_1273j_r2	0.14	53.16	45.78	0.26	0.05	0.000	0.007	0.000	0.234	0.017	0.075	0.000
DC215_1569b_unk1	23.11	0.02	20.64	0.44	10.67	0.000	0.003	0.000	0.022	0.000	0.000	0.071
DC215_1569b_unk2	17.51	0.06	24.87	0.76	7.74	0.000	0.013	0.002	0.023	0.000	0.000	0.062
DC215_1569c_unk1	6.46	0.09	53.78	0.24	2.25	0.000	0.026	0.005	0.039	0.000	0.210	0.023
DC215_1569c_unk2	20.54	0.02	18.19	0.57	10.32	0.000	0.012	0.000	0.028	0.000	0.000	0.056
DC215_1569c_unk3	16.87	0.05	24.92	0.60	10.54	0.000	0.022	0.000	0.017	0.000	0.000	0.063
DC215_1569c_unk4	18.68	0.05	26.65	0.73	8.26	0.000	0.014	0.006	0.033	0.000	0.000	0.060
DC215_1569c_unk5	22.05	0.04	20.86	0.51	9.63	0.000	0.011	0.002	0.018	0.000	0.000	0.064

EPMA point name	Bi	Zn	Ni	W	Co	Sn	Te	Se	Ti	Mo	Totals
DC124_1273h1_c	0.063	0.000	0.000	0.002	0.060	0.207	0.000	0.001	0.006	0.000	99.97
DC124_1273h1_r	0.000	0.002	0.000	0.000	0.055	0.013	0.000	0.000	0.000	0.000	97.30
DC124_1273h2_c	0.030	0.007	0.000	0.000	0.072	0.353	0.000	0.000	0.000	0.000	100.30
DC124_1273h2_r	0.000	0.005	0.016	0.000	0.064	0.000	0.000	0.000	0.000	0.000	97.42
DC124_1273h3_c1	0.036	0.007	0.000	0.000	0.077	0.046	0.000	0.003	0.000	0.000	100.63
DC124_1273h3_c2	0.000	0.072	0.000	0.027	0.082	0.113	0.000	0.029	0.036	0.000	102.92
DC124_1273h3_c3	0.000	0.007	0.016	0.000	0.089	0.117	0.000	0.002	0.018	0.000	99.69
DC124_1273h3_c4	0.136	0.041	0.001	0.059	0.070	0.114	0.000	0.008	0.000	0.000	100.21
DC124_1273h3_r1	0.000	0.000	0.000	0.006	0.056	0.002	0.000	0.000	0.000	0.000	96.79
DC124_1273h3_r2	0.000	0.007	0.000	0.000	0.060	0.001	0.000	0.002	0.000	0.000	96.84
DC124_1273h3_r3	0.000	0.018	0.004	0.000	0.065	0.000	0.000	0.000	0.004	0.000	95.06
DC124_1273h5	0.098	0.015	0.277	0.012	0.115	0.000	0.000	0.009	0.009	0.000	101.23
DC124_1273h6	0.078	0.000	0.233	0.000	0.098	0.000	0.000	0.002	0.000	0.000	101.44
DC124_1273h7	0.074	0.000	0.263	0.003	0.088	0.005	0.000	0.000	0.009	0.000	100.61
DC124_1273j_c1	0.028	0.000	0.087	0.000	0.075	0.009	0.000	0.005	0.008	0.000	98.87
DC124_1273j_c2	0.005	0.004	0.057	0.000	0.083	0.004	0.000	0.019	0.000	0.000	100.65
DC124_1273j_r1	0.011	0.008	0.370	0.009	0.115	0.000	0.000	0.015	0.012	0.000	101.09
DC124_1273j_r2	0.077	0.006	0.199	0.000	0.121	0.001	0.000	0.037	0.002	0.000	100.16
DC215_1569b_unk1	0.031	0.000	0.009	0.000	0.023	0.000	0.000	0.000	0.079	0.007	55.13
DC215_1569b_unk2	0.000	0.008	0.038	0.000	0.053	0.002	0.000	0.000	0.099	0.000	51.24
DC215_1569c_unk1	0.002	0.000	0.041	0.000	0.078	0.000	0.000	0.000	0.015	0.000	63.25
DC215_1569c_unk2	0.000	0.003	0.021	0.000	0.050	0.000	0.000	0.000	0.021	0.000	49.84
DC215_1569c_unk3	0.000	0.147	0.018	0.000	0.040	0.010	0.000	0.000	0.008	0.000	53.30
DC215_1569c_unk4	0.000	0.006	0.020	0.000	0.048	0.000	0.000	0.000	0.022	0.000	54.58
DC215_1569c_unk5	0.000	0.002	0.017	0.000	0.038	0.000	0.000	0.000	0.013	0.000	53.25

APPENDIX F

XRD DATA

Twelve samples were ground into a fine powder and analyzed by a PANalytical X'PERT Pro X-ray Diffraction Spectrometer housed in the UNLV XRD/XRF laboratory; XRD settings are reported in Table 3. Appendix F1 shows the peak list raw data collected for each sample. Appendix F2 displays the interpreted XRD patterns by using X'Pert Highscore Plus and Match!2 software packages.

Appendix F1. X-Ray Diffraction

CHUD 038 457’

Pos. [−2Th.]	Height [cts]	FWHM [−2Th.]	d-spacing [Å]	Rel. Int. [%]
5.1208	227.71	0.2519	17.25766	11.35
8.9085	1052.95	0.0708	9.92664	52.5
10.9475	70.24	0.0945	8.08197	3.5
11.9125	108.77	0.063	7.42936	5.42
13.1093	93.25	0.126	6.75365	4.65
14.7571	426.67	0.0394	6.00304	21.28
15.5445	680.46	0.0192	5.69598	33.93
16.142	238.54	0.063	5.49101	11.89
16.4668	1371.57	0.0354	5.38341	68.39
17.7927	383.66	0.126	4.98512	19.13
19.2477	129.53	0.063	4.61143	6.46
19.8676	491.04	0.0708	4.46893	24.49
20.4816	157.79	0.126	4.33632	7.87
20.9259	988.72	0.0472	4.24525	49.3
21.8872	228.93	0.1102	4.06093	11.42
23.0044	58.64	0.0945	3.86617	2.92
23.4669	58.26	0.0945	3.79102	2.9
23.9009	90.85	0.0945	3.72316	4.53
24.4735	314.5	0.0945	3.63732	15.68
24.7056	245.24	0.0472	3.60367	12.23
25.3592	216.4	0.063	3.51226	10.79
25.938	290.34	0.0472	3.43518	14.48
26.6984	2005.47	0.0384	3.33628	100
26.7659	1355.97	0.0384	3.33629	67.61
27.0188	390.04	0.048	3.29744	19.45
28.1058	672.8	0.0384	3.17233	33.55
28.1907	901.18	0.0384	3.16297	44.94
28.3336	1538.46	0.0576	3.14734	76.71
28.4091	780.23	0.0288	3.14695	38.91
29.1401	502.43	0.0576	3.06205	25.05
29.3046	503.76	0.0576	3.04523	25.12
29.4757	392.15	0.0672	3.02795	19.55
29.9483	305.55	0.048	2.98123	15.24
30.2554	255.98	0.048	2.95167	12.76
30.6132	725.38	0.0576	2.91798	36.17
30.6991	385.65	0.0576	2.91724	19.23
31.2865	203.03	0.0288	2.8567	10.12
31.9642	746.39	0.0336	2.79766	37.22

32.0443	369.81	0.0384	2.79778	18.44
32.3026	347.59	0.0384	2.76912	17.33
32.9053	680.17	0.0768	2.71976	33.92
33.1287	598.89	0.0384	2.70193	29.86
33.3703	582.72	0.0336	2.68292	29.06
33.4477	349.43	0.0384	2.68354	17.42
34.1864	185.09	0.048	2.62071	9.23
34.5998	378.22	0.0576	2.59034	18.86
35.1252	324.23	0.2688	2.55279	16.17
35.7008	149.99	0.0576	2.51294	7.48
36.1312	167.08	0.0768	2.48399	8.33
36.3536	205.36	0.0384	2.4693	10.24
36.5996	308.14	0.0576	2.45327	15.37
36.8818	177.23	0.1536	2.43514	8.84
37.5973	122.32	0.2304	2.39042	6.1
38.2415	83.5	0.2304	2.35163	4.16
39.5079	97	0.0576	2.27912	4.84
39.907	130.54	0.0576	2.25724	6.51
40.0475	169.43	0.0768	2.24964	8.45
40.3247	173.12	0.0576	2.23481	8.63
41.195	167.61	0.1152	2.18959	8.36
41.7098	72.59	0.1536	2.16375	3.62
42.4861	376.7	0.0576	2.12599	18.78
44.3513	55.9	0.0576	2.04081	2.79
45.3886	223.38	0.3456	1.99656	11.14
45.8327	140.79	0.0576	1.97824	7.02
46.8991	222.63	0.0576	1.93571	11.1
47.0831	1023.05	0.048	1.92857	51.01
47.1888	584.15	0.048	1.92928	29.13
48.3323	45.66	0.2304	1.8816	2.28
49.1497	122.12	0.0576	1.85221	6.09
49.6059	242.28	0.0576	1.83624	12.08
49.7612	99.87	0.0768	1.83542	4.98
50.1584	178.15	0.0768	1.8173	8.88
50.77	134.68	0.0768	1.79683	6.72
50.9135	92.55	0.0576	1.79656	4.61
51.2138	116.19	0.0576	1.7823	5.79
51.5959	118.56	0.1152	1.76999	5.91
52.3013	71.46	0.1152	1.74777	3.56
53.2346	109.22	0.0576	1.71931	5.45
53.7779	78.72	0.2304	1.70321	3.93
54.1147	129.12	0.0768	1.6934	6.44
54.6984	162.36	0.096	1.6767	8.1

54.9031	187.47	0.096	1.67094	9.35
55.8173	437.07	0.0384	1.64572	21.79
55.9672	258.56	0.0672	1.64166	12.89
57.3336	44.19	0.3072	1.60574	2.2
58.5787	65.3	0.3072	1.57454	3.26
59.988	172.45	0.096	1.54088	8.6
61.2508	100.66	0.0576	1.5121	5.02
61.9492	191.61	0.1536	1.49672	9.55
63.2998	99.8	0.1152	1.468	4.98
64.1157	108.86	0.1536	1.45127	5.43
65.3575	72.86	0.1536	1.42667	3.63
67.7772	83.24	0.1152	1.3815	4.15
68.3432	129.43	0.096	1.37144	6.45
68.7079	190.84	0.0576	1.36504	9.52
70.2559	58.84	0.384	1.33871	2.93
72.1149	22.39	0.4608	1.30871	1.12
73.4905	35.4	0.9216	1.28757	1.77
75.88	118.66	0.0768	1.25285	5.92

CHUD 044 303’

Pos. [−2Th.]	Height [cts]	FWHM [−2Th.]	d-spacing [Å]	Rel. Int. [%]
6.2771	153.91	0.0472	14.0809	0.84
8.8733	7431.29	0.0433	9.96603	40.49
9.9342	44.76	0.0945	8.90397	0.24
10.6513	473.94	0.0315	8.30608	2.58
17.657	300.36	0.0394	5.02313	1.64
18.786	84.71	0.0472	4.72372	0.46
19.3993	40.96	0.126	4.57575	0.22
21.2475	51.46	0.0945	4.18172	0.28
23.2021	801.79	0.0472	3.83368	4.37
24.3629	63.29	0.126	3.65359	0.34
26.2737	220.64	0.063	3.39205	1.2
26.5346	2061.33	0.048	3.3565	11.23
26.6069	981.62	0.0288	3.35587	5.35
27.3607	101.19	0.0576	3.25701	0.55
28.3807	153.05	0.0768	3.14222	0.83
28.7178	966.41	0.0336	3.1061	5.27
28.7925	460.29	0.0384	3.10592	2.51
29.547	18353.96	0.048	3.0208	100
29.6255	9796.77	0.0384	3.02046	53.38
30.6227	163.45	0.1536	2.91709	0.89

30.9857	222.11	0.1152	2.88374	1.21
31.5852	309.84	0.0672	2.83036	1.69
32.0237	71.42	0.0768	2.7926	0.39
33.0314	89.81	0.0768	2.70967	0.49
33.2357	88.8	0.0576	2.69347	0.48
34.3486	186.43	0.048	2.60871	1.02
35.5639	203.61	0.0672	2.5223	1.11
36.1154	1104.38	0.0432	2.48504	6.02
36.2146	591.96	0.048	2.48462	3.23
37.0071	112.37	0.0768	2.42718	0.61
38.6175	42.83	0.0576	2.32959	0.23
39.5596	1722.04	0.0528	2.27625	9.38
39.6636	900.64	0.0576	2.27617	4.91
41.563	102.7	0.0768	2.17105	0.56
43.3114	1679.24	0.0528	2.08737	9.15
43.4251	855.94	0.048	2.08734	4.66
44.8725	373.7	0.0672	2.01831	2.04
44.9786	220.69	0.0768	2.0188	1.2
45.4281	64.96	0.2304	1.99491	0.35
47.2635	436.34	0.0864	1.92163	2.38
47.6685	1886.36	0.048	1.90625	10.28
47.7934	1049.7	0.0672	1.90155	5.72
48.2151	157.79	0.048	1.8859	0.86
48.3498	118.68	0.0576	1.88096	0.65
48.6691	1759.66	0.0384	1.86937	9.59
48.7937	1018.68	0.0768	1.86488	5.55
50.4753	39.48	0.3072	1.80663	0.22
54.6764	104.17	0.0768	1.67733	0.57
55.8149	29.98	0.1152	1.64578	0.16
56.7151	239.86	0.0672	1.62178	1.31
56.875	133	0.0768	1.62161	0.72
57.5551	647.44	0.0672	1.60009	3.53
57.6991	331.73	0.0768	1.6004	1.81
58.2223	107.89	0.0576	1.58333	0.59
59.96	68.31	0.1536	1.54153	0.37
60.3815	103.57	0.1152	1.53177	0.56
60.826	382.25	0.0672	1.52164	2.08
60.988	228.63	0.0768	1.52176	1.25
61.1651	307.28	0.0864	1.51401	1.67
61.3188	194.78	0.0768	1.51434	1.06
61.529	207.93	0.096	1.50593	1.13
63.2023	123.59	0.0672	1.47003	0.67
64.4986	45.09	0.1152	1.44358	0.25

64.8079	386.76	0.0864	1.43743	2.11
64.9804	226.15	0.1152	1.43403	1.23
65.7618	263.91	0.096	1.41887	1.44
65.9553	154.91	0.096	1.4187	0.84
68.5711	58.65	0.1536	1.36743	0.32
69.3456	99.46	0.1152	1.35404	0.54
70.3991	144	0.096	1.33634	0.78
70.6267	68.09	0.096	1.3359	0.37
71.3366	15.04	0.3072	1.32106	0.08
71.9592	15.64	0.384	1.31115	0.09
73.0756	154.18	0.1344	1.29385	0.84
73.2739	95.33	0.0768	1.29405	0.52
73.8238	30.05	0.1152	1.28258	0.16
75.1624	23.48	0.1536	1.26302	0.13

CHUD 046 238’

Pos. [−2Th.]	Height [cts]	FWHM [−2Th.]	d-spacing [Å]	Rel. Int. [%]
5.1694	185.32	0.5038	17.09548	1.47
10.0281	940.44	0.1574	8.82075	7.47
15.7339	421.04	0.1102	5.6325	3.34
16.0892	217.03	0.0945	5.5089	1.72
17.9049	64.63	0.3149	4.95415	0.51
19.3721	259.34	0.1102	4.58212	2.06
20.9284	3955.03	0.0384	4.24125	31.4
20.9863	1589.23	0.0288	4.24018	12.62
23.3733	78.4	0.3072	3.80283	0.62
24.2639	46.38	0.4608	3.66524	0.37
25.2135	167.64	0.1152	3.5293	1.33
26.7067	12594.26	0.0528	3.33526	100
26.7772	5603.99	0.0384	3.33491	44.5
27.1287	402.06	0.192	3.28433	3.19
27.742	410.14	0.192	3.21311	3.26
29.6694	180.09	0.1152	3.00862	1.43
30.2779	376.35	0.1536	2.94952	2.99
31.0206	231.74	0.192	2.88058	1.84
31.7035	332.16	0.2304	2.82007	2.64
32.4037	803.29	0.2496	2.76071	6.38
34.1548	243.35	0.192	2.62307	1.93
35.533	149.12	0.2304	2.52443	1.18
36.0942	98.17	0.2304	2.48645	0.78
36.5905	1137.45	0.0576	2.45386	9.03

36.699	506.53	0.048	2.45293	4.02
38.2582	19.06	0.6912	2.35064	0.15
39.5178	744.65	0.048	2.27856	5.91
39.6251	390.63	0.0672	2.27829	3.1
40.3241	509.83	0.048	2.23484	4.05
40.4438	359.04	0.0576	2.22851	2.85
42.4885	791.73	0.0864	2.12588	6.29
42.6116	406.98	0.0576	2.12529	3.23
45.8269	398.42	0.0672	1.97847	3.16
45.9573	219.1	0.0576	1.97806	1.74
47.533	32.77	0.2304	1.91136	0.26
48.3176	46.32	0.384	1.88214	0.37
50.1833	1254.08	0.0864	1.81645	9.96
50.32	656.21	0.0768	1.81634	5.21
51.681	93.23	0.3072	1.76728	0.74
53.6245	28.24	0.4608	1.70772	0.22
54.9115	391.02	0.0672	1.6707	3.1
55.0539	229.28	0.0768	1.67086	1.82
55.3693	162.91	0.0576	1.65797	1.29
56.4572	133.37	0.3072	1.62857	1.06
58.9113	40.94	0.6144	1.56645	0.33
59.9815	931.27	0.0384	1.54103	7.39
60.1534	466.92	0.096	1.53704	3.71
62.1067	21.73	0.9216	1.4933	0.17
64.058	138.02	0.0768	1.45244	1.1
65.829	53.87	0.2304	1.41759	0.43
67.7772	477.39	0.048	1.3815	3.79
67.9514	290.42	0.0576	1.38181	2.31
68.1696	609.47	0.048	1.37451	4.84
68.3621	590.69	0.096	1.3711	4.69
73.4812	135.25	0.096	1.28771	1.07
75.6854	214.39	0.1152	1.25559	1.7

CHUD 046 283’

Pos. [−2Th.]	Height [cts]	FWHM [−2Th.]	d-spacing [Å]	Rel. Int. [%]
5.9142	620.08	0.2519	14.94393	18.5
9.9692	51.13	0.1889	8.87273	1.53
12.4226	379.52	0.1574	7.12544	11.32
14.51	316.41	0.1889	6.1047	9.44
15.1531	284.21	0.126	5.84704	8.48
16.9082	205.3	0.1574	5.24385	6.12

17.2641	94.75	0.126	5.13654	2.83
17.854	52.25	0.1574	4.96815	1.56
19.9201	447.97	0.1889	4.45728	13.36
20.4404	306.05	0.1889	4.34498	9.13
20.9114	506.69	0.1889	4.24816	15.11
23.1709	365.51	0.126	3.83876	10.9
25.2327	726.71	0.126	3.52958	21.68
26.712	1705.97	0.126	3.33737	50.89
28.4765	194.04	0.1889	3.13447	5.79
29.5212	3352.28	0.1574	3.02588	100
30.4833	344.01	0.126	2.93254	10.26
30.7281	461.3	0.1574	2.90973	13.76
31.5638	83.82	0.126	2.83458	2.5
32.313	62.87	0.126	2.77054	1.88
33.4908	40.73	0.1574	2.67576	1.21
35.0949	281.38	0.3149	2.55705	8.39
36.1004	453.99	0.1889	2.4881	13.54
36.5981	157.89	0.126	2.4554	4.71
38.4786	163.95	0.3779	2.33962	4.89
39.5119	577.73	0.1889	2.28078	17.23
40.3519	92.18	0.2519	2.23522	2.75
41.1397	54.9	0.2519	2.19422	1.64
42.1623	72.33	0.2204	2.14334	2.16
42.5013	83.3	0.1889	2.12703	2.48
43.2617	375.16	0.2204	2.09138	11.19
44.4007	24.43	0.3779	2.04034	0.73
45.816	62.9	0.2519	1.98056	1.88
46.4136	76.17	0.2204	1.95644	2.27
47.194	160.34	0.126	1.92589	4.78
47.607	487.19	0.1574	1.91015	14.53
48.5999	372.05	0.2204	1.87342	11.1
50.2254	108	0.1889	1.81653	3.22
51.6995	246.12	0.1889	1.76815	7.34
54.8943	128.91	0.126	1.67257	3.85
55.4337	87.12	0.4408	1.65756	2.6
56.7183	94.84	0.3149	1.62304	2.83
57.5103	161.36	0.126	1.60255	4.81
58.2525	18.73	0.1889	1.58389	0.56
59.9782	133.98	0.126	1.54238	4
60.8247	108.69	0.2519	1.52293	3.24
62.3595	163.36	0.1574	1.48909	4.87
63.2711	42.6	0.2519	1.46981	1.27
64.056	42.43	0.2519	1.45368	1.27

64.8366	84.69	0.3779	1.43806	2.53
65.8421	42.31	0.3779	1.41851	1.26
67.749	43.61	0.1889	1.38315	1.3
68.2575	58.07	0.2519	1.37409	1.73
69.3023	19.39	0.1889	1.3559	0.58
70.3491	54.27	0.1574	1.33827	1.62
73.217	74.46	0.2688	1.2917	2.22

CHUE 215 245'

Pos. [−2Th.]	Height [cts]	FWHM [−2Th.]	d-spacing [Å]	Rel. Int. [%]
8.9197	482.44	0.0472	9.91429	3.64
11.705	62.57	0.0945	7.5606	0.47
12.4695	157.4	0.0945	7.09873	1.19
17.8011	228.27	0.1574	4.98279	1.72
19.866	571.66	0.1102	4.46929	4.32
20.4761	207.69	0.126	4.33749	1.57
20.9308	4283.47	0.0624	4.24076	32.34
20.9895	2006.74	0.0336	4.23954	15.15
21.7406	71.9	0.2304	4.0846	0.54
24.1271	238.83	0.1344	3.68571	1.8
24.4773	230.7	0.2304	3.63375	1.74
25.0003	119.22	0.1536	3.55891	0.9
25.3814	115.12	0.096	3.50634	0.87
25.8844	113.8	0.2304	3.43933	0.86
26.7105	13246.08	0.072	3.3348	100
26.7897	5580.61	0.0384	3.33339	42.13
29.2138	251.58	0.192	3.05449	1.9
31.0265	2122.62	0.1056	2.88004	16.02
31.9664	98.75	0.0768	2.79747	0.75
32.3128	54.29	0.1536	2.76827	0.41
33.2287	169.56	0.1152	2.69403	1.28
33.5955	147.82	0.1152	2.66545	1.12
35.1217	346.98	0.192	2.55304	2.62
36.6016	1132.12	0.0672	2.45314	8.55
36.695	608.73	0.0576	2.45318	4.6
37.4287	221.43	0.096	2.40081	1.67
38.6234	46.56	0.2304	2.32925	0.35
39.526	712.3	0.0336	2.27811	5.38
39.6355	335.89	0.0576	2.27207	2.54
40.3471	454.47	0.048	2.23363	3.43
40.4531	212.32	0.0576	2.23355	1.6

41.1923	528.37	0.0672	2.18972	3.99
42.5146	769.56	0.0528	2.12463	5.81
42.6266	379.66	0.048	2.12457	2.87
43.8608	62.34	0.2688	2.06249	0.47
44.9949	274.95	0.1152	2.01311	2.08
45.858	388.25	0.0864	1.9772	2.93
45.9678	217.01	0.0576	1.97764	1.64
47.5465	24.34	0.3072	1.91085	0.18
49.3196	48.07	0.3072	1.84622	0.36
50.194	1232.53	0.1056	1.81609	9.3
50.3421	584.99	0.0768	1.8156	4.42
50.5844	251.83	0.2304	1.80299	1.9
51.1514	280.75	0.1536	1.78433	2.12
54.897	390.2	0.048	1.67111	2.95
55.0719	242.17	0.0768	1.66621	1.83
55.3791	199.74	0.0768	1.65769	1.51
56.3835	66.53	0.5376	1.63052	0.5
58.96	62.63	0.1152	1.56527	0.47
60.001	944.9	0.1056	1.54058	7.13
60.1588	487.34	0.096	1.54073	3.68
61.9441	157	0.2304	1.49683	1.19
63.4739	79.17	0.1536	1.46439	0.6
64.0732	138.49	0.1152	1.45213	1.05
65.2253	43.73	0.3072	1.42924	0.33
66.0254	29.81	0.4608	1.41385	0.23
67.4462	94.1	0.1536	1.38748	0.71
67.7783	476.99	0.1152	1.38148	3.6
67.9576	287.88	0.0768	1.3817	2.17
68.1802	597.72	0.0672	1.37432	4.51
68.3474	616.38	0.096	1.37136	4.65
70.502	54.89	0.3072	1.33464	0.41
72.9006	50.18	0.3072	1.29653	0.38
73.4964	164.01	0.1152	1.28748	1.24
73.7198	96.65	0.1152	1.28732	0.73
74.8054	25.13	0.4608	1.26816	0.19
75.692	218.74	0.1152	1.2555	1.65

CHUE 215 262.5’

Pos. [−2Th.]	Height [cts]	FWHM [−2Th.]	d-spacing [Å]	Rel. Int. [%]
5.096	450.14	0.1889	17.34143	7.87
6.2929	706.41	0.0551	14.0456	12.36

8.7916	701.6	0.0708	10.05839	12.27
9.5154	164.18	0.0787	9.29492	2.87
9.8381	79.53	0.0945	8.99074	1.39
10.5796	447.65	0.0708	8.36215	7.83
12.5198	666.98	0.063	7.07033	11.67
17.5321	71.85	0.1574	5.05863	1.26
18.7926	449.12	0.063	4.72209	7.86
19.7602	70.07	0.2519	4.49297	1.23
20.9087	266.68	0.126	4.24871	4.66
21.1764	70.84	0.0945	4.1956	1.24
22.0726	34.03	0.126	4.02723	0.6
23.1692	468.15	0.0315	3.83905	8.19
24.0815	100.44	0.1574	3.69564	1.76
25.1308	396.82	0.0551	3.54366	6.94
26.4343	391.69	0.0551	3.3718	6.85
26.6809	1380.02	0.0551	3.34119	24.14
27.2866	153.44	0.0787	3.2684	2.68
28.3223	70.92	0.126	3.15119	1.24
28.6396	490.51	0.0472	3.11699	8.58
29.5627	5717.59	0.0528	3.01923	100
29.6332	2917.79	0.048	3.01969	51.03
30.4993	217.09	0.1152	2.92861	3.8
30.9857	1818.04	0.2112	2.88374	31.8
31.5465	173.27	0.1344	2.83374	3.03
31.9647	88.38	0.0576	2.79762	1.55
33.1583	218.93	0.0768	2.69959	3.83
33.5778	65.93	0.192	2.66681	1.15
34.306	161.81	0.096	2.61185	2.83
34.6372	60.11	0.192	2.58763	1.05
35.4115	162.62	0.0768	2.53281	2.84
36.1154	598.54	0.0768	2.48504	10.47
36.6114	85.21	0.1344	2.45251	1.49
36.9695	116.94	0.1536	2.42957	2.05
37.3966	181.02	0.1152	2.40279	3.17
38.5354	78.59	0.0576	2.33437	1.37
39.5388	960.46	0.0672	2.2774	16.8
40.3335	39.18	0.2688	2.23434	0.69
41.1799	415.55	0.2112	2.19036	7.27
42.5246	48.39	0.2304	2.12415	0.85
43.3319	655.18	0.0768	2.08643	11.46
43.4588	358.25	0.0576	2.0858	6.27
43.8503	50.94	0.192	2.06296	0.89
45.0003	269.67	0.1536	2.01287	4.72

47.2883	211.19	0.1152	1.92068	3.69
47.7365	641.88	0.1536	1.90369	11.23
48.7274	704.26	0.0768	1.86727	12.32
49.3614	60.59	0.2304	1.84476	1.06
50.1756	166.87	0.1536	1.81671	2.92
50.519	207.8	0.2688	1.80517	3.63
51.111	247.67	0.1536	1.78564	4.33
54.6731	53.76	0.384	1.67742	0.94
55.7599	48.94	0.1152	1.64727	0.86
56.209	22.13	0.2688	1.63517	0.39
56.8189	104.17	0.1344	1.61906	1.82
57.6256	263.57	0.1344	1.5983	4.61
58.403	45.19	0.3072	1.57886	0.79
58.9655	49.5	0.3072	1.56513	0.87
60.0028	160.14	0.3456	1.54053	2.8
60.3632	108.82	0.1152	1.53219	1.9
60.9086	180.72	0.1152	1.51977	3.16
61.336	84.85	0.6144	1.5102	1.48
61.6659	91.86	0.1152	1.50665	1.61
63.3344	102.02	0.192	1.46728	1.78
64.8656	226.95	0.096	1.43629	3.97
65.9273	93.71	0.192	1.41571	1.64
67.4172	79.93	0.192	1.388	1.4
68.2246	57.25	0.3072	1.37353	1
69.5477	28.29	0.2688	1.3506	0.49
70.5741	66.5	0.4608	1.33345	1.16
73.1685	88.73	0.1536	1.29244	1.55
74.8999	13.85	0.5376	1.2668	0.24

DC 124 1037’

Pos. [−2Th.]	Height [cts]	FWHM [−2Th.]	d-spacing [Å]	Rel. Int. [%]
6.2922	67	0.1889	14.04719	0.48
8.8447	432.56	0.126	9.99816	3.09
9.899	28.72	0.1574	8.93551	0.21
10.6061	451.33	0.1889	8.34131	3.23
12.5555	139.06	0.1889	7.0503	0.99
17.6044	33.22	0.1889	5.03802	0.24
18.8064	89.86	0.126	4.71865	0.64
19.8165	39.17	0.126	4.48034	0.28
21.2358	59.28	0.1889	4.184	0.42
22.1027	16.15	0.1889	4.02181	0.12

23.1834	745.58	0.1889	3.83673	5.33
24.3275	3.75	0.2519	3.65882	0.03
25.1874	88.35	0.126	3.53583	0.63
26.5075	142.47	0.1574	3.36266	1.02
27.3504	70.26	0.1889	3.26091	0.5
28.7117	854.49	0.126	3.10932	6.11
29.5474	13992.82	0.126	3.02326	100
31.0565	222.19	0.1574	2.87971	1.59
31.5777	283.4	0.1574	2.83336	2.03
32.0265	72.72	0.1889	2.79467	0.52
33.2284	95.78	0.126	2.69628	0.68
35.4917	58.64	0.126	2.52936	0.42
36.109	1101.85	0.1574	2.48752	7.87
37.5361	18.35	0.2204	2.39617	0.13
37.8467	22.56	0.1574	2.37721	0.16
38.9091	24.35	0.126	2.31472	0.17
39.5396	1535.12	0.1574	2.27925	10.97
41.2296	41.36	0.126	2.18964	0.3
41.9143	28.43	0.1889	2.15544	0.2
43.2826	1249.68	0.126	2.09042	8.93
45.0698	42.76	0.3149	2.0116	0.31
45.4266	38.69	0.1574	1.99662	0.28
46.3434	15.64	0.3779	1.95924	0.11
47.2405	408.78	0.1574	1.9241	2.92
47.6335	1624.7	0.126	1.90914	11.61
48.63	1636.52	0.126	1.87233	11.7
50.4605	43.77	0.2519	1.80862	0.31
51.1602	28.46	0.2204	1.78552	0.2
54.6802	8.91	0.2519	1.67861	0.06
55.8589	26.51	0.1889	1.64595	0.19
56.7416	198.34	0.1889	1.62243	1.42
57.5681	472.53	0.2519	1.60108	3.38
58.2579	96.92	0.126	1.58376	0.69
60.8199	346.78	0.126	1.52304	2.48
61.5749	144.71	0.1889	1.50616	1.03
63.177	128.44	0.126	1.47177	0.92
64.7825	351.9	0.126	1.43913	2.51
65.7202	215.62	0.1574	1.42085	1.54
67.6068	9.3	0.3779	1.38572	0.07
69.3146	77.38	0.126	1.35569	0.55
70.3454	85.64	0.1574	1.33833	0.61
72.2314	15.99	0.1889	1.30796	0.11
73.0146	148.08	0.126	1.29586	1.06

73.8133	38.39	0.1536	1.28273	0.27

DC 124 1261’

Pos. [−2Th.]	Height [cts]	FWHM [−2Th.]	d-spacing [Å]	Rel. Int. [%]
8.9056	307.26	0.126	9.92989	2.45
11.867	28.09	0.1889	7.45777	0.22
13.0795	34.01	0.1889	6.76901	0.27
14.731	183.56	0.1889	6.01363	1.46
15.5321	253.16	0.126	5.70523	2.02
16.4553	607.24	0.126	5.38716	4.84
17.8023	144.57	0.1889	4.98245	1.15
19.2586	49.38	0.1889	4.60886	0.39
19.8568	430.69	0.126	4.47133	3.43
20.9114	3383.82	0.1889	4.24817	26.98
21.9044	118.98	0.126	4.05778	0.95
23.1558	53.5	0.1574	3.84124	0.43
24.4621	158.24	0.1574	3.63899	1.26
25.3828	91.61	0.1889	3.50905	0.73
25.8877	72.83	0.1889	3.44174	0.58
26.7119	12541.81	0.126	3.33739	100
28.1468	316.96	0.126	3.17043	2.53
28.3273	323.28	0.126	3.15064	2.58
29.527	542.47	0.1574	3.0253	4.33
29.9703	155.45	0.126	2.98155	1.24
30.617	313.82	0.126	2.92003	2.5
30.9981	476.66	0.2204	2.88501	3.8
32.2407	46.61	0.1889	2.77659	0.37
32.8868	408.52	0.126	2.72351	3.26
33.3568	133.28	0.126	2.68619	1.06
34.6139	143.68	0.126	2.59146	1.15
35.1101	275.1	0.126	2.55597	2.19
36.1161	113.5	0.126	2.48705	0.91
36.5942	1157.8	0.126	2.45565	9.23
37.5833	98.62	0.1574	2.39327	0.79
38.1958	46.41	0.126	2.35628	0.37
39.5118	743.18	0.1889	2.28079	5.93
40.3304	493.15	0.126	2.23636	3.93
41.1935	214.21	0.1574	2.19148	1.71
41.7249	48.88	0.126	2.16479	0.39
42.4829	797.55	0.1574	2.1279	6.36
43.3326	50.99	0.1889	2.08813	0.41

44.9649	92.77	0.126	2.01605	0.74
45.8232	463.14	0.126	1.98026	3.69
47.1855	72.9	0.2519	1.92622	0.58
47.6346	65.34	0.1889	1.9091	0.52
48.6103	83.48	0.1574	1.87304	0.67
49.1598	84.28	0.126	1.85339	0.67
50.2208	935.09	0.1889	1.81669	7.46
51.2006	77.99	0.1889	1.7842	0.62
51.9062	19.84	0.2519	1.7616	0.16
53.0139	18.33	0.1889	1.72737	0.15
53.7552	44.66	0.1889	1.70529	0.36
54.0961	58.12	0.1889	1.69535	0.46
54.9471	359.07	0.2519	1.67108	2.86
55.4133	154.47	0.126	1.65812	1.23
55.8967	124.12	0.1889	1.64493	0.99
56.3071	133.04	0.1889	1.63391	1.06
57.6639	48.48	0.1889	1.59865	0.39
58.5987	42.29	0.3149	1.57536	0.34
60.0215	704.47	0.1889	1.54137	5.62
62.0133	126.49	0.4408	1.49656	1.01
64.1161	114.13	0.1889	1.45246	0.91
65.8173	48.04	0.1889	1.41899	0.38
67.7551	494.86	0.126	1.38304	3.95
68.2654	502.11	0.3149	1.37395	4
70.405	35.81	0.3779	1.33735	0.29
73.4952	149.54	0.2304	1.2875	1.19

DC 213 1263’

Pos. [−2Th.]	Height [cts]	FWHM [−2Th.]	d-spacing [Å]	Rel. Int. [%]
5.8017	331.06	0.3779	15.23361	2.82
8.7756	516.56	0.0472	10.07671	4.4
12.4361	63.34	0.1889	7.11771	0.54
17.6248	53.13	0.0945	5.03222	0.45
19.8602	55.17	0.1889	4.47059	0.47
20.9426	55.28	0.126	4.24191	0.47
23.1461	964.12	0.0354	3.84282	8.21
25.0439	31.7	0.2519	3.55576	0.27
26.4337	217.49	0.0551	3.37188	1.85
26.7096	208.36	0.1102	3.33767	1.78
27.6371	19.15	0.1889	3.22773	0.16
29.4997	11738.69	0.0576	3.02553	100

29.5894	5431.01	0.0336	3.02406	46.27
30.9544	352.99	0.1536	2.88658	3.01
31.5512	243.74	0.0576	2.83333	2.08
34.3341	33.94	0.2304	2.60978	0.29
36.0713	1231.69	0.0768	2.48798	10.49
36.1574	743.7	0.0672	2.48841	6.34
37.4057	25.82	0.2304	2.40223	0.22
39.5135	1703.24	0.0768	2.27881	14.51
39.6219	912.17	0.0576	2.27847	7.77
41.1836	74.25	0.1152	2.19017	0.63
43.2669	1475.7	0.0288	2.08941	12.57
43.3843	807.28	0.0672	2.08403	6.88
44.7594	54.44	0.1152	2.02315	0.46
47.2357	452.82	0.0672	1.9227	3.86
47.3504	336.06	0.0576	1.92307	2.86
47.6186	1509.02	0.0384	1.90813	12.86
47.7535	874.83	0.0768	1.90305	7.45
48.6174	1581.76	0.096	1.87123	13.47
48.7681	830.58	0.0672	1.87044	7.08
50.4307	41.61	0.4608	1.80812	0.35
51.1699	46.96	0.3072	1.78373	0.4
54.707	26.37	0.3072	1.67646	0.22
56.681	250.83	0.0576	1.62267	2.14
56.8469	136.8	0.0576	1.62235	1.17
57.5338	630.24	0.0768	1.60063	5.37
57.6842	334.16	0.0768	1.60078	2.85
58.2117	82.61	0.0576	1.5836	0.7
59.9537	33.46	0.384	1.54168	0.29
60.7951	415.37	0.0672	1.52234	3.54
60.9677	250.46	0.0576	1.52221	2.13
61.1281	211.98	0.0768	1.51484	1.81
61.4977	165.03	0.096	1.50662	1.41
63.1752	125.63	0.1152	1.47059	1.07
64.7784	393.24	0.0384	1.43802	3.35
64.997	190.57	0.1152	1.43371	1.62
65.7333	223.26	0.0864	1.41942	1.9
65.9554	125.63	0.1152	1.41518	1.07
67.4439	11.46	0.4608	1.38752	0.1
68.4207	15.48	0.4608	1.37007	0.13
69.3264	71.19	0.1152	1.35437	0.61
70.3658	118.19	0.096	1.33689	1.01
73.054	148.34	0.1344	1.29418	1.26
73.2598	86.93	0.1152	1.29426	0.74

73.8034	41.2	0.1536	1.28288	0.35

DC 213 1281’

Pos. [−2Th.]	Height [cts]	FWHM [−2Th.]	d-spacing [Å]	Rel. Int. [%]
8.8634	250.22	0.2204	9.97706	1.31
17.7653	70.45	0.1889	4.99274	0.37
19.8124	303.41	0.1102	4.48127	1.59
20.894	4645.62	0.0672	4.24814	24.33
20.9607	1949.12	0.0288	4.24529	10.21
24.0653	158.76	0.1152	3.69503	0.83
25.3512	65.26	0.1152	3.51044	0.34
25.9073	75.62	0.2304	3.43634	0.4
26.6763	19097.4	0.0768	3.33899	100
26.7503	8617.29	0.048	3.3382	45.12
29.1234	53.12	0.384	3.06377	0.28
30.9259	1059.5	0.1728	2.88918	5.55
33.2	73.61	0.3072	2.69629	0.39
35.1173	269.75	0.2688	2.55335	1.41
36.5606	1368.34	0.0864	2.45579	7.17
36.655	788.34	0.0672	2.45577	4.13
37.3454	165.38	0.1536	2.40597	0.87
39.4789	1011.53	0.0864	2.28072	5.3
39.5942	544.78	0.0384	2.28	2.85
40.3125	583.43	0.0768	2.23546	3.06
41.1601	269.54	0.1344	2.19136	1.41
42.4688	883.35	0.0768	2.12682	4.63
42.5877	473.32	0.0672	2.12642	2.48
43.8099	24.77	0.4608	2.06477	0.13
44.9541	159.27	0.2688	2.01484	0.83
45.8016	530.03	0.096	1.97951	2.78
45.935	272.48	0.0576	1.97897	1.43
50.1475	1834.33	0.096	1.81767	9.61
50.2886	979.88	0.0576	1.8174	5.13
51.1029	143.8	0.2304	1.7859	0.75
54.8661	466.38	0.096	1.67198	2.44
55.0399	268.38	0.0768	1.67125	1.41
55.3412	230.09	0.0768	1.65874	1.2
57.264	29.12	0.2304	1.60753	0.15
58.8821	26.57	0.4608	1.56715	0.14
59.9563	1178.9	0.0576	1.54162	6.17
60.1281	595.48	0.096	1.53762	3.12

61.9921	107.82	0.2304	1.49579	0.56
63.4287	47.37	0.3072	1.46532	0.25
64.0244	197.42	0.0768	1.45312	1.03
65.7589	51.35	0.2304	1.41893	0.27
67.7328	658.87	0.0864	1.3823	3.45
67.9216	396.66	0.0768	1.38235	2.08
68.1268	873.3	0.096	1.37526	4.57
68.3266	820.98	0.1056	1.37173	4.3
70.4573	24.08	0.6144	1.33538	0.13
73.4806	208.1	0.1344	1.28772	1.09
73.6884	121.27	0.1152	1.28779	0.63
75.6293	270.7	0.1344	1.25638	1.42

DC 215 1316’

Pos. [−2Th.]	Height [cts]	FWHM [−2Th.]	d-spacing [Å]	Rel. Int. [%]
7.9324	93.74	0.5038	11.14593	0.58
8.9348	261.34	0.0945	9.89757	1.63
11.9214	38.62	0.1889	7.42381	0.24
14.7749	255.75	0.0236	5.99584	1.59
15.5579	260.43	0.063	5.6958	1.62
16.1625	131.95	0.063	5.48408	0.82
16.4947	722.02	0.0354	5.37438	4.5
17.8655	155.1	0.2519	4.96497	0.97
19.2677	49.93	0.0945	4.60671	0.31
19.8785	443.8	0.126	4.46651	2.77
20.9495	5465.61	0.0672	4.23702	34.05
20.9998	2484.69	0.0288	4.23749	15.48
21.9337	97.99	0.096	4.04906	0.61
24.1035	159.7	0.1152	3.68926	1
24.7306	115.62	0.1152	3.59711	0.72
25.3876	177.25	0.1152	3.50549	1.1
25.8877	146.46	0.192	3.4389	0.91
26.7209	16049.36	0.0624	3.33353	100
26.7947	7118	0.024	3.33278	44.35
28.1376	334.15	0.0576	3.16882	2.08
29.329	274.84	0.0576	3.04276	1.71
29.509	283.08	0.0576	3.0246	1.76
29.9704	120.99	0.2304	2.97908	0.75
30.2911	227.3	0.0384	2.94827	1.42
30.6268	322.54	0.0384	2.91671	2.01
31.0124	714.04	0.1728	2.88132	4.45

32.2746	40.83	0.2304	2.77146	0.25
32.9022	234.95	0.0672	2.72001	1.46
33.2994	228.46	0.0576	2.68847	1.42
34.6308	126.46	0.1536	2.5881	0.79
35.132	279.78	0.2688	2.55231	1.74
36.6049	1331.13	0.0864	2.45293	8.29
36.7079	699.9	0.0576	2.45236	4.36
37.4099	110.4	0.3072	2.40197	0.69
39.53	949.95	0.0624	2.27789	5.92
39.6433	460.74	0.0384	2.27729	2.87
39.9205	57.18	0.0576	2.2565	0.36
40.3414	548.72	0.0864	2.23393	3.42
40.4751	282.68	0.0672	2.23239	1.76
41.2098	228.42	0.0768	2.18883	1.42
42.5098	1115.94	0.0864	2.12486	6.95
42.6254	574.22	0.048	2.12463	3.58
43.2535	137.62	0.048	2.09003	0.86
44.9929	123.31	0.1536	2.01319	0.77
45.8542	539.19	0.0768	1.97736	3.36
45.9761	274.3	0.0768	1.9773	1.71
47.5906	56.02	0.192	1.90918	0.35
48.1273	11.46	0.2304	1.88914	0.07
48.5915	57.3	0.0576	1.87217	0.36
49.2075	40.8	0.2304	1.85017	0.25
50.1934	1554.52	0.1056	1.81611	9.69
50.34	761.58	0.0768	1.81567	4.75
51.158	96.57	0.3072	1.78411	0.6
51.9476	55.71	0.192	1.75883	0.35
53.1187	18.29	0.384	1.72278	0.11
54.2174	64.43	0.2304	1.69044	0.4
54.9171	502.29	0.0864	1.67054	3.13
55.0736	296.85	0.0768	1.6703	1.85
55.3824	211.46	0.096	1.6576	1.32
56.5315	46.04	0.6144	1.62661	0.29
57.3047	33.87	0.2304	1.60648	0.21
58.7505	22.15	0.4608	1.57035	0.14
60.0089	1085.91	0.096	1.54039	6.77
60.1471	600.74	0.0576	1.541	3.74
62.0954	141.22	0.2304	1.49355	0.88
63.6146	38.22	0.4608	1.46149	0.24
64.0671	143.69	0.1152	1.45225	0.9
64.7538	61.92	0.0768	1.4385	0.39
65.7991	52.71	0.1152	1.41816	0.33

67.7678	551.49	0.1152	1.38167	3.44
67.9872	332.18	0.0768	1.38117	2.07
68.201	696.46	0.1152	1.37395	4.34
68.3496	734.53	0.1152	1.37132	4.58
70.3677	32.3	0.4608	1.33686	0.2
73.5268	175.22	0.1152	1.28702	1.09
73.7408	83.53	0.1152	1.28701	0.52
75.6639	289.95	0.1344	1.25589	1.81

DC 215 1569’

Pos. [−2Th.]	Height [cts]	FWHM [−2Th.]	d-spacing [Å]	Rel. Int. [%]
8.962	261.13	0.1574	9.86754	2.53
10.0306	243.34	0.0787	8.81862	2.35
13.9182	156.82	0.063	6.36294	1.52
15.7163	87.18	0.126	5.63877	0.84
17.2841	114.7	0.0945	5.13066	1.11
17.5307	324.56	0.063	5.05904	3.14
19.2871	210.87	0.0787	4.60211	2.04
19.9299	281.62	0.1102	4.4551	2.72
20.9669	4566.64	0.0384	4.23354	44.16
21.0309	1951.55	0.0336	4.23128	18.87
22.1488	46.06	0.1152	4.01023	0.45
22.5963	76.18	0.1536	3.93182	0.74
24.1399	202.97	0.096	3.68378	1.96
24.9647	245.18	0.1152	3.5639	2.37
25.0596	267.69	0.1152	3.55063	2.59
25.4178	69.85	0.1152	3.50139	0.68
25.9764	110.26	0.1152	3.42736	1.07
26.7523	10341.75	0.0624	3.32969	100
26.817	5459.83	0.0336	3.33005	52.79
27.8972	1062.87	0.0672	3.19558	10.28
29.113	684.02	0.1536	3.06483	6.61
30.1917	101.38	0.192	2.95774	0.98
31.0227	2327.94	0.0864	2.88039	22.51
31.0708	2490.78	0.0576	2.88318	24.08
31.8695	408.46	0.0576	2.80575	3.95
32.3425	569.74	0.1536	2.76579	5.51
32.7734	262.79	0.1152	2.73041	2.54
33.6565	177.8	0.1152	2.66075	1.72
34.5272	105.72	0.1152	2.59563	1.02
34.8126	214.9	0.0768	2.57499	2.08

35.413	202.36	0.2688	2.5327	1.96
36.6356	1103.17	0.096	2.45094	10.67
36.7413	588.83	0.048	2.4502	5.69
37.4675	203.66	0.1728	2.39841	1.97
38.6772	56.16	0.192	2.32613	0.54
39.5634	502.2	0.0576	2.27605	4.86
39.6697	257.6	0.0576	2.27583	2.49
40.3725	403.63	0.0576	2.23228	3.9
40.4943	230.38	0.0576	2.23137	2.23
41.2262	627.06	0.1152	2.18801	6.06
41.7273	168.3	0.1344	2.16288	1.63
42.5404	830.1	0.0768	2.1234	8.03
42.6511	454.53	0.0576	2.12341	4.4
43.8865	121.96	0.0768	2.06134	1.18
44.4563	43.57	0.2304	2.03623	0.42
45.0294	334.45	0.1152	2.01164	3.23
45.8665	354.24	0.096	1.97686	3.43
48.1079	159.09	0.096	1.88986	1.54
48.7443	87.95	0.192	1.86666	0.85
49.3628	80.97	0.1536	1.84471	0.78
50.2265	1029.74	0.0864	1.81499	9.96
50.3481	615.19	0.0576	1.81539	5.95
50.6282	338.73	0.2304	1.80153	3.28
51.1739	367.75	0.1536	1.78359	3.56
53.2532	115.44	0.1536	1.71875	1.12
54.1499	114.37	0.192	1.69239	1.11
54.9519	313.2	0.0768	1.66957	3.03
55.1037	193.84	0.0768	1.66947	1.87
55.3941	134.7	0.0576	1.65728	1.3
56.3364	46.88	0.6144	1.63178	0.45
57.4608	80.47	0.0768	1.60249	0.78
58.445	54.79	0.2304	1.57783	0.53
58.9817	76.12	0.1152	1.56474	0.74
60.0352	866.19	0.0576	1.53978	8.38
60.1961	463.93	0.096	1.53605	4.49
62.0658	100.04	0.4608	1.49419	0.97
63.5159	101.34	0.1536	1.46352	0.98
64.1092	110.73	0.1344	1.4514	1.07
65.1931	71.14	0.384	1.42987	0.69
65.8375	54.43	0.2304	1.41743	0.53
66.4664	47.68	0.2304	1.40553	0.46
67.4618	134.92	0.1536	1.38719	1.3
67.8026	424.78	0.1152	1.38105	4.11

67.9854	257.09	0.0576	1.3812	2.49
68.2017	488.34	0.096	1.37394	4.72
68.3984	533.78	0.0672	1.37046	5.16
70.5414	72.22	0.3072	1.33399	0.7
73.0766	39.55	0.3072	1.29384	0.38
73.5213	117.26	0.0768	1.28711	1.13
74.7502	30.19	0.2304	1.26896	0.29
75.6796	172.59	0.1536	1.25567	1.67

Appendix F2. X-Ray Diffraction (X'Pert Highscore)

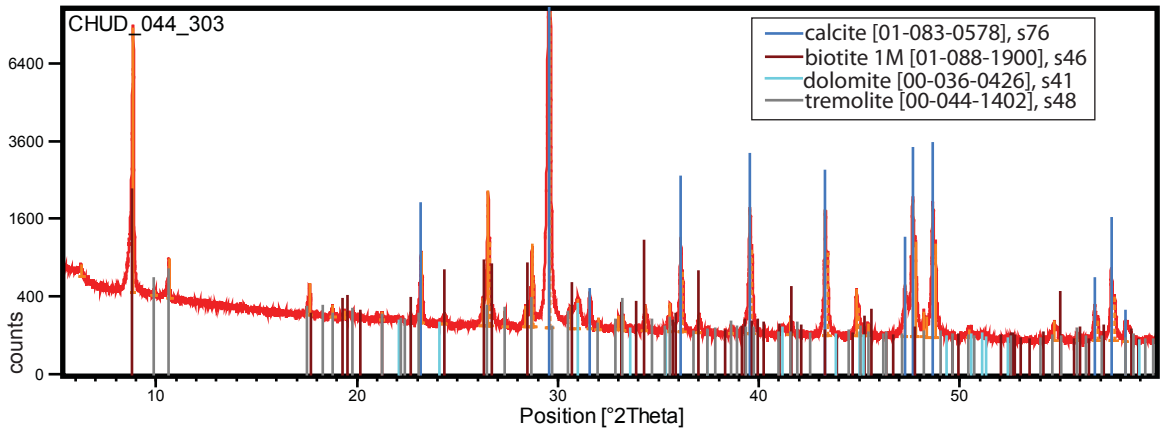

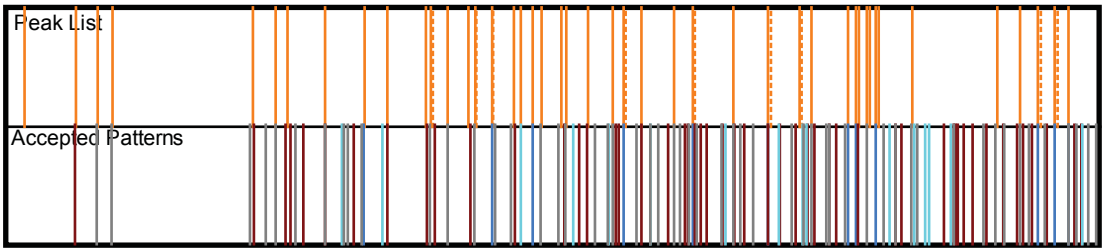

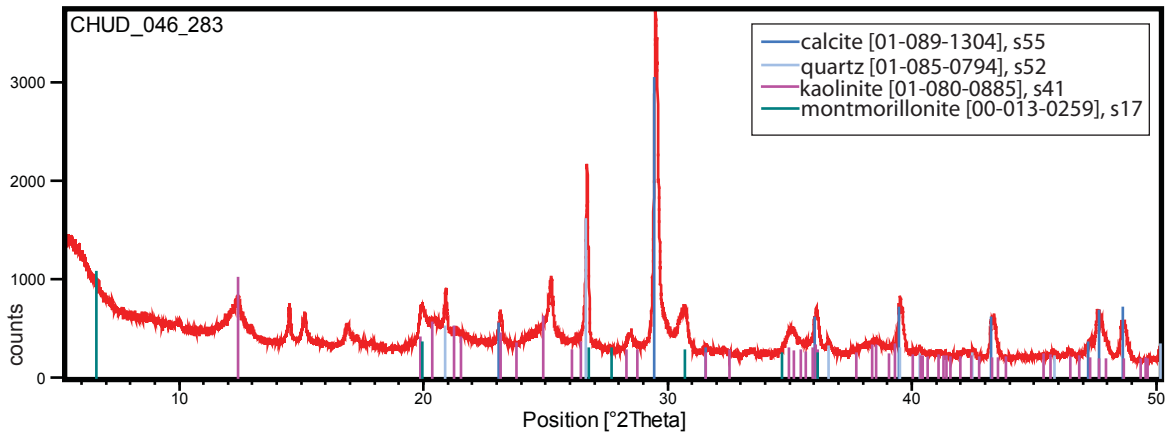

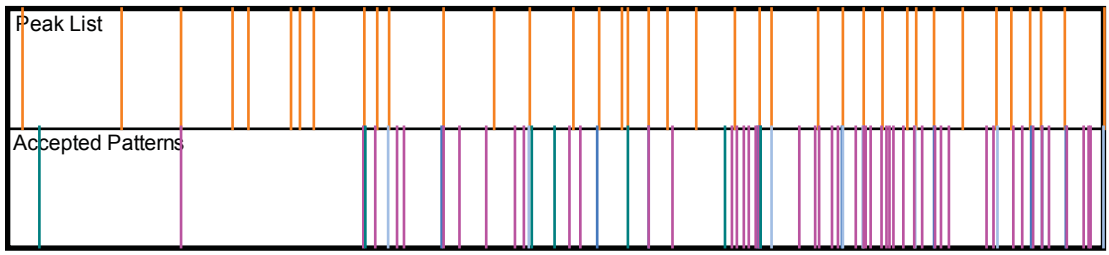

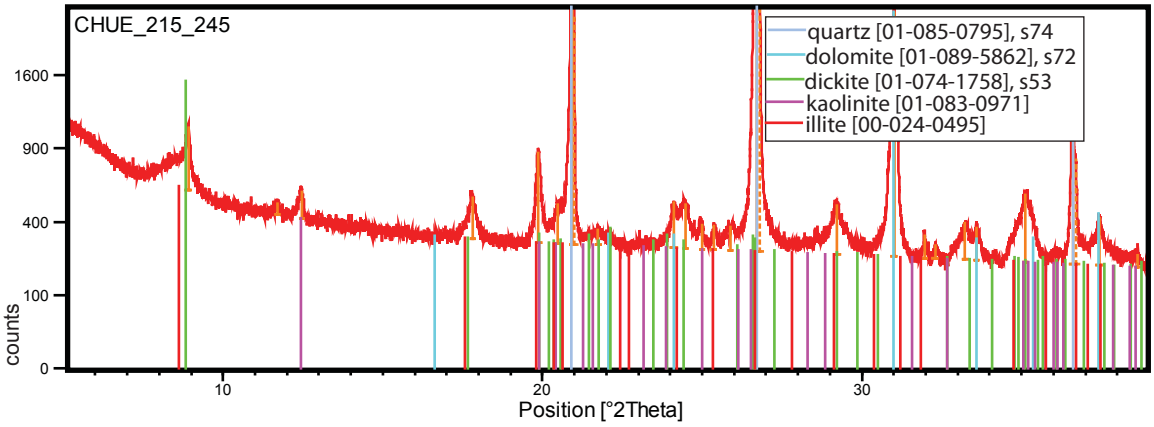
CHUE_215_245
quartz [01-085-0795], s74
dolomite [01-089-5862], s72
dickite [01-074-1758], s53
kaolinite [01-083-0971]
illite [00-024-0495]
counts
Position [°2Theta]

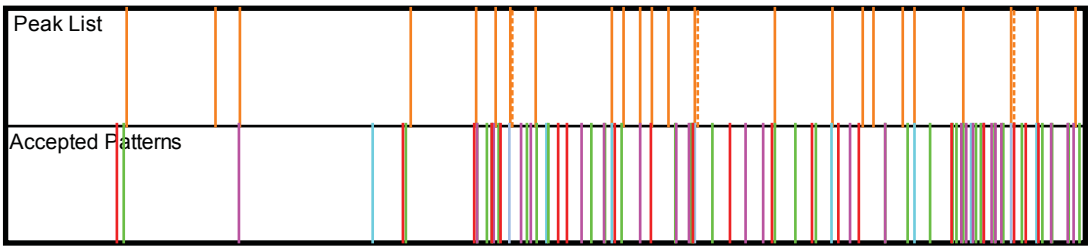
Peak List
Accepted Patterns

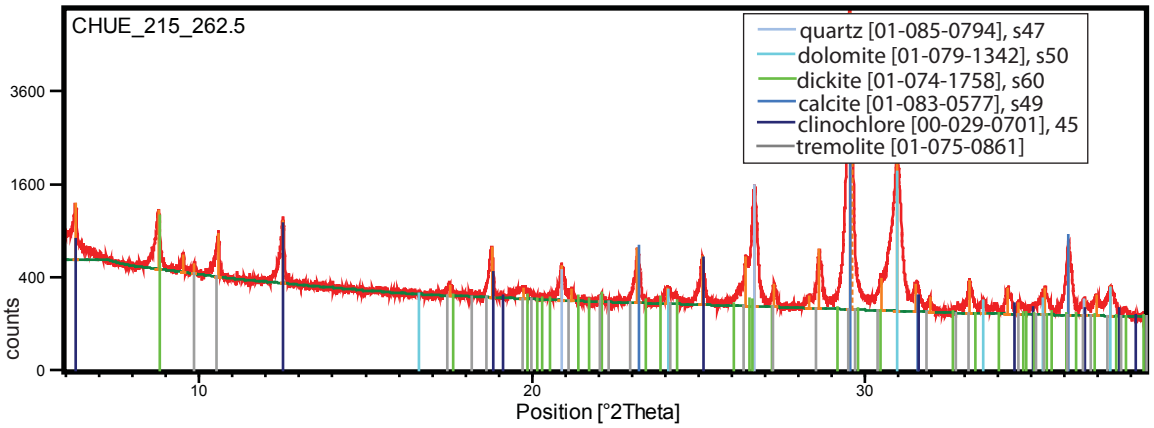
CHUE_215_262.5
quartz [01-085-0794], s47
dolomite [01-079-1342], s50
dickite [01-074-1758], s60
calcite [01-083-0577], s49
clinochlore [00-029-0701], 45
tremolite [01-075-0861]
counts
Position [°2Theta]

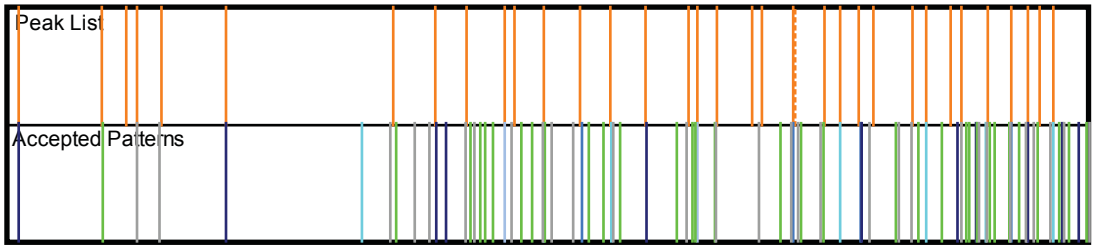
Peak List
Accepted Patterns

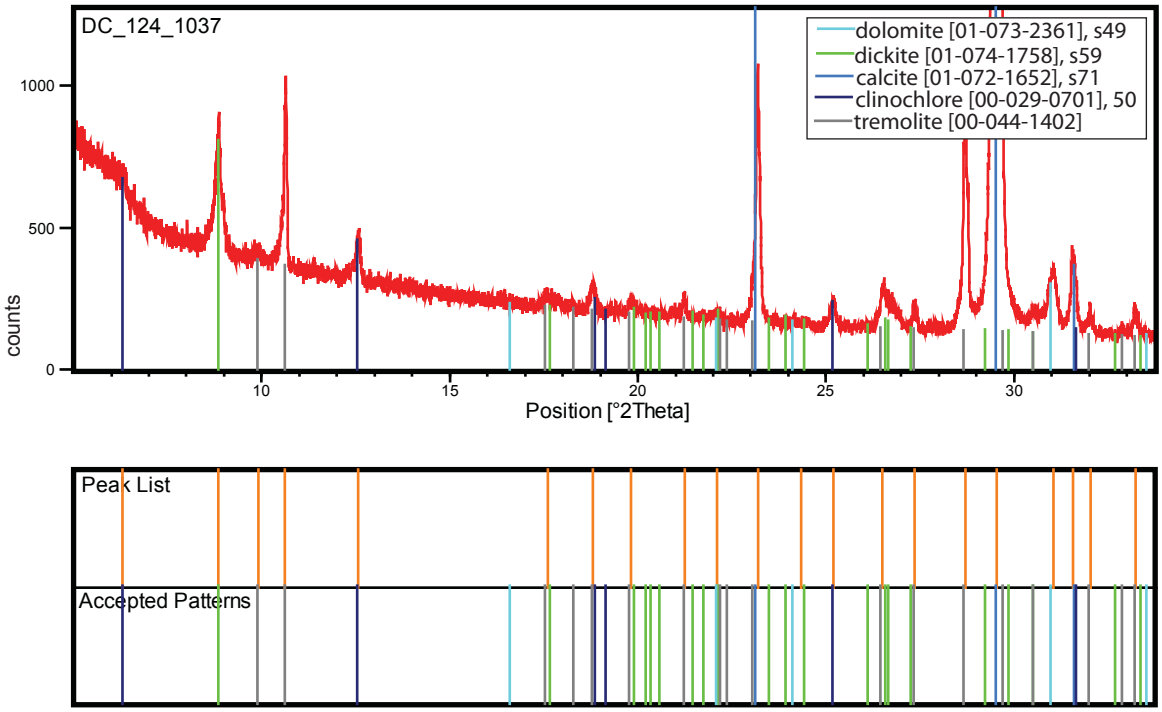
DC_124_1037
dolomite [01-073-2361], s49
dickite [01-074-1758], s59
calcite [01-072-1652], s71
clinochlore [00-029-0701], 50
tremolite [00-044-1402]
counts
1000
500
0
10
15
20
25
30
Position [°2Theta]
Peak List
Accepted Patterns

APPENDIX G

LA-ICP-MS DATA

Trace element relative counts and concentrations were determined by using laser ablation inductively-coupled plasma mass spectrometry (LA-ICP-MS) at the USGS Denver laboratory. A Photon Machines Analyte G2 LA system (193 nm, 4 ns Excimer laser) was coupled to a PerkinElmer DRC-e Inductively Coupled Plasma Mass Spectrometer. Typical operating conditions for these analyses are listed in Table 5.

Pyrite grains were analyzed by performing 5 micrometer spot analyses and line scans. Appendix G1 contains the plotted data for specific elements of interest collected from line scans and mapping of pyrite crystals. Please contact the author or committee chair to obtain the raw line scan data for all elements. Appendix G2 lists spot concentrations calculations conducted by using the protocol of Longerich et al. (1996), and ^{57}Fe was used as the internal standard. Spot data were collected to measure elements that were below EPMA method detection limit (MDL).

Appendix G1. LA-ICP-MS line scans and maps

CHUD 043 376.5’ b

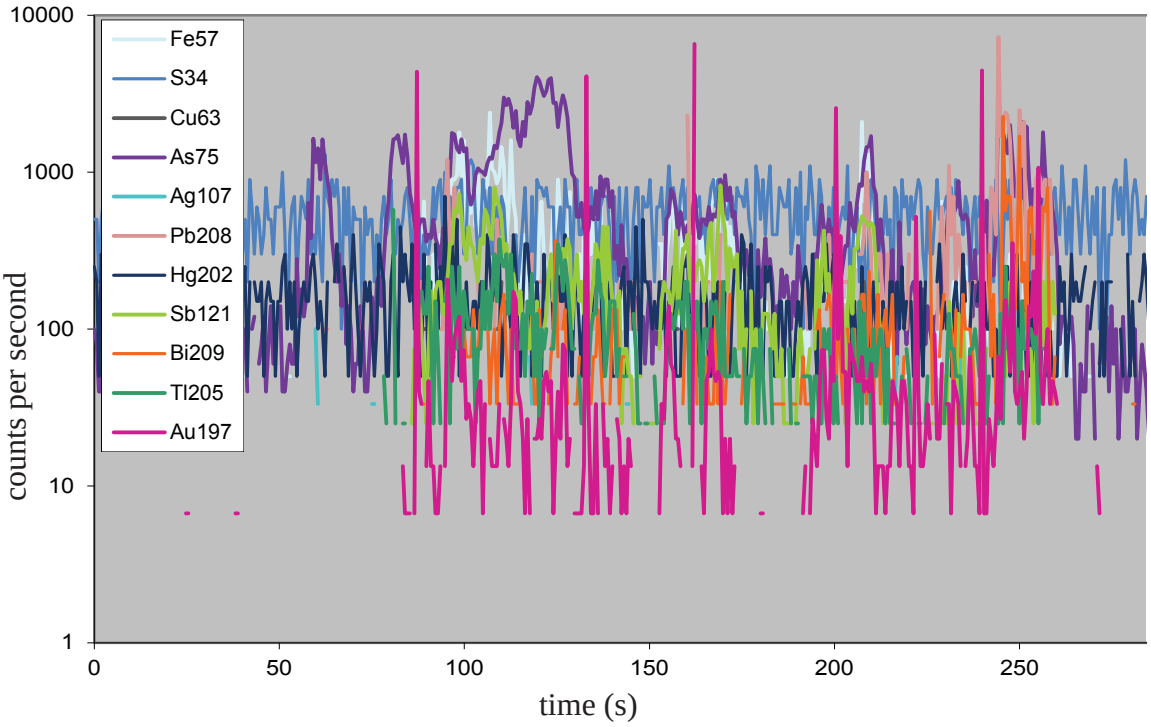

CHUE 019 485.5’g

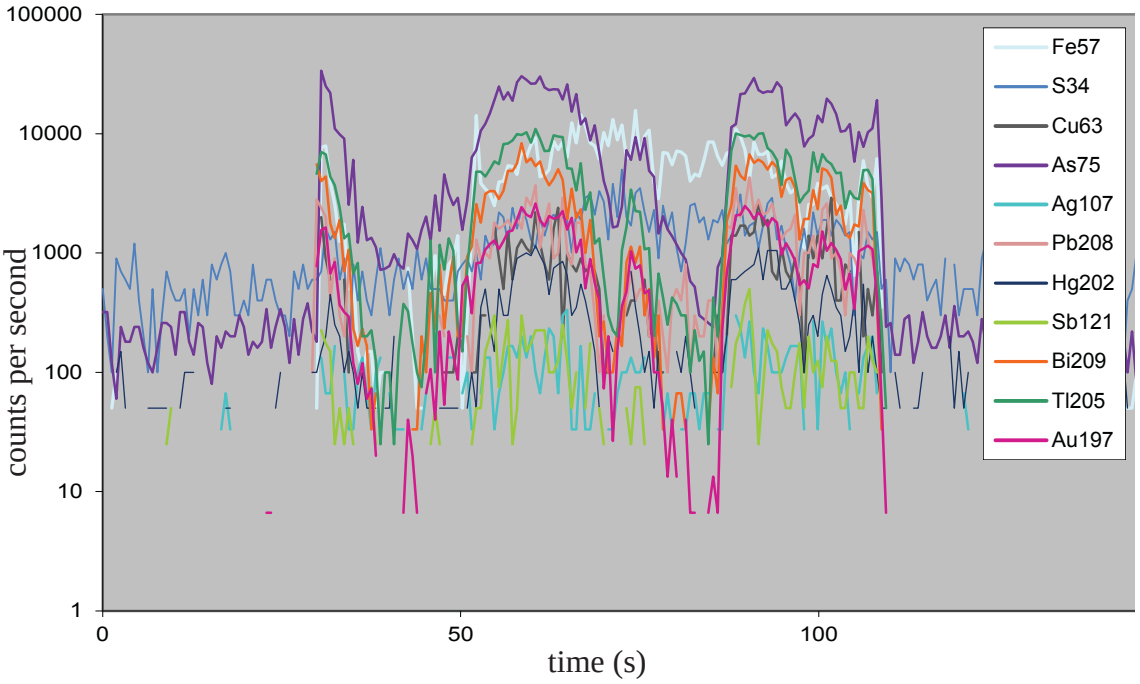

DC 114 1236.5’g

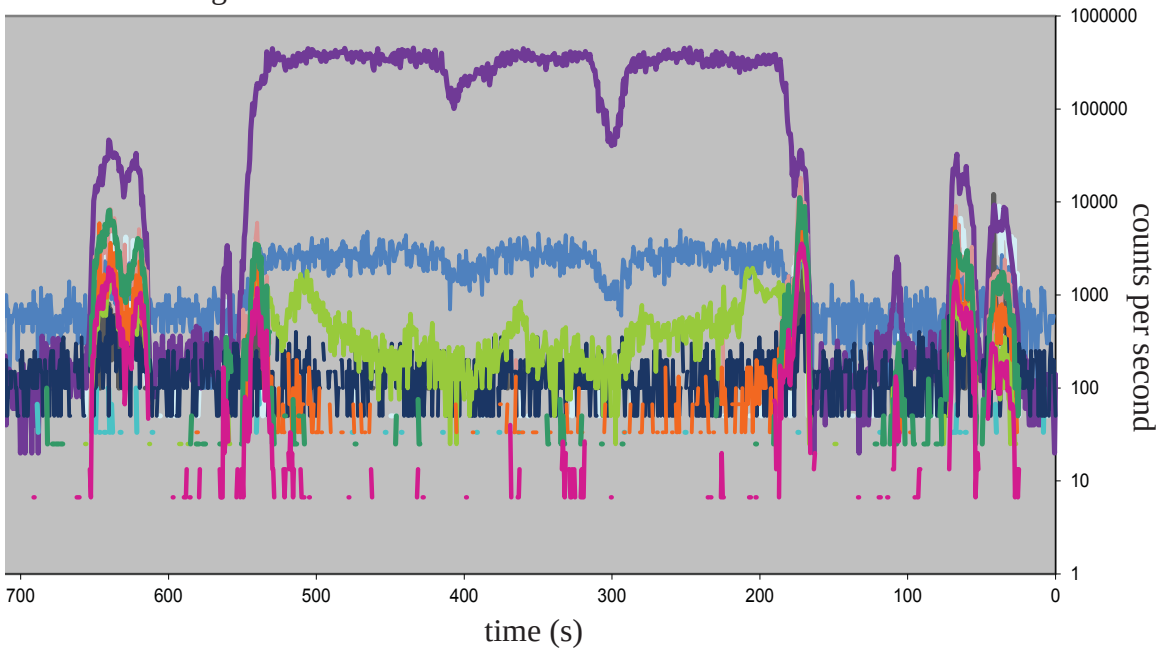

DC 114 1236.5’j

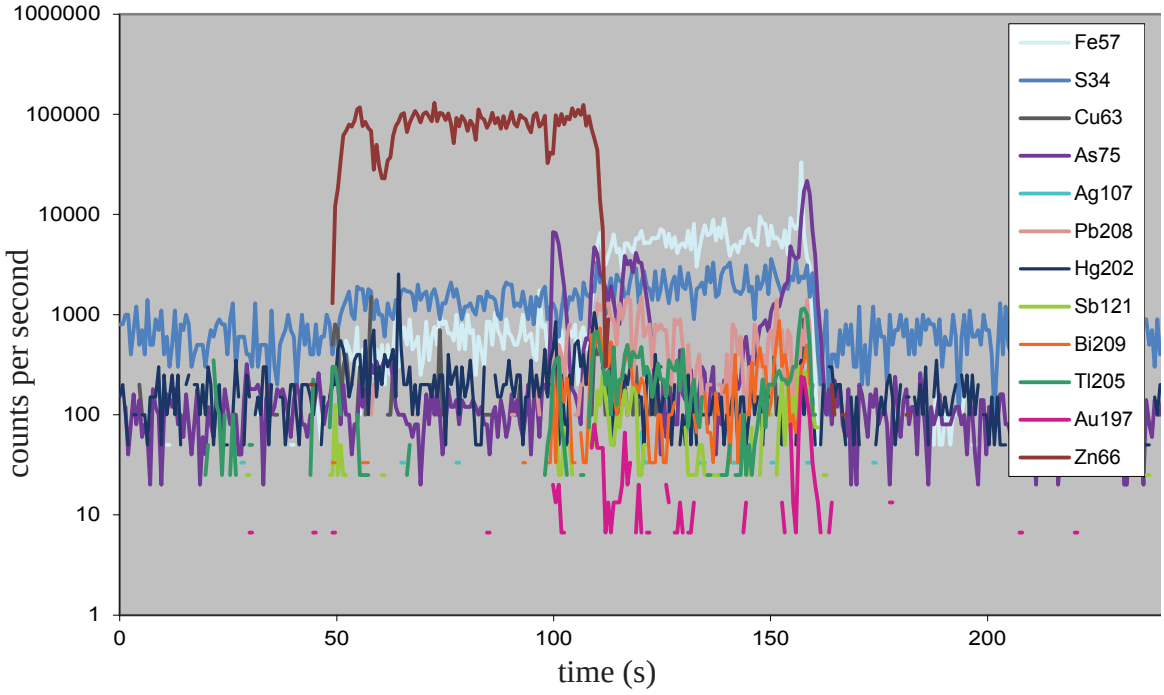

DC 114 1236.5’k

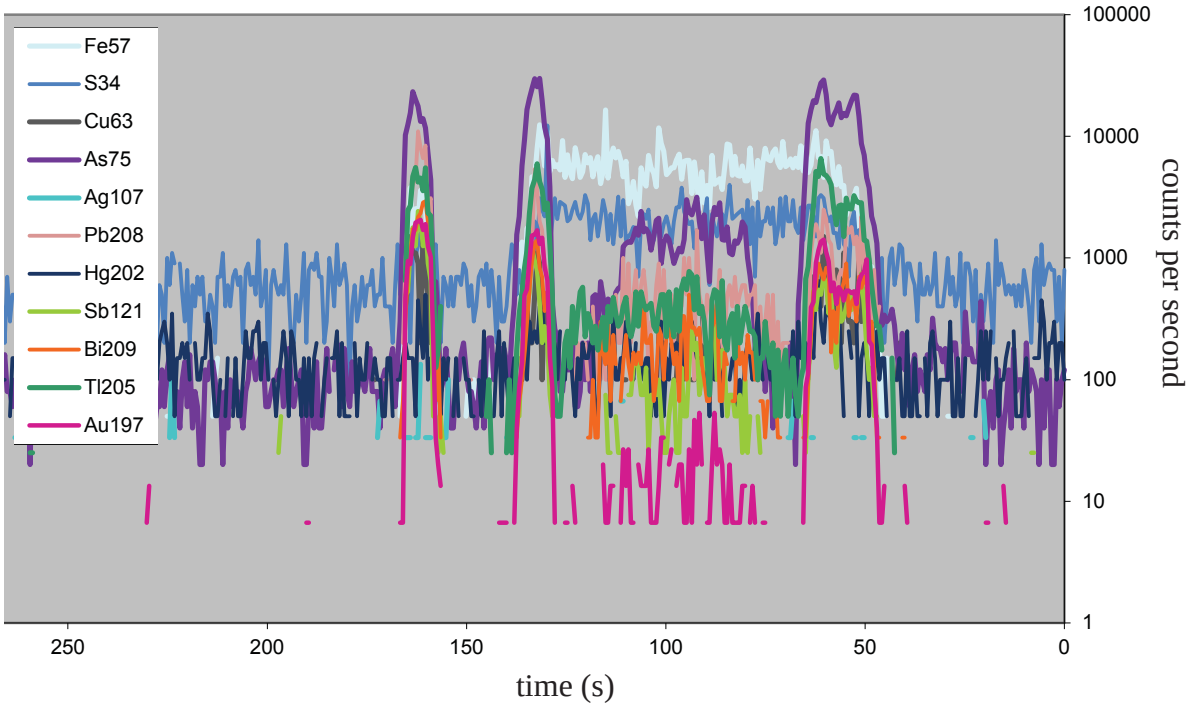

DC 114 1236.5’k2

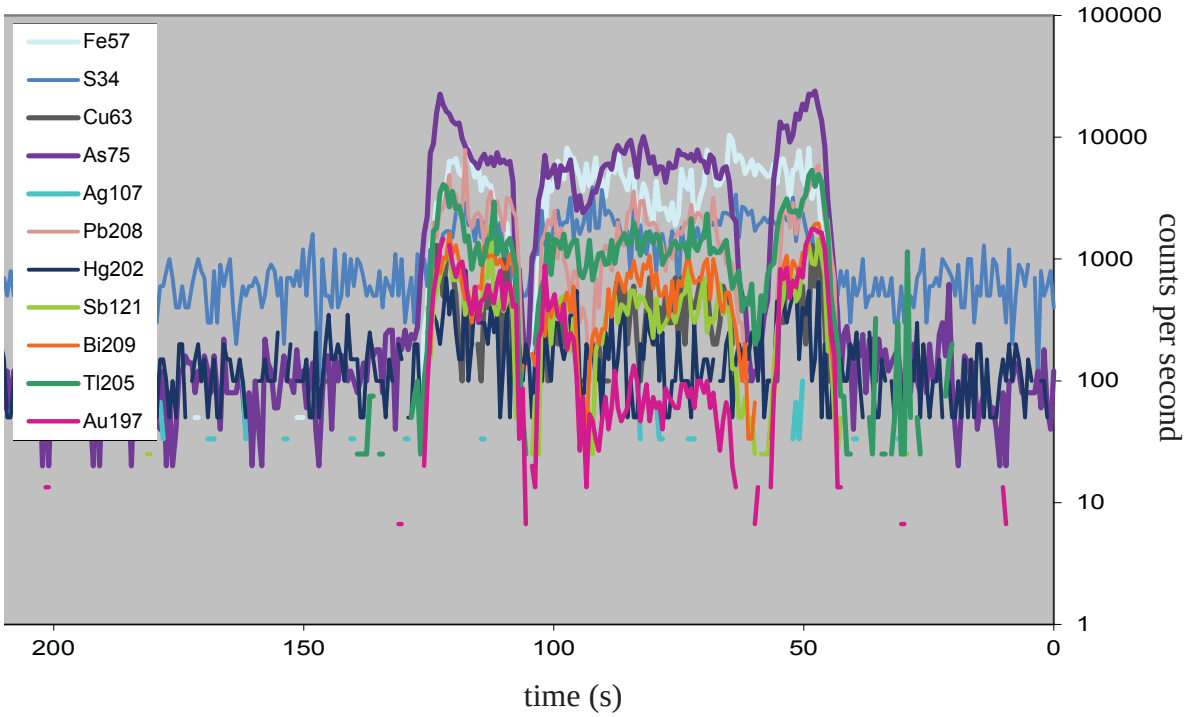

DC 124 1273'h

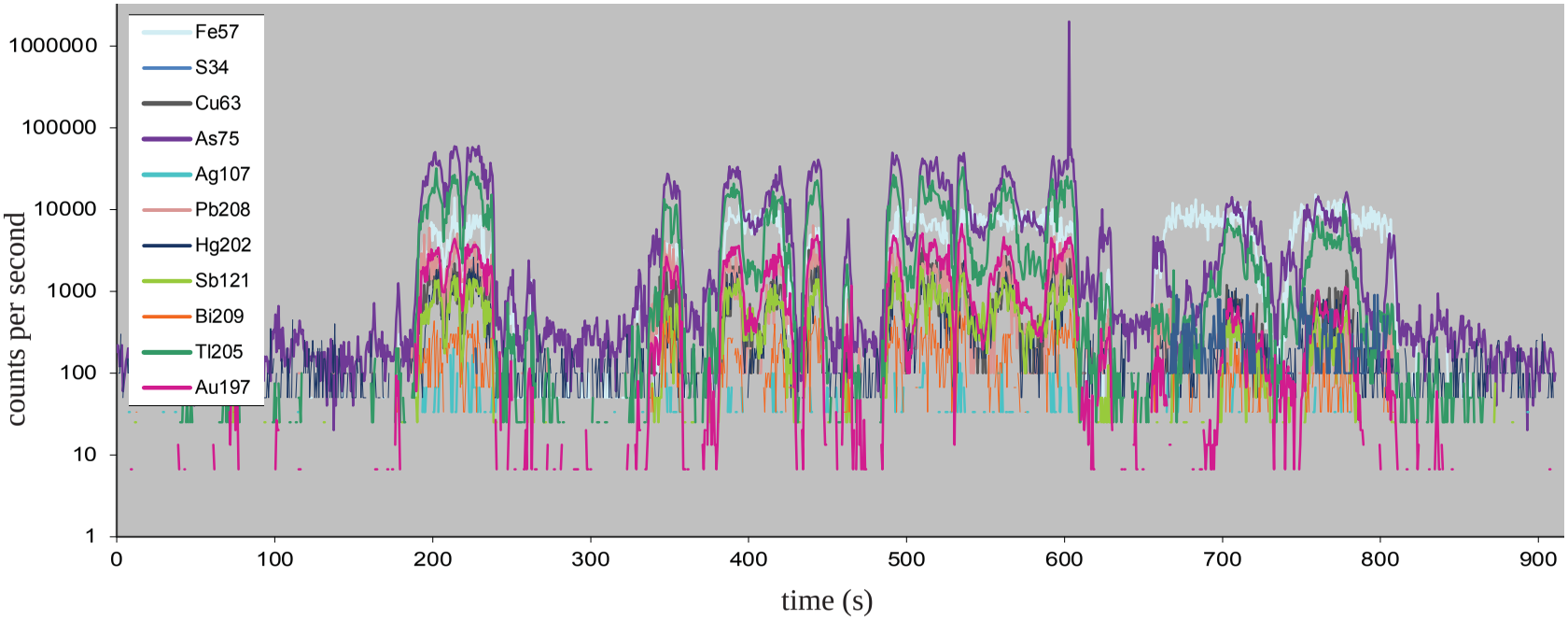
Fe57
S34
Cu63
As75
Ag107
Pb208
Hg202
Sb121
Bi209
Tl205
Au197
1000000
100000
10000
1000
100
10
1
counts per second
0
100
200
300
400
500
600
700
800
900
time (s)

DC 124 1281’c

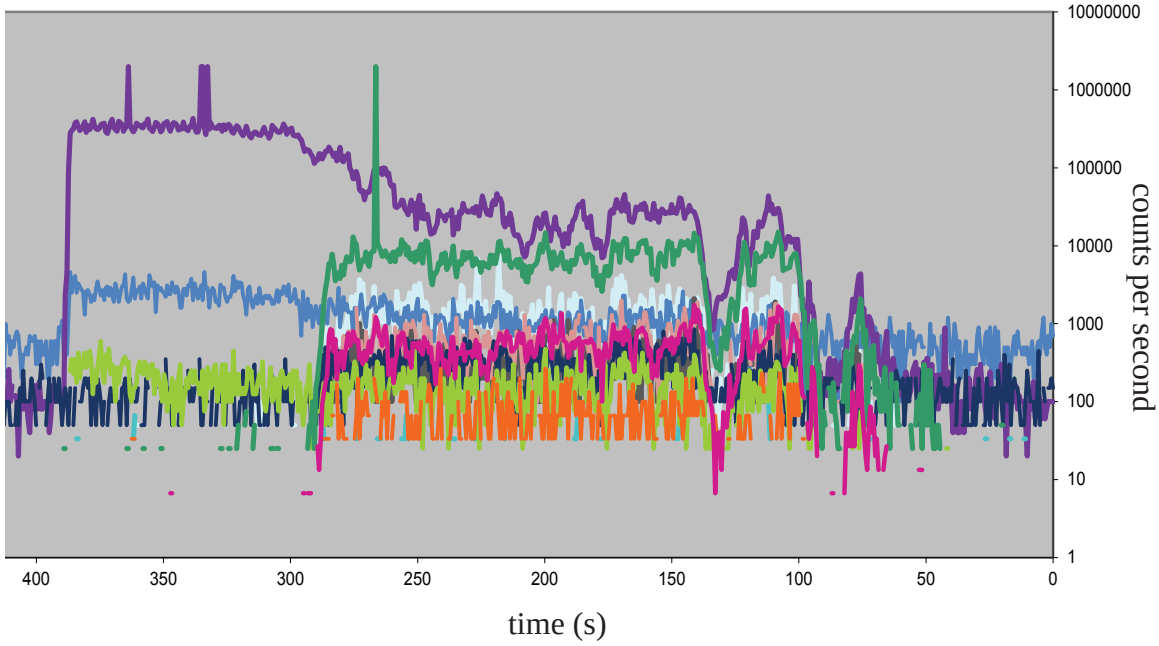

DC 215 1497’c

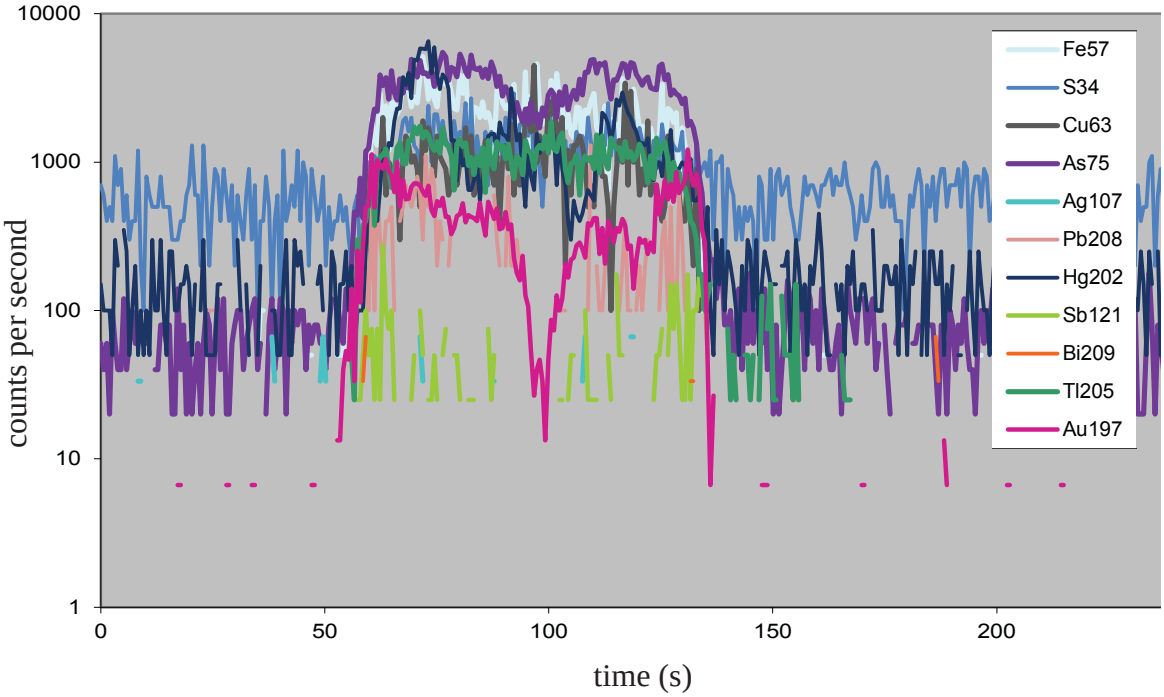

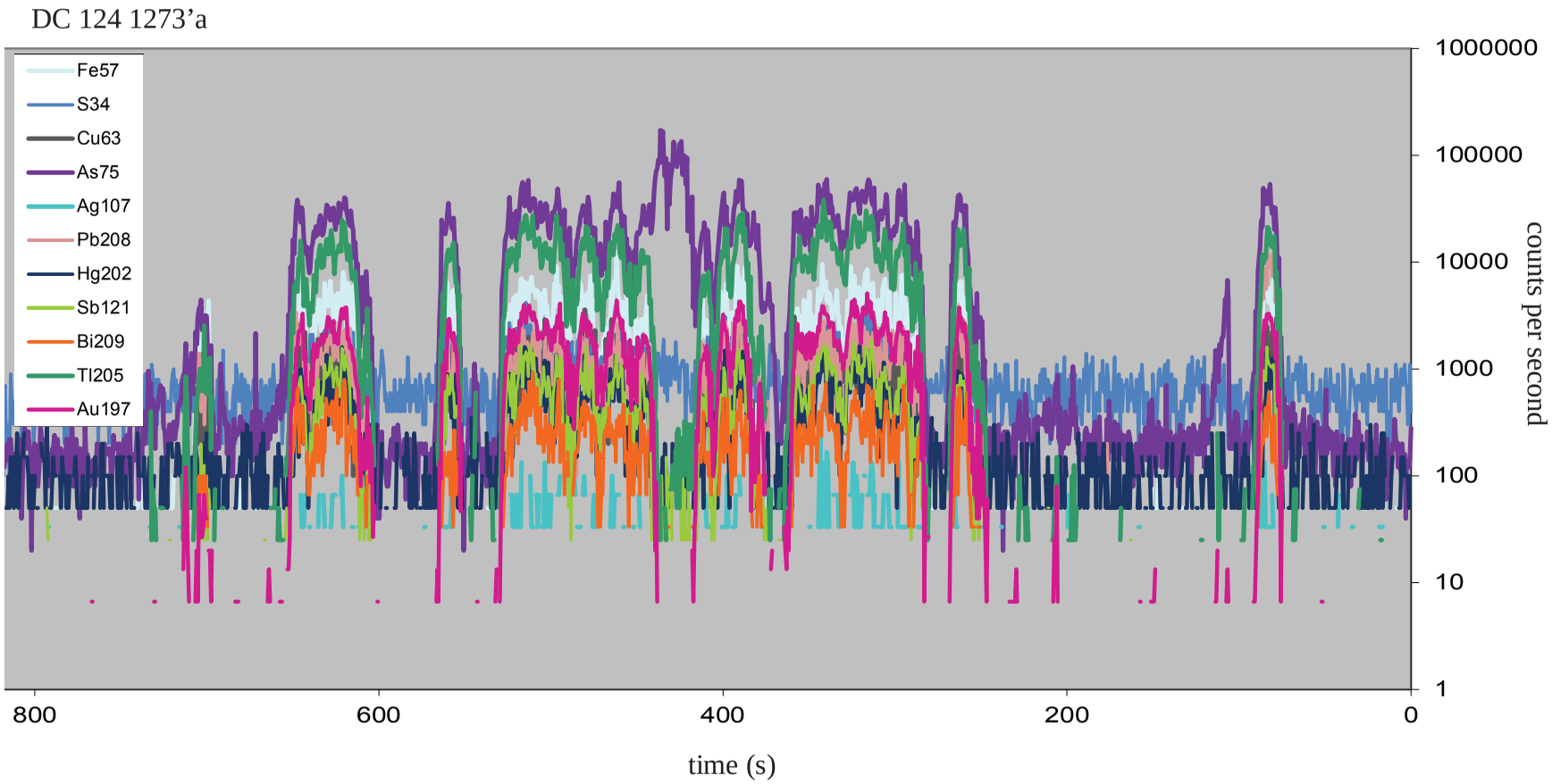
DC 124 1273'a
Fe57
S34
Cu63
As75
Ag107
Pb208
Hg202
Sb121
Bi209
Tl205
Au197
1000000
100000
10000
1000
100
10
1
counts per second
800
600
400
200
0
time (s)

CHUE 215 246.5’d

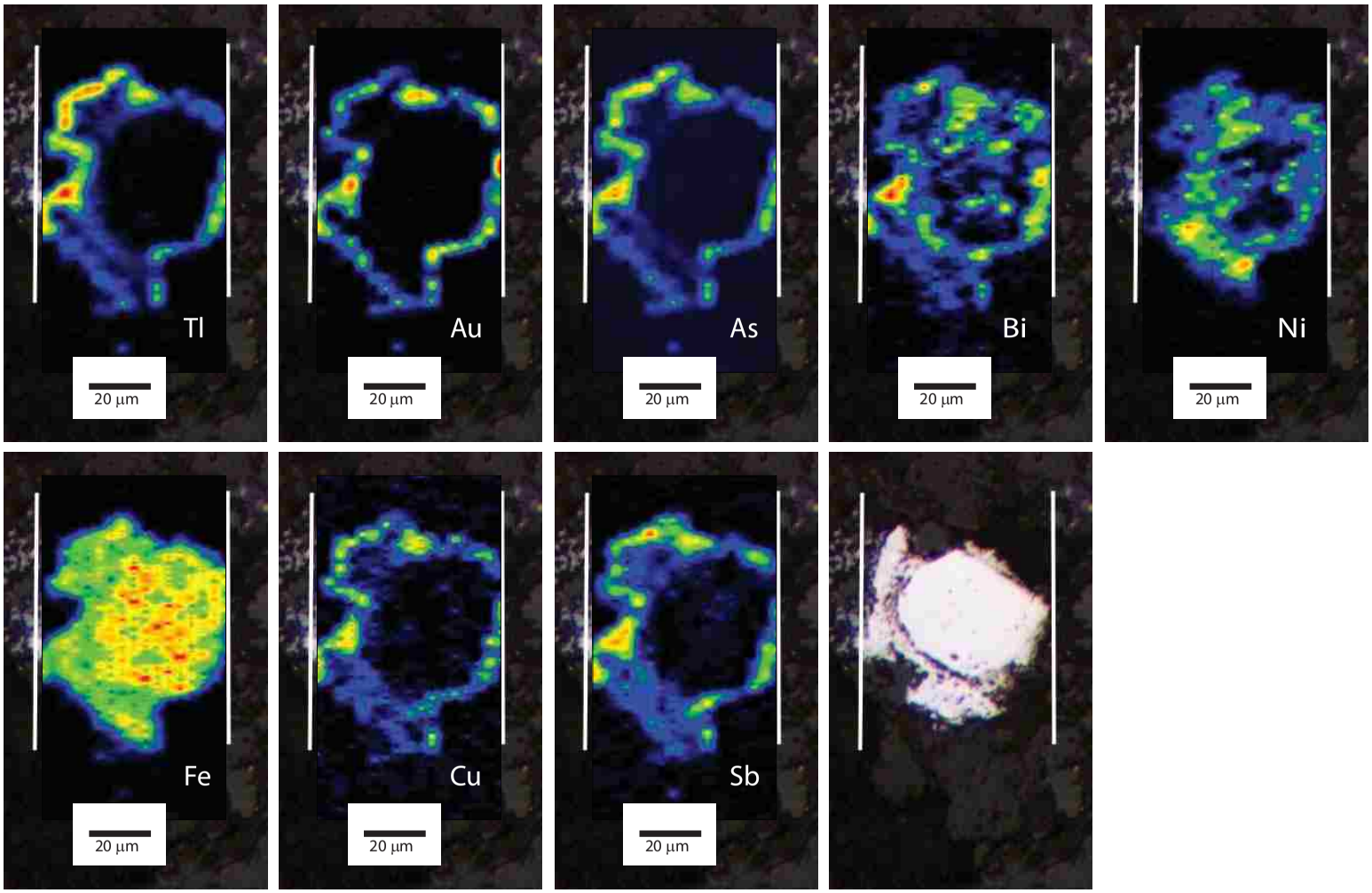

Appendix G2. LA-ICP-MS point data

	Fe (int std)	Co	Ni	Cu	Zn	As	Mo	Ag	Sb	Au	Hg	Tl	Pb	Bi
Day1 D.L.	4190.0	64.4	126.4	677.1	593.2	312.1	36.2	29.9	25.3	8.1	602.3	4.8	25.2	6.5
Day2 D.L.	5593.0	103.4	162.6	47.3	488.6	884.9	37.3	22.1	13.2	6.6	301.0	4.1	21.4	4.5

Day1	Fe57	Co59	Ni60	Cu63	Zn66	As75	Mo98	Ag107	Sb121	Au197	Hg202	Tl205	Pb208	Bi209
CHUE 019 485.5'g	450000	84	242			1158			28	152		286	107	100
CHUE 019 485.5'g	450000	324	583						72			27	290	142
CHUE 019 485.5'g	450000		162	2100		12851		104	161	1859		2575	557	875
CHUE 019 485.5'g	400000			1433		8703		58	77	681		1209	279	543
CHUE 019 485.5'g	400000			4327		29536		197	275	2326	760	4605	1181	2535
CHUE 019 485.5'g	400000			2733		28052		89	328	2076		4147	814	2183
CHUE 019 485.5'd	450000					2310			108	87		353		23
CHUE 019 485.5'd	450000					2595			102	108		253	31	25
CHUE 019 485.5'd	450000			1573		3343			64	78		439	27	64
CHUE 019 485.5'd	400000			3730		19529		106	250	2832		4103	903	1681
CHUE 019 485.5'd	400000			4983		17988		186	312	2832	759	4178	869	1716
CHUE 019 485.5'd	450000					3119			50	48		329		19
CHUE 019 485.5'd	450000					3181			70	42		257	28	25
CHUE 019 485.5'd	400000		139	5812		20947		185	327	3388	854	4610	1166	1927
CHUE 019 485.5'd	400000			6357		20180		211	289	3181	814	4804	1080	2314
DC 124 1264'b	390000					20386	39		8417		2715	13752	5666	34
DC 124 1264'b	430000					9118			3240		1665	6810	159	
DC 124 1264'b	430000					8177			2563		1374	5985		
DC 124 1264'a	430000	90				13898			1882		620	9114	1400	
DC 124 1264'a	430000					23275	38		2115	12		14919	1318	
CHUE 215 246.5'd	470000		2369	1449		8453	41	229	460	1270		971	219	72
CHUE 215 246.5'd	470000		383	1121		15769		51	511	1218		1719	156	67
CHUE 215 246.5'd	470000	191	1359	773		3577		90	250	1480		422	195	84
CHUE 215 246.5'd	470000		576											14
CHUE 215 246.5'd	430000		867					47	121			125		30
CHUE 215 246.5'd	430000		1371	873		6104		128	261	449		690	142	50

Day1	Fe57	Co59	Ni60	Cu63	Zn66	As75	Mo98	Ag107	Sb121	Au197	Hg202	Tl205	Pb208	Bi209
CHUE 215 246.5'd	430000		1189			353		36		16		41		8
CHUE 215 246.5'd	430000	64	1603			4822		128	190	271		483	141	59
CHUE 215 246.5'f	420000		325	1172		7400		112	217	624		804	141	44
CHUE 215 246.5'f	420000		1144	1806		5672		202	536	1027		802	212	76
CHUE 215 246.5'f	460000								71			8	157	38
CHUE 215 246.5'c	440000	108	687	1793		17390		372	920	2373		1285	401	101
CHUE 215 246.5'c	440000	67	1074	2667		13673	50	252	741	2065		1689	413	109
CHUE 215 246.5'c	440000		962	2125		9386		282	425	1499		1521	454	78
DC 124 1273'f	370000			4803		23311			981	1590	757	4614	207	16
DC 124 1273'f	370000	129		4282	107819	67911			1751	3490		7658	360	32
DC 124 1273'h	460000					3516			368	279		436		
DC 124 1273'h	460000					3457			322	348		474	29	
DC 124 1273'h	380000	147	267			627						163		
DC 124 1273'h	380000	165	270			1597						262	41	12
DC 124 1273'h	380000	211		1308		4797			207	375		1056	38	
DC 124 1273'h	380000	169	389			1332			44	67		484		
DC 124 1273'h	380000	212	689			618				18		237		
DC 124 1273'h	380000	134	451			1361				10		225		

Day 2	Fe57	Co59	Ni60	Cu63	Zn66	As75	Mo98	Ag107	Sb121	Au197	Hg202	Tl205	Pb208	Bi209
DC 124 1273'g	440000			5030		68058		34	1056	3147	1366	6462	392	22
DC 124 1273'g	440000			5474		68688			892	3152	1618	6552	343	28
DC 124 1273'g	440000			3862		34542			539	1557	900	3189	187	16
CHUE 119 326'b	380000		527		12195	6557			166	667			774	57
CHUE 119 326'b	380000	172	192		1337	2935			308	1028			1094	132
DC 114 1236.5'i	440000			3132		69179		38	2354	2396		2668	4464	1176
DC 114 1236.5'i	440000		371	4608		84923		35	2584	3009	715	2685	4822	1328
DC 114 1236.5'i	440000		961			3864			179	45		329	68	
DC 114 1236.5'i	440000			1566		5910			238	72		578	489	136

Abbreviations: D.L. = detection limit

APPENDIX H

LA-ICP-MS AND EPMA POINT LOCATIONS

This appendix is composed of photomicrographs that display the crystals that EPMA and LA-ICP-MS data were collected from. In the top left corner of each photomicrograph, the drill hole (ie. CHUD 038), footage (ie. 453'), and area within the sample (ie. b2) are typed. The location of each analytical spot is shown as a small solid black or white circle for EPMA data and a larger black circle with a white filling for each LA-ICP-MS spot. The name of each analytical spot is labeled adjacent to the circle. The solid long white and black lines indicate the locations of LA-ICP-MS line scans. The hollow large rectangles indicate the locations of LA-ICP-MS pyrite maps. All data collected from points, scans, and maps are reported in Appendix E (EPMA) and G (LA-ICP-MS).

Appendix H. LA-ICP-MS and EPMA point locations

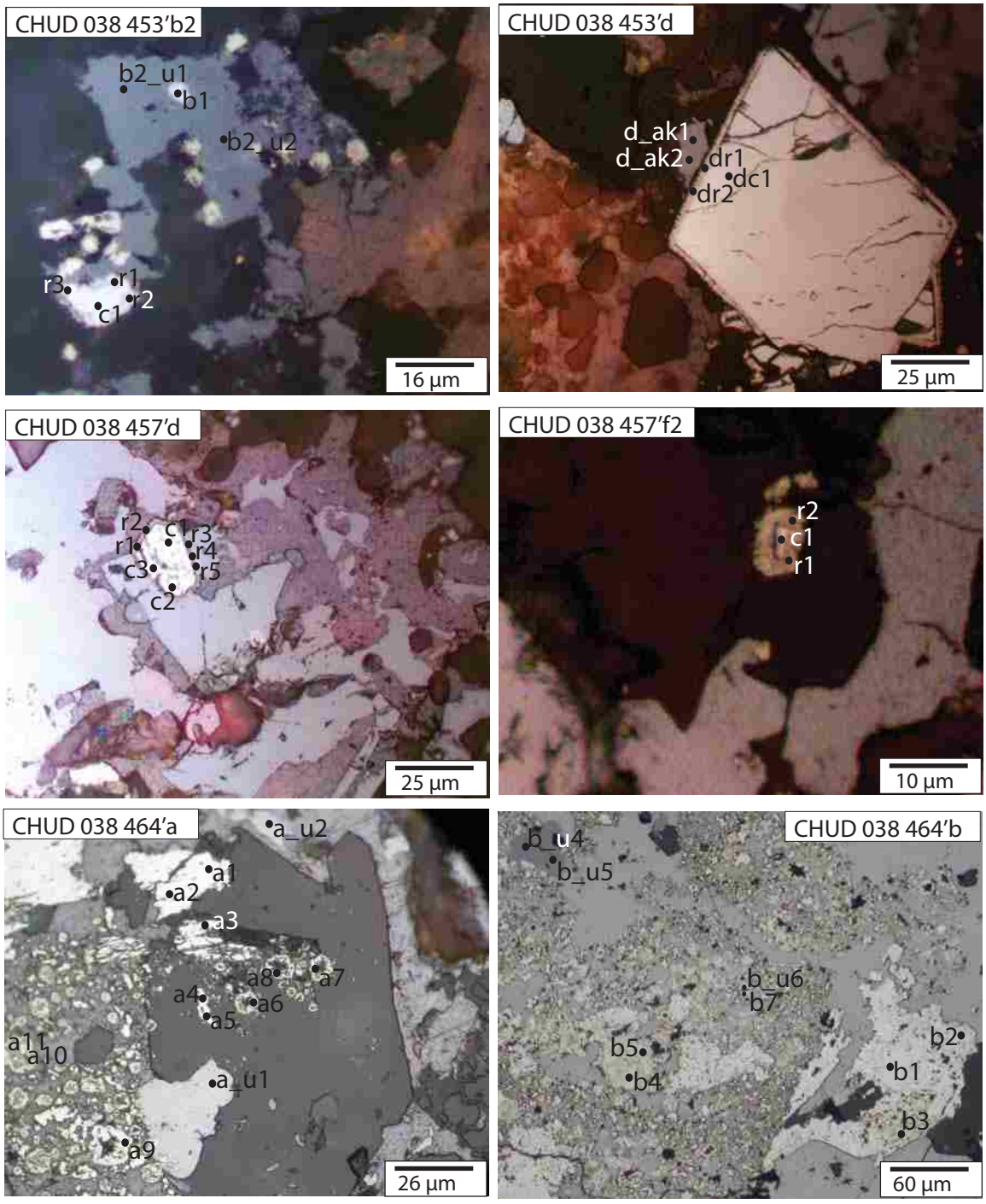

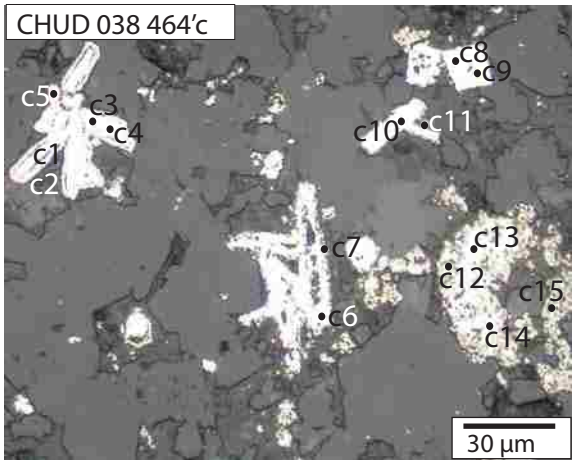
CHUD 038 464'c
c8
c9
c5
c3
c4
c10
c11
c1
c2
c7
c13
c12
c15
c6
c14
30 µm

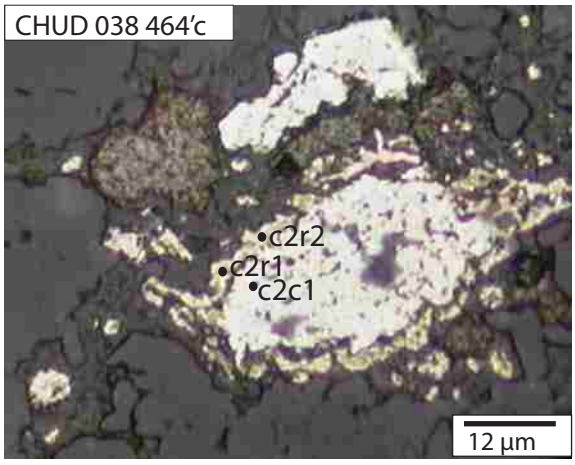
CHUD 038 464'c
c2r2
c2r1
c2c1
12 µm

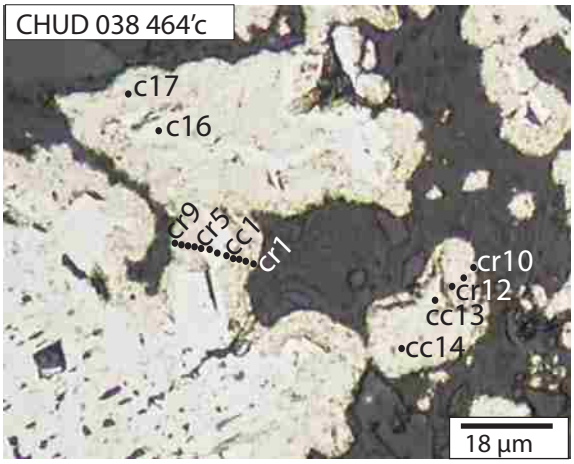
CHUD 038 464'c
c17
c16
cr9
cr5
cc1
cr1
cr10
cr12
cc13
cc14
18 µm

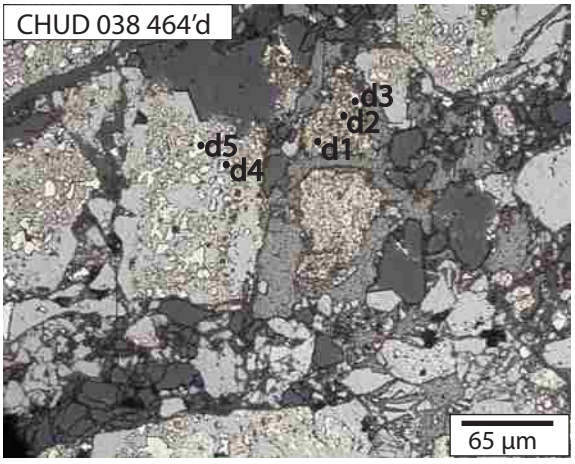
CHUD 038 464'd
d3
d2
d5
d1
d4
65 µm

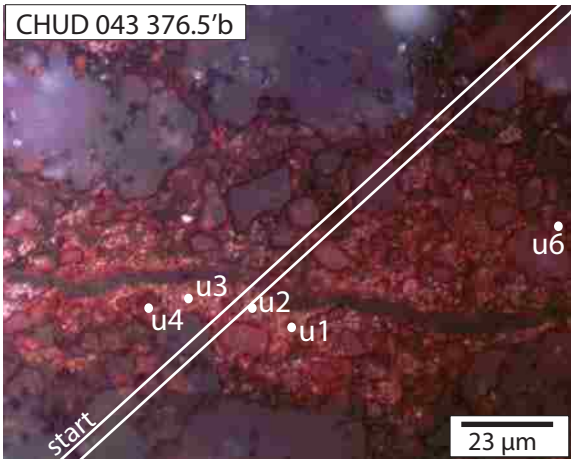
CHUD 043 376.5'b
u6
u3
u4
u2
u1
start
23 µm

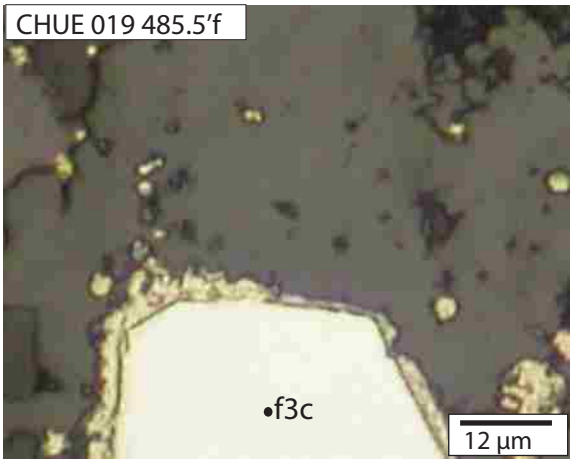
CHUE 019 485.5'f
f3c
12 µm

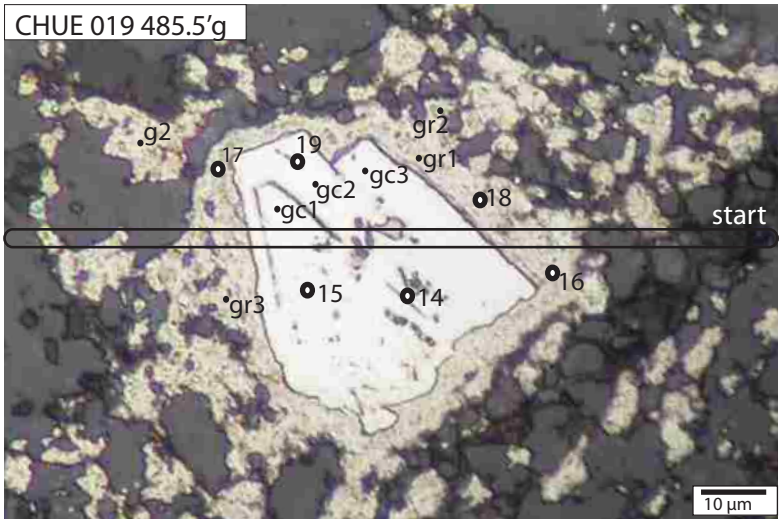
CHUE 019 485.5'g
g2
17
19
gr2
gr1
gc3
gc2
gc1
18
start
16
gr3
15
14
10 µm

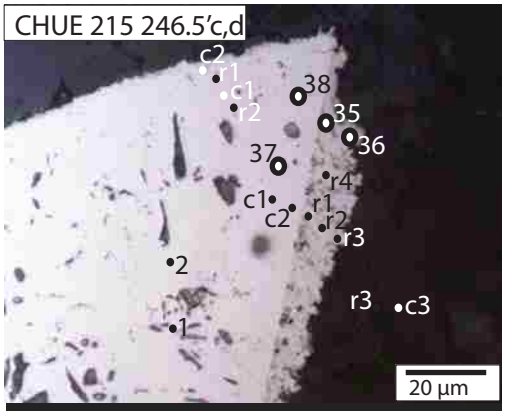
CHUE 215 246.5'c,d
c2
r1
c1
r2
38
35
36
37
r4
c1
r1
c2
r2
r3
2
r3
c3
1
20 µm

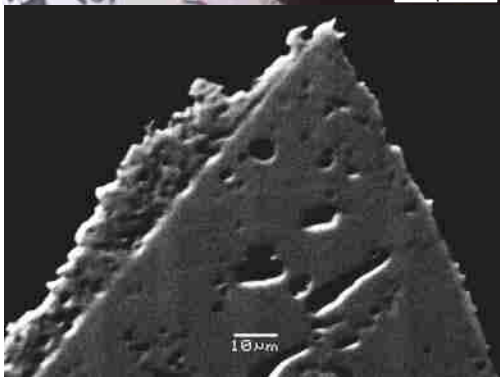
10µm

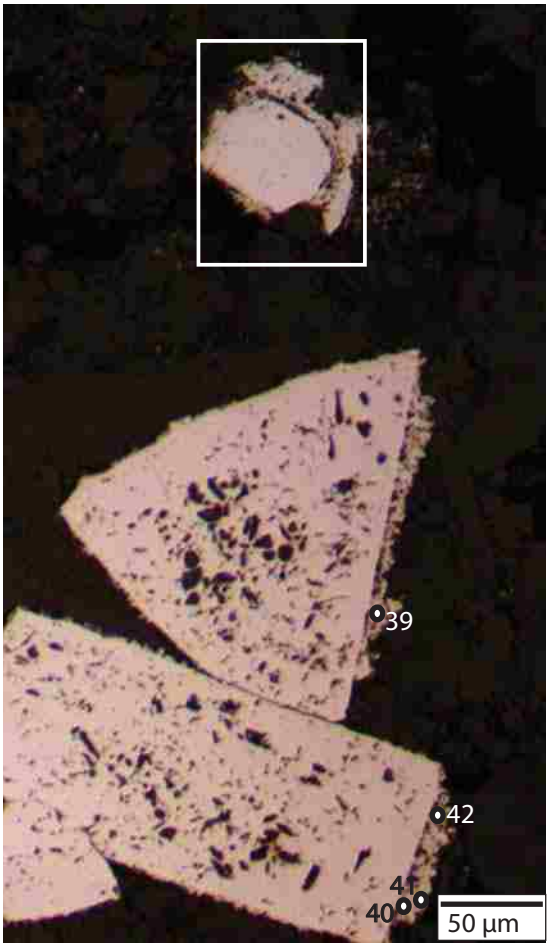
39
42
41
40
50 µm

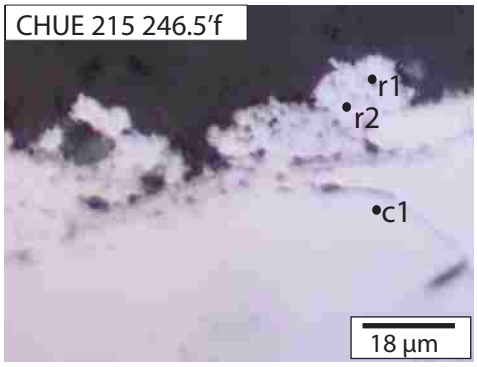
CHUE 215 246.5'f
r1
r2
c1
18 µm

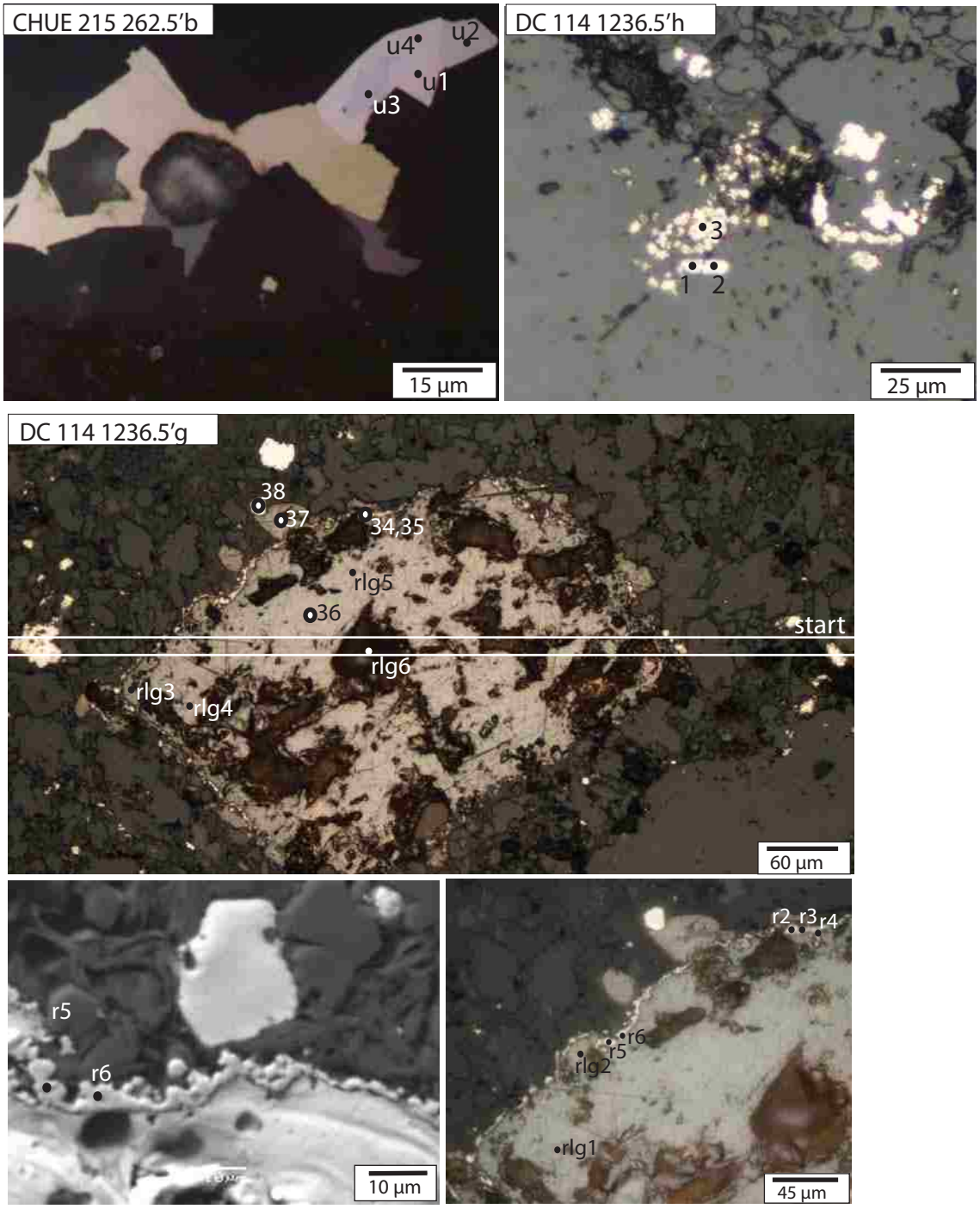
CHUE 215 262.5'b
u4
u2
u1
u3
15 µm
DC 114 1236.5'h
3
1
2
25 µm
DC 114 1236.5'g
38
37
34,35
rlg5
36
start
rlg6
rlg3
rlg4
60 µm
r5
r6
10 µm
r2
r3
r4
r6
r5
rlg2
rlg1
45 µm

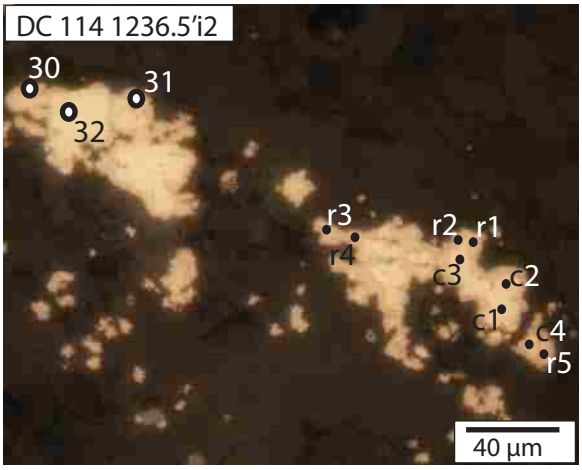
DC 114 1236.5'i2
30
31
32
r3
r2
r1
r4
c3
c2
c1
c4
r5
40 µm

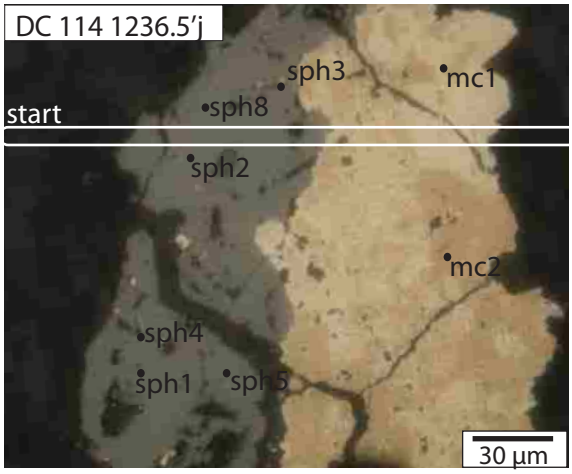
DC 114 1236.5'j
sph3
mc1
start
sph8
sph2
mc2
sph4
sph1
sph5
30 µm

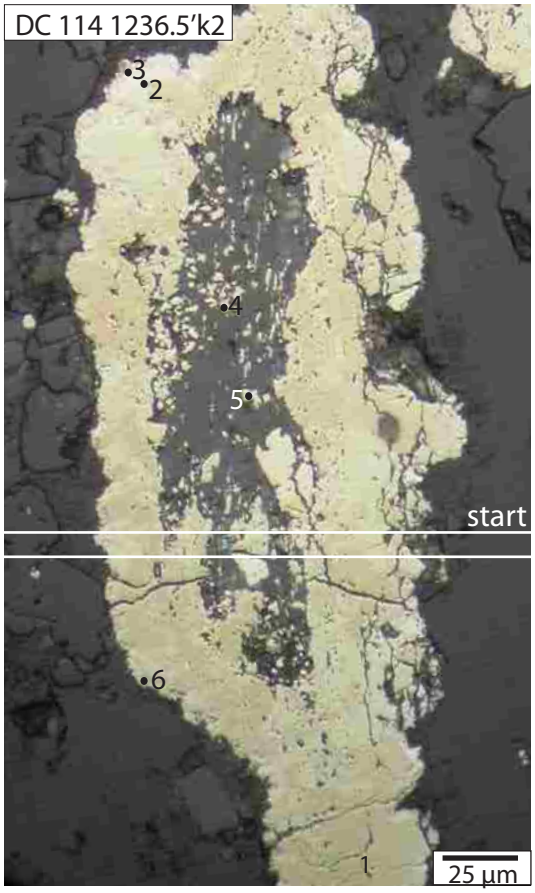
DC 114 1236.5'k2
3
2
4
5
start
6
1
25 µm

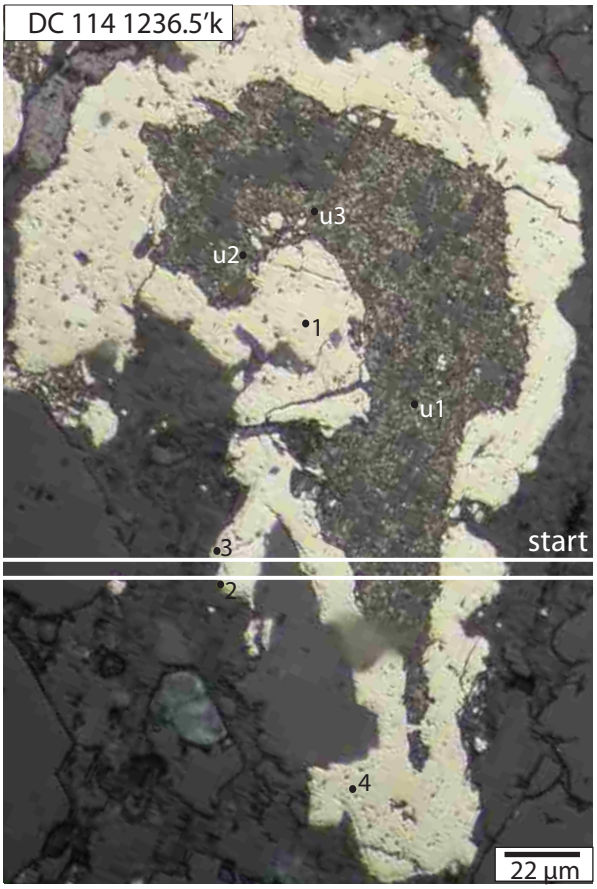
DC 114 1236.5'k
u3
u2
1
u1
3
start
2
4
22 µm

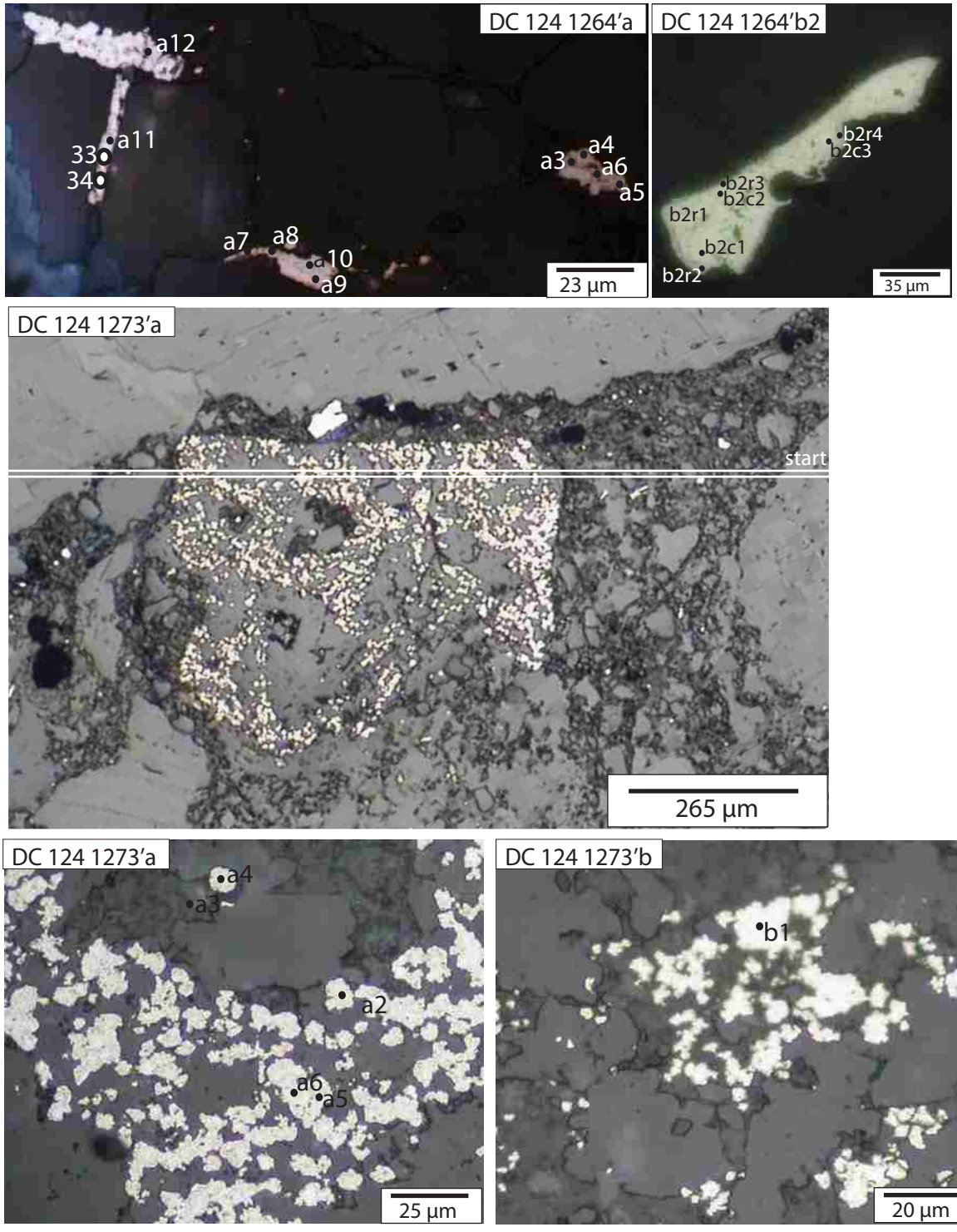
DC 124 1264'a
a12
a11
33
34
a3
a4
a6
a5
a7
a8
a10
a9
23 µm
DC 124 1264'b2
b2r4
b2c3
b2r3
b2c2
b2r1
b2c1
b2r2
35 µm
DC 124 1273'a
start
265 µm
DC 124 1273'a
a4
a3
a2
a6
a5
25 µm
DC 124 1273'b
b1
20 µm

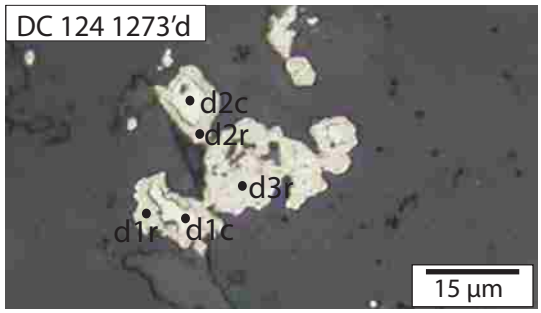
DC 124 1273'd
d2c
d2r
d3r
d1r
d1c
15 µm

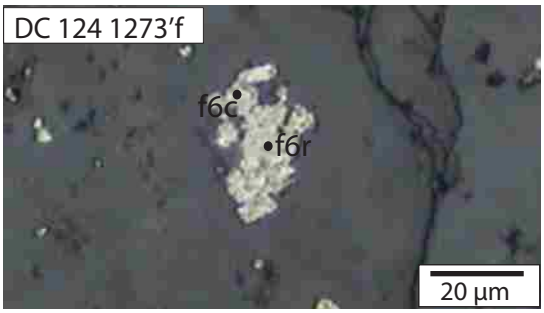
DC 124 1273'f
f6c
f6r
20 µm

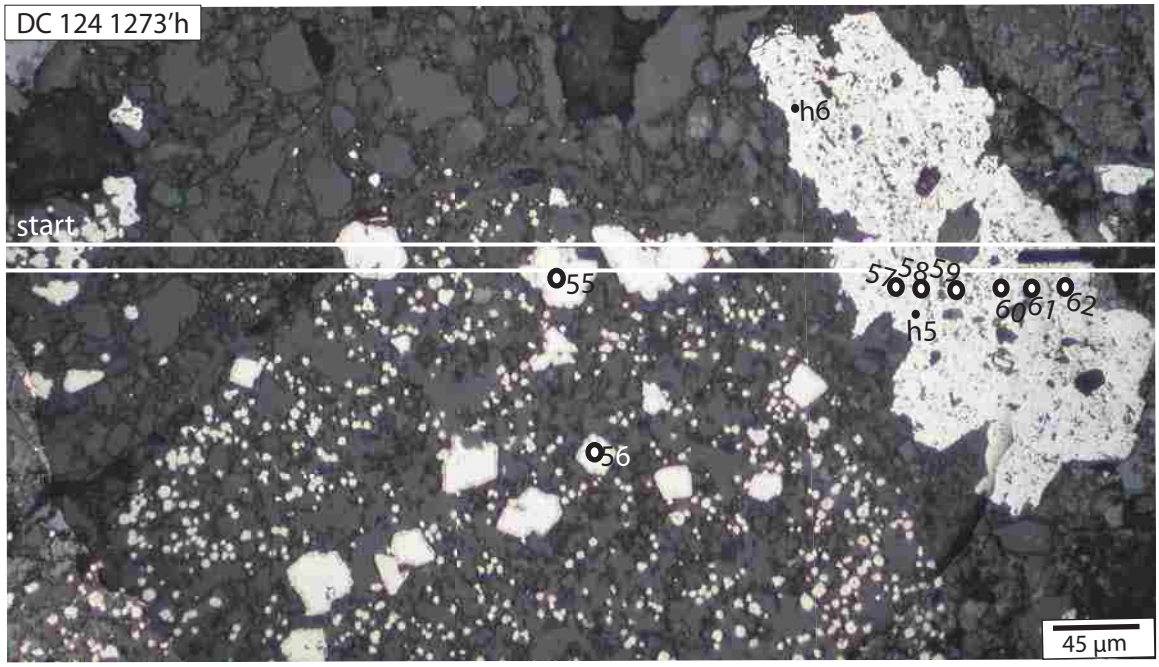
DC 124 1273'h
h6
start
55
57
58
59
60
61
62
h5
56
45 µm

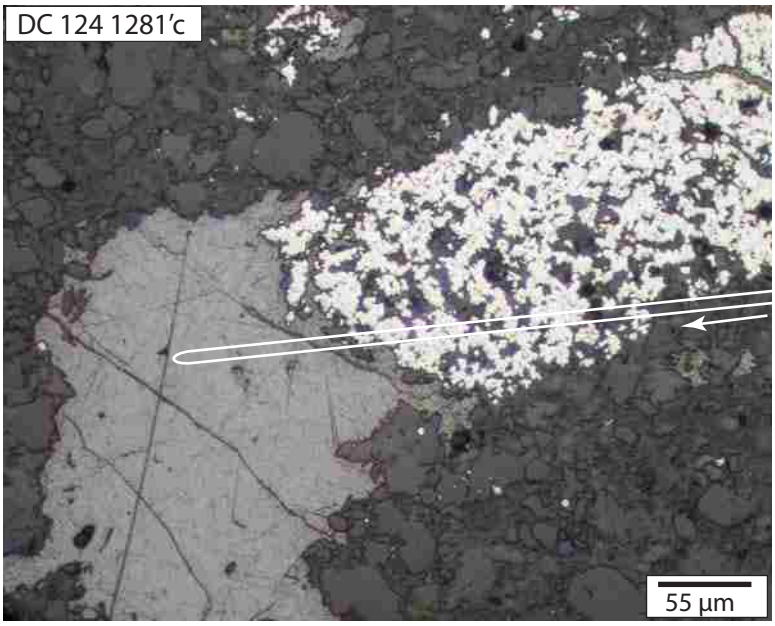
DC 124 1281'c
55 µm


DC 215 1497'c
15 µm

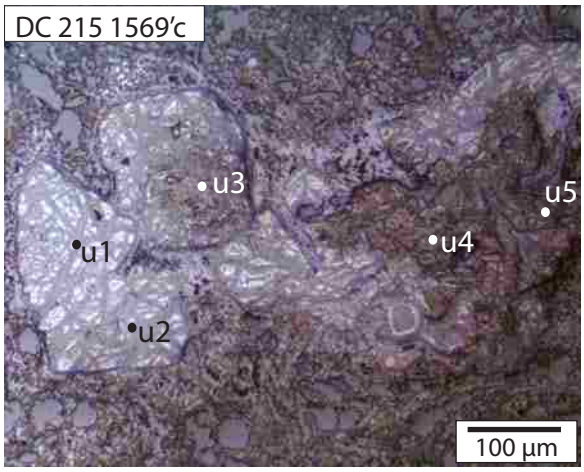
DC 215 1569'c
u1
u2
u3
u4
u5
100 µm

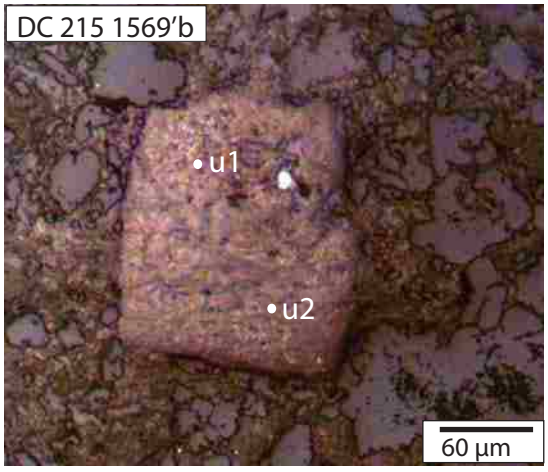
DC 215 1569'b
u1
u2
60 µm

REFERENCES

Almeida, C.M., Olivio, G.R., Chouinard, A., Weakly, C., and Poirier, G., 2010, Mineral paragenesis, alteration, and geochemistry of the two types of gold ore and host rocks from the Calrin-type Deposits in the southern part of the Goldstrike property, Northern Nevada: Implcations for sources of ore-forming elements, ore genesis, and mineral exploration: Economic Geology, v. 105, p. 971-1004.

Armstrong, R.L. and Ward, P.L., 1991, Evolving geographic patterns of Cenozoic magmatism in the North American Cordillera: The temporal and spatial association of magmatism and metamorphic core complexes: Journal of Geophysical Research, v. 96, p. 13,201–13,224.

Artz, Z.J., 2004, Igneous geochronology and petrography of the Cortez-Hills Carlin-type gold deposit, Cortez, Nevada: Unpublished M.Sc. thesis, Las Vegas, Nevada, University of Nevada Las Vegas, 40 p.

Barton, P.B, Jr., and Bethke, P.M., 1987, Chalcopyrite disease in sphalerite: Pathology and epidemiology: American Mineralogist, v. 72, p. 451-467.

Barrick Gold Corporation, 2012, Global Operations, North America, Cortez (http://www.barrick.com/GlobalOperations/NorthAmerica/Cortez/default.aspx).

Colgan, J. P., Henry, C.D., and John, D.A., 2011, Geologic map of the Caetano Caldera Lander and Eureka Counties, Nevada: Nevada Bureau of Mines and Geology Map 174, 1:75,000, 10 p.

Cook, H.E., and Corboy, J.J., 2004, Great Basin Paleozoic Carbonate platform: Facies, facies transitions, depostional models, platform architecture, sequence stratigraphy, and predictive mineral host models: USGS Open File report 2004-1078, 129 pp.

Cline, J.S., 2001, Timing of gold and arsenic sulfide mineral deposition at the Getchell Carlin-type gold deposit, North Central Nevada: Economic Geology, v. 96, p. 75-90.

Cline, J.S. and Hofstra, A.H., 2000, Ore-fluid evolution at the Getchell Carlin-type gold deposit, Nevada, USA: European Journal of Mineralogy, v. 12, p. 195-212.

Cline, J., Hofstra, A., Muntean, J., Tosdal, R., and Hickey, K., 2005, Carlin-type gold deposits in Nevada: Critical geologic characteristics and viable models, *in* Hedenquist, J.W., Thompson, J. F. H., Goldfarb, R. J., and Richards, J. P., eds., 100th Anniversary Volume: Society of Economic Geologists, Littleton, CO, p. 451-484.

Crafford, A.E.J., and Grauch, V.J.S., 2002, Geologic and geophysical evidence for the influence of deep crustal structures on Paleozoic tectonics and the alignment of

world class gold deposits, north central Nevada, USA: Ore Geology Reviews, v. 21, p. 157–184.

Dickinson, W., 2004, Evolution of the North American Cordillera: Annual Review Earth Planet Science, v. 32, p. 13–45.

Emsbo, P., Hofstra, A.H., Lauha, E.A., Griffin, G.L., and Hutchinson, R.W., 2003, Origin of high-grade gold ore, source of ore fluid components, and genesis of the Meikle and neighboring Carlin-type deposits, Northern Carlin Trend, Nevada: Economic Geology, v. 98, p. 1069-1100.

Evans, D., 2000, Carbonate-hosted breccias in the Meikle mine, Nevada and their relationship with gold mineralization: Unpublished M.S. thesis, Golden, Colorado, Colorado School of Mines, 266 p.

Gilluly, J., and Masursky, H., 1965, Geology of the Cortez Quadrangle, Nevada: U.S. Geological Survey Bu11etin 1175, 117 p.

Groff, J.A., Heizler, M.T., McIntosh, W.C., and Norman, D.I., 1997, 40Ar/39Ar dating and mineral paragenesis for Carlin-type gold deposits along the Getchell Trend, Nevada: Evidence for Cretaceous and Tertiary gold mineralization: Economic Geology, v. 92, p. 601–622.

Henry, C.D., and Boden, D.R., 1998. Eocene magmatism: the heat source for Carlin-type gold deposits of northern Nevada: Geology, v. 26, p. 1067–1070.

Henry, C., and Muntean, J., 2012, Mesozoic-Cenozoic magmatism and mineralization in the greater Cortez area: An example of NBMG framework studies: Geological Society of Nevada, Abstract, March 2012, Newsletter, v. 28, p. 3.

Hofstra, A.H., and Cline, J.S., 2000, Characteristics and models for Carlin-type gold deposits: Vikre, P., Thompson, T.B., Bettles, K., Christensen, O., and Parratt, R. eds., Society of Economic Geology Reviews, v. 13, p. 163-220.

Hofstra, A.H., Leventhal, J.S., Northrop, H.R., Landis, G.P., Rye, R.O., Birak, D.J., and Dahl, A.R., 1991, Genesis of sediment-hosted disseminated-gold deposits by fluid mixing and sulfidization: Chemical-reaction-path modeling of ore-depositional processes documented in the Jerritt Canyon district, Nevada: Geology, v. 19, p. 36-40.

Humphreys, E., 1995, Post Laramide removal of the Farallon slab, western United States: Geology, v. 23, p. 987-990.

Ilchik, R.P., and Barton, M.D., 1997, An amagmatic origin of Carlin-type gold deposits: Economic Geology, v. 92, p. 269–288.

Jackson, M., Arbonies, D., and Creel, K., 2010, Architecture of the Cortez Hills breccia body: Geological Society of Nevada, Symposium, Reno, Nevada, 14-22 May 2010, Proceedings, p. 97-123.

Jébrak, M., 1997, Hydrothermal breccias in vein-type ore deposits: A review of mechanisms, morphology, and size distribution: Ore Geology Reviews, v. 12, p. 111–134.

Johnston, M.K., and Ressel, M.W., 2004, Carlin-type and distal-disseminated Au-Ag deposits: related distal expressions of Eocene intrusive centers in North-central Nevada, *in* Muntean, J.L., Cline, J., Johnston, M.K., Ressel, Seedorff, E., and Barton, M.D., eds., Controversies on the origin of world-class gold deposits, Pt. I: Carlin-type gold deposits in Nevada: Society of Economic Geologists Newsletter, v. 59, p. 10–18.

Koenig, A.E., Rogers, R.R., and Trueman, C.N., 2009, Visualizing fossilization using laser ablation-inductively coupled plasma-mass spectrometry maps of trace elements in Late Cretaceous bones: Geology, v. 37, p. 511-514.

Large, R.R., Danyushevsky, C.H., Maslennikov, V., Maffre, S., Gilbert, S., Bull, S., Scott, R., Emsbo, P., Thomas, H., Sinch, B., and Foster, J., 2009, Gold and trace element zonation in pyrite using a laser imaging technique: Implications for the timing of gold in orogenic and Carlin-style sediment-hosted deposits: Economic Geology, v. 104, p. 635-668.

Leonardson, R.W., 2010, Barrick Cortez Gold Acres structure: Geological Society of Nevada, Symposium, Reno, Nevada, 14-22 May 2010, Proceedings, p. 17-29.

Longerich, H.P., Jackson, S.E., Günther, D., 1996, Laser ablation inductively coupled plasma mass spectrometric transient signal data acquisition and analyze concentration calculation: Journal of Atomic Spectrometry, v. 11, p. 899-904.

Lubben, J.D., 2004, Silicification across the Betze-Post Carlin-type Au deposit: Clues to ore fluid properties and sources, Northern Carlin Trend, Nevada: Unpublished M.S. thesis, Las Vegas, Nevada, University of Nevada Las Vegas, 156 p.

Mineral Data Publishing, 2001, Aktashite, version 1 (http://www.handbookofmineralogy.org/pdfs/aktashite.pdf)

Mineral Data Publishing, 2001, Christite, version 1 (http://www.handbookofmineralogy.org/pdfs/aktashite.pdf)

Mineral Data Publishing, 2001, Routhierite, version 1 (http://www.handbookofmineralogy.org/pdfs/aktashite.pdf)

Muir, T.L., 2002, The Hemlo gold deposit, Ontario, Canada; principal deposit characteristics and constraints on mineralization: Ore Geology Reviews, v. 21, p 1-66.

Muntean, J.L., Cline, S.C., Simon, A.C., and Longo, A.A., 2011, Magmatic-hydrothermal origin of Nevada's Carlin-type gold deposits: Nature Geoscience, DOI: 10.1038/NGE01064, 6 p.

Nevada Bureau of Mines and Geology, 2010, The Nevada mineral industry 2010: Special Publication MI-2010, Mackay School of Eartch Sciences and Engineering; Reno, Nevada, 151p.

Pan, Y. and Fleet, M.E., 1995, The late Archean Hemlo gold deposit, Ontario, Canada; a review and synthesis: Ore Geology Reviews, v. 9, p. 455-488.

Palenik, C.S., Utsunomiya, S., Reich, M., Kesler, S.E., Wang, L., and Ewing, R.C., 2004, "Invisible" gold revealed: Direct imaging of gold nanoparticles in a Carlin-type deposit: American Mineralogist, v. 89, p. 1359-1366.

Poole, F.G., Stewart, J.H., Palmer, A.R., Sandberg, C.A., Madrid, R.J., Ross, R.J., Hintze, L.F., Miller, M.M., and Wrucke, C.T., 1992, Latest Precambrian to latest Devonian time; development of a continental margin, *in* Burchfield, B.C., Lipman, P.W., and Zoback, M.L., eds., The Cordilleran Orogen: Conterminous U.S.: Boulder, Colorado, Geological Society of America, The Geology of North America, v. G-3 p. 9-56.

Radtke, A.S., Dickson, F.W., Slack., J.F., and Brown, K. L., 1977, Christite, a new thallium mineral from the Carlin gold deposit, Nevada: American Mineralogist, v. 62, p. 421-425.

Reich, M., Kesler, S.E., Utsunoyiya, S., Palenik, C.S., Chryssoulis, S., and Ewing, R.C., 2005, Solubility of gold in arsenian pyrite: Geochimica et Cosmochimica Acta, v. 69, p. 2781-2796.

Ressel, M. W. & Henry, C. D., 2006, Igneous geology of the Carlin trend, Nevada: Development of the Eocene plutonic complex and significance for Carlin-type gold deposits: Economic Geology, v. 101, p 347-383.

Roberts, R., Hotz, P., Gilluly, J., and Ferguson, H., 1958, Paleozoic rocks in north-central Nevada: American Association of Petroleum Geologists Bulletin, v. 42, p. 2813-2857.

Saleeby, J.B., Hannah, J.L., and Varga, R.J., 1987, Isotopic age constraints of middle Paleozoic deformation in the northern Sierra Nevada, California: Geology, v. 15, p. 757-760.

Seedorff, E., 1991, Magmatism, extension, and ore deposits of Eocene to Holocene age in the Great Basin—Mutual effects and preliminary proposed genetic relationships: Geology and ore deposits of the Great Basin: Geological Society of Nevada, Symposium, Reno-Sparks, April 1990, Proceedings, v. 1, p. 133–178.

Seedorff, E., Dilled, J.H., Proffett, J.M., Einaudi, M.T., Zurcher, L., Stavast., W.J.A., Johnson, D.A., and Barton., M.D., 2005, Porphry deposits: characteristics and orogeny of hypogene features, *in* Hedenquist, J.W., Thompson, J. F. H., Goldfarb, R. J., and Richards, J. P., eds., 100th Anniversary Volume: Society of Economic Geologists, Littleton, CO, p. 251-298.

Sillitoe, R.H., 1985, Ore-related breccias in volcanoplutonic arcs; Economic Geology, v. 80, p. 1467–1514.

Sillitoe, R., 2008, Major gold deposits of the North and South American Cordillera: Distribution, tectonomagmatic settings, and metallogenic considerations: Economic Geology, v. 103, p. 663-687.

Sillitoe, R.H., and Bonham, H.F., Jr., 1990, Sediment-hosted gold deposits: Distal products of magmatic-hydrothermal systems: Geology, v. 18, p. 157-161.

Spurr, J.E., 1898, Geology of the Aspen mining district, Colorado, with atlas: U.S. Geological Survey of Montana, v. 31, 260 p.

Stewart, J., 1980, Geology of Nevada: Nevada Bureau of Mines and Geology Special Publication 4, 136p.

Tosdal, R.M., Cline, J.S., Fanning, C.M., and Wooden, J.L., 2003, Lead in the Getchell-Turquoise Ridge Carlin-type gold deposit from the perspective of potential igneous and sedimentary rock sources in northern Nevada: Implications for the fluid and metal sources: Economic Geology, v. 98, p. 1189-1211.

Tosdal, R.M., Wooden, J.L., and Kistler, R.W., 2000, Inheritance of Nevadan mineral belts from Neoproterozoic continental breakup, *in* Cluer, J.K., Price, J.G., Struhsacker, E.M., Hardyman, R.F., and Morris, C.L., eds., Geology and Ore Deposits 2000: The Great Basin and Beyond: Reno, Geological Society of Nevada Symposium, Proceedings, p. 451–466.

Venendaal, J.F., 2007, Trace element geochemistry and carbonate alteration as indicators for gold mineralization at the Cortez Hills deposit, Lander County, Nevada: Unpublished M.Sc. thesis, Golden, Colorado, Colorado School of Mines, 116 p.

VITA

Graduate College
University of Nevada, Las Vegas

Lindsey R. Clark
lindsey.clark@gmail.com

Degrees:

Bachelor of Science, Geoscience, 2009
University of Nevada, Las Vegas

Thesis Title: Ore and Gangue Mineral Paragenesis of the Cortez Hills Carlin-Type Gold Deposit, Nevada: Evidence for Coincident High-Grade Gold Deposition and Collapse Brecciation

Thesis Examination Committee:

Co-Chairperson, Jean S. Cline, Ph. D.

Co-Chairperson, Adam C. Simon Ph. D.

Committee Member, John Muntean, Ph. D.

Graduate Faculty Representative, Barbara Luke, Ph. D.